# Manganese Promotion in Titania-Supported Cobalt Fischer-Tropsch Catalysis

**Fernando Morales Cano**

ISBN 90-393-4189-3

Drukkerij Ponsen & Looijen, Wageningen

# Manganese Promotion in Titania-Supported Cobalt Fischer-Tropsch Catalysis

Mangaanpromotie in titaangedragen kobalt
Fischer-Tropsch katalyse

(met een samenvatting in het Nederlands)

Proefschrift

ter verkrijging van de graad van doctor aan de Universiteit Utrecht
op gezag van de Rector Magnificus, Prof. Dr. W.H. Gispen, ingevolge het
besluit van het College voor Promoties in het openbaar te verdedigen op
woensdag 29 maart 2006 des middags te 12.45 uur

door

**Fernando Morales Cano**

geboren op 23 september 1977 te Madrid

Promoter: Prof. Dr. Ir. B.M. Weckhuysen
Faculteit Scheikunde, Universiteit Utrecht

Co-promoter: Dr. F.M.F. de Groot
Faculteit Scheikunde, Universiteit Utrecht

The research described in this thesis was financially supported by Shell Global Solutions

# Contents

# 1

# General Introduction

## Fischer-Tropsch synthesis

Franz Fischer, head of the Max-Planck Institut für Kohlenforschung in Mülheim (Germany) and Hans Tropsch, a co-worker of Fischer and professor of chemistry in Prague (Czech Republic), Mülheim (Germany) and Chicago (Illinois, USA), discovered in 1922 a catalytic reaction between CO and $H_2$, which yields mixtures of higher alkanes and alkenes [1-20]. This invention made it possible for Germany to produce fuels from its coal reserves and by 1938 nine Fischer-Tropsch (FT) plants were in operation making use of, *e.g.,* cobalt-based FT catalysts. The expansion of these plants stopped around 1940, but existing plants continued to operate during World War II. It is worthwhile to notice that in 1944, Japan was operating three FT plants based on coal reserves. Whilst being a major scientific as well as a technical success, the FT process could not compete economically with the refining process of crude oil, becoming important starting from the 1950s. All this coincided with major discoveries of oil fields in the Middle East and consequently the price of crude oil dropped. Although a new FT plant was built in Brownsville (Texas, USA) in 1950, the sharp increase in the price of methane caused the plant to shut down. Thus, due to bad economics FT technology became of little importance for the industrial world after World War II and no new FT plants were constructed. An exception was South Africa, which started making fuels and chemicals from gasified coal based on the FT process a half century ago due to embargoes initiated by the country's apartheid policies. Till today, South Africa's Sasol (South African Coal, Oil and Gas Corporation, Ltd.), which built its first commercial FT plant in 1955, Exxon Mobil and Shell Global Solutions are known as the major players in this field [21-23].

It is remarkable to notice that there is today a renewed interest in FT technology mainly due to:

(i) The rising costs of crude oil. For some time now, the oil prices are well above $ 50 per barrel.

(ii) The drive to supply environmentally friendly automotive fuels, more in particularly, the production of synthetic sulphur-free diesel, especially interesting for the European car fleet.

(iii) The commercialisation of otherwise unmarketable natural gas at remote locations. $CO_2$ emission regulations will certainly lead in the future to a ban on natural gas flaring near crude oil production wells.

This all has led to recent decisions on major investments by big petrochemical companies, such as Shell [22] and Exxon Mobil [23], to built large scale FT plants in Qatar. This will result in an important shift from crude oil to natural gas and coal as well as bio-fuels, as feedstock for the production of fuels and chemicals in the decades to come [24-27]. Industry projections estimate that by 2020 5% of the production of chemicals could be based on FT

technology with methane and coal instead of crude oil refining operations. All this is especially promising in view of the long-term reserves of coal, which are estimated to be more than 20 times that of crude oil. Furthermore, coal is still used as the carbon source at the largest and economically successful FT complex, namely the plants Sasol One to Three near Sasolburg in South Africa [21]. Other operating FT complex is the Shell Middle Distillate Synthesis (SMDS) plant in Bintulu (Fig. 1). This FT plant converts natural gas to long chain paraffins, which are subsequently hydrocracked to produce liquid fuels.

The stoichiometry of the FT process can be derived from the following two reactions, the polymerization reaction to produce hydrocarbon chains (1), and the water-gas shift reaction (2):

$$CO + 2\ H_2 \rightarrow -(-CH_2-)- + H_2O \qquad (1)$$

$$CO + H_2O \leftrightarrow H_2 + CO_2 \qquad (2)$$

The overall stoichiometry, in case reaction (2) is completely driven to the right, is:

$$2\ CO + H_2 \rightarrow\ -(-CH_2-)- + CO_2 \qquad (3)$$

with $\Delta H_{227}$ = -204.8 kJ, while the maximum attainable yield is 208.5 g of alkenes $C_nH_{2n}$ per $Nm^3$ of a mixture of 2 CO and $H_2$ for complete conversion [29-30]. The $CO/H_2$ is usually called synthesis gas, or in short syngas. The production of syngas, either by partial oxidation or steam reforming, can account for over 60% of the total cost of the FT complex since the gasification process is highly endothermic and therefore a high-energy input is required [29-31]. It should also be clear that the carbon source used, being either coal or natural gas, is available at low cost, while the gasification of methane is much more efficient than that of coal since coal simply has a much lower hydrogen content. The syngas produced is then fed into a FT reactor, which converts it into a paraffin wax that is subsequently hydrocracked to make a variety of chemicals, such as diesel, naphtha, lubricants and gases.

**Figure 1.** Shell Middle Distillate Synthesis (SMDS) Fischer-Tropsch plant in Bintulu (Malalysia) operating since 1993 and with a production level of 15000 bpd.

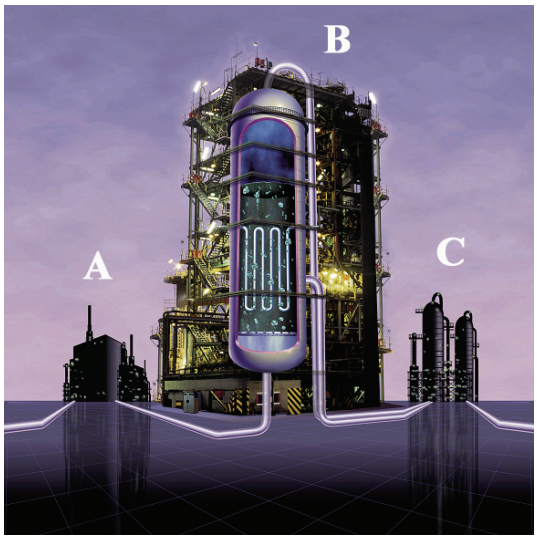


**Figure 2.** Picture illustrating the different steps in the Fischer-Tropsch process: syngas production (A), hydrocarbon formation (B), and product upgrade (C).

A scheme of the FT reaction process, including syngas production and hydrocracking of the wax, are given in Fig. 2 and 3 [28].

The FT reaction involves the following main steps at the catalyst surface:

(i) The adsorption and maybe dissociation of CO;

(ii) The adsorption and dissociation of $H_2$;

(iii) Surface reactions leading to alkyl chains, which may terminate by the addition or elimination of hydrogen, giving rise to either paraffin or olefin formation.

(iv) Desorption of the final hydrocarbon products, which can be considered as the primary products of the FT process.

(v) Secondary reactions taking place on the primary hydrocarbon products formed due to, *e.g.,* olefin readsorption followed by hydrogenation or chain growth reinitiation.

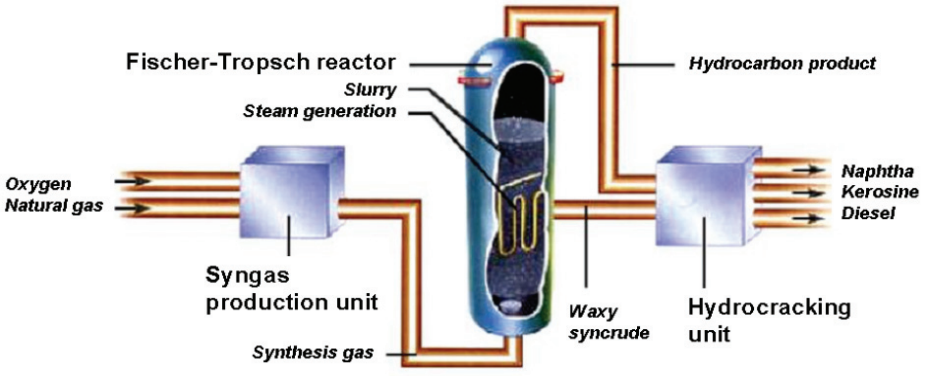


**Figure 3.** Detailed flow shart of the Fischer-Tropsch process based on natural gas as a feedstock.

Various detailed mechanisms have been proposed and this matter still remains a controversial issue in the literature.
Some of the scientific questions that arise are:

(i) Does the adsorbed CO molecule first dissociate into chemisorbed carbon and oxygen atoms? The chemisorbed carbon formed can then be hydrogenated to surface methyl and methylene groups in subsequent steps. Chain growth occurs by stepwise addition of $C_1$ monomers to a surface alkyl group.

(ii) Is the adsorbed CO molecule hydrogenated to a CHO or HCOH species, which inserts in the growing hydrocarbon chain?

(iii) Is CO directly inserted in the growing chain and then subsequently hydrogenated?

It should be clear that a discussion on the FT mechanism is beyond the scope of this thesis and we refer the interested reader to several review papers on this topic [6, 14, 32-42]. In this respect, it is noteworthy to mention the excellent updates by Dry on the challenges and technological implementations of Co FT synthesis [17-20].

The overall selectivity of the FT process is intimately related to the production of methane, which is not economic, since the back conversion to syngas encounters severe thermal and yield penalties. Consequently, substantial research efforts have been devoted to decrease the methane production by adjusting the catalyst composition. It is generally considered that the choice of the catalyst material is central to the FT process. The latest generation of FT catalysts are based on cobalt and the cobalt nanoparticles are usually supported on an oxide support, mostly silica, alumina and titania, while some promoters, e.g., some noble metals, are added to the catalyst material in order to enhance the Co dispersion. Other metal oxide promoters are often added to the catalysts to improve the FT selectivity, e.g., decreasing the methane production. Reducing the amount of promoter, especially in the case of noble metals, as well as the amount of cobalt are ways to reduce the catalyst production costs and it may be of no wonder that large research efforts in both academia and industrial laboratories have focused on finding the best performing, durable, but still cheap FT catalyst formulation. Almost every industrial player in the FT field has its own catalyst formulation, and is - as expected - very secretive about their exact composition of matter in the catalyst materials applied in pilot and/or industrial plants. The choice of the catalyst material is also related to the type of reactor used. In this respect, it is relevant to mention that Shell and BP use fixed bed reactors, whereas Sasol/Chevron and Exxon Mobil make use of slurry phase reactors. The latter plants require the continuous addition of catalyst material.

## Gas-to-liquid technology

At present, the main commercial interest in FT is the production of high quality sulfur-free synthetic diesel fuels from natural gas, currently being flared at crude oil production wells [21-27]. This renewed interest in FT synthesis has not just only come about as a result of the abundant supply of natural gas, but also because of the global development of fuel supplies and environmental regulations to improve air quality in cities around the world. While the concept of a hydrogen fuel economy remains an important option for the more distant future, synthetic diesel is being promoted by the fuel industry as the most viable next step towards the creation of a sustainable transport industry. Some advantages of synthetic diesel are:

- Low content of suphur and aromatic compounds
- High cetane number
- Low particulate formation
- Low $NO_x$ and CO emission

At the same time, increased efficiencies in the FT process and the ability – based on past experience - to build large-scale plants to capture the economies of scale have made the FT gas-to-liquid (GTL) technology attractive and competitive with the current crude oil refinery industries.

It has been estimated that FT GTL should be viable at crude oil prices of about $ 20 per barrel. For some time now the oil price has been well above $ 50 per barrel (more recently it has even topped above $ 70 per barrel), making it a very appealing technology for countries, having huge reserves of natural gas, but little local market for it and no major pipeline infrastructure to ship it to larger economies. Alternatively, such countries could crack ethane or propane to make ethylene or propylene and further convert it into polyethylene or polypropylene, which can then be shipped to more heavily populated areas in the world. All this holds for the Middle East countries and, *e.g.,* Saudi Arabia is known to heavily invest in propane dehydrogenation plants and polypropylene production facilities, while Qatar is focusing on FT GTL activities. These activities are concentrated near Ras Laffan in Qatar's northern gas field, holding 9% of the world's proven gas resources [25]. Table 1 gives a summary of the currently operated and recently announced FT plants based on natural gas, together with the expected production levels and the industrial companies and countries involved [21-23, 26]. Industry projections suggest that by 2020 the total GTL capacity in the world could reach more than $1.10^6$ bpd.

Currently, there are two FT plants operating on offshore methane. The first one is the Shell MDS plant in Bintulu (Malaysia), which produces 15000 barrels per day. The second

**Table 2**. Currently operating and recently announced FT plants based on methane, together with the industrial companies and countries involved, the used Co FT catalyst technology, the (expected) production levels and the (expected) year of start-up (barrels per day, bpd).

| Country | Company or companies | Technology | Production (bpd) | Start-up year |
|---|---|---|---|---|
| South-Africa | PetroSA | Sasol's slurry phase technology | 20000 | 1992 |
| Malaysia | Shell MDS | Shell middle distillate synthesis (SMDS) fixed-bed technology | 15000 | 1993 |
| Qatar | Sasol and Qatar Petroleum, in alliance with Chevron | Sasol's slurry phase technology | 34000 | 2006 (2 other plants are scheduled to operate in the coming years with the second FT plant having a scale of 65000 bpd) |
| Nigeria | Chevron Nigeria (Sasol/Chevron alliance) and Nigeria National Petroleum Company | Sasol's slurry phase technology | 34000 | 2007 |
| Qatar | Shell and Qatar Petroleum | Shell middle distillate synthesis (SMDS) fixed-bed technology | 140000 | 2009 (first train of 70000 bpd) /2010 (second train of 70000 bpd) |
| Qatar | Exxon Mobil and Qatar Petroleum | Advanced gas conversion for the 21th centure (AGC-21) technology | 154000 | 2011 |

one is the Moss Bay plant (PetroSA) located in South Africa. Recently, Sasol/Chevron, ExxonMobil and Shell announced major investments in GTL plants [21-23].

In addition, there are many small (mainly for local markets) and large (mainly for export) project proposals for FT GTL projects on the table. Most of the large project proposals are in the Middle East (Qatar), while the other envisaged projects are in Russia, Australia, Argentina, Egypt, Iran, Bolivia, Brazil, Indonesia, Malaysia and Trinidad. Especially, Russia is expected to have significant long-term potential for GTL technology taking into account the huge country's gas reserves.

## Fischer-Tropsch catalysts

It is well known that all Group VIII transition metals are active for FT synthesis. However, the only FT catalysts, which have sufficient CO hydrogenation activity for commercial application, are composed of Ni, Co, Fe or Ru as the active metal phase. These metals are orders-of-magnitude more active than the other Group VIII metals and some characteristics of Ni-, Fe-, Co- and Ru-based FT catalysts are summarized in Table 3.

**Table 3.** Overview of some characteristics of Ni-, Fe-, Co- and Ru-based F-T catalysts.

| Active metal | Price | FT activity | WGS activity | Hydrogenation activity |
|---|---|---|---|---|
| Ni | ++++ | + | +/- | +++++ |
| Fe | + | ++ | +++ | + |
| Co | +++ | +++ | +/- | +++ |
| Ru | +++++ | ++++ | +/- | +++ |

The exact choice of the active FT metal to be used in a particular catalyst formulation depends on a number of parameters, including the source of carbon used for making syngas, the price of the active element and the end products wanted. FT catalysts for the conversion of syngas made from a carbon-rich source, such as coal, are usually based on Fe. This is due to the high WGS activity of Fe, as given in reaction (2), so that less hydrogen is required and oxygen exits the reactor in the form of carbon dioxide. There are, however, new environmental considerations such as the greenhouse effect, which may preclude the future use of Fe precisely due to its high WGS activity. In the case of syngas production from hydrogen-rich carbon sources, such as natural gas, the preferred catalysts due to their lower WGS activities are based on Co or Ru.

Nickel FT catalysts, due to an easy dissociation of CO, possess too much hydrogenation activity, unfortunately, resulting in high yields of methane. In addition, with increasing reaction temperature the selectivity changes to mainly methane. This tendency is also observed with Co- and Ru-based catalysts. Instead, with Fe, the selectivity towards methane remains low even at high reaction temperatures. Ru is the most active FT element working at the lowest reaction temperature [43] (*e.g.* at 150°C very high molecular weight products have been isolated). However, the very low availability and as a consequence the high cost of Ru makes the use of this element in large-scale industrial FT applications questionable.

In general, Co and Fe are the most appropriate elements to prepare commercially interesting FT catalysts, and both systems have their own advantages and disadvantages. It is important to notice that although Co is much more active than Fe in FT, its price is over 250

times more expensive. Because of the relatively low cost of Fe, fresh catalyst material can be added on-line to fluidizied bed reactors, and this practice results in long runs at high conversion levels. This luxury cannot be afforded for the more expensive Co FT catalysts and therefore, it is vital that the amount of Co employed is minimized, while maintaining its high activity and long effective catalyst life. Co-based catalysts are preferred for the production of paraffins, as they give the highest yields for high molecular weight hydrocarbons from a relatively clean feedstock, and produce less oxygenates than Fe-based catalysts. This is due to a higher hydrogenation activity of Co-based compared to Fe-based catalysts. On the other hand, if linear olefins are wanted as the end product, it is better to employ Fe-based FT catalysts because there is less secondary hydrogenation of the primary formed olefins. However, Fe-based catalysts are also known to produce at high temperatures aromatics and oxygenated compounds, as by-products.

Another difference between Co and Fe is their sensitivity towards impurities in the gas feed, such as $H_2S$. In this respect, Fe-based catalysts have been shown to be more sulfur-resistance than their Co-based counterparts. This is also the reason why for Co FT catalysts it is recommended to use a sulphur-free gas feed. For this purpose, a zinc oxide bed is included prior to the fixed bed reactor in the Shell plant in Malaysia to guarantee effective sulphur removal. Co and Fe FT catalysts also differ in their stability. For instance, Co-based FT systems are known to be more resistant towards oxidation and more stable against deactivation by water, an important by-product of the FT reaction (reaction (1)). Nevertheless, the oxidation of cobalt with the product water has been postulated to be a major cause for deactivation of supported cobalt catalysts. Although, the oxidation of bulk metallic cobalt is (under realistic FT conditions) not feasible, small cobalt nanoparticles could be prone to such reoxidation processes.

## Cobalt-based Fischer-Tropsch catalysts

While there have been much activity in the literature addressing Fe, Ru and Ni F-T catalysts, the largest body of papers and patents in the last three decades have dealt with Co-based FT catalysts in attempts to make more active catalysts with high wax selectivities. It is, however, remarkable to notice that modern Co FT catalysts are still very similar to the ones prepared by Fischer and co-workers; *i.e.*, they consist of promoted cobalt particles supported on a metal oxide and most of, if not all, Co-based FT catalyst compositions contain the following components:

(i) Co as the primary FT metal;

(ii) A promoter metal, possessing noble metal behavior, e.g., Ru, Re, Pd, Pt, Rh and Ir. The main function of this promoter element is to facilitate the reduction of the

cobalt nanoparticles; and as a consequence to increase the number of active cobalt sites. As will be shown in the next chapter these promoters have also other beneficial effects on the catalyst performance;

(iii) An oxidic promoter elements, such as lanthanide and thorium oxide, ceria, zirconia, titania, vanadia, chromia and manganese oxides. However, their roles are much broader; and

(iv) A high surface area oxide support, mostly alumina, titania and silica, although the use of supports such as ceria, zirconia, magnesia, gallia, silica-alumina, zeolites (*e.g.* zeolite Y, silicalite, ZSM-5 and ETS-10), ordered mesoporous oxides (*e.g.* MCM- and SBA-type materials having high surface area and a narrow pore-size distribution) and delaminated zeolites (*e.g.* ITQ-2 and ITQ-6) are also reported in literature [44-53].

The role of the support material is rather well established. It provides mechanical strength and thermal stability to the Co nanoparticles, while facilitating a high Co dispersion. The choice of the support oxide largely determines the number of active Co metal sites stabilized after reduction, as well as the percentage of supported cobalt oxides that can be reduced to cobalt metal. This is due to a different Co-support oxide interaction. A strong Co-support oxide interaction, as it occurs in the case of alumina and titania, favors the dispersion of the supported Co particles, but at the same time decreases their reducibility, leading to catalyst materials with a limited number of accessible surface Co metal sites. On the contrary, a much weaker interaction leading to a higher Co reducibility occurs for $Co/SiO_2$ catalysts. In this case, the cobalt particles tend to agglomerate on the support surface during the thermal activation treatments resulting in a relatively low Co dispersion, and thus a low number of surface Co metal sites. Recent studies with ordered mesoporous oxides have shown that cobalt particles with defined particle sizes by confinement within the mesoporous channels are active for FT catalysis [44-53]. An increase of the average particle size of the supported Co particles was found with increasing the pore size of the mesopores silica; these larger particles are more reducible and lead to catalyst materials with higher FT activity. Similar effects have been observed for $Co/SiO_2$ catalysts made from commercial amorphous silicas with increasing pore diameters [54].

## Scope and outline of the thesis

The goal of the work described in this thesis is the investigation of the physicochemical and catalytic properties of $TiO_2$-supported cobalt Fischer-Tropsch catalysts and of the role played by MnO as a promoter. The main body of the thesis focuses on a detailed characterization of $Co/Mn/TiO_2$ catalyst systems using spectroscopic and microscopic techniques to provide new insights on the active site composition and the chemical state and location of manganese. Special attention has been directed towards the use of *in situ* spectroscopic techniques in order to study the catalyst composition under more realistic conditions.

Due to the relevance of promoter additives for FT catalysis and because of the large amount of information that can be found in the literature, we carried out a survey on all promoters that have been employed for Co-based FT catalysts, as reported in the last 25 years. In **Chapter 2** we present this review article, giving an extensive overview of the results, including a classification of the different modes of promotion action. In **Chapter 3** the synthesis and characterization of manganese promoted $Co/TiO_2$ catalysts is described. The choice of the preparation method turned out to be crucial to achieve the desired interaction between the manganese and cobalt species after calcination. In order to obtain different manganese locations in the catalysts, various synthesis methods were employed (e.g., incipient wetness impregnation, homogeneous deposition precipitation, or a combination of both). The characterization results obtained by XAFS, XPS, XRD, and STEM-EELS demonstrates that manganese can be either present in a separate or associated state with the $Co_3O_4$ particles. In **Chapter 4** we present our reduction studies of the $Co/TiO_2$ and $Co/Mn/TiO_2$ catalysts, showing the influence of a manganese promoter (placed in different locations) on the reducibility of the $Co_3O_4$ particles. Additionally, XAFS at the Co K-edge is used to quantify the degree of cobalt reduction after activation treatments, while the size and morphology of the cobalt particles are estimated by XAFS, XPS and TEM. The chapter ends with an attempt to correlate the structural results with the FT catalytic performances at pressures of 1 bar. **Chapter 5** deals with the characterization of the manganese phase in the reduced $Co/Mn/TiO_2$ catalysts. A combination of the XAFS at the Mn K-edge and STEM-EELS techniques to investigate the Mn local environment and location, turned out to be an excellent approach to elucidate the chemical structures of manganese in the different catalysts. Furthermore, quantitative XPS was used to illustrate a spreading of manganese occurring during the reduction process. In **Chapter 6** we have studied the effect of MnO loading on the CO and $H_2$ adsorption properties of $Co/Mn/TiO_2$ catalysts by using a combination of TEM, $H_2$ chemisorption and DRIFTS spectroscopy. With the DRIFTS results it is demonstrated that MnO species cover the surface of the cobalt metal particles inducing changes in the CO IR

adsorption properties. The use of DRIFTS is also applied to monitor the FT reaction by evaluating the development of various vibrational bands as a function of time. Furthermore, this chapter clearly illustrates the effect of the MnO loading on the FT activity and selectivity displayed by the various Co/Mn/$TiO_2$ catalysts. Finally, in **Chapter 7** we present the use of soft X-ray absorption spectroscopy as an interesting tool to investigate the surface composition of the FT catalytic systems. The results of the measurements at the Co and Mn L-edges after *in situ* reduction treatments and under FT conditions suggest that the cobalt active phase composition may undergo significant changes during FT operation. In addition, the strong influence of $TiO_2$ on the reducibility of the cobalt nanoparticles due to the so-called strong metal-support interaction is also illustrated. The thesis ends with a summary of the most remarkable findings and some concluding remarks (**Chapter 8**).

## References and notes


[1] A historical account on Fischer-Tropsch synthesis can be found on the web: http://www.fischer-tropsch.org.

[2] F. Fischer, H. Tropsch, *Brennstoff-Chemie*, 1926, 97.

[3] E.J. Hoffman, *Coal Conversion*, The Energon Company, Laramie, Wyoming, 1970, p. 223.

[4] J. Patzlaff, Y. Lieu, C. Graffmann, J. Gaube, *Appl. Catal. A :General*, 1999, **186**, 109.

[5] J.H. Gregor, *Catal. Lett.*, 1990, **7**, 317.

[6] H. Schulz, *Appl. Catal. A:General*, 1999, **186**, 3.

[7] D.J. Duvenhage, T. Shingles, *Catal. Today*, 2002, **71**, 227.

[8] S.T. Rie, R. Kirshna, *Appl. Catal. A: General*, 1999, **186**, 55

[9] B. Jager, R. Espinoza, *Catal. Today*, 1995, **23**, 17.

[10] P.J. Van Berge, S. Barradas, J. Van de Loodsdrecht, J.L. Visage, *Petrochemie*, 2001, 138.

[11] T.H. Fleisch, R.A. Sills, M.D. Briscoe, *J. Nat. Gas. Chem*., 2002, **11**, 1.

[12] P.J. Van Berge, S. Barradas, J. Van de Loodsdrecht, J.L. Visage, *Erdoel, Erdgas, Kohle*, 2001, **117**, 138.

[13] J.G. Goodwin, *Proc. of ACS Symp. Methane Upgrading*, Atlanta, GA, USA, 1991, p. 156.

[14] E. Iglesia, *Appl. Catal. A:General* 1997, **161**, 59.

[15] E. Iglesia, S.C. Reyes, R.J. Madon, S.L. Soled, *Adv. Catal.*, 1993, **39**, 221.

[16] M.E. Dry, in *Catalysis Science and Technology*, J.R. Anderson, M. Boudart (Eds.), Vol. 1, Springer, Berlin, 1981, p. 159.

[17] M.E. Dry, *J. Chem. Technol. Biotechnol.*, 2001, **77**, 43

[18] M.E. Dry, *Appl. Catal. A:General*, 1996, **138**, 319

[19] M.E. Dry, *Catal. Today*, 2002, **71**, 227

[20] M.E. Dry, *Appl. Catal. A:General*, 2004, **276**, 1.

[21] For more details we refer to the following website: http://www.sasol.com.

[22] Shell press release on March 9 2004 (http://www.shell.com).

[23] Exxon Mobil press release on July 14 2004 (http://www.exxonmobil.com).
[24] J. Jacometti, A. Ekvall, Shell in the Middle East, issue 17, april 2002, 1-3.
[25] G. Coupe, Step on the gas, in *The Engineer*, August 6 2004.
[26] F. Thackeray, Fischer-Tropsch GTL Approaches Treshold, in *World Petroleum Congress*, p. 150-151 (2003).
[27] A.H. Tullo, Catalyzing GTL, in *Chem. Eng. News*, 2003, **81**, 18.
[28] We express our gratude to A. Buchanan and A. Rautenbach, both from Sasol, for kindly providing us with these figures.
[29] V. Ponec, in *Handbook of Heterogeneous Catalysis*, Ertl, G., Knozinger, H., Weitkamp, J. (Eds.), Wiley-VCH, Weinheim, 1997, p. 1876.
[30] B. Cornils, W.A. Herrmann, R. Schlogl, C.H. Wong, *Catalysis from A to Z, A concise encyclopedia*, Wiley-VCH, Weinheim, 2000.
[31] J. Hagen*, Industrial Catalysis, A practical approach*, Wiley-VCH, Weinheim, 1999, p. 174.
[32] J.C. Geerlings, J.H. Wilson, G.J. Kramer, *Appl. Catal. A:General*, 1999, **186**, 27.
[33] A.A. Adesina, *Appl. Catal. A:General*, 1996, **138**, 345.
[34] M.E. Dry, *Appl. Catal. A:General*, 1999, **189**, 185.
[35] B. Jager, *Stud. Surf. Sci. Catal.*, 1997, **107**, 207.
[36] B. Davis, *Fuel Proc. Techn.*, 2001, **71**, 157.
[37] A.C. Vosloo, *Fuel Proc. Techn.*, 2001, **71**, 149.
[38] M.J. Overett, R.O. Hill, J.R. Moss, *Coord. Chem. Rev.*, 2000, **206-207**, 581.
[39] I. Wender, *Fuel Processing Technology*, 1996, **48**, 228.
[40] R.L. Espinoza, A.P. Steynberg, B. Jager, A.C. Vosloo, *Appl. Catal. A:General*, 1999, **186**, 13.
[41] R.B. Anderson, *The Fischer Tropsch Synthesis*, Academic Press, New York (1984).
[42] A.T. Bell, H. Heinemann, W.G. McKee, *Appl. Catal.*, 1982, **2**, 219.
[43] M.A. Vannice, *J. Catal.* 1975, **37**, 462.
[44] P. Concepcion, C. Lopez, A. Martinez, V.F. Puntes, *J. Catal.*, 2004, **228**, 321.
[45] A.Y. Khodakov, A. Griboval-Constant, R. Becchara, F. Villain, *J. Phys. Chem. B*, 2001, **105**, 9805.
[46] A. Khodakov, A. Griboval-Constant, R. Bechara, V.L. Zholobenko, *J. Catal.*, 2002, **206**, 230.
[47] D. Yin, W. Li, W. Yang, H. Xiang, Y. Sun, B. Zhong, S. Peng, *Micropor. Mesopor. Mater.,* 2001, **47**, 15.
[48] S. Suvato, T.A. Pakkanen, *J. Mol. Catal. A:Chemical*, 2000, **164**, 273.
[49] J. Panpranot, J.G. Goodwing, Jr., A. Sayari, *Catal. Today*, 2002, **77**, 269.
[50] A.Y. Khodakov, R. Bechara, A. Griboval-Constant, *Appl. Catal. A:General*, 2003, **254**, 273.
[51] A. Martinez, C. Lopez, F. Marquesz, I. Diaz, *J. Catal.*, 2003, **220**, 486.
[52] D.J. Koh, J.S. Chung, Y.G. Kim, *Ind. Eng. Chem. Res.*, 1995, **34**, 1969.
[53] Y. Ohtsuka, T. Arai, S. Takasaki, N. Tsubouchi, *Energy and Fuels*, 2003, **17**, 804.
[54] A.M. Saib, M. Claeys, E. van Steen, *Catal. Today*, 2002, **71**, 395.

# 2

# Promotion Effects in Cobalt-based Fischer-Tropsch Catalysis –*A Review-*


## Abstract

This review aims to discuss some fundamental insights to understand the effect of promoter elements on the state of the active cobalt nanoparticles supported on high-surface area oxides, such as silica, alumina and titania. This will be done by giving an overview of the main advances in the development of new cobalt-based FT catalyst formulations reported in the last three decades in the open literature and by presenting an attempt to rationalize these published data in terms of different modes of promotion action. Special attention will be directed towards maganese as promoter element. The obtained insights provide potential guidelines for designing new or improved catalyst formulations. It will be shown that (1) advanced characterization techniques, including spectroscopy and microscopy, are needed in order to study these complex catalytic systems and (2) that the addition of each promoter element exhibit multiple effects on the catalyst performances. Future studies should be focused on obtaining detailed information on the location, structure and electronic state of the active cobalt phase as well as the promoter element under realistic FT reaction conditions.

## Introduction

An increasing demand for clean fuels and chemicals are expected to lead to an important shift from crude oil to natural gas as feedstock for chemical industries. This will certainly involve the use of Fischer-Tropsch (FT) technology, in which high molecular weight hydrocarbons are synthesized by catalytic hydrogenation of CO using cobalt-based FT catalysts. These catalysts are often loaded with small amounts of promoter elements that enhance their overall catalytic performances and catalyst lifetime. These beneficial effects are, however, only obtained if the promoter element is added in the appropriate manner and in a limited range of promoter loading. Although catalyst promotion is heavily studied in the field of heterogeneous catalysis, not so much is known about the physicochemical origin of cobalt FT promotion effects.

Over the past decades a large number of studies have been reported on supported cobalt FT catalysts. Generally, these studies indicate that the number of available surface cobalt metal atoms determines the catalyst activity and attempts to enhance the catalytic activity have been focusing on two interconnected issues: (1) to reduce the cobalt-support oxide interaction and (2) to enhance the number of accessible cobalt atoms available for FT reaction. It has been shown that the number of catalytically active cobalt atoms as well as their selectivity can be largely enhanced by the addition of small amounts of various elements, called promoters, to the catalyst material. However, the exact role of these promoters, as is the case for many other heterogeneous catalysts as well, remains often unclear.

The aim of this chapter is to give an extensive overview of the different promoters used to develop new or improved cobalt-based FT catalysts. Special attention is directed towards a more fundamental understanding of the effect of the different promoter elements on the catalytically active cobalt nanoparticles. Due to the extensive open and patent literature, we have mainly included research publications of the last three decades in this chapter [1-135, 178-202]. In addition, we will limit ourselves to catalyst formulations composed of oxide supports, excluding the use of other interesting and promising support materials, such as, *e.g.,* carbon nanofibers studied by the group of de Jong [136-137].

The chapter starts with a general introduction on promotion and a classification for the different modes of promotion effects will be proposed. Furthermore, each promoter element reported in the literature will be accordingly evaluated. The obtained insights have led to guidelines to design improved Co-based FT catalysts. A third part will deal with some highlights on the literature of Mn-promoted FT catalysts and a comparison between supported and unsupported Mn-promoted Fe-, Ru- and Co-based FT catalysts will be made. It will be shown that many advanced characterization techniques, including spectroscopy and

microscopy, are necessary to reveal physicochemical insights in these very complex catalytic systems. The chapter ends with some concluding remarks and a look into the future.

## Promotion effects

The catalyst surface often contains substances that are added deliberately to modify the turnover rate for a given catalytic reaction [140-142]. The simplest case being an additive that increases the rate per site per second. It is, in this respect, useful to recall the concepts of catalyst promotion. Promoters are doping agents added to catalyst materials in small amounts to improve their activity, selectivity and/or stability [138]. It is generally accepted that promoter elements may induce these beneficial effects in several manners. All this has led researchers to come up with a classification scheme for promoter effects and in the case of the Co FT literature the following names (including often different definitions!) have been given to the different types of promotion: structural or structure promoters, electronic promoters, textural promoters, stabilizers and catalyst-poison-resistant promoters. Since many of the above-mentioned effects tend to overlap in practice, it is sometimes difficult to precisely define the observed function of a promoter. In addition, the degree to which additives modify a catalyst's activity in the positive or negative manner is also dependent on the amount of the additive, the support oxide under consideration and the exact preparation method, causing them to act either as a promoter or a poison. In line with this reasoning, the term modifier should be more appropriate according to Paal and Somorjai [139]. Finally, it is important to mention that promoter elements are mostly discovered in a serendipitous manner and this holds most probably also for the field of Co FT catalysis. Only a few of them are expected to be the result of *a priori* catalyst design.

In this chapter we have chosen to divide the family of promoter elements into two classes according to their intended function. *Structural promoters* affect the formation and stability of the active phase of a catalyst material, whereas *electronic promoters* directly affect the elementary steps involved in each turnover on the catalyst. The latter group of promoters affect the local electronic structure of an active metal mostly by adding or withdrawing electron density near the Fermi level in the valence band of the metal. This results in a modification of the chemisorption properties of the active metal. Hence, this affects the surface coverage of reactants and, as a consequence, the catalysis done by the metal. In addition to these two groups of promoters we have included in our classification the group of synergistic promotion effects. Although promoter elements are not considered themselves to be catalytically active, they may play other roles under FT conditions. This may indirectly affect the behaviour of the catalytic active element, still dominating the overall catalytic

performances of the catalyst material. We will now discuss more in detail the different promoter effects encountered in Co FT catalysis.

***Structural promoters***

The main function of structural promoters is to influence the cobalt dispersion by governing the cobalt-support oxide interaction [138]. A high Co dispersion results in a high active Co metal surface and, therefore, in a high coverage by the reactants, and as a consequence an improved catalyst activity. Structural promotion may lead to an increased catalyst activity and stability, but in principle does not influence the product selectivity since it merely increases the number of active sites in a catalyst material. This increase in active sites can be achieved by a stabilization of the Co active phase due to the promoter element, which either avoids the formation of metal-support compounds, or prevents the agglomeration and sintering of the Co particles under F-T operation conditions.

*I. Stabilizing the support oxide*

Promoter elements can be added to the support oxide resulting in a decreased Co compound formation with the support oxide. This is illustrated in Fig. 1(a). More specifically, strategies should be followed to avoid the formation of either cobalt titanate, cobalt silicate or cobalt aluminate as a result of Co solid-state diffusion under reducing or regeneration conditions in the subsurface of these support oxides. A related problem is the reduction in the support surface area. This is especially a problem in the case of titania, where the anatase polymorph is only stable under oxidative regeneration conditions from about 400°C to 750°C. The addition of Si, Zr and Ta as promoter elements may avoid or diminish surface collapse of the support oxide.

*II. Glueing the cobalt particles on the support oxide*

Some promoter elements can act as an oxidic interface between the supported Co particle and the support oxide, leading to an increased stability of the cobalt particles against sintering during reduction or oxidative regeneration. A plausible schematic representation of this promotion effect is shown in Fig. 1(d).

*III. Promoters leading to increased cobalt dispersion*

The addition of promoter elements may also lead to increased cobalt dispersion after preparation. In the absence of the promoters, relatively large cobalt crystals are formed, whereas, by adding these additives, smaller supported cobalt particles can be made. Such promotion effect is illustrated in Fig. 1(c).

Related to this effect it is important to mention that small metal particles composed of a promoter element can dissociate hydrogen in the neighbourhood of a supported cobalt particle leading to the formation of atomic hydrogen that may spill over by diffusion to cobalt [30], as illustrated in Fig 1(b). This can result in an enhanced degree of cobalt reduction and therefore a higher amount of surface cobalt metal atoms. The result of this promotion is an increase in the number of active sites and therefore a higher catalyst activity, leaving the catalyst selectivity unaltered. Noble metals, such as Re, Pt and Ru, are known to act in this manner.

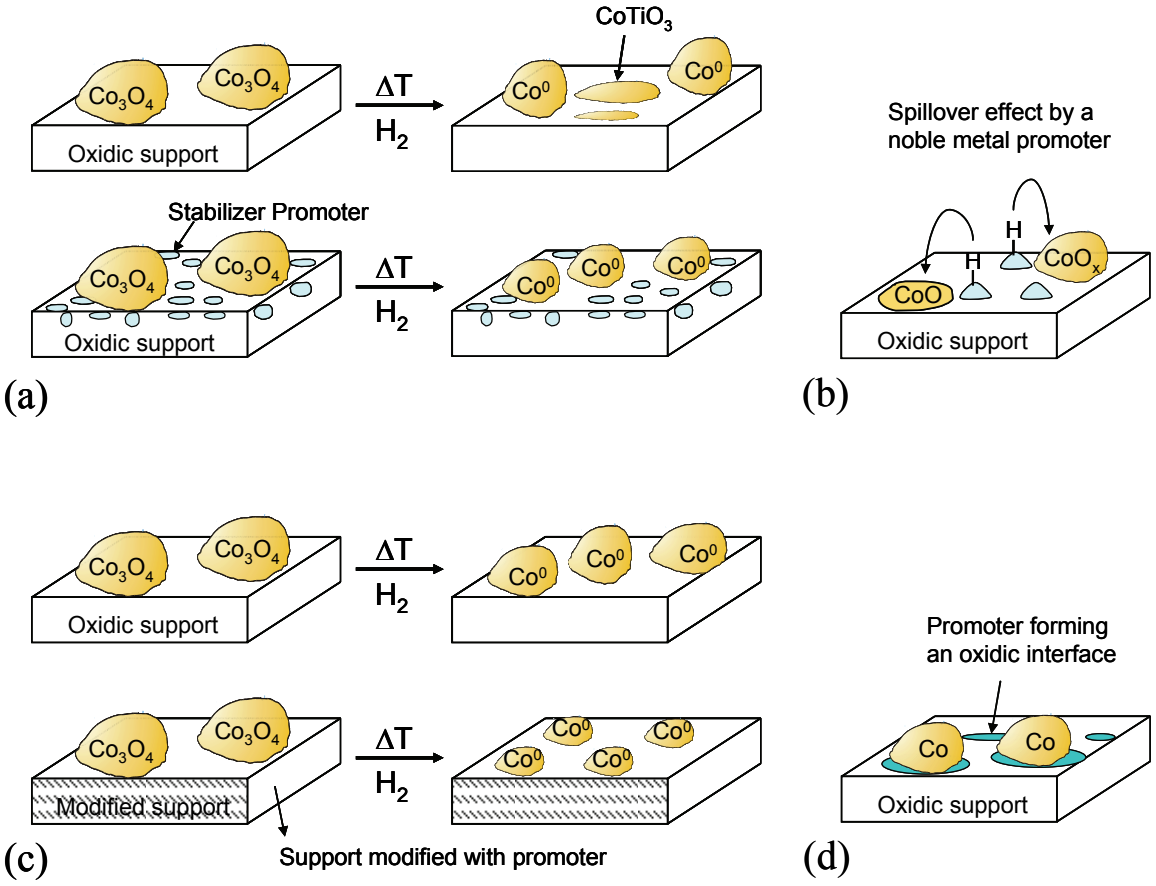


**Figure 1.** The different modes of action of structural promoters in Co-based FT catalysis: (a) structural promoters can lead to a decreased compound formation with the support oxide; (b) $H_2$ spillover effect, leading indirectly to a higher dispersion of the supported Co particles; (c) oxide promoters can be used to modify the support leading to increased dispersions; and (d) structural promoters can act as an oxidic interface between the supported Co particle and the support oxide.

***Electronic promoters***

In contrast to structural promoters, electronic effects are much less obvious to be detected in an unambiguous manner. Electronic promotion can be best understood in terms of ligand effects. The surrounding (electronic) environment of an active Co site can be altered by the presence of a promoter element. This leads to an electronic donation or withdrawal leading to an increased intrinsic turnover frequency or change in product selectivity. Ligand effects may also result in a decreased deactivation rate by altering the adsorption/desorption properties of the reagents/reaction products. Electronic promotion can only occur when there is a direct chemical interaction between the promoter element and the cobalt active surface. It is important to mention that electronic metal-support effects have been found to exist in heterogeneous catalysis, but these effects should only play a minor role in Co FT catalysis since the active Co particles are relatively large and the contact area between support and cobalt particle is therefore very small. Finally, electronic effects induced by promoter elements may be responsible for an increased resistance of the supported Co nanoparticles to re-oxidation or even their stability against deactivation in general.

*I. Promoter metal oxide decoration of the cobalt surface*

A first way to induce a ligand effect is to decorate the active cobalt surface with metal oxides. It should be clear that a beneficial catalytic effect can only be obtained if the deposited metal oxides are not blocking (all) the active cobalt sites, which would lead to a decreasing hydrogen or CO chemisorption. The decoration effect of a supported Co particle by transition metal oxides is illustrated in Fig. 2(a).

A similar effect may occur with the support oxide as decorating material. This effect is generally known as the “strong metal-support interaction” or SMSI effect [138, 143]. The SMSI effect is explained in Figure 2(c). When metals supported on, *e.g.,* titania are heated in hydrogen at relatively high temperatures, a dramatic decrease in hydrogen and CO chemisorption occurs. This observation is due to a partial encapsulation of the supported metal particle by the support oxide since reduced $TiO_x$ ensembles can migrate over the metal surface, leading to a (partial) decoration of the metal particle.

*II. Cobalt-promoter alloy formation*

Metal alloying or bimetallic alloy formation may also influence the activity and selectivity of Co FT catalysts. Indeed, cobalt and a promoter metal may form an integral metal particle deposited on the support oxide, altering the electronic properties of the surface cobalt metal atoms (Fig. 1(b)). Depending on the promoter element added to the Co cluster, alloying might lead to an increased catalyst activity, selectivity, as well as stability.

***Synergistic promotion effects***

As was already mentioned promoter elements are not considered themselves to be catalytically active, but it is fair to say that this is not always the case. This promoter activity may indirectly affect the behaviour of the catalytic active element since it will alter, *e.g.,* the local feed composition or may, due to its catalytic properties, influence the overall reaction product distribution. The following effects, illustrated in Fig. 3, are expected to occur in a promoted Co FT catalyst.

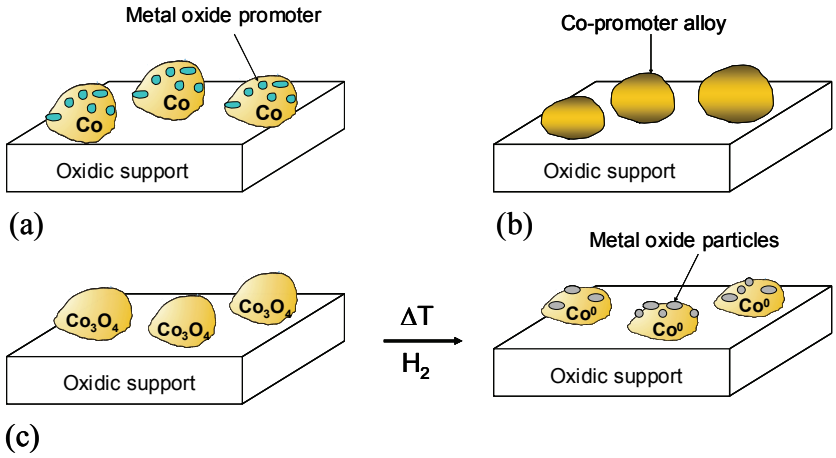


**Figure 2**. The different modes of action of electronic promoters in Co-based FT catalysts: (a) promoter metal oxide decoration of the cobalt surface; (b) cobalt–promoter alloy formation; and (c) metal oxide decoration effect occuring upon reduction with some oxidic supports.

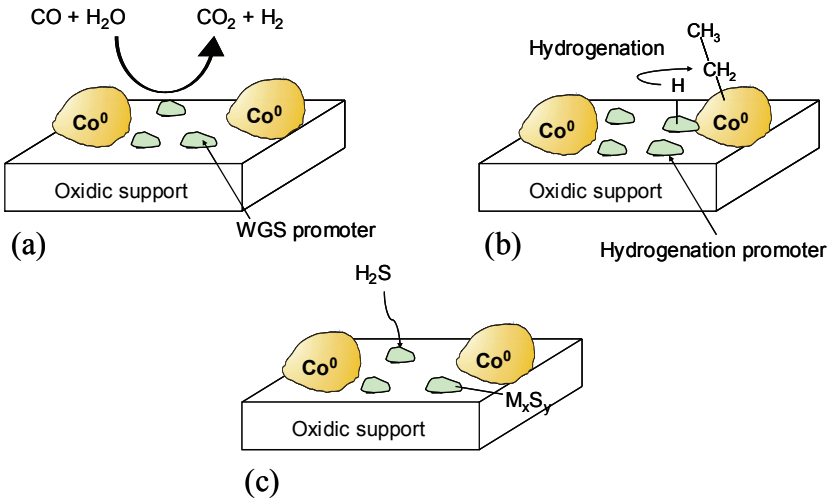


**Figure 3**. Survey of possible synergistic promotion effects occurring in Co-based FT catalysis: (a) water-gas shift reaction; (b) hydrogenation/dehydrogenation reactions; and (c) $H_2S$ adsorption.

*I. Water-gas shift reaction*

The water-gas shift reaction (i.e., $CO + H_2O = H_2 + CO_2$) made by particles composed of a promoter element close to a supported cobalt particle leads to a change in the local $CO/H_2$ ratio, which may affect the surface coverage of cobalt. As a result, both the activity and the selectivity of the catalyst can be altered. Transition metal oxides could act as WGS reagents.

*II. Hydrogenation/dehydrogenation reactions*

The end products of the FT process are a mixture of higher alkanes and alkenes. The promoter elements could show under FT conditions some activities for hydrogenation or dehydrogenation reactions leading to a shift in the relative ratio of alkanes to alkenes.

*III. Coke burning during regeneration*

Co FT catalysts deactivate due to coke formation blocking the active sites. This coke can be burned off by an oxidative treatment. The addition of promoter elements may decrease the temperature of this oxidative treatment, preventing the possible clustering of supported cobalt particles.

*IV. $H_2S$ adsorption reaction*

As was already mentioned, Co FT catalysts are prone to $H_2S$ poisoning and the addition of specific promoter elements may lead to an increased $H_2S$ tolerance. Crucial for this are the use of promoter elements, such as B and Zn, which make stable surface compounds with sulfur.

## Overview of the promoter elements used in Co-based F-T catalysts

The following chemical elements have been investigated as promoters in Co-based FT catalysis: B, Mg, K, Ti, V, Cr, Mn, Ni, Cu, Zr, Nb, Mo, Ru, Rh, Pd, La, Re, Ir, Pt, Ce, Gd and Th [1-135, 178-202]. Taking the above described classification scheme into account, we have made an attempt to identify for every reported promoter element its beneficial effect for Co FT catalysis. The result of this effort is summarized in Table 3. It is clear from this table that different promoter elements could have multiple modes of promotion action. Furthermore, in making this table we encountered several research papers giving opposite conclusions on the observed promotion effect. Such differences can only be explained by the different loadings and preparation methods employed in making the promoted Co FT catalysts, as well as a the different FT reaction conditions employed, leading to different conversions and selectivities. In what follows, we discuss some highlights on noble metal and transition metal oxide promotion of Co-based FT catalysts.

**Table 4.** Overview of the promotion effects displayed by the different elements reported in the literature for the Co Fischer-Tropsch catalytic performances.

| Promotion type | Promotion mode | Influence on catalyst | | | Element reported in literature to play a role in this promotion effect |
|---|---|---|---|---|---|
| | | activity | selectivity | stability | |
| Structural | Support stabilization | + | | + | Mg, Si, Zr, Nb, Rh, La, Ta, Re, Pt |
| | Cobalt glueing | + | | + | B, Mg, Zr |
| | Cobalt dispersion increase | + | | + | Ti, Cr, Mn, Zr, Mo, Ru, Rh, Pd, Ce, Re, Ir, Pt, Th |
| Electronic | Decorating cobalt surface | + | + | + | B, Mg, K, Ti, V, Cr, Mn, Zr, Mo, La, Ce, Gd, Th |
| | Cobalt alloying | + | + | + | Ni, Cu, Ru, Pd, Ir, Pt, Re |
| Synergistic | Watergas shift | + | + | | B, Mn, Cu, Ce |
| | Hydrogenation/ dehydrogenation | | + | | nr[a] |
| | Coke burning | | | + | Ni, Zr, Gd |
| | $H_2S$ adsorption | | | + | B, Mn, Zn, Zr, Mo |

[a] One may anticipate that hydrogenation and dehydrogenation reactions can be catalyzed by metals and metal oxides known to be active for this reaction. Examples are $CrO_x$ and Pt.

***Noble metal promotion effects***

In the group of noble metals; Ru, Re and Pt have been extensively studied as promoter elements in Co-based FT catalysis, whereas other metals, such as Rh, Pd, Os and Ir, are only reported in limited occasions. Hence, we will focus our attention on the promotion effects induced by Ru, Re and Pt.

*Ruthenium*

Ru is the most studied noble metal promoter and it has been frequently showed to play a role both in structural and electronic promotion [1-42, 104, 107, 113, 115, 118-126, 128, 132, 134, 135, 195, 201]. In the early nineties, Hoang and Bruce observed that the addition of Ru to $Co/CeO_2$ catalysts drastically increased the Co FT activity without modifying the catalyst selectivity [2-3]. Results obtained from XPS and TPR indicated that Ru caused a decrease of the reduction temperature of supported $Co_3O_4$ nanoparticles. The authors proposed that Ru facilitates the reduction of cobalt via a hydrogen spillover from Ru to Co, thereby leading to

an increase in the number of exposed $Co^0$ sites and consequently, to an increase in the CO hydrogenation rate. This structural promotion of Ru has been shown to take place independently of the support material; *i.e.*, the addition of Ru to $Co/Al_2O_3$ [7], $Co/SiO_2$ [115] and $Co/TiO_2$ [4] catalysts decreases the temperature at which $CoO_x$ is reduced to $Co^0$ during activation, leading to catalysts with improved cobalt dispersions.

The role of Ru as an electronic promoter has also been extensively investigated. In this respect, it is worthwhile to point out that Co-Ru catalysts exhibit exceptional high selectivities to $C_{5+}$ products and higher turnover rates compared to unpromoted Co catalysts [104]. A remarkable insight into Ru promotion has been gained from the work of Iglesia *et al.* [1, 4]. This group observed that at reaction conditions that favor the formation of higher hydrocarbons (*i.e.*, high pressures and high conversions), the apparent turnover numbers on cobalt catalysts are independent of the support material, but are markedly increased by the addition of small amounts of Ru. They found large increases in the turnover rates and the $C_{5+}$ selectivity when Ru was added to $Co/TiO_2$ catalysts in a ratio of $Ru/Co < 0.008$ [4]. The experimental results indicated that Ru inhibits the deactivation of the catalysts by keeping the Co surface "clean" and hence, preventing a carbon deposition on the Co particles. This promotion appeared to require an intimate contact between Co and Ru atoms, since a bimetallic nature of the active sites was found to exist and this nature was enhanced by oxidation treatments at high temperatures (> 573 K). On the other hand, the higher $C_{5+}$ selectivities found for the Ru-promoted catalysts were discussed in terms of an increase in the Co site density. Apparently, a higher Co site density inherent in the Co-Ru catalysts leads to diffusion-enhanced readsorption of α-olefins, which reverses the β-hydrogen abstraction termination step and thus, favors the formation of higher hydrocarbons [11].

Many other groups have recently reported on the effects of Ru promoter in the performances of Co FT catalysts. For example, Sun *et al.* observed that the addition of small amounts of Ru to $Co/SiO_2$ catalysts increased the TOF, whereas it did not affect the $CH_4$ selectivity [27]. Ru appeared to be enriched at the metallic cobalt surface after reduction, modifying the adsorption properties of the $Co^0$ sites. Price *et al.* investigated $Co/TiO_2$ and $Co\text{-}Ru/TiO_2$ catalysts with IR spectroscopy making use of CO as a probe molecule [11]. They concluded that their Ru-Co and Co catalysts had different surface structures and confirmed the existence of Co-Ru interactions. Finally, Hosseini *et al.* investigated the effect of Ru loading on a 20 wt% $Co/Al_2O_3$ catalyst [39], and observed that Ru promotion was only achieved for Ru loadings of 0.5 and 1.0 wt%. Higher Ru loading of 1.5 and 2.0 wt% led, however, to a decrease in the CO hydrogenation activity. On the other hand, the $C_{5+}$ selectivity remained almost unaffected by the Ru loading.

*Rhenium*

Re promotion has also been widely investigated in Co-based FT catalysis [43-56, 111, 126, 129, 132, 135, 194]. Re is regarded as a structural promoter and it has been frequently reported to increase the Co reducibility *via* a hydrogen spillover effect, leading to catalysts with enhanced Co dispersions. Re reduces to a metallic state at higher temperatures than Ru and therefore, can facilitate the second cobalt reduction step, from CoO to $Co^0$ [54].

Hilmen *et al.* performed TPR experiments on $Co/Al_2O_3$ and $Co\text{-}Re/Al_2O_3$ catalysts, and on physical mixtures of $Co/Al_2O_3$ and $Re/Al_2O_3$, and they suggested that no direct contact between Re and Co is necessary to achieve the promotion by Re [44]. Hence, Re might be in many cases located on the support material rather than decorating the surface of Co. In line with the above reasoning, Rygh *et al.* showed with DRIFTS that the presence of Re on $Co/Al_2O_3$ catalysts increased the amount of bridged CO-adsorbed species without any sign of electronic interaction between the two metals [47]. Moreover, the oxidation or hydrogenation revealed bands arising from Re carbonyl species, suggesting that the Re was located at the catalyst surface. Nonetheless, other authors have reported the existence of bimetallic interactions between Co and Re. For example, Bazin *et al.* have investigated the effect of Re on the structure of $Re\text{-}Co/Al_2O_3$ catalysts by EXAFS [52] and the analysis of the Co K edge and Re $L_{III}$ edge provided direct evidences for Re-Co bond formation. Their results suggest that Re prevents the formation of cobalt surface phases, such as cobalt aluminate, resulting in an increase of the catalyst activity. They also considered that Re prevents the agglomeration of small metal particles in oxidizing environments and thus their migration and sintering. In another paper, Ronning *et al.* showed from the Re $L_{III}$ edge that small bimetallic particles were formed after reduction of $Co\text{-}Re/Al_2O_3$ catalysts containing 4.6 wt% Co and 2 wt% Re [49]. More recently, Jacobs *et al.* have reported EXAFS data on $Co\text{-}Re/Al_2O_3$ systems [54]. They proposed that a direct contact of Re with the Co atoms existed, while evidence for Re-Re bonds was not observed. In addition, they observed that the average Co cluster size decreased with increasing Re loading.

It is generally believed that the addition of Re to Co-based catalysts leads to an increase in the FT activity as a result of the increased number of exposed sites, although the intrinsic activity of the Co sites is not expected to change. For instance, Li *et al.* showed that the addition of 0.34 wt% Re to $Co/TiO_2$ catalysts with 10 wt% Co, resulted in the highest FT conversion compared to unpromoted and Ru-promoted $Co/TiO_2$ catalysts [126]. On the other hand, the selectivity of the Co sites is generally expected to be not directly affected by the presence of Re [111], although some authors have reported improvements in the $C_{5+}$ selectivity when using Re [52,129]. A possible explanation may be the influence of Re on the Co particle sizes distribution, which may also have an indirect effect on the selectivity due to

the changes in the Co surface density. Some differences found in literature may also arise from comparisons of the catalysts at different conversions, which lead to significant variations in selectivities.

*Platinum*

Pt is another noble metal considered to play a role as structural promoter, and it is frequently reported to enhance the Co dispersion in supported Co F-T catalysts [57-66, 108, 111, 118, 120, 122, 124-125, 134-135, 199, 201-202]. In the early nineties, Zsoldos *et al.* reported XPS results on Pt-promoted $Co/Al_2O_3$ catalysts, in which the Co reducibility was largely improved when combined with small amounts of Pt [57]. They observed that the highly dispersed, but difficult to reduce surface cobalt particles were largely reduced in the Pt-$Co/Al_2O_3$ catalyst, whereas only the larger $Co_3O_4$ particles were reduced in the $Co/Al_2O_3$ catalyst. It was suggested that Pt would prevent the formation of Co aluminates during catalyst preparation and that the Pt might partially cover the surface of the Co metal and even form bimetallic Pt-Co particles. These findings were further evidenced in two following papers [58-59]. A year later, Zsoldos and co-workers showed using XPS that Pt-$Co/Al_2O_3$ catalysts with a high Pt/Co ratio (Co atomic fraction of 0.2-0.5) contained $CoPt_3$ bimetallic particles at the surface of the Co nanoparticles [60]. The existence of Co-Pt interactions in these catalytic systems was further confirmed by Tang *et al.* making use of IR with CO as probe molecule [62]. The results suggested that there was a strong interaction between Pt and Co atoms. Very recently, Jacobs *et al.* have reported on Co-Pt/$Al_2O_3$ catalysts investigated by EXAFS at the Pt L-edge, and they concluded that insolated Pt atoms interact with the supported cobalt clusters without forming Pt-Pt bonds [65]. The Co K-edge was used to verify that the cobalt cluster size increased slightly for those systems with Pt promotion, in which the cobalt reduction extent increased by a factor of two and the formation of Co aluminates was prevented.

Pt promotion has been also investigated with other support materials. For example, Schanke *et al.* studied the influence of small amounts of Pt (0.4 wt%), on the reducibility of $Co/SiO_2$ and $Co/Al_2O_3$ catalysts containing 9 wt% Co, and observed that the presence of Pt decreased in all cases the reduction temperature of $Co_3O_4$, although the effect was more pronounced for alumina-supported Co FT catalysts [61]. In this work the CO hydrogenation rates at pressures of 1 bar were found to be 3-5 times higher in the Pt-promoted catalysts than in the unpromoted catalysts. However, steady state and transient kinetic experiments indicated constant turnover frequencies for CO hydrogenation in all catalysts, independently of the support or the presence of Pt. Thus, the higher apparent turnover numbers for the Pt-promoted catalysts were considered to be due to a higher coverage of intermediates and not by an

increase in the intrinsic activity. In addition, the FT selectivity was not influenced by the presence of Pt. Similar findings were reported by Vada *et al.* They observed that the addition of 1 wt% Pt to a $Co/Al_2O_3$ catalyst containing 8.7 wt% Co, significantly increased the CO hydrogenation rate, whereas the selectivity was unaffected [111]. Hence, it was argued that Pt increases the cobalt reduction extent and therefore the CO hydrogenation rate, although the average Co site activity is not altered. Finally, Das *et al.* have reported on Pt-promoted $Co/Al_2O_3$ catalysts with 25 wt% Co and have observed that Pt promotion does not alter the Co dispersion but increases the amount of Co reduced [199]. Both unpromoted and Pt-promoted catalysts were found to decline in activity at the same rate.

***Transition metal oxide promotion effects***

Many transition metal oxides have been investigated as potential promoters for Co-based FT catalysts [78-97, 101-103, 105-107, 109-110, 112, 116-119, 123-124, 126-131, 192-193, 196-200]. Although different promotion functions are proposed in the literature, mostly, transition metal oxides have been regarded as electronic promoters, having a direct influence on the intrinsic activity and/or selectivity of the Co sites. This effect is manifested through direct interaction of the supported cobalt particles with the transition metal oxides. Hence, the transition metal oxide promoters are thought to be spreading over the cobalt surface in submonolayer coverages, modifying the adsorption properties of the Co active sites. In this respect, it is worthwhile to highlight the work of Bartholomew *et al.* [76], in which the activity of supported Co nanoparticles was compared with different oxide supports. The following decreasing order in activity was found: $Co/TiO_2 > Co/SiO_2 > Co/Al_2O_3 > Co/MgO$. Since the Co dispersion was found to be very similar in the first three catalysts, the enhanced activity in the case of $Co/TiO_2$ appeared to be due to an electronic effect induced by the $TiO_2$. This was attributed to the SMSI taking place with $TiO_2$, as discussed in more detail before.

Early in the nineties Guerrero Ruiz *et al.* reported enhanced catalyst activities and increased selectivities to alkenes and higher hydrocarbons upon addition of V, Mg, and Ce oxides to Co-based FT catalysts [109]. These variations were attributed to electronic effects induced by the metal oxide. Similar results were obtained by Bessel *et al.* using a Cr promoter in Co/ZSM-5 catalysts [110]. This group observed that the addition of Cr improved the catalyst activity, and shifted the selectivity from methane to higher, generally more olefinic, hydrocarbons. Based on $H_2$ and CO chemisorption, as well as TPR and TPD results, they suggested that the promotion was caused by an interaction between the transition metal oxide and the cobalt oxide, which inhibits cobalt reduction and improves Co dispersion. Furthermore, it was considered that Cr increased the Co–CO and decreased the Co–H bond strengths, resulting in a higher relative amount of CO/H adsorbed on the Co particles. This

effect would certainly lead to a lower hydrogenation rate during FT synthesis. In other work, Kikuchi *et al.* reported the effect of Cr, Ti, Mn and Mo on the FT performances of catalysts loaded with ultrafine Co particles [116]. The addition of these promoters effectively enhanced the catalyst activity, lowered the methane selectivity and increased the $C_{5+}$ production. They attributed these effects to a structural promotion, causing a decrease of the Co particle sizes in the catalysts. However, an electronic effect induced by the transition metal oxide promoters was not considered. Another promotion effect induced by Mn and Mo was reported by the group of Belosludov [127]. This group investigated the addition of Mn and Mo to Co-based FT catalysts using computational chemistry. Interestingly, they found that the transition metal oxides under investigation improved the sulfur tolerance of the catalysts.

In recent years, some more detailed studies on transition metal oxide promotion have been reported. For example, Mendes *et al.* have reported on the promotion of Nb on $Co/Al_2O_3$ catalysts, which were characterized using the temperature programmed surface reaction (TPSR) and diffuse reflectance spectroscopy (DRS) techniques [196]. The results revealed a transient behaviour of the catalysts, which allowed identifying a $Nb_2O_5$ phase in the catalysts. The authors proposed that an existent $Co^0$-$Co^{2+}$ interface is responsible for the methanation reaction, whereas a $Co^0$-$NbO_x$ is responsible for the hydrocarbon chain growth. The relative amount of each species on the surface was found to influence the selectivity of CO hydrogenation. Another recent study by Xiong *et al.* has reported on the FT catalytic performances of Zr-modified $Co/Al_2O_3$ catalysts [198]. The $CoAl_2O_4$ spinel phase was detected in the prepared catalysts and its content decreased with increasing Zr loading. Thus, Zr appeared to inhibit the Co-support formation. Moreover, they observed improved activities and $C_{5+}$ selectivities upon the addition of Zr, which were attributed to the increase of the amount of Co metal sites. Similar results have been reported by Zhang *et al.* using a Mg promoter in $Co/Al_2O_3$ catalysts [197]. They observed that the addition of Mg decreased the formation of a cobalt surface phase, which was detected by XPS. Small amounts of Mg were found to increase the catalyst activity by means of decreasing the formation of Co aluminates. However, large amounts of Mg caused a decrease in the reducibility of the catalysts due to the formation of MgO-CoO solid solutions.

## Mn-promoted Fischer-Tropsch Catalysts

We now discuss the main literature results on Mn-promotion for unsupported as well as supported Fe-, Ru-, and Co-based Fischer-Tropsch catalysts. Such comparison between Fe-, Ru- and Co-based catalysts has been shown to be very useful because it places the role of Mn as a promoter in FT catalysis in a broader perspective.

### *Mn-promoted Fe-based Fischer-Tropsch catalysts*

*a. Unsupported Fe-Mn Fischer-Tropsch catalysts*

Iron-based FT catalysts possess both hydrogenation and WGS activity, imposing a flexible option as a working catalyst for typical coal-derived CO-rich syngas conversion. Iron-based catalysts often contain small amounts of K and some other metals/metal oxides as promoters to improve their activity and selectivity. Mn has been widely used as one of the promoters for unsupported Fe-based FT catalysts, particularly in promoting the production of $C_2$-$C_4$ olefins [144-153].

Initially Mn was discovered to lower the methane selectivity and increase the olefin selectivity. More specifically, it was reported by Kolbel and Tillmetz [144] that "more than 50% Mn the remainder being Fe" or by Bussemeir *et al.* [145-146] "about equal parts of Fe and Mn" led to beneficial FT effects. In contrast to these results, van Dijk *et al.* [147] did not find any changes in the product formation when adding manganese oxide to a Fe FT catalyst, although this work had been performed at atmospheric pressures, whereas the work of Kolbel and Tillmetz and Bussemeier was done at conditions close to industrial ones.

The findings of Bussemeier *et al.* and Kolbel and Tillmetz were, however, later on confirmed by Barrault and co-workers [148-149], and a maximum increase in light olefin production was found for bulk chemical composition Fe/Mn ratios of 1. This group also explained the promotion effects in terms of electronic changes in the metal atoms by the surrounding manganese compounds; *i.e.*, an electronic promotion effect. On the other hand, Barrault *et al.* also concluded that the beneficial effect of the promoter was related to the preparation method used, and more specifically to the formation of specific $Fe_xMn_yO_z$ precursor compounds. Other preparation routes were found to lead to other precursor species and, as a consequence, the final catalyst materials where also able to show less activity and selectivity. Calcination and reduction temperatures were found to be crucial in this respect. This important set of observations may explain the initial conflicting views on the promotion effect of Mn in Fe-based FT catalysis.

In a series of seminal contributions by the group of Baerns it was reported that both the activity and selectivity of Fe-based FT catalysts are affected by the addition of manganese oxides [150-151]. More specifically, the authors observed that (1) Mn-rich catalysts are rather resistant to deactivation; (2) the olefin to paraffin ratio is affected by the Mn content; the best selectivities towards olefins being obtained when Mn concentrations are about 15-20 wt%; (3) a reduction temperature of 400°C for the oxidic Mn-Fe catalyst precursors results in high initial activity, particularly for Fe-rich catalysts which then, however, deactivate rather severely as compared to when a 300°C reduction temperature is applied. The same authors also studied the changes in the catalyst materials after reduction and under conditions of FT

synthesis. It was found that during reaction the catalyst material was transformed into $Fe_2MnO_4$ and partly into the $Fe_5C_2$ phase. Only minor amounts of $Fe^0$ could be detected during FT synthesis. Years later, Bian *et al.* showed that the pre-reduction of the catalyst with CO or $H_2$ has a remarkable effect on the catalyst performances [152]. This was explained in terms of different types of iron carbide species formed. CO-reduced catalysts exhibit remarkably higher catalytic activity for FT synthesis than the $H_2$-reduced catalysts. Furthermore, CO reduction was shown to be more effective for the formation of iron carbide ($Fe_xC$).

The promotion effects of Mn on unsupported Fe-based FT catalysts were also studied by Jensen and Massoth [153]. These authors concluded that the incorporation of Mn chemically and electronically promotes the active Fe surface. More particularly, it appears to alter the CO hydrogenation reaction path by suppressing the direct formation of paraffins from the reactive intermediate, leading to the increased production of higher olefins. Finally, Das *et al.* also observed that the addition of moderated amounts of Mn promoter to unsupported Fe FT catalysts promotes the catalytic activity as well as the selectivity towards lower alkenes [154].

Due to the importance of the $Fe_xMn_yO_z$ precursor compounds to make true Mn-promoted Fe FT catalysts, several groups have focused on the study of Fe, Mn-oxide compounds [155-159]. For example, Hearne and Pollak studied the coprecipitation of iron and manganese oxides, and a mixture of two compounds was found to exist with the same Fe: Mn ratio [159]. The two compounds are cubic spinels with the same crystallographic parameters; however, one compound is a defect spinel while the other is not. A similar work has been done by Delgado and co-workers [157]. In another study, Goldwasser *et al.* synthesized five perovskite oxides containing La, K, Fe and Mn [158] and observed that the activity of the solids in FT synthesis is strongly dependent on the presence of Fe carbides. Mn was found to increase significantly the production of alkenes, and the combined presence of K and Mn resulted in a stable catalyst with a high yield of $C_2$-$C_4$ alkenes.

More recently, Koizumi *et al.* observed that Mn has an additional beneficial effect in unsupported Fe-based FT catalysts [160]. These authors studied the sulfur resistance of Mn-Fe catalysts and they observed superior catalyst stabilities, especially when the catalysts were pre-reduced in CO. This group also used IR spectroscopy in combination with CO as a probe molecule to compare Fe and Mn-Fe catalysts. It was found that the addition of Mn led to the appearance of several well-resolved bands upon CO adsorption. The appearance of the bands arising from bridged-bonded CO on $Fe^0$ indicated that the size of the $Fe^0$ particles were clearly larger than in the case of the unpromoted catalysts. They attributed the decreased reactivity towards $H_2S$ to the observed increase in $Fe^0$ particle size.

*b. Supported Fe-Mn Fischer-Tropsch catalysts*

A much more limited number of studies have dealt with supported Mn-promoted Fe FT catalysts. In this respect, it is worthwhile to mention the work of Xu *et al.* [161]. These authors added MnO to a Fe/silicalite catalyst and observed an enhanced selectivity towards light olefins. Meanwhile the yields for methane as well as for $CO_2$ formation were almost unaffected by MnO addition. Moreover, the conversion of CO was also insensitive to the addition of the MnO promoter. The results also indicated that the addition of MnO leads to an increased CO adsorption capacity. Das and co-workers also reported on the addition of Mn to silicalite supported Fe catalysts [154]. They observed that the addition of Mn reduces the particle size of the iron oxide precursor, leading to an increase in alkene selectivity. Another important study is by Abbot *et al.* [162]. This group studied the addition of Mn to alumina-supported Fe catalysts and found that promotion led to an increase in the selectivity towards light olefins and a suppression of the selectivity towards methane. These effects were attributed to a change in the Fe dispersion (structural promotion) as well as to an electronic promotion.

***Mn-promoted Ru-based Fischer-Tropsch catalysts***

To the best of our knowledge the first claim on Mn-promoted Ru FT catalysts was made in the patent literature by Kugler and co-workers [163]. Furthermore, it seems that only the group of Hussain have investigated these catalyst systems in great detail [164-176]. Hussain *et al.* observed that the addition of Mn to $Ru/Al_2O_3$, $Ru/SiO_2$ and $Ru/TiO_2$ catalysts produced new or improved active CO hydrogenation sites, which are responsible for the enhancement in the production of high molecular weight as well as unsaturated hydrocarbons. The authors discussed the addition of Mn in terms of an electronical and geometrical modification of the catalytically active Ru surface. In a continuation of their work, the same group used IR and CO as a probe molecule to characterize the metal surface of the supported Mn-Ru catalysts. The results indicated that Mn was present as a layer on the surface of the supported Ru nanoparticles. An increasing Mn loading led to a decreasing CO adsorption intensity, indicating that the excess of Mn masked the active Ru sites responsible for CO adsorption. No CO adsorption was found to occur on isolated Mn sites. In addition, it was found that the addition of Mn resulted in (1) the formation of a low frequency band in the IR spectrum and (2) a shift of the IR bands of Ru-adsorbed CO. Both observations were explained in terms of an electronic promotion effect, giving rise to different electronic properties of the surface Ru sites as well as changes in the local geometry of surface Ru sites. A necessary condition for promotion is that small Mn oxides decorate the surface of the supported Ru nanoparticles.

Related to this decoration of the Ru surface, it is anticipated that the sites responsible for the production of $CH_4$ are blocked by the addition of Mn.

In order to gain additional information on the promotion effect of Mn, Hussain performed XPS, and secondary ion mass spectrometry (SIMS), to investigate the adsorption of adsorbed CO on the supported Mn-Ru FT catalysts [172]. XPS revealed that the addition of CO causes a negative binding energy shift of the Ru peak on silica- and alumina-supported catalyst systems. This shift was higher on the corresponding Mn-promoted catalysts. This was attributed to the combined affect of Ru and Mn on the CO adsorption geometry. On titania-supported systems the unusual shift in Ru binding energy is the result of the formation of $TiO_x$ covering the surface due to the SMSI effect. The SIMS data further supported the findings of the XPS study and $RuCO^+$, $RuO^+$, $MnO^+$ peaks were obtained. No evidence for CO adsorption on Mn or MnO could be detected. All the experimental findings were consistent with the presence of linearly bonded CO on top of Ru nanoparticles supported on $Al_2O_3$ and $SiO_2$.

The SMSI effect in Mn-promoted $Ru/TiO_2$ catalysts was studied in more detail making use of the SIMS technique, as well as with TEM, and selective chemisorption experiments [173]. The SIMS technique revealed the presence of $TiO_x$ forming two new surface sites, $TiO_x$-Ru and $TiO_x$-Mn. These species were found to be located at the immediate vicinity of the Ru nanoparticles. These new surface sites were considered to alter the electronic properties of the Ru metal surface and, as a consequence, the product selectivity.

A similar study was performed by the same group on a model catalyst system; *i.e.*, a Mn/Ru (0001) surface, prepared by sputtering Mn on a Ru (0001) surface at room temperature using a sputtered ion gun [171]. The techniques of choice were SIMS, EELS and TPD. It was concluded that Mn reduces the coverage of CO adsorbed on the surface by physically blocking the adsorption sites. The adsorbed CO molecule is predominantly linearly bonded, whereas EELS indicated a possible existence of an electronic interaction between the deposited Mn and Ru. This was reflected by the change in the CO stretching frequency to lower wavenumbers once Mn was deposited on the Ru surface.

Tercioglu and Akyurtlu also studied the Mn promotion effect on $Ru/Al_2O_3$ catalysts [177]. They observed that the three catalysts under study, 2.5 wt% $Ru/Al_2O_3$, 6.3 wt% Mn-2.5 wt% $Ru/Al_2O_3$ and 6.3 wt% Mn-5 wt% $Ru/Al_2O_3$, showed different olefin selectivities. It was found that (1) the manganese-containing catalysts had higher selectivity for ethylene, which was three times higher than the corresponding umpromoted catalyst, and (2) the olefin-to-paraffin ratio was also affected by the presence of Mn and increased with increasing Mn content. The authors also noticed a similar influence of the Ru: Mn ratio on the formation of longer chain hydrocarbons. Finally, Shapovalova and Zakumbaeva studied Mn-promoted

$Ru/Al_2O_3$ catalysts with adsorption microcalorimetry, XPS and IR [178]. They concluded that Mn also acts as a structural promoter since it increases the dispersion of the Ru nanoparticles.

### *Mn-promoted Co-based Fischer-Tropsch catalysts*

*a. Unsupported Co-Mn Fischer-Tropsch catalysts*

Van der Riet *et al.* were the first to report on the use of Mn as promoter in unsupported Co-based FT catalysts [179]. They reported on a stable Co-containing CO hydrogenation catalyst with a high selectivity for $C_3$ hydrocarbons and suppressed $CH_4$ selectivity. This finding was rationalized in terms of competing hydrogenation and oligomerization reactions of the primary hydrocarbon products. In continuation of this work, Hutchings *et al.* reported in a detailed investigation on the mechanism of CO hydrogenation catalyzed by the Mn-Co catalyst [180]. The results of this study indicate that hydroformylation of a $C_2$ surface intermediate cannot account for the high yields of propene and the low yields of methane observed. Based on their findings, a reaction mechanism for carbon-carbon bond formation was proposed involving α-hydroxylated metal-alkyl as an important intermediate, the formation of which involves the coupling of a number of electrophilic and nucleophilic $C_1$ surface intermediates. *In-situ* XRD studies of the same research group showed that the active catalysts contained bcc metallic Co supported on MnO [181]. This uncommon phase is metastable and readily transforms into the stable fcc structure after exposure to air and slight pressure at room temperature.

Based on this work and that of many other research groups [182-188] it can be stated that oxidized Mn-Co unsupported catalysts are composed of mixed cobalt manganese spinels of $Co_2MnO_4$ and $CoMn_2O_4$, the ratio of which depends upon composition and pretreatment of the catalyst materials. Reduction of the catalysts in $H_2$ results in a material that contains metallic cobalt, MnO and a certain amount of mixed spinels. An interesting study in line with the above description was reported by Liang *et al.* [182]. These authors investigated in detail the influence of the preparation method of Co/Mn oxides and their corresponding Co/Mn ratios on the hydrogenation of CO. Nanometer spinel-type Co/Mn oxides with different Co/Mn ratios ($Co_{3-x}Mn_xO_4$, $0 < x < 1.4$), single phase composition and large specific surface area (> 70 $m^2/g$) were prepared by the sol-gel method. These materials were compared with those prepared by nitrate decomposition and solid-state reaction methods. CO hydrogenation tests indicated that the Co/Mn oxide catalysts had much higher selectivities for light olefins and possessed a lower catalytic activity and methane production capability than the corresponding coprecipitated catalysts with the same composition.

*In-situ* IR experiments on Co and Mn-Co FT catalysts were performed by Jiang *et al.* to study in more detail the effect of the addition of Mn on the surface properties of the catalyst materials [186]. The authors used CO and CO + $H_2$ as probe molecules under flowing conditions. It was found that metallic cobalt particles are formed on both Co and Mn-Co catalysts after reduction. This was manifested by the occurrence of the bands corresponding to CO adsorbed on metallic Co sites. On the reduced Co sample, however, the molecularly adsorbed CO species were rather difficult to detect because of the rapid dissociation of CO on the fine active metallic cobalt particles formed. For the Mn-Co catalyst, however, distinct IR bands appeared and their intensities increased with increasing Mn loading. These bands were attributed to linearly, bridged, and multiply bridged-bonded CO. The authors considered that the sizes of the Co particles in the reduced Mn-Co catalyst were larger than those in the reduced Co catalyst, and that the stability of the Co particles could be remarkably enhanced with the incorporation of Mn promoter. This enhanced catalyst stability might be manifested by a decreased deactivation and an increased $H_2S$ tolerance.

Keyser *et al.* studied Mn-Co FT catalysts and found that, under industrial relevant conditions, the WGS activity of the catalysts increases with increasing Mn content, but decreases with increasing pressure [183-184]. A lower olefin yield was also observed at high pressures. It was stated that structural changes in the cobalt spinel occur over a long period of time and are responsible for the increased hydrogenation activity and increased WGS activity. Mn seems in this respect not to be able to stabilize the cobalt spinel structure in order to retain the olefin activity. Finally, Riedel *et al.* also noticed the WGS activity of MnO and that the addition of this compound to Co FT catalysts led to the production of $CO_2$ [187]. In other words, Mn can be regarded as a water-gas shift promoter under FT conditions.

*b. Supported Co-Mn Fischer-Tropsch catalysts*

The synthesis of lower hydrocarbons on silicalite-1 supported Co and Co-Mn catalysts was reported by Das *et al.* [68, 77]. $Co_3O_4$ was found to be the only phase present in the Mn-free catalysts after calcination, while the addition of Mn favored the formation of a mixed spinel structure of the type $(Co_{1-x}Mn_x)_3O_4$. They considered that the addition of Mn decreased the reduction temperature of $Co_3O_4$ and presumably its particle size. The catalysts showed good activity and selectivity for light hydrocarbons in the $C_2$-$C_4$ range, particularly propene, and also showed very low WGS activity. Furthermore, the addition of Mn increased the CO conversion, while the selectivity towards alkenes slightly decreased.

Another interesting use of zeolites in FT catalysis is the addition of pentasil zeolites, *e.g.* ZSM-5, to the unsupported Mn-Co FT catalyst in order to shift the product distribution [67]. Two modes of operation were tested. The first was a single bed reactor with a mechanical

mixture of the two components. The second mode of operation consisted of a dual bed approach with the Mn-Co and zeolite in separate reactors. This method of operation led to the formation of aromatic compounds, due to the transformation of olefinic and oxygen containing hydrocarbons. Additionally, high molecular weight hydrocarbons were cracked into lower alkanes. It was concluded that the dual bed arrangement with separate reactors was preferred since it allowed to adjust the optimum temperature for the F-T as well as the zeolite system and to regenerate the zeolite component independently.

Zhang *et al.* studied the Mn promotion in $Co/Al_2O_3$ catalysts [74]. It was found that the addition of Mn improves the catalytic activity, as well as the $C_{5+}$ selectivity, while the formation of methane and $C_{2-4}$ hydrocarbons is significantly suppressed. They observed that Mn improved the dispersion of the active Co phase and also favored the formation of bridge-type adsorbed CO as probed with IR. A small amount of Mn was also able to increase the $H_2$ uptake, although it was again decreased with an excess of Mn.

A very detailed characterization study on Mn-promoted $Co/SiO_2$ catalysts was carried out by the group of Klabunde [70-71]. They prepared their catalyst materials making use of the solvated metal atom dispersion (SMAD) technique. In this process metal atoms such as Co and Mn are solvated at low temperature in toluene or other appropriate solvents. Upon warming the nucleation begins. The catalysts prepared were investigated with EXAFS and tested in the hydrogenation reaction of olefins. It was found that the reduced catalysts contained Mn in the oxidized state and Co in both the metallic and oxidized state. The presence of Mn might permit an appreciable increase in metallic Co. The EXAFS results also indicated that the most active $Mn\text{-}Co/SiO_2$ catalyst had the largest amount of metallic cobalt and it was argued that the more oxophilic metal, Mn, would scavenge oxygen, allowing Co to remain in the metallic state. Chemisorption studies revealed that the addition of Mn increased the Co dispersion and it was proposed that Mn, in addition to aiding in the dispersion, also influenced the catalytic performances by an electronic effect. The authors also noticed that Mn was most probably bound to the support as a highly dispersed MnO phase, while Co metal could be stabilized on the MnO.

The effects of Mn promoter on $Co/TiO_2$ catalysts were investigated by Voβ *et al.* [75]. They observed that the formation of $CoTiO_3$ was more evident in the presence of Mn. XPS revealed that Mn was much more dispersed than Co in the catalyst system and no appreciable shifts in Co2p XPS binding energies were noticed when Mn was present in the catalyst. Mn was in the reduced catalysts present as MnO and it was assumed that MnO had no influence on the catalytic properties and served as an additional support. Recently, Martinez *et al.* reported the use of mesoporous Co/SBA-15 catalysts promoted with Mn for FT synthesis [72]. They observed that Mn favored the formation of long-chain n-paraffins ($C_{10+}$), while

decreasing the selectivity towards methane. The Mn-promoted catalysts, however, turned out to be less active than the unpromoted ones.

## Concluding remarks and outlook

Fischer-Tropsch synthesis making use of cobalt-based catalysts is a hotly pursued scientific topic in the catalysis community since it offers an interesting and economically viable route for the conversion of *e.g.* natural gas to sulphur-free diesel fuels. As a result, major oil companies have recently announced to implement this technology and major investments are under way to build large Fischer-Tropsch plants based on cobalt-based catalysts in *e.g.* Qatar. Promoters have shown to be crucial to alter the catalytic properties of these catalyst systems. For this reason, almost every chemical element of the periodic table has been evaluated in the open literature for its potential beneficial effects on the activity, selectivity and stability of supported cobalt nanoparticles.

The addition of promoter elements to cobalt-based FT catalysts can affect (1) directly the formation and stability of the active cobalt phase (*structural promotion*) by altering the cobalt-support interfacial chemistry, (2) directly affect the elementary steps involved in the turnover of the cobalt active site by altering the electronic properties of the cobalt nanoparticles *(electronic promotion*) and (3) indirectly the behaviour of the active cobalt phase, by changing the local reaction environment of the active site as a result of chemical reactions performed by the promoter element itself (*synergistic promotion*).

Despite major research efforts, not so much fundamental insights exist in the origin and the exact mode of operation of these promotion effects. Furthermore, the same promoter can exhibit several effects on the catalyst performances. In addition, there are some contradictions in the literature on the proposed effects of specific promoter elements. Several reasons can be put forward to explain these general observations:

(1) Promoted cobalt-based FT catalysts are from material scientist perspective very complex systems. As a consequence, most characterization techniques, including surface as well as bulk spectroscopies, are not suitable for discriminating between the multiple cobalt and promoter species present at the surface of the support oxide. As a result, only detailed physicochemical insight can be obtained by making use of a combination of advanced characterization techniques. Since each technique has its own sensitivity towards the different active and spectator species present at the catalyst surface, a more complete picture will only emerge by combining the information gathered by the different spectroscopic techniques employed.

(2) Promoter elements only exhibit their beneficial effect in a limited concentration range as the addition of the promoters in a too high amount may lead to a complete decoration of

the active cobalt surface, and as a consequence, result in a decrease of the catalyst activity. In addition, the preparation method is crucial in achieving the envisaged promotion effect. Both arguments may be responsible for the conflicting views in the literature on the different promotion effects of a specific element added to the catalyst material. On the other hand, all this indicates that catalyst preparation tools should be improved to add promoter elements in a precise and controlled manner to the catalyst material. It is, however, important to recall that such synthesis tools should be at a later stage still attractive to the large-scale industrial production of cobalt-based Fischer-Tropsch catalysts.

(3) It is far from easy to distinguish structural, electronic and synergistic promotion effects. Structural promotion is, in this respect, the most easily to observe. Most synergistic effects are also widely discussed in the literature in enhancing the catalytic performance of supported cobalt nanoparticles. Instead, promotion as a result of electronic effects are much more difficult to detect. The main reason is that one has to discriminate between the number of surface cobalt sites and the intrinsic activity of a surface cobalt site (turnover frequency). This is especially difficult in view of the complexity of the catalyst material. It also requires spectroscopic tools, which are able to detect changes in the electronic structure of the supported cobalt nanoparticles.

(4) The characterization tools to investigate cobalt-based FT catalysts are mostly used to study the catalyst materials under conditions far from industrially relevant reaction conditions; *i.e.*, in the presence of CO and $H_2$, as well as of the reaction products, including $H_2O$; at reaction temperatures and at high pressures. Since catalytic solids are dynamic materials undergoing major changes under reaction conditions it can be anticipated that the currently obtained information on the active site is at least incomplete. This holds also for the active state and location of the promoter element under reaction conditions. For example, an electronic effect on the cobalt active phase induced by a promoter element can maybe exist only at high pressures and will remain - due to the lack of the appropriate instrumentation - unnoticed to the catalyst scientist. Therefore, major efforts should be directed to the development of advanced *in-situ* spectroscopy-microscopy techniques to study promoted Co-based FT catalysts in action.

Summarizing, there are still many scientific challenges and major opportunities for the catalysis community in the field of cobalt-based Fischer-Tropsch synthesis to design improved or totally new catalyst systems. However, such improvements require a profound knowledge of the promoted catalyst material. In this respect, detailed physicochemical insights in the cobalt-support, cobalt-promoter and support-promoter interfacial chemistry are of paramount importance. Advanced synthesis methods and characterization tools giving

structural and electronic information of both the cobalt and the support element under reaction conditions should be developed to achieve this goal. This is the topic of this thesis with the $Co/Mn/TiO_2$ catalyst as the showcase system under study.

## References and notes


[1] E. Iglesia, S.L. Soled, R.A. Fiato, *J. Catal*., 1993, **143**, 345.

[2] M. Hoang, A.E. Hughes, T.W. Turney, *Appl. Surf. Sci*., 1993, **72**, 55.

[3] L.A. Bruce, M. Hoang, A.E. Hughes, T.W. Turney, *Appl. Catal. A: General*, 1993, **100**, 51.

[4] E. Iglesia, S.L. Soled, R.A. Fiato, G.H. Via, *Stud. Surf. Sci. Catal.*, 1994, **81**, 433.

[5] J. Vaarl, J. Lahtinen, P. Hautojarvi, *Surf. Sci*., 1996, **346**, 11.

[6] C.L. Bianchi, R. Carli, S. Merlotti, V. Ragaini, *Catal. Lett*., 1996, **41**, 79.

[7] A. Kogelbauer, J.G. Goodwin, R. Oukaci, *J. Catal*., 1996, **160**, 125.

[8] G.D. Zakumbayeva, L.B. Shapovalova, I.G. Yefremenko, A.V. Gabdrakipov, *Petroleum Chem*., 1996, **36**, 428.

[9] A.R. Belambe, R. Oukaci, J.G. Goodwin, *J. Catal*., 1997, **166**, 8.

[10] J.G. Price, D. Glasser, D. Hildebrandt, N.J. Coville, *Stud. Surf. Sci. Catal.*, 1997, **107**, 243.

[11] E. Iglesia, *Stud. Surf. Sci. Catal.*, 1997, **107**, 153.

[12] M. Niemela, M. Reinikainen, J. Kiviaho, *Stud. Surf. Sci. Catal.*, 1998, **118**, 229.

[13] C.L. Bianchi, S. Vitali, V. Ragaini, *Stud. Surf. Sci. Catal.*, 1998, **119**, 167.

[14] M. Reinikainen, M.K. Niemela, N. Kakuta, S. Suhonen, *Appl. Catal. A: General*, 1998, **174**, 61.

[15] L. Guczi, G. Stefler, Z. Koppany, V. Komppa, M. Reinikainen, *Stud. Surf. Sci. Catal.*, 1999, **121**, 209.

[16] P.M. Maitlis, R. Quyoum, H.C. Long, M.L. Turner, *Appl. Catal. A: General*, 1999, **186**, 363.

[17] Y. Borodko, G.A. Somorjai, *Appl. Catal. A: General*, 1999, **186**, 355.

[18] M. Kraum, M. Baerns, *Appl. Catal. A: General*, 1999, **186**, 189.

[19] Y.L. Zhang, D.G. Wei, S. Hammache, J.G. Goodwin, *J. Catal*., 1999, **188**, 281.

[20] L. Huang, Y. Xu, *Catal. Lett*., 2000, **69**, 145.

[21] J.L. Li, L.G. Xu, R. Keogh, B. Davis, *Catal. Lett*., 2000, **70**, 127.

[22] L. Huang, Y.D. Xu, *Appl. Catal. A: General*, 2001, **205**, 183.

[23] H.A.J. van Dijk, J.H.B. Hoebink, J.C. Schouten, *Chem. Eng. Sci*., 2001, **56**, 1211.

[24] G. Jacobs, Y. Zhang, T.K. Das, J. Li, P.M. Patterson, B.H. Davis, *Stud. Surf. Sci. Catal*., 2001, **139**, 415.

[25] B. Jongsomjit, J. Panpranot, J.G. Goodwin, *J. Catal*., 2001, **204**, 98.

[26] S. Hammache, J.G. Goodwin, R. Oukaci, *Catal. Today*, 2002, **71**, 361.

[27] S. Sun, K. Fujimoto, Y. Yoneyama, N. Tsubaki, *Fuel*, 2002, **81**, 1583.

[28] J. Panpranot, J.G. Goodwin, A. Sayari, *J. Catal*., 2002, **211**, 530.

[29] M.L. Turner, N. Marsih, B.E. Mann, R. Quyoum, H.C. Long, P.M. Maitlis, *J. Am. Chem. Soc*., 2002, **124**, 10456.
[30] J. Panpranot, J.G. Goodwin, A. Sayari, *Catal. Today*, 2002, **77**, 269.
[31] J. Panpranot, J.G. Goodwin, A. Sayari, *J. Catal*., 2003, **213**, 78.
[32] D. Bazin, I. Kovacs, J. Lynch, L. Guczi, *Appl. Catal. A: General*, 2003, **242**, 179.
[33] L.B. Shapovalova, G.D. Zakumbaeva, A.V. Gabdrakipov, *Pet. Chem*., 2003, **43**, 170.
[34] M. Shinoda, Y. Zhang, Y. Shiki, Y. Yoneyama, K. Hasegawa, N. Tsubaki, *Catal. Comm*., 2003, **4**, 423.
[35] M. Johns, P. Collier, M.S. Spencer, T. Alderson, G.J. Hutchings, *Catal. Lett*., 2003, **90**, 187.
[36] H.A.J. van Dijk, J.H.B.J. Hoebink, J.C. Schouten, *Top. Catal.*, 2003, **26**, 111.
[37] H.A.J. van Dijk, J.H.B.J. Hoebink, J.C. Schouten, *Top. Catal*., 2003, **26**, 163.
[38] F.M.T. Mendes, F.B. Noronha, C.D.D. Sluza, M.A.P. da Silva, A.B. Gaspar, M. Schmal, *Stud. Surf. Sci. Catal*., 2004, **147**, 361.
[39] S.A. Hosseini, A. Taeb, F. Feyzi, F. Yaripour, *Catal. Comm*., 2004, **5**, 137.
[40] L.B. Shapovalova, G.D. Zakumbaeva, A.A. Zhurtbaeva, *Stud. Surf. Sci. Catal*., 2004, **147**, 373.
[41] G.D. Zakumbaeva, L.B. Shapovalova, *Petr. Chem*., 2004, **44**, 334.
[42] M. Cerro-Alarcon, A. Maroto-Valiente, I. Rodríguez-Ramos, A. Guerrero-Ruiz, D. Schanke, A.M. Hilmen, E. Bergene, K. Kinnari, E. Rytter, E. Adnanes, A. Holmen, *Catal. Lett*., 1995, **34**, 269.
[43] L.E.S. Rygh, I. Gausemel, O.H. Ellestad, P. Klaeboe, C.J. Nielsen, E. Rytter, *J. Mol. Struc*., 1995, **349**, 325.
[44] A.M. Hilmen, D. Schanke, A. Holmen, *Catal. Lett*., 1996, **38**, 143.
[45] A.M. Hilmen, D. Schanke, A. Holmen, *Stud. Surf. Sci. Catal.,* 1997, **107**, 237.
[46] A.M. Hilmen, D. Schanke, K.F. Hanssen, A. Holmen, *Appl. Catal. A: General*, 1999, **186**, 169.
[47] L.E.S. Rygh, C.J. Nielsen, *J. Catal*., 2000, **194**, 401.
[48] A.M. Hilmen, E. Bergene, O.A. Lindvag, D. Schanke, S. Eri, A. Holmen, *Catal. Today*, 2001, **69**, 227.
[49] M. Ronning, D.G. Nicholson, A. Holmen, *Catal. Lett*., 2001, **72**, 141.
[50] L. Guczi, G. Stefler, Z. Koppany, L. Borko, *React. Kin. Catal. Lett*., 2001, **74**, 259.
[51] L. Guczi, L. Takacs, G. Stefler, Z. Koppany, L. Borko, *Catal. Today*, 2002, **77**, 237.
[52] D. Bazin, L. Borko, Z. Koppany, I. Kovacs, G. Stefler, L.I. Sajo, Z. Schay, L. Guczi, *Catal. Lett*., 2002, **84**, 169.
[53] L. Guczi, G. Stefler, L. Borko, Z. Koppany, F. Mizukami, M. Toba, S. Niwa, *Appl. Catal. A: General*, 2003, **246**, 79.
[54] G. Jacobs, J.A. Chaney, P.M. Patterson, T.K. Das, B.H. Davis, *Appl. Catal. A: General*, 2004, **264**, 203.
[55] C.J. Bertole, C.A. Mims, G. Kiss, *J. Catal*., 2004, **221**, 191.

[56] C. Aaserud, A.M. Hilmen, E. Bergene, S. Eric, D. Schanke, A. Holmen, *Catal. Lett*., 2004, **94**, 171.
[57] Z. Zsoldos, T. Hoffer, L. Guczi, *J. Phys. Chem*., 1991, **95**, 798.
[58] L. Guczi, T. Hoffer, Z. Zsoldos, S. Zyade, G. Maire, F. Garin, *J. Phys. Chem*., 1991, **95**, 802.
[59] G.M. Lu, T. Hoffer, L. Guczi, *Catal. Lett*., 1992, **14**, 207.
[60] Z. Zsoldos, L. Guczi, *J. Phys. Chem*., 1992, **96**, 9393.
[61] D. Schanke, S. Vada, E.A. Blekkan, A.M. Hilmen, A. Hoff, A. Holmen, *J. Catal*., 1995, **156**, 85.
[62] S. Tang, J. Lin, K.L. Tan, *Surf. Int. Anal*., 1999, **28**, 155.
[63] G.W. Huber, C.H. Bartholomew, T.L. Conrad, K.W. Woolley, C.G. Guymon, *Am. Chem. Soc. Abstracts*, 2000, **219**, 261.
[64] J. Li, X. Zhang, Y. Zhang, G. Jacobs, T. Das, H. Davis, *Appl. Catal. A: General*, 2002, **228**, 203.
[65] G. Jacobs, T.K. Das, P.M. Patterson, J. Li, L. Sanchez, B.H. Davis, *Appl. Catal. A: General*, 2003, **247**, 335.
[66] G. Jacobs, J.A. Chaney, P.M. Patterson, T.K. Das, J.C. Maillot, B.H. Davis, *J. Synchrot. Rad*., 2004, **11**, 414.
[67] D.J. Koh, J.S. Chung, Y.G. Kim, *Ind. Eng. Chem. Res.*, 1995, **34**, 1969.
[68] D. Das, G. Ravichandran, D.K. Chakrabarty, *Catal. Today*, 1997, **36**, 285.
[69] G. Baurle, K. Guse, M. Lohrengel, H. Papp, *Stud. Surf. Sci. Catal.*, 1993, **75**, 2789.
[70] B.J. Tan, K.J. Klabunde, T. Tanaka, H. Kanai, S. Yoshida, *J. Am. Chem. Soc.*, 1998, **110**, 5951.
[71] K.J. Klabunde, Y. Imizu, *J. Am. Chem. Soc.*, 1984, **106**, 2721.
[72] A. Martinez, C. Lopez, F. Marquez, I. Diaz, *J. Catal.*, 2003, **220**, 486.
[73] H.Y. Gao, J.G. Chen, H.W. Xiang, J.L. Yang, Y.W. Li, Y.H. Sun, *Chin. J. Catal.*, 2001, **22**, 133.
[74] J.L. Zhang, J. Ren, J.G. Chen, Y.H. Sun, *Acta Physico-Chimica Sin.*, 2002, **18**, 260.
[75] M. Voβ, D. Borgmann, G. Wedler, *J. Catal.*, 2002, **212**, 10.
[76] C.H. Bartholomew, R.C. Reuel, *Ind. Eng. Chem. Prod. Res. Dev.*, 1985, **24**, 56.
[77] D. Das, G. Ravichandran, D.K. Chakrabarty, *Appl. Catal. A:General*, 1995, **131**, 335.
[78] J.L. Li, N.J. Coville, *Appl. Catal. A: General*, 1999, **181**, 201.
[79] J.L. Li, N.J. Coville, *Appl. Catal. A: General*, 2001, **208**, 177.
[80] N.J. Coville, J. Li, *Catal. Today*, 2002, **71**, 403.
[81] J.L. Li, N.J. Coville, *South African J. Chem.*, 2003, **56**, 1.
[82] J.L. Li, N.J. Coville, *Am. Chem. Soc.*, 2003, 226.
[83] S. All, B. Chen, J.G. Goodwin, *J. Catal*., 1995, **157**, 35.
[84] R. Oukaci, J.G. Goodwin, G. Marcelin, A. Singleton, *Am. Chem. Soc. Abstracts*, 1995, **209**.
[85] G.R. Moradi, M.M. Basir, A. Taeb, A. Kiennemann, *Catal. Comm*., 2003, **4**, 27.
[86] B. Jongsomjit, J. Panpranot, J.G. Goodwin, *J. Catal.*, 2003, **215**, 66.
[87] W. Zhou, J.G. Chen, Y.H. Sun, *Chin. J. Catal*., 2004, **25**, 467.

[88] S. Vada, A.M. Kazi, F.K. Beduaddo, B. Chen, J.G. Goodwin, *Stud. Surf. Sci. Catal.*, 1994, **81**, 443.

[89] S. Vada, B. Chen, J.G. Goodwin, *J. Catal*., 1995, **153**, 224.

[90] G.J. Haddad, B. Chen, J.G. Goodwin, *J. Catal*., 1996, **161**, 274.

[91] G.J. Haddad, B. Chen, J.G. Goodwin, *J. Catal*., 1996, **160**, 43.

[92] J. Vaari, J. Lahtinen, A. Talo, P. Hautojarvi, *Surf. Sci*., 1991, **251**, 1096.

[93] I. Puskas, T.H. Fleisch, J.B. Hall, B.L. Meyers, R.T. Roginski, *Stud. Surf. Sci. Catal*. 1993, **75**, 2813.

[94] M.K. Niemela, A.O.I. Krause, *Catal. Lett*., 1995, **34**, 75.

[95] A.F.Y. Alshammary, I.T. Caga, A.Y. Tata, J.M. Winterbotton, *Eur. J. Sol. State Inorg. Chem*., 1991, **28**, 453.

[96] X.P. Dai, C.C. Yu, S.K. Shen, *Chin. J. Catal*., 2001, **22**, 104.

[97] H.B. Shi, Q. Li, X.P. Dai, C.C. Yu, S.K. Shen, *Stud. Surf. Sci. Catal*., 2004, **147**, 313.

[98] E.A. Blekkan, A. Holmen, S. Vada, *Act. Chem. Scand*., 1993, **47**, 275.

[99] G.P. Huffman, H. Shan, J.M. Zhao, F.E. Huggins, T.E. Hoost, S. Halvorsen, J.G. Goodwin, *J. Catal*., 1995, **151**, 17.

[100] S.J. Jenkins, D.A. King, *J. Am. Chem. Soc*., 2000, **122**, 10610.

[101] G.W. Huber, S.J.M. Butala, M.L. Lee, C.H. Bartholomew, *Catal. Lett*., 2001, **74**, 45.

[102] H.K. Woo, R. Srinivasan, L. Rice, R.J. Deangelis, P.J. Reucroft, *J. Mol. Catal*., 1990, **59**, 83.

[103] J.E. Baker, R. Burch, S.J. Hibble, P.K. Loader, *Appl. Catal*., 1990, **65**, 281.

[104] A.L. Lapidus, A.Y. Krylova, M.P. Kapur, E.V. Leongardt, A.B. Fasman, S.D. Mikhailenko, *Bull. Russ. Acad. Sci.-Div. Chem. Sci.*, 1992, **41**, 45.

[105] S.E. Colley, M.J. Betts, R.G. Copperthwaite, G.J. Hutchings, N.J. Coville, *J. Catal*., 1992, **134**, 186.

[106] A.F.Y. Alshammary, I.T. Caga, A.Y. Tata, J.M. Winterbottom, I.R. Harris, *J. Chem. Tech. Biotech*., 1992, **55**, 375.

[107] I.R. Harris, I.T. Caga, A.Y. Tata, J.M. Winterbottom, *Stud. Surf. Sci. Catal*., 1993, **75**, 2801.

[108] M.P. Kapoor, A.L. Lapidus, A.Y. Krylova, *Stud. Surf. Sci. Catal*., 1993, **75**, 2741.

[109] A.G. Ruiz, A.S. Escribano, I.R. Ramos, *Appl. Catal. A: General*, 1994, **120**,71.

[110] S. Bessell, *Stud. Surf. Sci. Catal*., 1994, **81**, 479.

[111] S.Vada, A. Of., E. Adnanes, D. Schanke, A. Holmen, *Top. Catal*., 1995, **2**, 155.

[112] J. Barrault, N. Biwole, *Bull. Soc. Chim. Belg.*, 1995, **104**, 149.

[113] M. Niemela, M. Reinikainen, *Stud. Surf. Sci. Catal*., 1998, **119**, 161.

[114] D.O. Uner, *Ind. Eng. Chem. Res*., 1998, *37*, 2239.

[115] K. Okabe, X.H. Li, T. Matsuzaki, M. Toba, H. Arakawa, K. Fujimoto, *J. Jap. Petrol. Inst*., 1999, **42**, 377.

[116] E. Kikuchi, R. Sorita, H. Takahashi, T. Matsuda, *Appl. Catal. A: General*, 1999, **186**, 121.

[117] A. Frydman, D.G. Castner, C.T. Campbell, M. Schmal, *J. Catal*., 1999, **188**, 1.

[118] S. Sun, N, Tsubaki, K. Fujimoto, *Chem. Lett*., 2000, **2**, 176.

[119] J.L. Li, L.G. Xu, R.A. Keogh, B.H. Davis, *Am. Chem. Soc*. *Abstracts*, 2000, **219**.

[120] N. Tsubaki, S.L. Sun, K. Fujimoto, *J. Catal*., 2001, **199**, 236.

[121] K. Okabe, X.H. Li, T. Matsuzaki, H. Arakawa, K. Fukimoto, *J. Sol-Gel Sci. Tech*., 2000, **19**, 519.

[122] C.L. Bianchi, *Catal. Lett*., 2001, **76**, 155.

[123] D.G. Wei, J.G. Goodwin, R. Oukaci, A.H. Singleton, *Appl. Catal. A: General*, 2001, **210**, 137.

[124] G. Jacobs, T.K. Das, Y.Q. Zhang, J.L. Li, G. Racoillet, B.H. Davis, *Appl. Catal. A: General*, 2002, **233**, 263.

[125] G. Jacobs, P.M. Patterson, Y.Q. Zhang, T. Das, J.L. Li, B.H. Davis, *Appl. Catal. A: General*, 2002, **233**, 215.

[126] J.L. Li, G. Jacobs, Y.Q. Zhang, T. Das, B.H. Davis, *Appl. Catal. A: General*, 2002, **223**, 195.

[127] R.V. Belosludov, S. Skahara, K. Yajima, S. Takami, M. Kubo, A. Miyamoto, *Appl. Surf. Sci*., 2002, **189**, 245.

[128] T. Riedel, G. Schaub, *Top. Catal*., 2003, **26**, 145.

[129] A. Martinez, C. Lopez, F. Marquez, I. Diaz, *J. Catal*., 2003, **220**, 486.

[130] M. Wei, K. Okabe, H. Arakawa, *J. Jap. Petrol. Inst*., 2003, **46**, 339.

[131] W.S. Yang, D.H. Yin, J. Chang, H.W. Xiang, Y.Y. Xu, Y.W. Li, *Acta Chim. Sinica*., 2003, **61**, 681.

[132] F.M.T. Mendes, F.B. Noronha, C.D.D. Souza, M.A.P. da Silva, A.B. Gaspar, M. Schmal, *Stud. Surf. Sci. Catal*., 2004, **147**, 361.

[133] N. Koizumi, K. Murai, T. Ozaki, M. Yamada, *Catal. Today*, 2004, **89**, 465.

[134] K. Nagaoka, K. Takanabe, K. Aika, *Appl. Catal. A: General*, 2004, **268**, 151.

[135] D. Bazin, L. Guczi, *Stud. Surf. Sci. Catal*., 2004, **147**, 343.

[136] G.L. Bezemer, U. Falke, A.J. van Dillen, K.P. de Jong, *Chem. Commun.*, **2005**, 701.

[137] G.L. Bezemer, P.B. Radstake, U. Falke, H. Oosterbeek, A.J. van Dillen, K.P. de Jong, J. Catal., 2006, 237, 152.

[138] B. Cornils, W.A. Herrmann, R. Schlogl, C.H. Wong, *Catalysis from A to Z, A concise encyclopedia*, Wiley-VCH, Weinheim, 2000.

[139] A.M. Saib, M. Claeys, E. van Steen, *Catal. Today*, 2002, **71**, 395.

[140] Z. Paal, G.A. Somorjai, in *Handbook of Heterogeneous Catalysis*, Ertl, G., Knozinger, H., Weitkamp, J. (Eds.), Wiley-VCH, Weinheim, 1997, p. 1084.

[141] G. Ertl, H. Knozinger, J. Weitkamp (Eds.), *Preparation of Solid Catalysts*, Wiley-VCH, 1999.

[142] M.P. Kiskinova, *Stud. Surf. Sci. Catal.*, 1992, **70**.

[143] The term SMSI was introduced by Tauster *et al.* (S.J. Tauster, S.C. Funk, R.L. Garten, *J. Am. Chem. Soc.*, 1978, **100**, 170) to denote the effect responsible for the drastic decrease in CO and $H_2$ chemisorption on titania-supported metals after incrasing the reduction temperature frok 200 to 500ºC. More details on this effect can be found in a review paper of Hadjiivanov and Klissurski (K.I. Hadjiivanov, D.G. Klissurski, *Chem. Soc. Rev.*, 1996, **25**, 61).

[144] H. Kolbel, K.D. Tillmetz, *Germ. Pat. Appl.* 2 507 647 (1976).

[145] B. Bussemeier, C.D. Frohning, B. Cornils, *Hydrocarbon Process.*, 1976, **56**, 105.

[146] B. Bussemeier, C.D. Frohning, G. Horn, W. Kluy, *Germ. Pat. Appl.* 2 518 964 (1976).

[147] W.M. van Dijk, J.W. Niemantsverdriet, A.M. Van der Kraan, H.S. Van der Baan, *Appl. Catal.*, 1982, **2**, 273.
[148] J. Barrault, C. Renard, *Appl. Catal.*, 1985, **14**, 133.
[149] J. Barrault, C. Forquy, V. Perrichon, *Appl. Catal.*, 1983, **5**, 119.
[150] R. Malessa, M. Baerns, *Ind. Eng. Chem. Res.*, 1988, **27**, 279.
[151] G.C. Maiti, R. Malessa, M. Baerns, *Appl. Catal.*, 1983, **5**, 151.
[152] G.Z. Bian, A. Oonuki, N. Koizumi, H. Nomoto, M. Yamada, *J. Mol. Catal. A:Chemical*, 2002, **186**, 203.
[153] K.B. Jensen, F.E. Massoth, *J. Catal.*, 1985, **92**, 109.
[154] C.K. Das, N.S. Das, D.P. Choudhury, G. Ravichandran, D.K. Chakrabarty, *Appl. Catal. A:General*, 1994, **111**, 119.
[155] J. Yang, Y. Lieu, J. Chang, Y.N. Wang, L. Bai, Y.Y. Xu, H.W. Xiang, Y.W. Li, B. Zhong, *Ind. Eng. Chem. Res.*, 2003, **42**, 5066.
[156] Y. Liu, J. Yang, L. Bai, Y. Li, L.J. Liu, H.W. Xiang, Y.W. Li, B. Zhong, *Chin. J. Catal.*, 2003, **24**, 299.
[157] S.M. Rodulfo-Baechler, S.L. Cortes-Gonzalez, J. Orozco, A.J. Mora, G. Delgado, *Revista Mex. Fisica*, 2003, **49**, 195.
[158] M.R. Goldwasser, V.E. Dorantes, M.J. Perez-Zurita, P.R. Sojo, M.L. Cubeiro, E. Pietri, F. Gonzalez-Jimenez, Y.N. Lee, D. Moronta, *J. Mol. Catal. A:Chemical*, 2003, **193**, 227.
[159] G.R. Hearne, H. Pollak, *Hyperfine Interact.*, 1991, **67**, 559.
[160] N. Koizumi, K. Murai, T. Ozaki, M. Yamada, *Catal. Today*, 2004, **89**, 465.
[161] L.Y. Xu, Q.X. Wang, D.B. Liang, X. Wang, L.W. Lin, W. Cui, Y.D. Xu, *Appl. Catal. A:General*, 1998, **173**, 19.
[162] J. Abbot, N.J. Clark, B.H. Baker, *Appl. Catal.*, 1986, **26**, 141.
[163] E.L. Kugler, S.J. Tauster, S.C. Fung, *US. Pat.* 4,206,134 (1980).
[164] S.T. Hussain, *J. Chem. Soc. Pakistan*, 1993, **15**, 97.
[165] S.T. Hussain, *J. Chem. Soc. Pakistan*, 1993, **15**, 110.
[166] S.T. Hussain, *J. Chem. Soc. Pakistan*, 1993, **15**, 162.
[167] S.T. Hussain, *J. Chem. Soc. Pakistan*, 1993, **15**, 234.
[168] S.T. Hussain, *J. Chem. Soc. Pakistan*, 1994, **16**, 87.
[169] S.T. Hussain, *J. Chem. Soc. Pakistan*, 1995, **17**, 133.
[170] S.T. Hussain, *J. Trace Microprobe Techn.*, 1996, **14**, 353.
[171] S.T. Hussain, *J. Trace Microprobe Techn.*, 1996, **14**, 361.
[172] S.T. Hussain, *J. Trace Microprobe Techn.*, 1996, **14**, 367.
[173] S.T. Hussain, *J. Trace Microprobe Techn.*, 1996, **14**, 681.
[174] S.T. Hussain, *Ads. Sci. Techn.*, 1996, **13**, 489.
[175] S.T. Hussain, M.A. Atta, *Turkish J. Chem.*, 1997, **21**, 77.
[176] S.T. Hussain, F. Larachi, *J. Trace Microprobe Techn.*, 2002, **20**, 197.
[177] T. Tercioglu, J.F. Akyurtlu, *Appl. Catal. A:General*, 1996, **136**, 105.
[178] L.B. Shapovalova, G.D. Zakumbaeva, *Petroleum Chem.*, 2000, **40**, 151.

[179] M. van der Riet, G.J. Hutchings, R.G. Copperthwaite, *J. Chem. Soc., Chem. Commun.*, 1986, 798.
[180] G.J. Hutchings, M. van der Riet, R. Hunter, *J. Chem. Soc., Faraday Trans. 1*, 1989, **85**, 2875.
[181] S.E. Colley, R.G. Copperthwaite, G.J. Hutchings, S.P. Terblanche, M.M. Thackeray, *Nature*, 1989, **339**, 129.
[182] Q. Liang, K. Chen, W. Hou, Q. Yan, *Appl. Catal. A:General*, 1998, **166**, 191.
[183] M.J. Keyser, R.C. Everson, R.L. Espinoza, *Appl. Catal. A:General*, 1998, **171**, 99.
[184] M.J. Keyser, R.C. Everson, R.L. Espinoza, *Ind. Eng. Chem. Res.*, 2000, **39**, 48.
[185] S.M. Rudolfo-Baechler, S.L. Gonzalez-Cortes, J. Orozco, V. Sagredo, B. Fontal, A.J. Morea, G. Delgado, *Mater. Lett.*, 2004, **58**, 2447.
[186] M. Jiang, N. Koizumi, T. Ozaki, M. Yamada, *Appl. Catal. A:General*, 2001, **209**, 59.
[187] T. Riedel, M. Claeys, H. Schulz, G. Schaub, S.S. Nam, K.W. Jun, M.J. Choi, G. Kishan, K.W. Lee, *Appl. Catal. A:General*, 1999, **186**, 201.
[188] K. Guse, H. Papp, *Fres. J. Anal. Chem.*, 1993, **346**, 84.
[189] D.G. Wickham, W.J. Croft, *J. Phys. Chem. Sol.*, 1958, **7**, 351.
[190] S. Naka, M. Inagaki, T. Tanaka, *J. Mater. Sci.* 1972, **7**, 441.
[191] A. Knop-Gericke, M. Havecker, T. Schedel-Niedrig, R., Schlogl, *Top. Catal.*, 2000, **10**, 187.
[192] N.N. Madikizela-Mnqanqeni, N.J. Coville, *J. Mol. Catal. A: Chemical*, 2005, **225**, 137
[193] Y. Zhang, M. Koike, N. Tsubaki, *Catal. Lett*., 2005, **99**, 193.
[194] S. Storsaeter, O. Borg, E.A. Blekkan, B. Totdal, A. Holmen, *Catal. Today*, 2005, **100**, 343.
[195] S.A. Hosseini, A. Taeb, F. Feyzi, *Catal. Comm*., 2005, **6**, 233.
[196] F.M.T. Mendes, C.A.C. Perez, F.B. Noronha, M. Schmal, *Catal. Today*, 2005, **101**, 45.
[197] Y.H. Zhang, H.F. Xiong, K.Y. Liew, J.L. Li, *J. Mol. Catal. A: Chemical*, 2005, **237**, 172.
[198] H.F. Xiong, Y.H. Zhang, K. Liew, J.L. Li, *J. Mol. Catal. A: Chemical*, 2005, **231**, 145.
[199] T.K. Das, G. Jacobs, B.H. Davis, *Catal. Lett*., 2005, **101**, 187.
[200] A. Infantes-Molina, J. Merida-Robles, E. Rodriguez-Castellon, B. Pawelec, J.L.G. Fierro, A. Jimenez-Lopez, *Appl. Catal. A: General*, 2005, **286**, 239.
[201] D.Y. Xu, W.Z, Li, H.M. Duan, Q.J. Ge, H.Y. Xu, *Catal. Lett*., 2005, **102**, 229.
[202] Z.W. Liu, X.H. Li, K. Asami, K. Fujimoto, *Catal. Today*, 2005, **104**, 41.

# 3

# Synthesis and Characterization of Titania-Supported Cobalt Fischer-Tropsch Catalysts Promoted with Manganese Oxide


## Abstract

A series of $TiO_2$-supported cobalt Fischer-Tropsch catalysts promoted with manganese oxide have been synthesized by incipient wetness impregnation (IWI), homogeneous deposition precipitation (HDP) or by combination of both techniques. Characterization was performed after calcination by XRD, XPS, and XAFS at the Co and Mn K-edges, whereas quantitative XPS was applied to estimate the size of the cobalt and manganese oxide particles. In addition, the spatial location of the different species in the Mn-promoted catalysts was investigated by STEM-EELS. The oxidized catalysts turned out to be composed of $Co_3O_4$ clusters and an $\alpha$-$MnO_2$-type phase, of which the location and level of dispersion was largely dependent on the preparation method. The IWI method favored the formation of larger $Co_3O_4$ clusters (20-33 nm) and a dispersed $MnO_2$ phase mainly located on the $TiO_2$ surface. In contrast, the use of the HDP method led to the formation of smaller $Co_3O_4$ particles (8-15 nm), while facilitating the deposition of $MnO_2$ on top of the $Co_3O_4$. This effect resulted in the formation of $Co_{3-x}Mn_xO_4$ spinel-type solid solutions at the interface of both compounds, as evidenced by the longer Co–O and Mn–O distances measured with XAFS, and by the chemical maps produced by STEM-EELS. Finally, the XPS results indicated that a fraction of the cobalt phase contained in the HDP catalysts likely exists in a highly segregated state over the $TiO_2$ surface as a result of the occurrence of Co-$TiO_2$ interactions.

## Introduction

Co-based catalysts, due to their excellent catalytic properties for CO hydrogenation, have been widely studied for the Fischer-Tropsch (FT) synthesis to produce heavy paraffin products. Supported cobalt catalysts have been shown to be very selective towards long chain hydrocarbons, giving higher turnover rates compared to other metal-based catalysts [1-2]. Co metal is also known to be inactive in the water-gas shift reaction [3] and therefore, is suitable when a rich $H_2$/CO feed of syngas is used, e.g., from natural gas. Because of the high price of cobalt it is desirable to minimize the amount used as well as to maximize the available surface area of the metal. Thus, the cobalt active phase is generally deposited on an oxidic support, e.g. $SiO_2$, $Al_2O_3$ and $TiO_2$, which provides good mechanical strength and thermal stability, while facilitating the formation of well-dispersed $Co^0$ nanoparticles within the pores of the support [4-6]. Moreover, the catalysts are easily shaped into macroscopic dimensions [7], which is required for applications in industrial reactors.

Supported catalysts are complex assemblies and their preparation is generally a challenging task. Typical synthesis methods employed to prepare supported cobalt catalysts are for example, the incipient wetness impregnation and the deposition precipitation techniques [8]. The synthesis of high cobalt surface area catalysts in principle requires the initial formation of very small CoO or $Co_3O_4$ crystallites, which is generally enhanced by the occurrence of strong Co-support interactions. This effect, however, can result in a low reducibility of the cobalt phase as a result of the formation of stable compounds, which are known to be highly unreducible [9].

A broad variety of promoters have been investigated over the last decades to enhance the activity, selectivity and/or stability of Co-based FT catalysts [10]. These beneficial effects are, however, only obtained provided the promoter is added in the appropriate manner and a limited range of loading. Although promotion is heavily studied in the field of heterogeneous catalysis, the exact role of many promoters in the FT catalysis has been only scarcely described. Promoters often used for Co-based FT catalysis are for instance noble metals (e.g., Ru, Pt, Re) and some metal oxides (e.g., Zr, La, Mn). The effectiveness of promoters appears to be largely related to their location on the catalyst surface and their interaction with the active metal particles. For example, a ruthenium promotion effect in Co/$TiO_2$ catalysts has been found to require an intimate interaction between the cobalt and ruthenium atoms, inducing a bimetallic nature of the active sites [11]. This nature was enhanced by calcination treatments at high temperatures (>300 ºC). In a similar way, the metal oxide promoters require an intimate interaction with the cobalt particles in order to influence their intrinsic activity and/or selectivity. Hence, transition metal oxides are thought to spread on top of the

cobalt particles in submonolayer coverages, thereby altering the adsorption properties of the active sites.

An accurate investigation of supported cobalt catalysts requires the use of characterization techniques that provide complementary information on the cobalt active site composition and location of promoters. Given the high complexity and number of species involved in $TiO_2$-supported cobalt catalysts our approach has been the use of various spectroscopic techniques with a different sensitivity towards the catalytic species present at the different stages of preparation. In this research we have employed scanning transmission electron microscopy with electron energy loss spectroscopy (STEM-EELS), X-ray absorption fine structure spectroscopy (XAFS) and X-ray photoelectron spectroscopy (XPS). These techniques have been widely used in the field of heterogeneous catalysis [12-14]. STEM-EELS offers a unique possibility for correlating spectroscopic information to a detailed structural knowledge of a material [12]. In STEM-EELS a monochromatic beam of electrons is incident on the sample and the changes in energy of the beam are measured while propagating through the material. The EELS spectra thus give detailed information on the chemical composition of the material under study at spatial resolutions of a fraction of a nanometer. To investigate the bulk structure of nano-dispersed and bimetallic materials, XAFS spectroscopy is a particularly well-suited method [13], providing insight into the electronic structure and the local order around a selected type of atom. Indeed, XAFS does not rely on long-range order and allow for an extensive characterization of the geometrical structures and bond distances in materials, which lack detectable long-range order. Another advantage of XAFS is that it is elemental specific and thus allows the local order around cobalt and manganese atoms to be investigated independently. Finally, XPS due to its surface sensitivity is often applied to investigate the surface composition of catalysts [14] and allows an estimation of the size of supported nanoparticles [15].

The aim of the work presented in this chapter is the preparation of a series of Mn-promoted Co/$TiO_2$ Fischer-Tropsch catalysts with manganese present in all possible locations. The choice of a suitable preparation method was found to be crucial to attain different interactions of manganese with the $Co_3O_4$ particles and the $TiO_2$ support. All major cobalt and manganese compounds as well as other minor phases present in the oxidized Co/$TiO_2$ and Co/Mn/$TiO_2$ catalyst were carefully evaluated making use of a variety of surface and bulk characterization techniques, namely STEM-EELS, XRD, XAFS and XPS. Based on the combined information obtained, a deep insight into the catalytic structures was gained. As a consequence, a schematic model of the oxidized catalyst containing the main existent compounds as well as their location is presented.

## Experimental

*Catalyst preparation and characterization*

Two groups of $TiO_2$-supported cobalt catalysts were synthesized using respectively the homogeneous deposition precipitation (HDP) and the incipient wetness impregnation (IWI) methods. The synthesis were performed using aqueous precursor solutions of $Co(NO_3)_2.6H_2O$ (Acros Organics, p.a.) and $Mn(NO_3)_2.4H_2O$ (Merck, p.a.), and Degussa P25 $TiO_2$ (surface area of 45 $m^2/g$ and pore volume of 0.27 $cm^3/g$) as support material. In the HDP synthesis $TiO_2$ powder was suspended in aqueous solutions containing the metal nitrates and the pH was increased by urea decomposition at 90 ˚C during 18 h under continuous stirring [16]. The materials were subsequently washed with demineralised water, dried at 110 °C in air and sieved to 0.22-0.5 mm before the following preparation step. For the IWI method a pre-sieved $TiO_2$ material (0.22-0.5 mm) was used. In all cases the calcinations were carried out in a flow of air at 400 ˚C for 4 h (ramp 5 ˚C/min).

The first $Co/TiO_2$ catalyst coded H-Co was prepared in one HDP step to load the cobalt followed by calcination to give the catalyst. A portion of this dried $Co/TiO_2$ precursor was loaded with manganese in a IWI step and calcined to give the H-CoMn catalyst. Finally a third catalyst was prepared from a mixture of cobalt and manganese nitrate solutions in a single HDP step followed by calcination to obtain the catalysts coded Hcop-CoMn. Using the IWI method a first catalyst denoted I-Co was prepared in a single step to load the cobalt followed by drying and calcination. A portion of this oxidized $Co/TiO_2$ precursor was subsequently loaded with manganese and calcined again leading to a catalyst coded I-CoMn. A last catalyst was prepared in two IWI steps as the previous one, but inverting the order of impregnation, first manganese and then cobalt. All the prepared catalysts together with the preparation method and metal loadings are summarized in Table 1.

**Table 1.** Overview of the catalysts prepared with the corresponding sample code, and metal loadings as obtained from X-ray fluorescence analysis.

| Sample code | Preparation method | Wt % Co[a] | Wt % Mn[a] |
|---|---|---|---|
| I-Co | IWI Co | 14.6 | 0 |
| I-CoMn | IWI Co + IWI Mn | 14.3 | 1.6 |
| I-MnCo | IWI Mn + IWI Co | 12.6 | 1.6 |
| H-Co | HDP Co | 9.9 | 0 |
| H-CoMn | HDP Co + IWI Mn | 9.9 | 3.0 |
| Hcop-CoMn | HDP Co + Mn | 10.0 | 7.2 |

[a] Wt % calculated assuming cobalt and manganese to be in the form of $Co_3O_4$ and $MnO_2$, respectively.

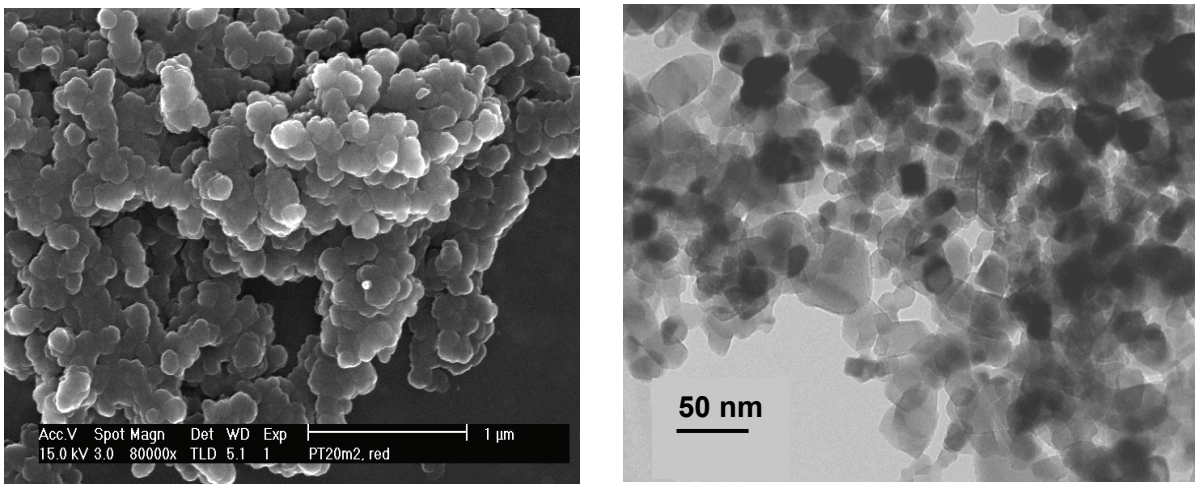


**Figure 1.** SEM (left) and TEM (right) images of $TiO_2$ P25 degussa used as support material for the preparation of the $Co/TiO_2$ and $Co/Mn/TiO_2$ Fischer-Trospch catalysts.

X-ray fluorescence (XRF) analysis to determine cobalt and manganese loadings in the catalysts was carried out with a Spectro X-lab 2000 spectrometer. From these results, the total weight % of cobalt and manganese was calculated assuming them to be present in the form of $Co_3O_4$ and $MnO_2$.

All the oxidized catalysts were analyzed by powder X-ray diffraction (XRD) using an ENRAF-NONIUS XRD system equipped with a curved position-sensitive INEL detector, and applying a Co $K\alpha_1$ radiation source ($\lambda$ = 1.78897 Å). The mean $Co_3O_4$ crystallite sizes were determined using the line broadening of the reflections localized at 42.9, 70.1 and 77.4°, applying the Scherrer equation.

The physical state of the $TiO_2$ support was visualized in the micrographs obtained by transmission electron microscopy (TEM) and scanning electron microscopy (SEM). The TEM measurements were performed with a Tecnai 20 FEG TEM microscope operating at 200 kV. The SEM images were taken with a Philips XL-30 Field Emission Gun (FEG) microscope. It was found that the $TiO_2$ is composed of spherical particles in the range of 20-60 nm (Fig. 1).

*X-ray absorption spectroscopy*

The local environment and electronic properties of cobalt and manganese atoms in the calcined catalysts were investigated by extended X-ray absorption fine structure spectroscopy (EXAFS) at the Co and Mn K-edges. The XAFS measurements were carried out at RT in flow of He using an in-house reactor cell operating at 1 bar [17]. Appropriate amounts of sample were finely crushed and pressed at 2 bar into 0.7 $cm^2$ pellets. XAFS data were collected on the DUBBLE beamline (BM26A) at the European Synchrotron Radiation

Facility (ESRF, Grenoble, France), operating under beam conditions of 6 GeV, 200 mA, 2x1/3 filling mode, and using a Si (111) double-crystal monochromator. XAFS signals were measured in fluorescence mode both at the Co K edge (7716 eV) and Mn K edge (6539 eV). $Co_3O_4$ (Merck, p.a) $Mn_2O_3$, and $MnO_2$ (Aldrich, 99.999%) materials were used as reference materials.

Data reduction of the experimental X-ray absorption spectra was performed with the program EXBROOK [18]. A pre-edge background subtraction and normalization was carried out by fitting a linear polynomial to the pre-edge region and a cubic spline at the post-edge region of the absorption spectrum. A smooth atomic background was then obtained. EXAFS refinements were performed with the EXCURV98 package [18]. Phase shifts and backscattering factors were calculated *ab initio* using Hedin-Lundqvist potentials. Refinements were carried out using $k^1$ and $k^3$ weighting in the range of 3.5 to 12 $Å^{-1}$ and 3.5 to 9 $Å^{-1}$ for the Co and Mn K-edges, respectively. The amplitude reduction factors (AFAC parameters) calibrated from the fit of the cobalt and manganese metal foils were fixed at 0.68 for the Co K-edge and at 0.80 for the Mn K-edge.

*X-ray photoelectron spectroscopy*

The surface composition of the oxidized catalysts was measured by X-ray photoelectron spectroscopy (XPS). $Co_{2p}$ spectra were collected with a Vacuum Generators system, using a CLAM-2 hemispherical analyzer for electron detection. Non-monochromatic Al ($K_\alpha$) X-ray radiation was used, employing an anode current of 20 mA at 10 keV. The binding energies obtained for $Co_{2p}$, $Ti_{2p}$, and $Mn_{2p}$ photoelectron peaks were corrected for charge shifts using the $C_{1s}$ = 285 eV peak as reference. $Co_3O_4$ was also measured and corrected for charge shifts using the $C_{1s}$ = 285 eV peak as reference. In addition, the 2p peaks of the three elements (Co, Ti, and Mn) were used for quantitative analysis in order to estimate the $Co_3O_4$ and $MnO_2$ particle sizes making use of the program XPSLAYER [19]. For this calculation the composition of the samples was assumed to be uniform throughout the area probed by XPS. To calculate the 2p peak areas of the three elements, backgrounds were subtracted according to the procedure suggested by Shirley [20]. These areas are proportional to the number of photo electrons produced for a given flux of incoming X-rays ($\phi_x$), the number of incident X-ray photons per $cm^2$.s. The number of photoelectrons (N) produced per $\phi_x$ depends only on the material constants:

$$\frac{N}{\phi_x \mathrm{A}} = \sigma\rho\lambda$$

Where A is the probed area of the sample, σ is the cross section for photoinization, ρ the atomic density, and λ the inelastic mean free path, provided that only electrons perpendicular

to the surface are detected. For an infinitely thick sample $I_{obs}$ is defined as the observed intensity, which can be calculated for any chemical compound knowing the σ (tabulated for all chemical compounds), ρ and λ. The observed intensities obtained for a given compounds were computed with the program XPSLAYER [19] in order to estimate the layer thickness of the different compounds, knowing the molecular weight of the compounds, their density and the number of atoms in the formula units. The calculation was carried out assuming different situations with respect to the location of manganese in the different catalysts; i.e., considering the manganese to be either located on the $TiO_2$, on the $Co_3O_4$, or physically mixed with the $Co_3O_4$ phase. The obtained thickness for a given value of θ (coverage) was converted to a hemisphere radius by multiplying it 3/2, as shown in detail by Kuipers *et al.* [15].

*Scanning transmission electron microscopy with electron energy loss spectroscopy*

The spatial distributions of cobalt, manganese and titanium compounds in the I-CoMn, H-CoMn, and Hcop-CoMn catalysts were investigated by scanning transmission electron microscopy with electron energy loss spectroscopy (STEM-EELS). The Ti, Mn, and Co $L_{2,3}$ edges and the O K-edge were monitored by using a 100 keV STEM instrument (VG HB 501) equipped with a field emission source and a parallel Gatan 666 EELS spectrometer. The instrument was in operation in Orsay and produced EELS-spectra with 0.5 eV energy resolutions and a sub-nanometer spatial resolution within a typical acquisition time less than a second per pixel. More specifically, the sub-nanometer probe (typically 0.5 nm in diameter) could be positioned with an accuracy higher than 0.2 nm on the sample, and it could scan the sample digitally with spatial increments as small as 0.3 nm, as described in more detail by Stephan *et al.* [12]. The samples were first sonicated in ethanol and then dropped on a holey amorphous carbon film supported on a copper grid. After scanning the sample, appropriate areas were selected for measuring detailed 2D TEM-EELS images. Coloured chemical maps were generated by overlap of the individual chemical maps obtained for Ti, Co, and Mn elements. For the calcined H-CoMn sample three chemical maps were analysed in detail containing six $Co_3O_4$ particles, for the I-CoMn sample eight chemical maps were analysed containing seven $Co_3O_4$ particles and for the Hcop-CoMn sample two chemical maps containing three cobalt particles were analysed.

## Results and discussion

### *Bulk characterization of the $Co/TiO_2$ and $Co/Mn/TiO_2$ catalysts*

The XRD patterns of the oxidized catalysts are shown in Fig. 2. In addition to reflections originating from the anatase and rutile $TiO_2$ phases, the diffraction peaks corresponding to a spinel $Co_3O_4$ phase are detected at 2θ = 36.4°, 42.9°, 52.3°, 70.1°, and 77.4°, indicating the formation of $Co_3O_4$ crystallites in all catalysts. These reflections are much weaker in H-Co and H-CoMn, suggesting a less crystalline character of the $Co_3O_4$ phase, and/or the presence of some amorphous cobalt phase in these catalysts. In the Hcop-CoMn catalyst the position of these reflections are slightly shifted towards smaller 2θ angles, indicating an enlargement of the $Co_3O_4$ unit cell. As will be discussed later, this increase of the cell parameter is due to the incorporation of $Mn^{3+}$ ions into the $Co_3O_4$ structure leading to the formation of $Co_{3-x}Mn_xO_4$ solid solutions. The estimation of the average stoichiometry of the Hcop-CoMn catalyst corresponding to the reflections shift using the Vegard plot reported for the $Co_{3-x}Mn_xO_4$ solid solutions [21] gives $Co_{2.1}Mn_{0.9}O_4$. We note that this calculation gives the average composition of the Co/Mn particles in the Hcop-CoMn catalyst, although the actual manganese concentration may vary among different particles and even within each particle. The mean $Co_3O_4$ particle sizes resulting from XRD calculations were somewhat smaller in the catalysts prepared by HDP (~ 13-17 nm) than in the IWI catalysts (~31-33 nm), with the exception of the I-MnCo catalyst, in which values of 18 nm were obtained. These values are summarized in Table 4 to compare with the results of particle sizes obtained by XPS.

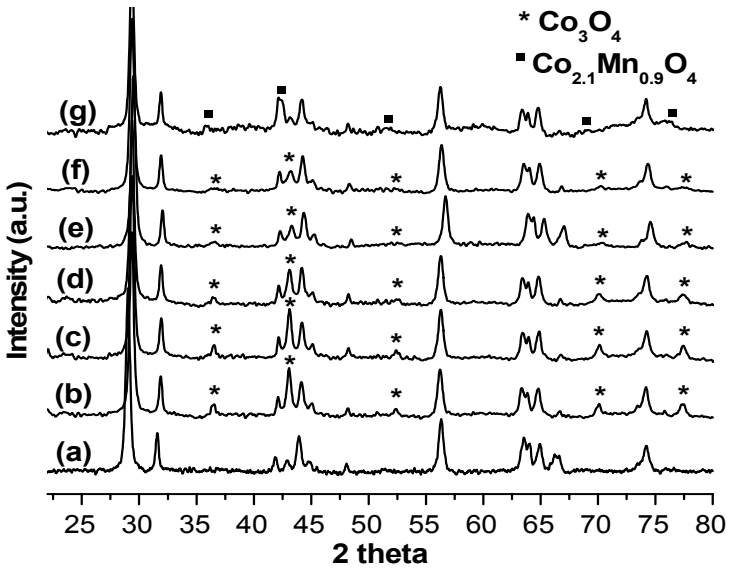


**Figure 2.** XRD patterns of $TiO_2$ P25 (a), and I-Co (b), I-CoMn (c), I-MnCo (d), H-Co (e), H-CoMn (f), and Hcop-CoMn (g) catalysts after calcination.

The results of the EXAFS refinements for the first three coordination shells (Co–O and Co–Co) are summarized in Table 2. Except H-CoMn and Hcop-CoMn, which show slightly longer bond distances, all the catalysts present similar results. The first oxygen shell coordination number ranges from 4.2 in Hcop-CoMn to 5.5 in I-Co, whereas all the samples exhibit the same Co–O distance of 1.91 Å, except the H-CoMn and Hcop-CoMn catalysts which feature slightly longer bond distances of 1.92 and 1.93 Å, respectively. The second and third Co shells are also very similar in all the catalysts with 3.3 to 4.4 Co atoms at 2.85 Å, and 7 to 10 Co atoms at 3.36 Å. Once again H-CoMn and Hcop-CoMn present longer distances of 2.86 and 2.87 Å for the first Co shell and 3.38 and 3.40 Å for the second Co shell, respectively. In agreement with the XRD results, the EXAFS results indicate that in all the catalysts except H-CoMn and Hcop-CoMn cobalt belongs entirely to a $Co_3O_4$ phase.

Indeed, the Co environment obtained with EXAFS corresponds to a spinel arrangement of atoms in $Co_3O_4$ with $Co^{2+}$ and $Co^{3+}$ ions located respectively in $T_d$ and $O_h$ coordination [22], giving an average environment around the Co atoms of 5.3 O at 1.91 Å and 4 and 8 Co at 2.85 and 3.36 Å.

The longer inter-atomic distances found for H-CoMn and Hcop-CoMn combined with the slight shift of the $Co_3O_4$ reflections in the XRD patterns are certainly pointing towards the

**Table 2.** EXAFS results at the Co K-edge for the calcined Co/$TiO_2$ and Co/Mn/$TiO_2$ catalysts and for a $Co_3O_4$ reference material.

| **Sample code** | **R (Å) Co–O** | **N atoms** | **$2\sigma^2$ (Å)** | **R (Å) Co–Co** | **N atoms** | **$2\sigma^2$ (Å)** |
|---|---|---|---|---|---|---|
| $Co_3O_4$ | 1.92 | 5.3 O | 0.005 | 2.85 | 4.0 Co | 0.005 |
| | | | | 3.36 | 8.0 Co | 0.008 |
| I-Co | 1.91 | 5.5 O | 0.009 | 2.84 | 3.9 Co | 0.005 |
| | | | | 3.35 | 8.0 Co | 0.012 |
| I-CoMn | 1.91 | 4.7 O | 0.003 | 2.85 | 3.5 Co | 0.006 |
| | | | | 3.35 | 7.0 Co | 0.011 |
| I-MnCo | 1.91 | 5.2 O | 0.003 | 2.85 | 3.8 Co | 0.005 |
| | | | | 3.36 | 7.3 Co | 0.010 |
| H-Co | 1.91 | 5.4 O | 0.004 | 2.85 | 3.3 Co | 0.003 |
| | | | | 3.35 | 8.3 Co | 0.013 |
| H-CoMn | 1.92 | 5.1 O | 0.004 | 2.86 | 4.4 Co | 0.007 |
| | | | | 3.37 | 8.2 Co | 0.014 |
| Hcop-CoMn | 1.93 | 4.2 O | 0.003 | 2.87 | 4.1 Co | 0.013 |
| | | | | 3.40 | 9.9 Co | 0.018 |

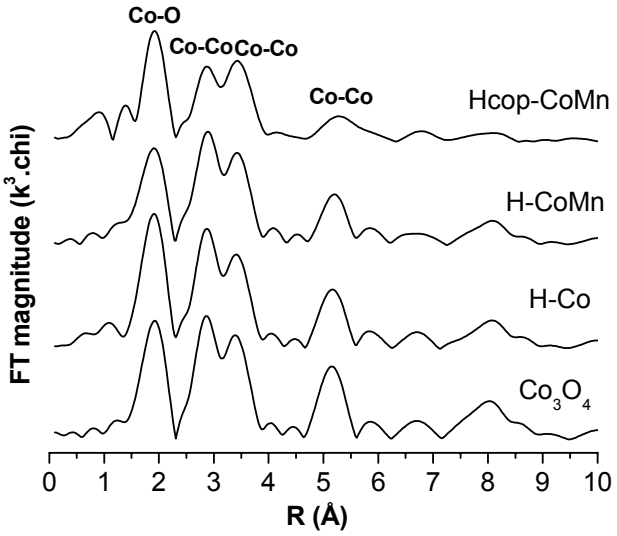


**Figure 3.** $k^3$-weighted Fourier transforms of the experimental EXAFS spectra at the Co K-edge for $Co_3O_4$, and the H-Co, H-CoMn, and Hcop-CoMn catalysts after calcination.

formation of $Co_{3-x}Mn_xO_4$-type solid solutions by substitution of $Co^{3+}$ by $Mn^{3+}$ in the $Co_3O_4$ structure. These solid solutions can indeed be prepared in a broad range of compositions and readily form at conditions of high temperature and oxygen environment [23-24]. Due to the greater atomic radius of $Mn^{3+}$ (1.37 Å) with respect to $Co^{3+}$ (1.25 Å) [25], substitution of $Co^{3+}$ by $Mn^{3+}$ in the $O_h$ sites results in a cell expansion, increasing steadily with increasing Mn content in the $Co_3O_4$ structure [22, 26-27]. This phenomenon is also reflected in the Fourier transforms for the HDP catalysts, as illustrated in Fig. 2, which shows a decrease of the fourth Co–Co shell intensity as the manganese loading increases. This indicates the presence of a higher level of disorder in the structure of these catalysts that is very likely induced by the incorporation of $Mn^{3+}$ ions into the $Co_3O_4$ lattice. Furthermore, this effect is more pronounced in Hcop-CoMn since a higher amount of manganese is mixed with the $Co_3O_4$ phase.

The oxidation state of manganese was investigated in the first derivative of the XANES spectra, which were compared with those of suitable reference materials [28]. The first derivative spectra for the oxidized $Co/Mn/TiO_2$ catalysts and $MnO_2$ and $Mn_2O_3$ materials are shown in Fig. 4. All catalysts contain a main component of $Mn^{4+}$, as deduced from the main peak at 6559 eV also present in spectra for $MnO_2$. The high similarity between the spectra for $MnO_2$ and the I-CoMn sample suggest that this catalyst contains merely $Mn^{4+}$ species, probably in the form of $MnO_2$. In the other catalysts a $Mn^{3+}$ state is also detected in the spectra by the peak with a maximum at 6548 eV corresponding to $Mn_2O_3$. Therefore, the XANES results show that in all the catalysts after calcinations the manganese exists mainly in a $Mn^{4+}$ state and with some admixture of $Mn^{3+}$, which is clearly present in larger amounts in the H-CoMn and Hcop-CoMn catalysts. Additionally, a little $Mn^{3+}$ component is also detected for the I-MnCo sample suggesting that $Mn^{3+}$ species may also exist dispersed at the $TiO_2$

**Table 3.** Results of the EXAFS analysis at the Mn K edge for calcined Co/Mn/$TiO_2$ catalysts and a $\alpha$-$MnO_2$ reference material.

| Sample | R (Å) Mn–O | N atoms | $2\sigma^2$ (Å) | R (Å) Mn–Mn | N atoms | $2\sigma^2$ (Å) |
|---|---|---|---|---|---|---|
| $MnO_2$ | 1.88 | 6.0 O | - | 2.88 | 4.2 Mn | - |
| | | | | 3.38 | 6.4 Mn | - |
| I-CoMn | 1.88 | 5.7 O | 0.002 | 2.87 | 2.5 Mn | 0.001 |
| | | | | 3.43 | 2.6 Mn | 0.003 |
| I-MnCo | 1.88 | 6.0 O | 0.011 | 2.87 | 2.2 Mn | 0.001 |
| | | | | 3.45 | 3.6 Mn | 0.030 |
| H-CoMn | 1.91 | 5.7 O | 0.007 | 2.87 | 4.2 Mn | 0.010 |
| | | | | 3.39 | 1.8 Mn | 0.009 |
| H-CoMncop | 1.91 | 4.2 O | 0.007 | 2.89 | 4.7 Mn | 0.013 |
| | | | | 3.43 | 12.4 Mn | 0.034 |
| | | | | 3.73 | 8.8 Mn | 0.023 |

surface. This is also suggested by the little structure observed in the spectrum, being indicative of a low-range ordered manganese structure. Taking into account that the I-MnCo sample was prepared loading the manganese before the cobalt and with a calcination step in between, it is likely that some manganese species (e.g., $Mn^{3+}$) are also present at the interface of $Co_3O_4$ and $TiO_2$.

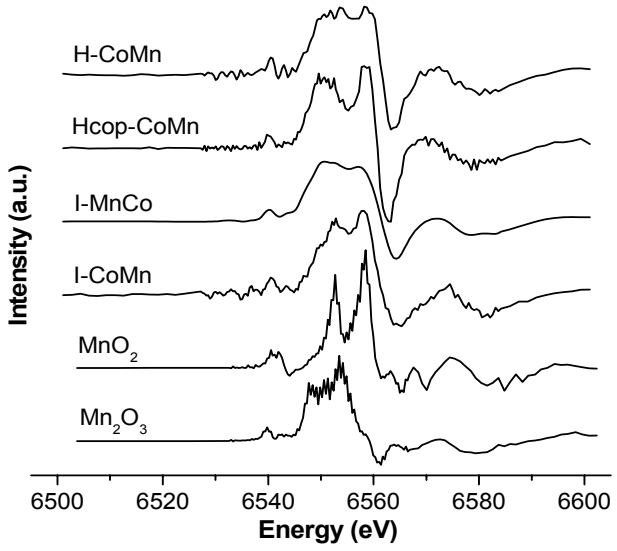


**Figure 4.** First derivative of the normalized XANES spectra for the I-CoMn, I-MnCo, H-Co and Hcop-CoMn catalysts after calcination and for the $MnO_2$ and $Mn_2O_3$ reference materials.

The results of the EXAFS refinement for the catalysts and for the α-$MnO_2$ reference material are summarized in Table 2. All the catalysts except H-CoMn and Hcop-CoMn give the same inter-atomic distances with a first shell of 5.7-6 O at 1.88 Å and a second and third Mn–Mn shells at distances of ca. 2.88 and 3.38-3.45 Å, respectively. H-CoMn and Hcop-CoMn feature slightly larger Mn–O bond distances of 1.91 Å, similarly to the results obtained at the Co K-edge. In Hcop-CoMn, however, the O coordination of 4.2 shows a marked drop compared to all the other catalysts. Therefore, in agreement with the XANES analysis, EXAFS confirms that most of the manganese atoms in I-CoMn and I-MnCo belong to a α-$MnO_2$-type phase. However, this manganese phase is amorphous and/or possesses a strong nanocrystalline character, since the XRD patterns do not show any corresponding visible reflections. This is also confirmed by the relatively flat shape of the XANES derivative indicative of a highly dispersed phase, as well as by the very low intensity of the second and third peaks in the Fourier transforms (not shown) [29]. In contrast, the clearly longer Mn–O bond distance of 1.91 Å found in the HDP catalysts strongly suggests the presence of other phases in addition to α-$MnO_2$. Indeed, EXAFS at both the Co and Mn K-edges reveal for H-CoMn and Hcop-CoMn a marked elongation of the bond distances around both Co and Mn atoms. These results combined with the XRD results clearly point towards the formation of solid solutions of the spinel type $Co_{3-x}Mn_xO_4$ in both catalysts.

Whilst the increase in the Co–O bond distance correlates directly to the increase of the cell volume upon manganese incorporation, the increase of the Mn–O bond distance on the other hand correlates to the fraction of manganese atoms incorporated in these solid solutions. Thus, the Mn–O distances measured in the HDP catalysts are the average between those of $MnO_2$ (1.88 Å) and those of $Co_{3-x}Mn_xO_4$ (1.92-1.96 Å) [26]. Hence, the formation of $Co_{3-x}Mn_xO_4$ solid solutions occurs not only in Hcop-CoMn, but also in H-CoMn as revealed by EXAFS giving in both catalysts Mn–O distances of 1.91 Å. Nonetheless, taking into account the higher manganese loading contained in Hcop-CoMn compared to H-CoMn and in turn, the same Mn–O bond distances measured with EXAFS (1.91 Å), this catalyst is expected to contain also a significant fraction of $MnO_2$.

***Location of Mn in calcined Mn/Co/$TiO_2$ catalysts***

The location and level of segregation of the manganese phase in the calcined catalysts were investigated in the chemical maps produced from the EELS absorption spectra at the Ti, Mn, and Co $L_{2,3}$ edges. In these images the luminosity is proportional to the number of atoms encountered in each sub-area (every pixel) by the electron beam. Fig. 4 shows the situation obtained for the calcined I-CoMn sample presented in three individual chemical maps, respectively for the Ti, Co and Mn elements. In Fig. 4B a large $Co_3O_4$ particle (>20 nm) can

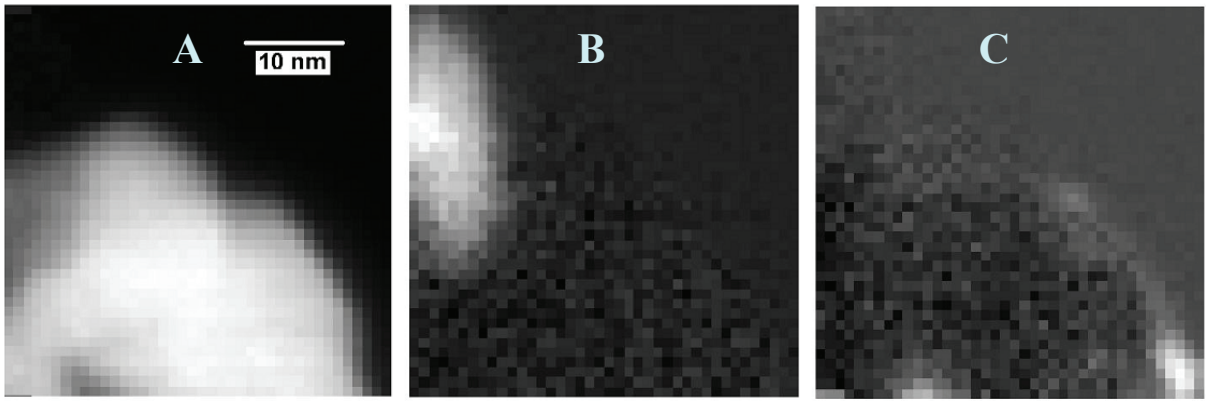


**Figure 4.** Grayscale EELS chemical maps for the I-CoMn catalyst after calcination; A (Ti $L_{2,3}$ edges), B (Co $L_{2,3}$ edges), and C (Mn $L_{2,3}$ edges). The image was recorded with a spatial increment of 1 nm.

be seen at the edge of the $TiO_2$ support. The manganese can be observed in Fig. 4C covering the $TiO_2$ support and without exhibiting any interaction with the $Co_3O_4$ particle. Some other examples of EELS images obtained for the I-CoMn catalyst are presented in Appendix A (p. 165). These colored images have been created by merging the individual chemical maps of Ti, Co and Mn, which were previously given in green, red and blue false colors, respectively. In general, the $MnO_2$ phase is observed for the I-CoMn catalyst in a rather dispersed state as a layer covering the $TiO_2$ and in the form of small particles (< 5 nm), whilst no significant Co-Mn interactions were found. These results are in agreement with XAFS and XRD, confirming the existence of large $Co_3O_4$ clusters and a dispersed $\alpha$-$MnO_2$-type phase located at the $TiO_2$ surface in the I-CoMn catalyst. In the I-MnCo catalyst, although no EELS images are available, the manganese location is expected to be similar as the XAFS results showed, although with a larger degree of dispersion.

A totally different situation with respect to the manganese location was found for the HDP catalysts. As already discussed, XAFS showed that in these catalysts manganese does not only exist in the form of $MnO_2$, but also partially incorporated in the $Co_3O_4$ structure as solid solutions ($Co_{3-x}Mn_xO_4$) with a variable composition. Hence, some manganese should be in direct contact with the $Co_3O_4$ nanoparticles. This statement was indeed demonstrated by STEM-EELS. Fig. 5 presents the EELS chemical maps for the H-CoMn sample. In image 5B the manganese is observed clearly associated with the $Co_3O_4$ particles, given that the Co and Mn EELS signals are closely correlated. These results in combination with XAFS, is a strong argument demonstrating that in the H-CoMn sample the $Co_3O_4$ nanoparticles are covered by $MnO_2$ and to some extent mixed as $Co_{3-x}Mn_xO_4$ solid solutions. Other colored chemical maps for the H-CoMn sample are presented in Appendix A (p. 167). For example, in Fig. A2 (B) a $TiO_2$-supported $Co_3O_4$ particle is visualized while some small manganese spots decorate the

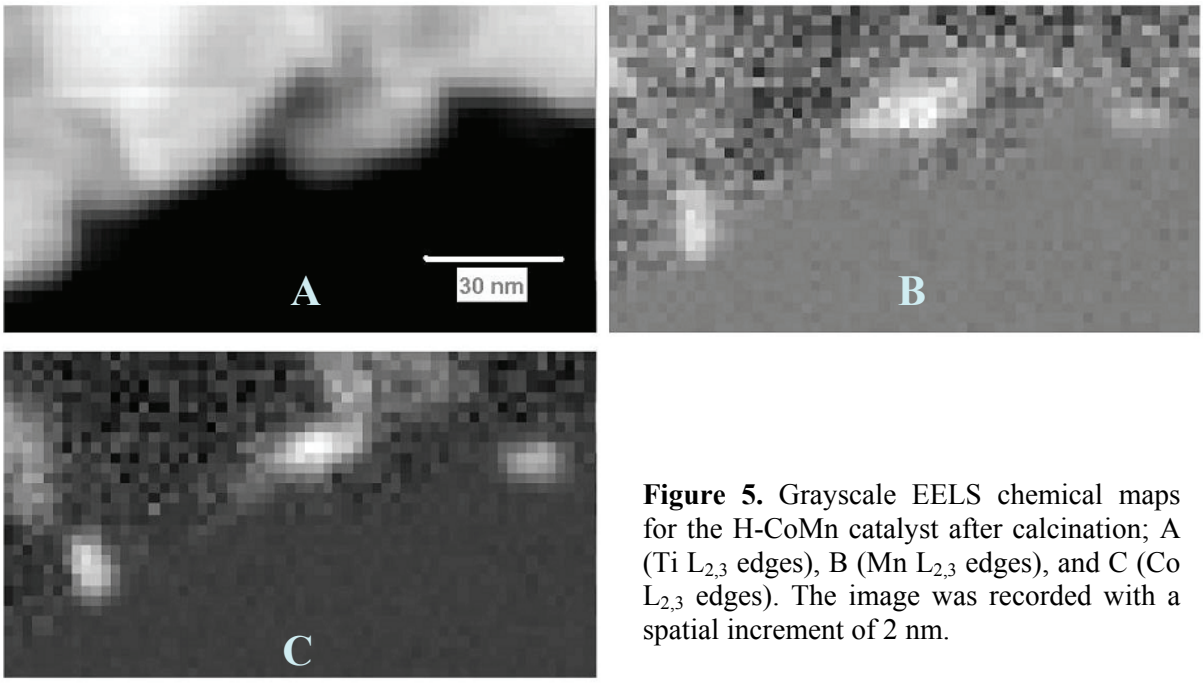


**Figure 5.** Grayscale EELS chemical maps for the H-CoMn catalyst after calcination; A (Ti $L_{2,3}$ edges), B (Mn $L_{2,3}$ edges), and C (Co $L_{2,3}$ edges). The image was recorded with a spatial increment of 2 nm.

particle as thought manganese ions are dissolved within the $Co_3O_4$ structure. In Fig A2 (C) manganese is found associated with $Co_3O_4$ while no manganese exists at the $TiO_2$ surface.

The overall results nicely show that in the H-CoMn catalyst $MnO_2$ co-exists with the $Co_3O_4$ nanoparticles leading to the formation of $Co_{3-x}Mn_xO_4$ solutions at the interface of both metal oxides. In addition, some $Co_3O_4$ particles with small amounts of manganese directly incorporated in the $Co_3O_4$ have been also detected (Fig. A2 (B)). Nevertheless, it is not ruled out that some amounts of $MnO_2$ may exist also at the surface of $TiO_2$, as can be visualized in image A2 (B), although it should be just a small fraction of the total manganese content. On the other hand, the $Co_3O_4$ particles in H-CoMn were found to be clearly smaller than in the IWI catalysts, being in the range of 8-15 nm, which is in good agreement with the XRD particle size calculation.

Fig. 6 displays the Ti, Co and Mn chemical maps obtained for the Hcop-CoMn sample. It can be observed that cobalt and manganese compounds are located in the same areas of the images (B and C) indicating the existence of mixed oxide compounds. A large $TiO_2$-supported particle (> 50 nm) is visualized in the chemical map containing cobalt and manganese mixed in the form of spinel-type $Co_{3-x}Mn_xO_4$ solutions, as was revealed from the EXAFS results. Moreover, there is manganese-rich area in the particle, showing that the relative composition of the particles is variable. This manganese-rich area is most probably composed of nearly pure $MnO_2$, which existence was previously reported with EXAFS. The colored chemical map for the Hcop-CoMn sample is shown in p. 168 of Appendix A.

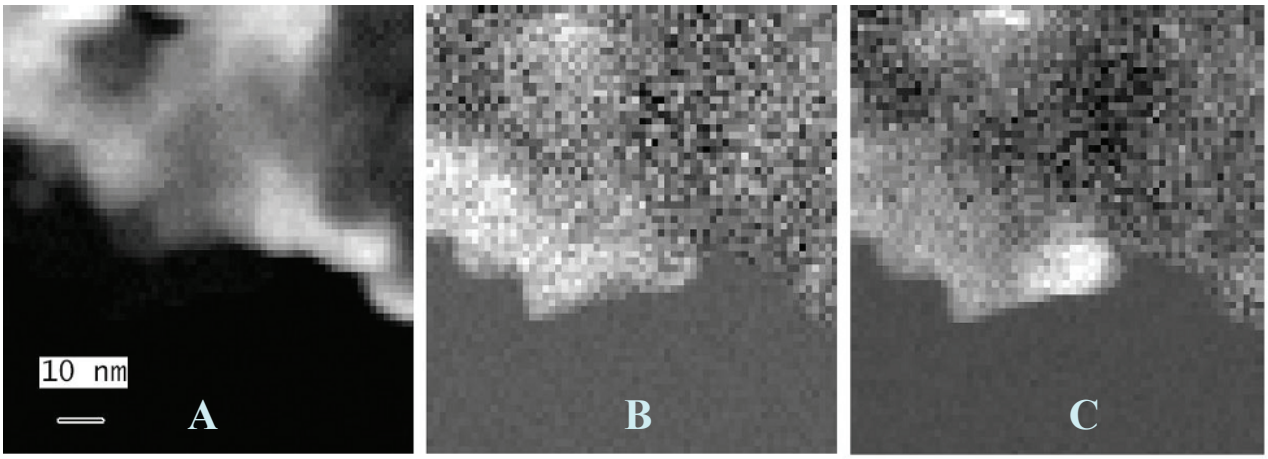


**Figure 6.** Grayscale EELS chemical maps for the Hcop-CoMn catalyst after calcination; A (Ti $L_{2,3}$ edges), B (Co $L_{2,3}$ edges), and C (Mn $L_{2,3}$ edges). The image was recorded with a spatial increment of 1 nm.

### *Surface characterization of the Co/TiO$_2$ and Co/Mn/TiO$_2$ catalysts*

The Co 2p spectra obtained for the calcined catalysts and for a $Co_3O_4$ bulk material are shown in Fig. 7. The energy positions of both Co2p photoelectron peaks are nearly the same in all the catalysts and in the bulk $Co_3O_4$, with values of ca. $2p_{3/2}$ ~ 779.9 eV and $2p_{1/2}$ ~ 795.2 eV. In agreement with other work [30] these energy values indicate that $Co_3O_4$ is the major cobalt compound existing at the surface of all the catalysts after calcination. The binding energies of the $Co2p_{3/2}$ peak and the energy separation between Co $2p_{3/2}$ and Co $2p_{1/2}$ are summarized in Table 4.

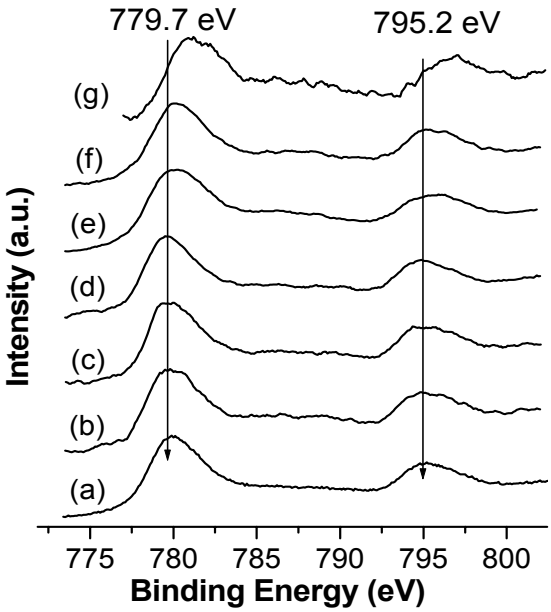


**Figure 7.** Normalized Co 2p spectra of bulk $Co_3O_4$ (a), and I-Co (b), I-CoMn (c), I-MnCo (d), H-Co (e), H-CoMn (f), and Hcop-CoMn (g) catalysts after calcination.

For the catalyst prepared by the IWI method the values for the Co $2p_{3/2}$ peak are in all cases 779.7 eV as in the $Co_3O_4$ compound, pointing to the same surface structure. In the HDP catalysts, however, the energies of the Co $2p_{3/2}$ peak are slightly higher (780.1, 780.2, and 780.6 eV), suggesting the presence of small amounts of $Co^{2+}$ species, such as CoO or $CoTiO_3$. According to literature [9] the binding energy given by CoO is only slightly higher than for $Co_3O_4$, but the separation between the $Co2p_{3/2}$ and $Co2p_{1/2}$ peaks is significantly larger (15.5 eV or even higher). Moreover, these species should exist in a highly dispersed and/or amorphous state, since they were not detected by either of the other techniques used in this work (XRD, EXAFS and STEM-EELS). These findings point towards a stronger Co-$TiO_2$ interaction resulting from the use of the HDP preparation method. Since the $Co_3O_4$ particles formed in the HDP catalysts are smaller than in the IWI catalysts, they are more prone to interact with the $TiO_2$ leading to the formation of cobalt surface phases [9].

Finally, the Hcop-CoMn catalyst displays the highest binding energies ($Co2p_{3/2}$ = 780.6 eV and $Co2p_{3/2}$-$Co2p_{1/2}$ =15.8 eV) reflecting the highest amount of $Co^{2+}$. As discussed before, this catalyst contains the largest amount of $Co_{3-x}Mn_xO_4$ solution, wherein $Mn^{3+}$ substitute for $Co^{3+}$ in the $Co_3O_4$ structure. This effect certainly leads to the lowest $Co^{3+}$ to $Co^{2+}$ ratio in the catalyst, which accounts for the highest value of binding energy. For a better insight in the Co 2p spectra, a detailed interpretation of the Co 2p XPS spectral shapes is given in the papers of Okada and Kotani [31].

Quantification of the XPS data was carried out to estimate $MnO_2$ and $Co_3O_4$ particles sizes. In this calculation we assumed hemispherical shapes to model all possible locations of $MnO_2$ and $Co_3O_4$ at the surface of the catalysts (Fig. 8). The resultant particle sizes for each model are summarized in Table 4. For the simplest case as in the manganese-free I-Co and H-Co catalysts, $Co_3O_4$ particles of respectively 27 nm and 9.6 nm are obtained. This is in agreement with XRD indicating that H-Co contains smaller $Co_3O_4$ particles than I-Co. For the I-CoMn catalyst it was previously shown that both $MnO_2$ and $Co_3O_4$ exist on the $TiO_2$ support without interacting with each other. This model (a) was applied to calculate the particle sizes for I-CoMn leading to values of 36 nm for $Co_3O_4$ and 3.3 nm for $MnO_2$. For the I-MnCo catalyst two different situations were considered; the same as in model (a) and the presence of $MnO_2$ species in between $TiO_2$ and $Co_3O_4$ (model (b)). This situation is expected based on the preparation method, since the loading of manganese was done before that of cobalt and with a calcination step in between. The results for both models give mean $Co_3O_4$ particles of 20.4 nm and $MnO_2$ particles of 2.3 nm and 0.7 nm for models (a) and (b). Hence, the actual $MnO_2$ size in I-MnCo is expected to range between 0.7 and 2.3 nm depending on its degree of dispersion. The results suggest that the $MnO_2$ phase in I-MnCo is more dispersed than in I-CoMn and that the $Co_3O_4$ particles are smaller, which is in line with the XRD and XAFS

**Table 4.** Overview of the Co2p XPS data and XPS particle sizes calculation for the calcined $Co/TiO_2$ and $Co/Mn/TiO_2$ catalysts according to models (a), (b), (c), and (d), illustrated in Fig. 8. The table includes the $Co_3O_4$ particle size calculation from XRD.

| Sample | Co $2p_{1/2}$ (eV) | $\Delta 2p_{3/2}$-$2p_{1/2}$ | XPS $Co_3O_4$ size (nm) | XPS $MnO_2$ size (nm) | XRD $Co_3O_4$ size (nm) |
|---|---|---|---|---|---|
| I-Co | 779.7 | 15.3 | 27.0 | | 31 |
| I-CoMn | 779.7 | 15.2 | 36.0 [a] | 3.3 [a] | 33 |
| I-MnCo | 779.7 | 15.1 | 20.4 [a] | 2.3 [a] – 0.7 [b] | 18 |
| H-Co | 780.2 | 15.6 | 9.6 | | 15 |
| H-CoMn | 780.1 | 15.2 | 10.4 [a] – 5.1 [c] - 4.4[d] | 2.8 [a] – 2.9[c] - 4.4[d] | 13 |
| Hcop-CoMn | 780.9 | 15.8 | 25.0 [a] – 6.8[c] – 7.0 [d] | 9.1 [a] – 9.2[c] – 7.0 [d] | 17 |

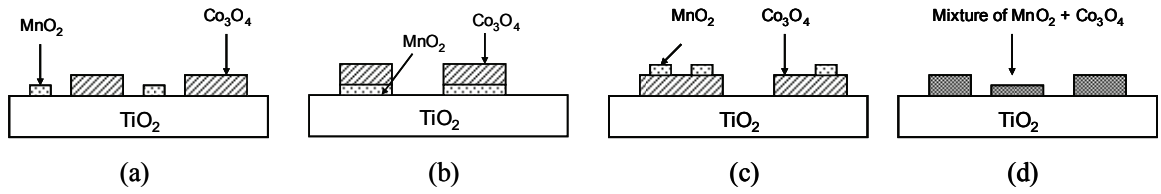


**Figure 8.** Schematic representation of the models applied for the XPS calculation to estimate particle sizes.

results. Hence, the calcination treatments may increase the spreading of manganese over the surface of $TiO_2$ as in the case of the I-MnCo catalyst.

To estimate the particle sizes for the H-CoMn and Hcop-CoMn catalysts, two other situations concerning the $Co_3O_4$ and $MnO_2$ distributions were used for the calculation. According to the EXAFS results, the $Mn^{4+}$ and $Mn^{3+}$ ions largely interact with the $Co_3O_4$ nanoparticles in these two catalysts. This interaction takes place either through coverage of $Co_3O_4$ by $MnO_2$ (model (c)), or by a mixing of both compounds (model (d)). Hence, in addition to the simplest model (a), the size of the particles was estimated for the HDP catalysts applying models (c) and (d). $Co_3O_4$ particle sizes ranging from 10.4 nm (a) to 5.1 nm (c) and 4.4 nm (d) were obtained for the H-CoMn catalyst. Since a fraction of the $Co_3O_4$ particles is known to be covered or mixed with the manganese their size should range between 10.4 and 4.4 nm according to XPS. This $Co_3O_4$ particle size is smaller than that estimated by XRD. On the other hand, the $MnO_2$ particles in the H-CoMn catalyst are found

to be around 2.8 - 4.4 nm. Considering the $MnO_2$ phase to be present as a layer covering the $Co_3O_4$, the layer thickness is estimated to be in the range 0.6 - 0.9 nm and 21-25 % coverage. Finally, for Hcop-CoMn XPS leads to $Co_3O_4$ particles of 25.9 nm, 6.8 nm and 7.0 nm, respectively for models (a), (c) and (d). Therefore, the size of the cobalt oxide particles in this catalyst is highly dependent on the amount of manganese associated with the cobalt phase. Interestingly, as in the former catalyst, the $Co_3O_4$ particles are smaller when calculated by XPS than by XRD, which suggests that a fraction of the Co phase may be present at the $TiO_2$ surface in a more highly dispersed state (e.g. CoO or $CoTiO_3$). This explanation would account for the smaller values of particle size obtained by a surface sensitive technique (i.e., XPS). The overall results point to the existence of stronger Co-$TiO_2$ interactions as a result of using the HDP preparation method.

The combined information revealed by the multi-technique characterization approach provided a deep insight into the physico-chemical properties of the catalyst precursors. An overview of the different species contained in all the Co/Mn/$TiO_2$ catalysts after calcination is illustrated in Fig. 9. The Hcop-CoMn catalyst contains the highest amount manganese mixed with the $Co_3O_4$ as $Mn_xCo_{3-x}O_4$ solutions, whereas the IWI catalysts contain an $\alpha$-$MnO_2$-type phase merely located at the $TiO_2$ surface.

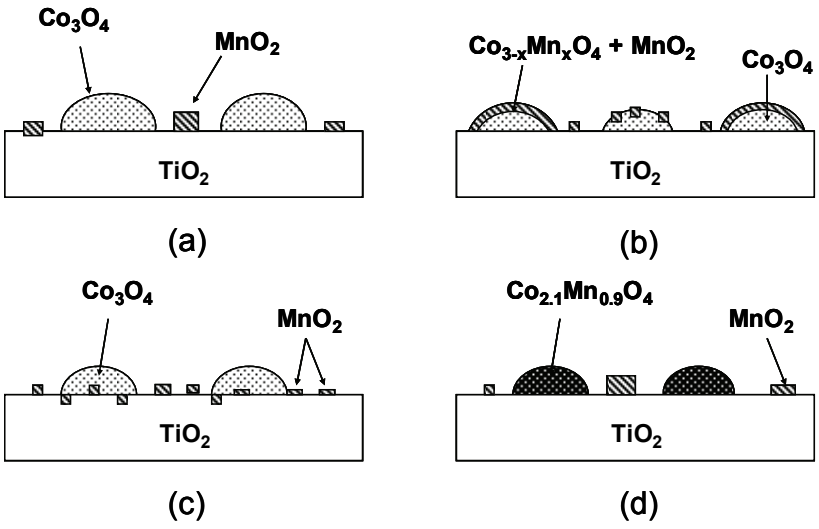


**Figure 9.** Schematic representation of the I-CoMn (a), H-CoMn (b), I-MnCo (c) and Hcop-CoMn (d) samples after calcination. The drawings represent the main cobalt and manganese phases present in the Co/Mn/$TiO_2$ Fischer-Tropsch catalysts after calcination. Different manganese locations were obtained as a result of the preparation method employed.

## Conclusions

The preparation of Co/Mn/$TiO_2$ Fischer-Tropsch catalyst precursors with various manganese locations was successfully attained by controlling the synthesis procedure, which led to different Co-Mn interactions after calcination. The Co/Mn/$TiO_2$ oxidized catalysts were composed of $Co_3O_4$ particles with a variable range of sizes, and a $MnO_2$ phase interacting differently with the $Co_3O_4$ or $TiO_2$ support in function of the preparation method employed. The use of the IWI method resulted in the formation of rather large $Co_3O_4$ clusters (~18 - 35 nm) and a $MnO_2$ phase distributed over the $TiO_2$ surface. In contrast, the combined HDP and IWI methods resulted in smaller $Co_3O_4$ particles (5 - 15 nm), and facilitated the deposition of $MnO_2$ on the $Co_3O_4$ surface. As a consequence, some amounts of $Co_{3-x}Mn_xO_4$-type solid solutions were also formed at the interface of $Co_3O_4$ and $MnO_2$ phases. Finally, a single HDP step to load cobalt and manganese into the $TiO_2$ led to the formation of $Co_{3-x}Mn_xO_4$ solid solutions with a high manganese content. On the other hand, the XPS results suggested that the catalysts prepared by the HDP method might also contain a highly dispersed cobalt phase (e.g., $CoO_x$ or cobalt titanate) in addition to the $Co_3O_4$ clusters.

## Acknowledgements

The authors gratefully acknowledge the University of Nord (Orsay, Paris) and Odile Stephan and Alexandre Gloter for the STEM-EELS measurements. The E.S.R.F synchrotron (Grenoble) is acknowledged for the XAFS measurements. We kindly thank S. Nikitenko for his assistance and advice during the XAFS experiments.

## References

[1] E. Iglesia, *Appl. Catal,.A*, 1997, **161**, 59.
[2] H. Schulz, *Appl. Catal., A*, 1999, **186**, 3.
[3] M.E. Dry, *Catal. Today*, 2002, **71**, 227.
[4] C.H. Bartholomew, R.C. Reuel, *Ind. Eng. Chem*., 1985, **24**, 56.
[5] R. Riva, H. Miessner, R. Vitali, G. del Piero, *Appl. Catal. A: General*, 1999, **196**, 111.
[6] M. Vob, D. Borgmann, Wedler. *J. Catal.* 2002, **212**, 10.
[7] M. Kraum, M. Baerns, *Appl. Catal. A: General*, 1999, **186**, 189.
[8] E.B.M. Doesburg, K.P. de Jong, J.H.C. van Hoff, J.W Geus, J.A.R. van Veen, *Stud. Surf. Sci. Catal.*, 1999, **123**, chapters 9 and 10.
[9] Y. Brik, M. Kacimi, M. Ziyad, F. Bonzon-Verduraz, *J. Catal*., 2001, **202**, 118.
[10] F. Morales, B.M. Weckhuysen, *Catalysis, Royal Society of Chemistry*, 2006, **19**, in press.
[11] E. Iglesia, S.l. Soled, R.A. Fiato, G.H. Via, *Stud. Sur. Sci. Catal.,* 1994, **81**, 433.

[12] O. Stephan, A, Gloter, D. Imhof, M. Kociak, K. Suenaga, M. Tence, C. Colliex, *Surf. Rev. Lett*., 2000, **7**, 475.

[13] D.C. Koningsberger, B.L. Mojet, G.E. Van Dorssen, D.E. Ramaker, *Top. Catal*., 2000, **10**, 143.

[14] A. Venecia, *Catal. Today*, 2003, **77**, 359.

[15] H.P.C.E. Kuipers, *Sol. St. Ion*, 1985, **16**, 15.

[16] K.P. de Jong, *Stud. Surf. Sci. Catal*. 1991, **63**, 19.

[17] M. Vaarkamp, B.L. Mojet, M.J. Kappers, J.T. Miller, D.C. Koningsberger, *J. Phys. Chem*., 1995, **99**, 16067.

[18] Binstead, N., Campbell, J. W., Gurman, S. J., Stephenson, P. C., EXAFS Analysis Programs; Laboratory, D., Ed. Warrington, 1991.

[19] O.L.J. Gijzeman, XPS Layer Analysis Program, Debye Institute, Surface Science Division, Utrecht University, The Netherlands.

[20] D.A. Shirley, *Phys, Rev. B*, 1972, **5**, 4709.

[21] E. Rios, P. Chartier, J.L. Gautier, *Solid State Sci*., 1999, **1**, 267.

[22] K.J. Kim, Y.R. Park, *Sol. St. Commun.*, 2003, **127**, 25.

[23] S. Naka, M. Inagaki, T.J. Tanaka, *J. Mat. Sci.*, 1972, **7**, 441.

[24] J.L. Gautier, E. Rios, M. Garcia, J.F. Marco, J.R. Gancedo, *Thin Sol. Films*, 1997, **311**, 51.

[25] Wells, A.F., Structural Inorganic Chemistry, 5$^{th}$ Ed., Clarendon Press, Oxford, 1984.

[26] J.L. Martin de Vidales, E. Vila, R. Rojas, O. Garcia-Martinez, *Chem. Matter.*, 1995, **7**, 1716.

[27] E. Vila, R.M. Rojas, J.L. Martin de Vidales, O. Garcia-Martinez, *J. Matter. Chem.*, 1996, **8**, 1078.

[28] D. Ciaparu, P. Haider, M. Fernandez-Garcia, Y. Chen, S. Lim, G.L. Haller, L. Pfefferle, *J. Phys. Chem. B*, 2005, **109**, 16332.

[29] F. Morales, D. Grandjean, F.M.F. de Groot, O. Stephan, B.M. Weckhuysen, *Phys. Chem. Chem. Phys*., 2005, **7**, 568.

[30] R. Riva, H. Miessner, R. Vitali, G. del Piero, *Appl. Catal. A: General,* 1999, **196**, 111.

[31] K. Okada, A. Kotani, *J. Phys. Soc. Jpn*., 1992, **61**, 449.

# 4

# Influence of Manganese on the Physicochemical and Catalytic Properties of Titania-Supported Fischer-Tropsch Catalysts


## Abstract

The effects of the addition of manganese to a series of $TiO_2$-supported cobalt Fischer-Tropsch catalysts prepared by different methods were studied by a combination of TPR, XAFS, XPS and TEM. The cobalt active site composition in the catalysts after reduction at 300 °C and 350 °C was linked to the catalytic performances obtained at reaction conditions of 220 °C, 1 bar, and $H_2/CO = 2$. The XAFS, XPS, and TEM results revealed the presence of very small $Co^0$ particles (around 2-6 nm) in most of the reduced catalysts, indicating that the cobalt phase re-disperses during the reduction process from $Co_3O_4$ to $Co^0$. The presence of manganese in the catalysts was found to hamper the cobalt reducibility, this effect being more severe when $Co_{3-x}Mn_xO_4$ solutions were initially present in the catalyst precursors. Moreover, the manganese generally led to the formation of larger Co agglomerates (ca. 8-15 nm), probably as a consequence of the decrease in the cobalt reducibility. The catalysts with larger Co particles (ca. > 5 nm) and lower cobalt reduction extent displayed a higher intrinsic activity and a longer catalyst lifetime. Interestingly, the manganese effectively promoted these larger Co particles by increasing the $C_{5+}$ selectivity and lowering the $CH_4$ production, while it did not significantly influence the selectivity of the catalysts containing smaller Co particles.

## Introduction

In recent years an increasing interest in the Fischer-Tropsch synthesis has led to many studies aiming to understand the relationship between the cobalt active phase in supported-Co FT catalysts and its behaviour in the CO hydrogenation reaction. The nature of the cobalt particles produced upon activation treatments depends on the reducibility of the catalyst precursor, being largely influenced by the interaction of cobalt with the support material, e.g., $TiO_2$, $Al_2O_3$ and $SiO_2$ [1-3]. For supports without a strong interaction such as $SiO_2$, highly reducible cobalt oxide clusters are generally formed after calcination [4-5]. On the contrary, supports like $TiO_2$ and $Al_2O_3$ have been shown to exhibit a strong metal- support interaction, which makes the cobalt particles more difficult to reduce most likely due to a strong Co–O interaction or the formation of other stable compounds such as $CoTiO_3$ [6] and $CoAl_2O_3$ [7-8]. The formation of hardly reducible compounds is thought to occur during the reduction of $Co_3O_4$ to Co metal, by diffusion of $Co^{2+}$ species into the support lattice, leading to the undesired loss of the catalytically active phase. On the other hand, the occurrence of strong Co-support interactions may also favour the formation and stabilization of small particles [2]. The reducibility of supported-Co particles furthermore, is influenced by the synthesis method used [9-10], and the use of small amounts of additives, namely the so-called promoters (see chapter 2). The addition of suitable promoters may prevent the formation of cobalt surface phases and may enhance the catalytic properties for the FT reaction. For instance, promoters like Ru, Re and Pt, have been frequently reported to facilitate the cobalt reducibility in a variety of support materials [8, 11-12] resulting in higher catalytic activities. Other types of promoters such as transition metal oxides can be employed to enhance the catalyst selectivity towards the desired products [13-15].

It is well known that the FT catalytic properties of supported cobalt catalysts are largely dependent on both the cobalt reduction extent and size of the $Co^0$ crystallites formed upon catalyst activation. For this reason many studies have aimed to establish clear relationships between the cobalt active sites distribution and their FT catalytic performances. In the early eighties, it was reported that the CO hydrogenation at 1 bar on $Co/Al_2O_3$ catalysts is structure-sensitive [16], since it was possible to correlate (1) an increasing turnover rate with a decreasing $Co^0$ dispersion and (2) the variations in selectivity with changes in the rate of chain termination relative to the rate of chain propagation. Nonetheless, the possibility that unreduced cobalt present at the catalyst surface would account for the changes in activity and selectivity could not be ruled out. In other work [17], it was reported that the cobalt reduction extent plays an important role in the CO hydrogenation over $Al_2O_3$-supported cobalt catalysts, since they observed higher turnover frequencies for catalysts with a lower reduction extent.

Iglesia and co-workers claimed that FT is a structural-insensitive reaction for supported cobalt catalysts with dispersions in between 0.45 % to 9.5 %, which correspond to particle sizes of 230 and 10 nm, respectively [18]. Within this dispersion range the reactivity of surface cobalt atoms in the FT synthesis is not influenced by the size or chemical identity of the metal oxide support and hence, it is expected that a catalyst would yield activities as a function of the number of available $Co^0$ sites. However, structural changes of the cobalt particles during FT synthesis may result in a variation of the number of available sites [19-20]. The structural changes during FT operation may include the transformation of metallic cobalt to cobalt oxides, and/or cobalt carbides, and the sintering or segregation of the particles. Another possible cause of deactivation may be the loss of active phase as a result of strong-metal support interactions (SMSI). SMSI have been shown to occur in $TiO_2$-supported Co catalysts at high reduction temperatures, at which $TiO_2$ may be reduced to $TiO_x$, which can migrate onto the surface of the $Co^0$ particles causing a blockage of the active sites and thus a decrease of CO adsorption [21-22]. Similar SMSI effects are also expected to occur when an excess of oxide promoter is employed, e.g., in the case of transition metal oxides. These promoters may exhibit a similar mobility towards the cobalt surface leading to the poisoning and deactivation of small supported particles.

Very recently, Bezemer *et al.* have reported on the particle size effects for FT Co-based catalysts supported on carbon nanofibers (CNF) [23]. It is remarkable to notice that the use of CNF provides clear advantages to study cobalt particle size effects, since a decrease in activity caused by the SMSI effects occurring with metal oxide supports, can be ruled out. Their results reveal that the CO hydrogenation activity is structure-insensitive with Co dispersion ranges between 3.6 and 16.0 %. Smaller cobalt particles than 6 nm exhibited a decrease in the turnover rate, resulting in poor activities for the FT reaction. In-situ XAFS studies revealed that the lower activities are not related to Co-C or Co-O formation during FT synthesis and they proposed that CO induced non classical particle size effects are responsible for the observed influence of size on the FT performance.

The use of a Mn promoter for Co-based FT catalysts has only been reported a few times in the open literature. For instance some papers deal with the potential of manganese to shift the product distribution in the FTS by increasing the olefin selectivity and decreasing the undesired $CH_4$ production [24-25]. Other works have reported that manganese oxide acts as a CO shift converter promoter and thus, to catalyze the water-gas shift reaction (i.e., the transformation from $CO + H_2O$ to $H_2 + CO_2$) [26, 27]. The occurrence of this reaction can influence the reaction kinetics in the FT reaction and may be interesting when a rich CO syngas composition is used (e.g. the syngas obtained from high temperature coal gasification [28]). The use of manganese for Co-based FT catalysts can be found in the patent literature

[29]. However, the exact role of manganese and its influence on the cobalt active site composition remains largely unclear.

In this chapter we present a detailed study of the cobalt phase contained in a series of manganese oxide-promoted $Co/TiO_2$ FT catalysts, which initially contain the manganese in all possible locations on the catalyst surface. The influence of the synthesis method and the manganese on the physico-chemical state and reducibility of the cobalt particles have been evaluated using a variety of characterization techniques, namely TPR, XAFS, XPS and TEM. In addition, the cobalt particle sizes and reduction extents have been correlated with the FT catalytic results in order to establish structure-performances relationships.

## Experimental

### *Catalyst synthesis*

A series of $TiO_2$-supported cobalt catalysts promoted by manganese were synthesized by different methods as described in chapter 3. An overview of the properties of the catalyst precursors is given in Table 1, including preparation procedure and $Co_3O_4$ particle sizes. In addition, schematic representations of the catalyst materials are shown in Fig. 1.

**Table 1.** Overview of the $Co/TiO_2$ and $Co/Mn/TiO_2$ catalysts under study with their corresponding sample codes, preparation method, metal loadings and $Co_3O_4$ particle sizes.

| Sample code | Preparation method[a] | Wt % Co[b] | Wt % MnO[b] | $Co_3O_4$ size[c] (nm) |
|---|---|---|---|---|
| I-Co | IWI Co | 11.1 | - | 27 |
| I-CoMn | IWI Co + IWI Mn | 11.0 | 1.4 | 36 |
| I-MnCo | IWI Mn + IWI Co | 9.5 | 1.3 | 20 |
| H-Co | HDP Co | 8.0 | - | 10 |
| H-CoMn | HDP Co + IWI Mn | 7.8 | 2.6 | 8 |
| Hcop-CoMn | HDP Co + Mn | 7.7 | 7.0 | 15 |

[a]Preparation steps to load the Co and Mn, [b]XRF analysis, [c]Particle sizes reported in chapter 3.

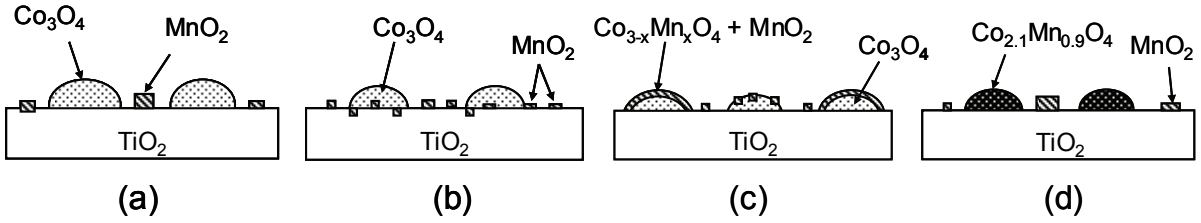


**Figure 1.** Schematic drawings of I-CoMn (a), I-MnCo (b), H-CoMn (c), and Hcop-CoMn (d) catalysts in the oxidized state. The figures indicate the different manganese structures and locations achieved after calcination.

***Catalyst characterization***

The bulk reducibility of the Co/$TiO_2$ and Co/Mn/$TiO_2$ catalysts was investigated by temperature programmed reduction (TPR) using a Thermo electron TPDRO 1100 instrument. The calcined materials were loaded in a tubular quartz reactor and flushed with Ar at 120 °C for 1 h. Subsequently the reactor was cooled down to RT and the gas flow was adjusted to 5% $H_2$/Ar. The temperature was then raised from RT to 700 °C at a rate of 10 °C/min and the content of $H_2$ in the gas outlet was monitored with a thermo-conductivity detector throughout the reduction process.

X-ray absorption fine structure spectroscopy (XAFS) at the Co K-edge was used to investigate the local environment and electronic properties of the cobalt atoms in the catalysts during and after reduction. Appropriate amounts of samples were finely crushed and pressed at 2 bar into 0.7 $cm^2$ pellets. The XAFS measurements were carried out *in situ* under dynamic atmosphere in an in-house reactor cell [30] operating at 1 bar. The temperature was raised at a rate of 5 ºC/min from RT to the final reduction temperature and held until the end of the measurements. Reduction of the catalysts was performed at 300 and 350 ºC for 2 h with 100 ml/min of 50%$H_2$/He flow. After reduction the measurements were carried out at the final reduction conditions. X-ray absorption near edge spectroscopy (XANES) spectra were collected continuously throughout the temperature increase, whilst extended X-ray absorption fine structure spectroscopy (EXAFS) spectra were measured at the end of each reduction treatment. XAFS data were collected at the DUBBLE beamline (BM26A) at the European Synchrotron Radiation Facility (ESRF, Grenoble, France), operating under beam conditions of 6 GeV, 200 mA, 2x1/3 filling mode and using a Si (111) double-crystal monochromator. XAFS signals were measured in fluorescence mode at the Co K-edge (7716 eV). Data reduction of experimental XAFS data was performed with the program EXBROOK [31]. A pre-edge background subtraction and normalization was carried out by fitting a linear polynomial to the pre-edge region and a cubic spline at the post-edge region of the absorption spectrum. A smooth atomic background was then obtained. EXAFS refinements were performed with the EXCURV98 package [31]. Phase shifts and backscattering factors were calculated *ab initio* using Hedin-Lundqvist potentials. Refinements were carried out using $k^1$ and $k^3$ weighting in the range 3.5-12 $Å^{-1}$. The effects of anharmonicity due to the presence of very small cobalt particles were corrected with the cumulant expansion feature implemented in EXCURV98 applying a linear expansion coefficient of 14.6 $10^{-6}$ m/ºC for cobalt metal. Amplitude reduction factors (AFAC parameters) were calibrated from the fit of the cobalt foil, which was fixed at 0.65.

X-ray photoelectron spectroscopy (XPS) was applied to investigate the surface of the reduced and passivated catalysts. The catalysts were initially dried in a flow of air at 120 °C

for 30 min. Subsequently, the flows were adjusted to 50 % $H_2$/He and the temperature was raised to 350 °C at a rate of 5 °C/min. After 2 h reduction at 350 °C the temperature was decreased to 150 °C and a passivation was carried out in a 5 % $CO_2$/He flow during 30 min. The reduced/passivated samples were powdered and deposited onto a carbon holder for the XPS measurements. $Co_{2p}$, $Ti_{2p}$, $Mn_{2p}$, and $C_{1s}$ spectra were collected using a Vacuum Generators system, with a CLAM-2 hemispherical analyzer for electron detection. Non-monochromatic Al ($K_\alpha$) X-ray radiation was used, employing an anode current of 20 mA at 10 keV. All spectra were corrected for charge shifts using the $C_{1s}$ = 285 eV peak as reference. In addition, the areas of the $Co_{2p}$, $Ti_{2p}$, and $Mn_{2p}$ photoelectron peaks were subtracted according to the procedure suggested by Shirley [32] and the obtained areas were used to estimate cobalt particle sizes using the software XPSLAYER [33]. For this calculation was assumed the cobalt and manganese to be in the form of CoO and MnO. In addition, three models were applied to simulate the Co and Mn distributions on the $TiO_2$ surface, i.e., CoO and MnO can both cover the $TiO_2$, MnO may be located on top of the CoO, and MnO and CoO may form a mixed compound. For each situation the thickness of the CoO layer was obtained and converted into a hemisphere radius by multiplying by 3/2. For details concerning this XPS particle size calculation we refer to the work of Kuipers *et al.* [34].

In the reduced catalysts, the general morphology of the material and the cobalt particle size distribution were examined by transmission electron microscopy (TEM) using a Tecnai 20 FEG TEM microscope operating at 200 kV equipped with a EDX analyzer. The reduced/passivated catalysts described above were initially crushed and ultrasonically dispersed in ethanol. A drop of suspension was then air-dried on a holey carbon grid and bright field micrographs were collected. The average diameter of the coblat particles was estimated by measuring 200-300 single particles contained in 5-10 TEM images for each of the catalysts and applying the formula: average Co size (nm) = $\sum n^3/\sum n^2$, being $n$ the diameter of each measured particle in nm.

***Catalytic testing***

The behavior of the Co/$TiO_2$ and Co/Mn/$TiO_2$ catalysts in the Fischer-Tropsch reaction was investigated under isothermal plug-flow conditions. Typically, in a glass reactor the oxidized catalyst particles (0.2-0.5 mm) were diluted at 20 % with SiC particles (0.2 mm). The samples were activated in 20 ml/min flow of $H_2$ at 300 ˚C and 350 ˚C for 2 h before adjusting the reaction conditions. The Fischer-Tropsch reaction was carried out at 1 bar, 220 °C, and a syngas flow of 12 ml/min ($H_2$/CO ratio of 2). Gas hourly space velocities of 3010 $h^{-1}$ were used in all experiments leading to CO conversions in the range of 2–6 %. The reaction temperature was measured simultaneously with two thermocouples; one under and the other

inserted in the catalyst bed. The hydrocarbon product composition was analyzed on-line during the first 60 h of reaction using a Varian CP-3800 gas chromatograph equipped with a fused silica column of 50 m length and a flame ionization detector (FID). Catalytic performances were measured every 1 h and monitored during 60 h FT reaction. Results were evaluated by means of Co-time yield ($10^{-5}$ mol CO (g Co)$^{-1}$ s$^{-1}$), TOF ($10^{-3}$.s$^{-1}$), and selectivity expressed in percentages of CO converted to $CH_4$ and $C_{5+}$ fraction of products.

## Results

### *Redox behavior of the Co/TiO$_2$ and Co/Mn/TiO$_2$ catalysts*

The change in cobalt oxidation state occurring in the catalysts throughout the reduction was monitored by XANES at the Co K-edge. XANES spectra collected continuously during the temperature increase were used as fingerprints to identify the cobalt oxidation state at the different stages of reduction [35]. As an example, Fig. 2 shows the XANES spectra collected at RT, 240 °C, 310 °C, and 350 °C during reduction of the I-Co catalyst. The figure also includes the spectra of the Co foil and CoO for comparison. Dramatic changes both in terms of white line intensity, oscillation shape and edge position, are occurring as a function of the temperature. Observation of the shape of the spectra suggests that the reduction of $Co_3O_4$ into cobalt metal takes place in several steps with a marked intermediate stage at 240 °C. Detailed comparison of the spectrum measured at 240 °C with that of CoO that features the same shape and edge position at 7721 eV shows that this intermediate stage corresponds to a CoO phase. CoO is then fully reduced into Co$^0$ in a second stage at ca. 350 °C as indicated by the large decrease in intensity of the white line in the XANES spectra. The reduction behavior was

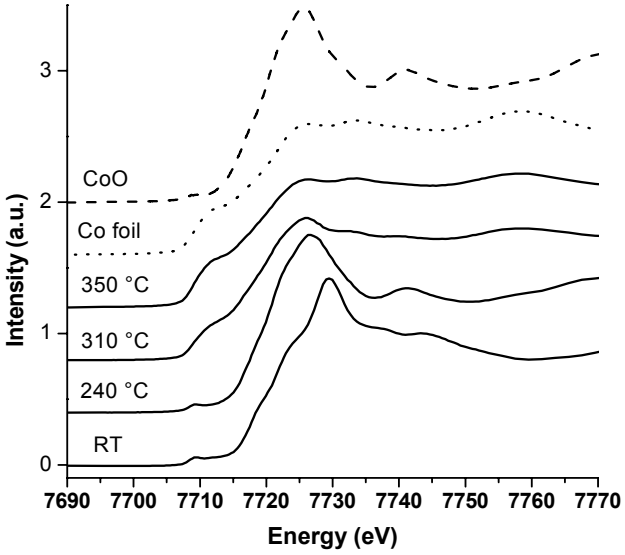


**Figure 2.** Normalized XANES spectra at the Co K-edge of the I-Co catalyst measured at RT, 240 °C, 310 °C, and 350 °C during reduction in $H_2$/He flow. The graph includes the spectra of Co$^0$ foil (dotted line) and CoO (dashed line) as reference/model materials.

found to be similar in all catalysts investigated although full reduction from CoO to cobalt metal was not always achieved when using the HDP preparation method and manganese as promoter. For this reason, the XANES spectra measured after the reduction treatments correspond for some catalysts to mixtures of $Co^0$ and $Co^{2+}$ oxidation states, as will be shown later.

Fig. 3 displays the TPR profiles obtained for the FT catalysts, illustrating the cobalt reducibility according to the preparation method and the presence of manganese. Two main peaks are observed in all cases corresponding respectively to the reduction steps from $Co_3O_4$ to CoO (equation (1)), and consecutively from CoO to metallic cobalt (equation (2)).

$$Co_3O_4 + H_2 \rightarrow 3CoO + H_2O \qquad (1)$$

$$3CoO + 3H_2 \rightarrow 3Co^0 + 3H_2O \qquad (2)$$

In the IWI catalysts both reduction steps take place at around 280 and 425 °C and are not largely influenced by the presence of manganese. Nevertheless, for the I-CoMn catalysts both peak maxima are shifted to 305 and 450 °C suggesting a slight decrease of the cobalt reducibility. The TPR profiles for the H-Co and H-CoMn catalysts also exhibit both typical reduction steps, although the second step is broader and contains two peak maxima at ca. 350 and 465 °C, most likely due to a different interaction of the cobalt particles with $TiO_2$. Moreover, the peak at 465 °C is somewhat more pronounced for H-CoMn than for H-Co, again suggesting a lower cobalt reducibility caused by manganese. Hence, the HDP catalysts appear to be less reducible than the IWI catalysts, pointing to the occurrence of stronger Co-support interactions. In addition, manganese retards the cobalt reducibility in the I-CoMn and H-CoMn materials. A very different reduction profile was obtained for the Hcop-CoMn

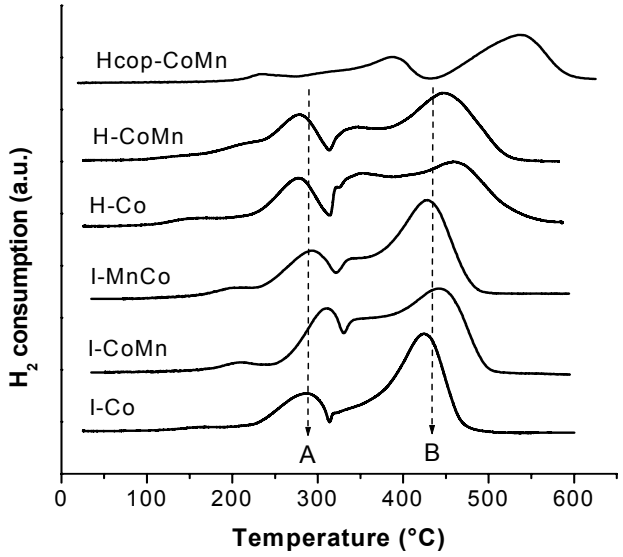


**Figure 3.** TPR profiles of the $Co/TiO_2$ and $Co/Mn/TiO_2$ catalysts obtained during reduction in $H_2$/Ar flow from RT to 600 °C at a rate of 10 °C/min.

catalyst, showing the $H_2$-consumption peaks at 370 and 550 °C. This indicates much lower cobalt reducibility compared to the other catalysts. This effect is caused by the manganese, which is incorporated in the $Co_3O_4$ structure as discussed in chapter 3, and is in agreement with other work in which TPR experiments with mixed Co-Mn spinels led to similar reduction profiles [36]. On the other hand, a small peak observed at 230 °C for Hcop-CoMn and at 200 °C for the other Mn-promoted catalysts is attributed to the reduction of $MnO_2$ species, which are known to exist in the oxidized catalysts.

As a consequence of this multi-stage process, reduction of the catalysts led to different cobalt reduction degrees largely influenced by the preparation method used and the presence of manganese promoter. Fig. 4 shows the XANES spectra obtained for all catalysts after 2 h reduction at 300 and 350 °C. Cobalt oxide is fully reduced to metal at 350 °C in I-Co, I-CoMn, and I-MnCo, as indicated by the XANES spectral shape and edge position featuring a $Co^0$ oxidation state. H-Co and H-CoMn reduced at 350 °C, however, still contain a small fraction of $Co^{2+}$, as evidenced by a weak white line present at 7725 eV. Finally, the Hcop-CoMn catalyst reduced at 350 °C gives a XANES spectrum corresponding almost to a pure $Co^{2+}$ state, with very similar features as the spectra for CoO pure material shown in Fig. 4. Hence, in agreement with the TPR results, the Hcop-CoMn catalyst is by far the most resistant against reduction. The reason for this reduction behavior is that this catalyst contains particles composed of $Co_{3-x}Mn_xO_4$ solid solutions that largely suppress the cobalt reducibility.

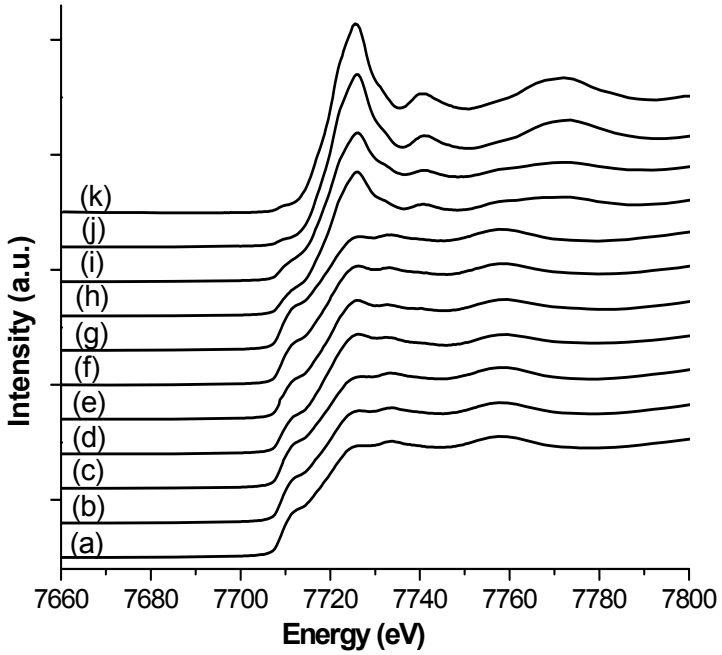


**Figure 4.** Normalized XANES at the Co K edge of the I-Co (a), I-CoMn (b), I-MnCo (c), H-Co (d), H-CoMn (e) and Hcop-CoMn (k) catalysts after 2 h reduction at 350 °C, and of the I-Co (f), I-CoMn (g), I-MnCo (h), H-Co (i), H-CoMn (j) after 2 h reduction at 300 °C.

Reduction at 300 °C on the other hand, led to different mixtures of $Co^0$ and CoO that are varying among the catalysts. The cobalt reduction extents were further quantified by means of a linear combination of the XANES spectra of pure CoO and $Co^0$ references. The percentages of $Co^0$ obtained in each catalyst are summarized in Table 3. All the reduced IWI catalysts gave 100 % of $Co^0$ with the exception of I-CoMn reduced at 300 °C, in which 48 % $Co^0$ was found. Lower reduction degrees were obtained for H-Co and H-CoMn with values respectively of 95 and 90 % $Co^0$ at 350 °C and 40 and below 5 % at 300 °C. Based on these results it is concluded that manganese suppresses the cobalt reducibility, this effect being more prominent when Co-Mn interactions exist as in the case of the Hcop-CoMn and H-CoMn catalysts. Furthermore, the occurrence of stronger Co-support interactions in the HDP catalysts generally led to lower cobalt reducibility [1].

***EXAFS study of the Co phase in reduced $Co/TiO_2$ and $Co/Mn/TiO_2$ catalyst***

To gain insight into the local environment of the Co atoms in the reduced catalysts, EXAFS spectra at the Co K-edge were collected [30]. Measurements after in situ reduction treatments at 300 and 350 ºC show spectra characteristic of either Co metal, CoO, or mixtures of both compounds. This can be observed at a first glance in the Fourier transforms (Fig. 5), which show very different shapes for each catalysts, with peaks corresponding to a combination of the Fourier transforms of the cobalt metal and CoO reference materials also presented in Fig. 5. Indeed, the Fourier transforms reflect the different cobalt reduction extents achieved in the catalysts with the shells of cobalt metal dominating in the highly reduced catalysts, e.g., the I-Co catalyst reduced at 300 °C, whilst the two Co–O and Co–Co shells of CoO increase in intensity as the cobalt reduction extent decreases.

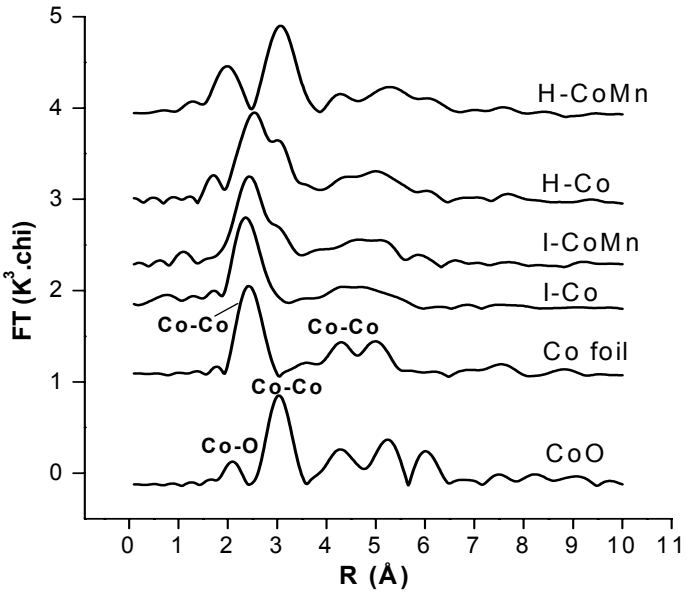


**Figure 5.** Fourier transforms in $k^3$ weighting of Co foil and CoO model/reference compounds, and of the I-Co, I-CoMn, H-Co and H-CoMn catalysts reduced at 300 ºC in $H_2$/He flow for 2 h.

**Table 3.** EXAFS results at the Co K-edge for all the catalysts reduced 2 h in H2/He flow at 300 and 350 °C. The data for a Co metal and CoO materials are included for comparison. Extents of Co reduction calculated by a linear combination of the XANES spectra of pure Co metal and CoO. (n.a) = not applicable

| Sample code | Reduction Temp. (°C) | % $Co^0$ | N atoms $Co^0$ shell) | R (Å) distance | $2\sigma^2$ (Å) | N atoms (CoO shell) | R (Å) distance | $2\sigma^2$ (Å) |
|---|---|---|---|---|---|---|---|---|
| Co metal | n.a | 100 | 12 Co | 2.51 | n.a | n.a | n.a | n.a |
| CoO | n.a | 0 | n.a | n.a | n.a | 6.0 O<br>12 Co | 2.13<br>3.02 | n.a |
| I-Co | 300 | 92 | 9.4 Co | 2.51 | 0.020 | n.a | n.a | n.a |
| | 350 | 100 | 9.3 Co | 2.51 | 0.022 | n.a | n.a | n.a |
| I-CoMn | 300 | 48 | 6.8 Co | 2.50 | 0.023 | 4.7 O<br>9.9 Co | 2.13<br>3.04 | 0.033<br>0.036 |
| | 350 | 100 | 10.2 Co | 2.52 | 0.027 | n.a | n.a | n.a |
| I-MnCo | 300 | 97 | 11.2 Co | 2.53 | 0.029 | n.a | n.a | n.a |
| | 350 | 100 | 9.6 Co | 2.52 | 0.021 | n.a | n.a | n.a |
| H-Co | 300 | 40 | 2.3 Co | 2.49 | 0.008 | 3.9 O<br>10.2 Co | 2.12<br>3.02 | 0.042<br>0.032 |
| | 350 | 95 | 9.4 Co | 2.52 | 0.023 | n.a | n.a | n.a |
| H-CoMn | 300 | >5 | 1.7 Co | 2.527 | 0.014 | 3.8 O<br>10.2 Co | 2.22<br>3.09 | 0.023<br>0.026 |
| | 350 | 90 | 11.4 Co | 2.52 | 0.027 | n.a | n.a | n.a |
| Hcop-CoMn | 350 | <5 | 1.0 Co | 2.485 | 0.014 | 3.8 O<br>15.0 Co | 2.18<br>3.11 | 0.028<br>0.033 |

The EXAFS results, summarized in Table 3, confirmed the preliminary observation since all reduced catalysts could be fitted with the combination of the structural parameters of Co metal and CoO. As a result, the structure of all reduced catalysts consists of various shells with similar inter-atomic distances to those found in $Co^0$ and CoO materials, and with coordination numbers closely related to the relative fractions of CoO and $Co^0$ present in the catalysts. All catalysts feature a Co–Co shell with distances of around 2.51-2.53 Å, and with coordination numbers ranging from 1.0 to 11.2. This shell belongs to the metallic phase with either fcc or hcp structure that feature in average a first shell of 12 Co atoms at 2.52 Å, as determined by the EXAFS fit of the cobalt foil in agreement with the crystallographic data [37]. The low Co–Co coordination numbers in the catalysts therefore reflect the occurrence of numerous surface atoms that characterize nanosized cobalt particles as well as the presence of an oxidic phase next to the cobalt metal in the incompletely reduced catalysts. In fact, the number of Co neighboring atoms forming this shell drastically decreases as a function of the reduction degree and/or the $Co^0$ particle size. For instance, the I-Co catalyst reduced at 350 ºC gives 10.3 Co neighbor atoms in contrast to the reference $Co^0$ material with 12. In the I-CoMn catalyst reduced at 300 ºC, the number of Co atoms is 6.8 due to the low reduction degree of 48 %.

Two additional Co–O and Co–Co shells were obtained for the catalysts with low reduction extents. These shells belong to the fraction of unreduced CoO and have coordination numbers respectively between 3.8-4.7, and 9.9-10.2. In agreement with the crystallographic data, the EXAFS fit of the CoO cubic structure [37] gives Co atoms six-fold coordinated by oxygen atoms and Co–O and Co–Co distances of 2.13 and 3.02 Å, respectively (Table 3). It is remarkable to notice that the Co–O and Co–Co distances obtained for the catalysts are in some cases significantly longer than those in the CoO reference material. For instance, H-CoMn features Co–O and Co–Co distances of 2.22 and 3.09 Å and Hcop-CoMn of 2.18 and 3.11 Å, respectively. This elongation indicates the occurrence of a cell expansion of the CoO phase that is very likely resulting from the formation of $Mn_{1-x}Co_xO_{1-x}$ solid solutions, as will be discussed in detail in chapter 4 with the EXAFS results at the Mn K-edge. Indeed, due to the greater ionic radius of $Mn^{2+}$ ions compared to $Co^{2+}$, $Mn_{1-x}Co_xO_{1-x}$ compounds feature a larger cell parameter [38], and longer inter-atomic distances compared to the CoO reference material. These results, therefore, reflect an intimate mixing of MnO with CoO in some of the catalysts.

As was already pointed out, the cobalt reduction degree are reflected in the coordination number of the Co–Co shell at 2.51-2.52 Å, which decreases from a maximum of twelve in a fully reduced bulk $Co^0$ material, to zero in pure CoO. Thus, for a fully reduced catalyst the decrease of the number of Co neighboring atoms is due to a geometric artifact caused by the

nanosized character of the metallic particles. Although coordination numbers are determined with a relatively low accuracy with EXAFS (10-20 %), they can still be used to roughly estimate particle sizes in the reduced catalysts. The accuracy of this technique is nonetheless, enhanced in the case of particles smaller than 3-5 nm. Among the catalysts studied, the XANES results revealed that merely I-Co, I-CoMn, and I-MnCo catalysts contain 100 % $Co^0$ after reduction at 350 °C. Thus, their coordination numbers may be directly used to calculate the $Co^0$ particle sizes formed after reduction. In the H-Co and H-CoMn catalysts, however, reduction degrees of respectively 95 and 90 % were obtained, and hence the coordination numbers had to be corrected in order to take into account the CoO fraction. In the Hcop-CoMn catalyst the low extent of cobalt reduction (< 5 % $Co^0$) made it not possible to apply this calculation method.

The results of the $Co^0$ particle sizes in the catalysts reduced at 350 °C are presented in Table 5. The particles turned out to be in the range of 3-6 nm, with the exception of the H-CoMn catalyst, which seems to contain larger particles according to the high coordination number. The existence of such small particles interestingly suggests that a re-dispersion of the cobalt phase occurs during reduction, leading to a dramatic decrease in the particle size. As will be shown later, these values of particle size are in good agreement with those obtained by XPS and TEM analysis.

### *XPS study of the surface Co phase in reduced Co/TiO$_2$ and Co/Mn/TiO$_2$ catalysts*

XPS was used to investigate the surface composition of the catalysts after reduction and to estimate cobalt dispersions. The Co2p spectra of the reduced/passivated catalysts are presented in Fig. 6. They all exhibit Co2p$_{3/2}$ and Co2p$_{1/2}$ peaks at 781.1–781.2 eV and 796.5-796.8 eV, respectively, and an energy separation between the Co2p$_{3/2}$ and Co2p$_{1/2}$

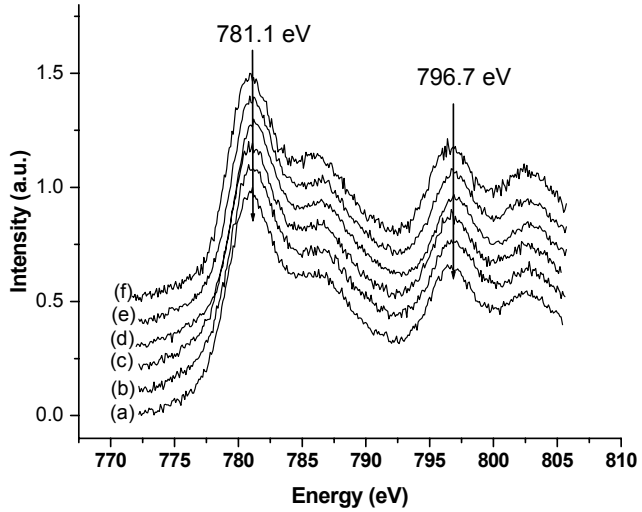


**Figure 6.** Co 2p XPS spectra for I-Co (a), I-CoMn (b), I-MnCo (c), H-Co (d), H-CoMn (e), and Hcop-CoMn (f) catalysts after reduction in $H_2$/He at 350 °C and passivation in $CO_2$ at 150 °C.

peaks of around 15.5-15.8 eV. Furthermore, an additional peak is present in the spectra at slightly higher energies (ca. 786.5 eV), as a result of the so-called shake-up process. This peak corresponds to photoelectrons emitted from a cobalt atom in which a second electron in a 2p orbital goes into an excited state as a consequence of the sudden change in the atom central potential produced by the photoelectron ejection [39]. The appearance of shake up features in the Co2p spectra evidences the presence of $Co^{2+}$ species [40]. Since passivation leads to a re-oxidation of the outer layer of the cobalt particles, detection of $Co^{2+}$ at the surface is expected. For this reason, all the Co2p spectra of the reduced catalysts reflect a $Co^{2+}$ oxidation state (Fig. 5), on account of the fact that the thickness of the probed surface is in the order of 2 nm. This value corresponds to the inelastic mean free path of photoelectrons travelling through the CoO phase [41]. Based on these results it can be concluded that all the cobalt probed with XPS belongs to a CoO-type phase.

Under this assumption the size of the CoO particles were accurately estimated using the intensity of $Co_{2p}$, $Ti_{2p}$, and $Mn_{2p}$ photoelectron peaks. We note that the size and shape of the cobalt particles are not expected to vary significantly after the passivation, and under this

**Table 4.** Results of the CoO layer thickness and particle sizes in the reduced catalysts as calculated by quantitative XPS analysis for the three different situations represented in Fig. 7.

| Sample code | Model A | | Model B | | Model C | |
|---|---|---|---|---|---|---|
| | Size hemisph. (nm) | Layer thickness, % coverage | Size hemisph. (nm) | Layer thickness, % coverage | Size hemisph. (nm) | Layer thickness, % coverage |
| I-Co | 4.0 | 0.9 nm, 53 % | - | - | - | - |
| I-CoMn | 5.8 | 1.3 nm, 37 % | 4.6 | 1.0 nm, 30 % | 4.9 | 1.1 nm, 49 % |
| I-MnCo | 3.7 | 0.8 nm, 50 % | 3.4 | 0.7 nm, 55 % | 3.2 | 0.7 nm, 66 % |
| H-Co | 1.3 | 0.3 nm, 115% | - | - | - | - |
| H-CoMn | 2.8 | 0.6 nm, 53 % | 1.7 | 0.4 nm, 85 % | 1.5 | 0.3 nm, 126 % |
| Hcop-CoMn | 8.9 | 1.9 nm, 17 % | 3.9 | 0.9 nm, 38 % | 4.4 | 0.9 nm, 64 % |

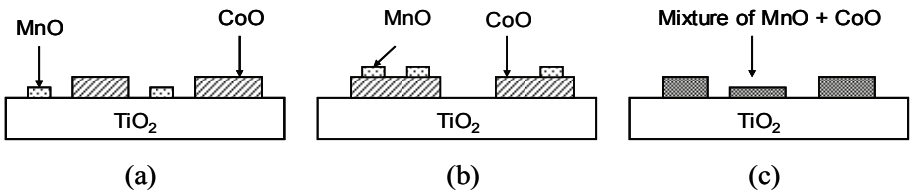


**Figure 7.** Schematic representation of the three models (A, B and C) applied for the XPS calculation to estimate CoO layer thickness and particle size.

assumption XPS provides an approximate value of the mean size of the cobalt particles. Additionally, the particle sizes were calculated according to three different models (A, B, and C), as illustrated in Fig. 7. The distribution of cobalt and manganese in the catalysts may vary as a function of the amount of manganese located on the $TiO_2$ surface (model A), on the CoO (model B) or mixed with the CoO (model C). The results of layer thickness and hemisphere size obtained for the six catalysts are summarized in Table 4. A layer thickness of 0.9 nm and 53 % coverage are obtained for I-Co that corresponds to hemispherical particles of 4.0 nm. For I-CoMn and I-MnCo slightly larger particles respectively of 5.8, 4.6, and 4.9 nm and 3.7, 3.4, and 3.2 nm result from each of the models. Thus, similar cobalt dispersions are found in I-CoMn and I-MnCo, regardless their manganese location. These results are in a good agreement with EXAFS, confirming the existence in the IWI catalysts of cobalt particles in the range of 4-6 nm.

Smaller particles are obtained for the HDP catalysts, being 1.3 nm in H-Co, and 2.8, 1.7 and 1.5 nm in H-CoMn for the different manganese locations. For the Hcop-CoMn catalyst, particles of 8.9, 3.9 and 4.4 nm are obtained for the three models, respectively. Thus, the calculation assuming CoO/MnO mixtures or coverage of CoO by MnO leads generally to smaller values of particle size. It is worthwhile to note that particle sizes obtained for the HDP catalysts by XPS are much smaller than those calculated by EXAFS. This deviation between XPS and EXAFS points to the existence of cobalt surface phases in the HDP catalysts. Since XPS is a surface sensitive technique, it cannot discriminate between crystalline particles and dispersed phases. As a consequence, the presence of cobalt species highly dispersed at the surface of the catalysts would lead to an increase of the Co2p photoelectron intensity and thereby, to smaller values of particle size. These surface species, on the other hand, cannot be detected by the bulk sensitive technique (i.e., EXAFS). The presence of larger particles in the HDP catalysts will be also confirmed by the TEM analysis. Therefore, the results reveal that the HDP catalysts may contain a small fraction of the cobalt in the form of highly dispersed $CoTiO_3$ or CoO.

***TEM study of the Co particles in reduced Co/$TiO_2$ and Co/Mn/$TiO_2$ catalysts***

The reduction effect on the cobalt phase distribution and morphology was investigated by TEM. Fig. 8 shows a comparison between the $TiO_2$ material and a reduced Co/$TiO_2$ catalyst. It can be observed that the cobalt particles are clearly distinguishable from $TiO_2$ by the different size, being the $TiO_2$ and cobalt particles in the range of 30-60 nm and 2-10 nm, respectively. As a result of the passivation treatments, the surface of the cobalt particles was re-oxidized and hence, it is expected that particles smaller than 5 nm are composed merely of

CoO, whereas larger particles may also contain a metallic cobalt core and CoO at the outer-layer.

The TEM images obtained for the group of IWI catalysts are given in Fig. 9. Very small cobalt particles can be clearly seen covering the $TiO_2$ and leading to an irregular surface. The cobalt is nicely visualized at the edges of the $TiO_2$ particles, and can be occasionally distinguished on top or underneath the $TiO_2$ given by a darker contrast. Fig. 9A and 9B show the situation for the I-Co catalyst, in which very small particles with sizes of around 2.5-5 nm and nearly hemispherical shapes can be seen homogeneously covering the $TiO_2$ surface. In the absence of manganese the cobalt particles appear to have a well-defined shape and are located on the $TiO_2$ without an apparent interaction. Additionally, cobalt is also found in some spots as a highly dispersed thin layer (ca. 3 nm) on the $TiO_2$ surface, as well as in the form of larger clusters of around 6-8 nm. Nevertheless, large clusters were not often observed in the I-Co catalyst. For the I-CoMn and I-MnCo catalysts, the distribution of the cobalt particles slightly differs from I-Co, as observed in Fig. 9C and 9D. These catalysts also contain very small particles of around 3-6 nm, although larger agglomerates (ca. 6-10 nm) are more frequently detected. Furthermore, the $TiO_2$ surface appears to be less regular in the Mn-promoted catalysts most likely as a result of the manganese species highly spread out over the catalyst surface. An estimation of the mean cobalt particle sizes for the I-Co, I-CoMn, and I-MnCo catalysts resulted in values of 4.3, 4.9 and 4.8 nm, respectively (Table 5). Therefore, the presence of manganese slightly favored the formation of larger cobalt particles, leading also to a broader particle size distribution.

The TEM results for the HDP catalysts are presented in Fig. 10. For the H-Co catalyst (Fig. 10A and 10B) very small particles in the range of 1.5-5 nm can be visualized very homogeneously on the $TiO_2$ surface. The situation resembles that of the I-Co catalyst,

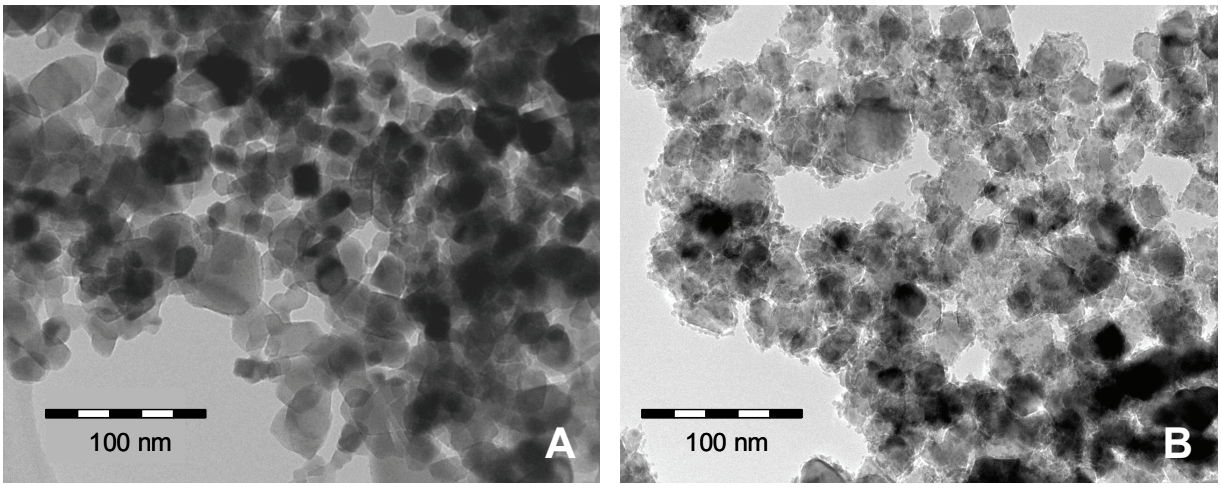


**Figure 8.** TEM images of $TiO_2$ Degussa P25 (A) and the I-Co catalyst after reduction (B).

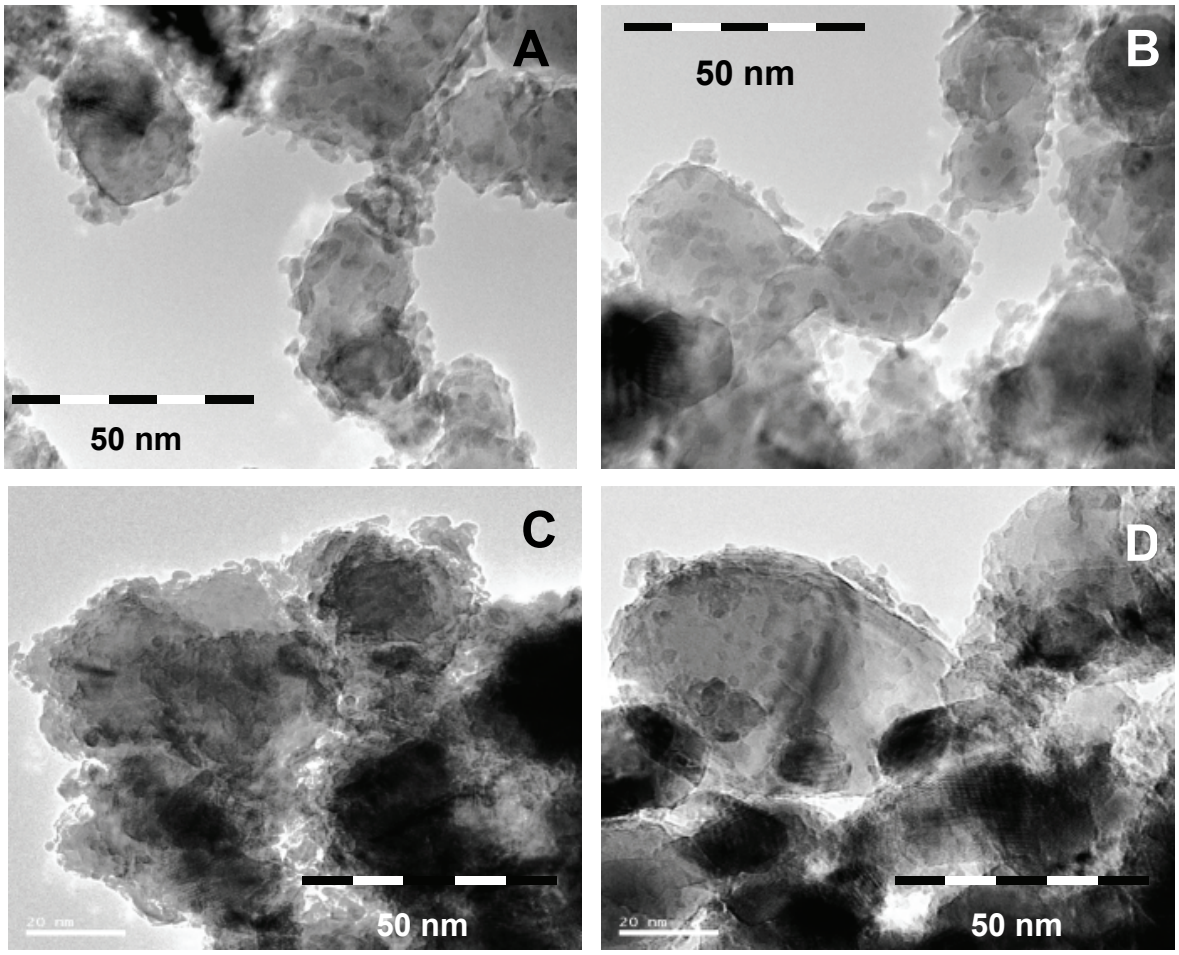


**Figure 9.** TEM images for the I-Co (A and B), I-CoMn (C), and I-MnCo (D) catalyst after reduction at 350 °C in $H_2$/He flow and passivation in $CO_2$ at 150 °C.

although the cobalt phase is even more highly dispersed and more often found in the form of thin layers on the $TiO_2$ leading to a rough catalyst surface. The existence of some amounts of cobalt titanate in this catalyst was already suggested by the XAFS results that indicated lower cobalt reducibility compared to the IWI catalysts. The fraction of the non-reducible cobalt phase is thus thought to be in intimate contact with the $TiO_2$, presumably in the form of titanates, which are well known to be difficult to reduce. On the other hand, Fig. 10C and 10D reveal that for the H-CoMn and Hcop-CoMn catalysts, the presence of manganese has a large influence on the cobalt particle distributions. It can be observed that the H-CoMn and Hcop-CoMn catalysts contain much larger cobalt clusters, in addition to smaller particles in the range of 3-6 nm. For example, several clusters with sizes of around 10-15 nm can be visualized in Fig. 11C for the H-CoMn catalyst. Interestingly, these clusters appear to be composed of smaller particles embedded together. On the other hand, small particles were also detected in the H-CoMn catalyst, although to a much lower extent that for H-Co.

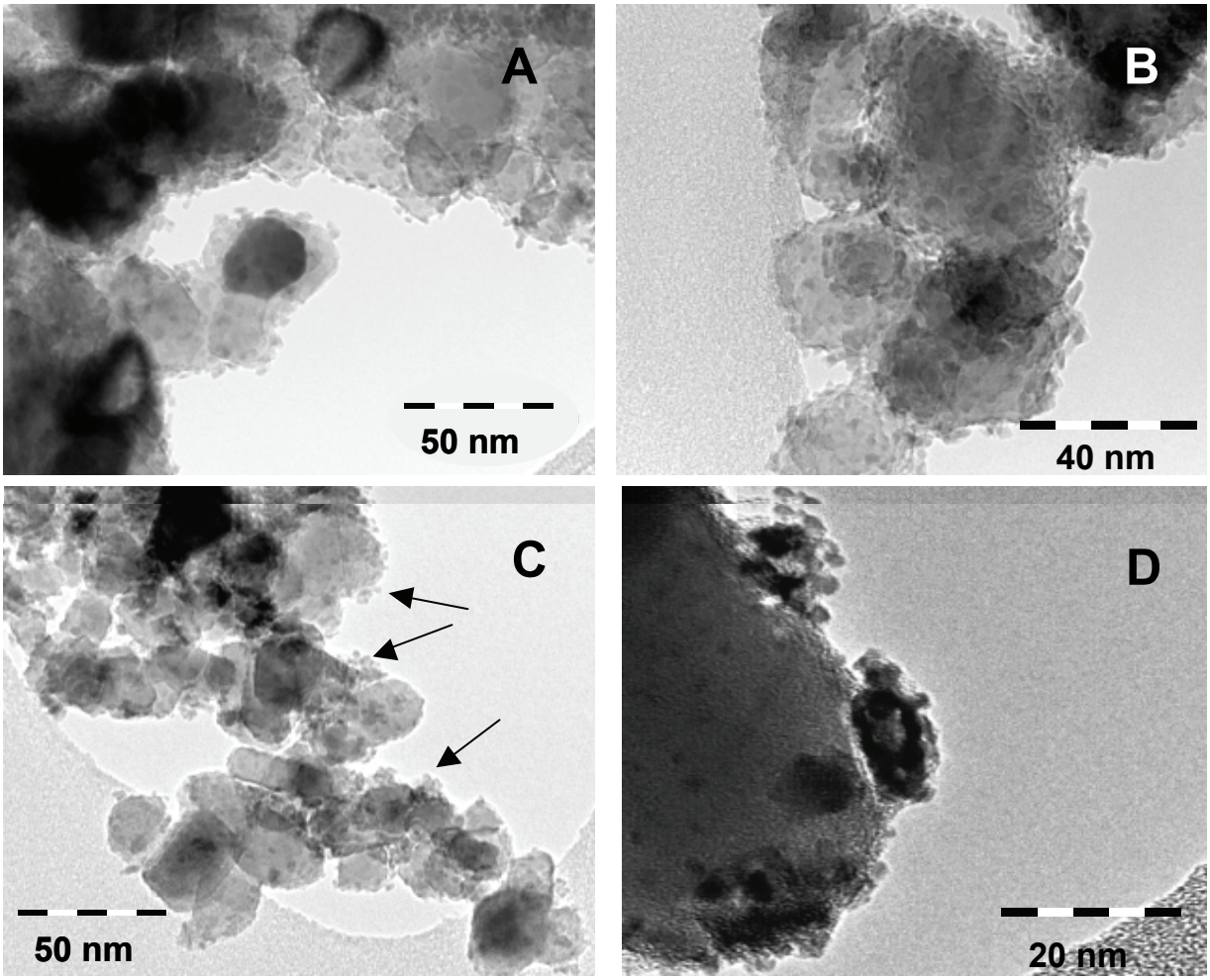


**Figure 10.** TEM images for the H-Co (A and B), H-CoMn (C), and Hcop-MnCo (D) catalyst after reduction at 350 °C in $H_2$/He flow and passivation in $CO_2$ at 150 °C.

Finally, in the Hcop-CoMn catalyst numerous cobalt clusters were found with much larger sizes than in all the other catalysts. As an example, Fig. 10D shows an image in which a large $TiO_2$ particle is observed and three cobalt clusters of about 10-20 nm are clearly distinguishable at the $TiO_2$ surface, giving a darker contrast. Additionally, other very small black dots are observed on top of the $TiO_2$ particle indicating the presence of also some small particles. The mean cobalt particle size obtained for the H-Co, H-CoMn and Hcop-CoMn catalysts were respectively of 3.5, 5.6, and 10.5 nm, reflecting a dramatic influence of the presence of manganese on the cobalt particle size distribution for the HDP catalysts. This marked influence most probably results from the Co-Mn interactions taking place in the catalyst before reduction.

A comparison between the cobalt particle size results obtained by the three different techniques is given in Table 4. The particle sizes estimated by the three methods are in a

rather good agreement, with the exception of the HDP catalysts, which have smaller particles according to the XPS results and in contrast with the other techniques. This discrepancy with the results is most likely related to the existence of highly dispersed cobalt species in the HDP catalysts, which results in a higher exposure of cobalt atoms at the surface, thereby increasing the cobalt XPS signal.

**Table 4.** Overview of the cobalt particle size calculation obtained by EXAFS, XPS, and TEM techniques in the catalyst reduced at 350 °C.

| Sample code | EXAFS Co size (nm) | XPS Co size (nm) | TEM Co size[a] (nm) |
|---|---|---|---|
| I-Co | 2.5 | 4.0 | 4.3 |
| I-CoMn | 3.7 | 5.8 – 4.9 | 4.9 |
| I-MnCo | 2.7 | 3.7 – 3.2 | 4.8 |
| H-Co | 3.2 | 1.3 | 3.5 |
| H-CoMn | >10 | 2.8 – 1.5 | 5.6 |
| Hcop-CoMn | n.a. | 8.9 – 4.4 | 10.5 |

[a]Particle size calculated from the formula N (nm) = $\sum n^3/\sum n^2$, being N the average cobalt diameter size and $n$ the diameter of each measured cobalt particle in nm.

***Fischer-Tropsch catalytic performances***

The evolution of the activity for all catalysts under study during the first 60 h FT reaction is presented in Fig. 11. The IWI catalysts suffer from a rapid deactivation during the first 30 h reaction as indicated by the initial drop in activity, after which the Co-time yields stabilize in a pseudo-steady state (Fig. 11a). Interestingly, the I-Co catalyst deactivates more rapidly and during longer times than I-CoMn and I-MnCo, independently of the reduction temperature. The group of the HDP catalysts also suffer a marked deactivation though only during the first 5 h FT reaction (Fig. 11b), after which they maintain steady Co-time yields. The exception is the H-Co catalyst reduced at 350 °C, which initially leads to the highest Co-time yields above 3.0 $10^{-5}$ mol CO (g Co)$^{-1}$s$^{-1}$, and subsequently deactivates throughout 60 h reaction. In contrast, the H-CoMn catalyst reduced at 350 °C shows a less pronounced deactivation and leads to the highest Co-time yield (2.57 $10^{-5}$ mol CO (g Co)$^{-1}$s$^{-1}$) among all the catalysts.

The overall catalytic results are summarized in Table 6. The catalytic performances correspond to a pseudo-stationary behavior obtained after 60 h FT reaction. For the IWI catalysts the highest activities are obtained after reduction at 300 °C, with similar Co-time yields of about 2.31- 2.34 $10^{-5}$ mol CO (g Co)$^{-1}$s$^{-1}$. The activities are, however, lower after reduction at 350 °C, with values of 1.64, 1.31, and 2.12 for the I-Co, I-CoMn and I-MnCo catalysts, respectively. This negative effect observed after reduction at 350 °C is likely related

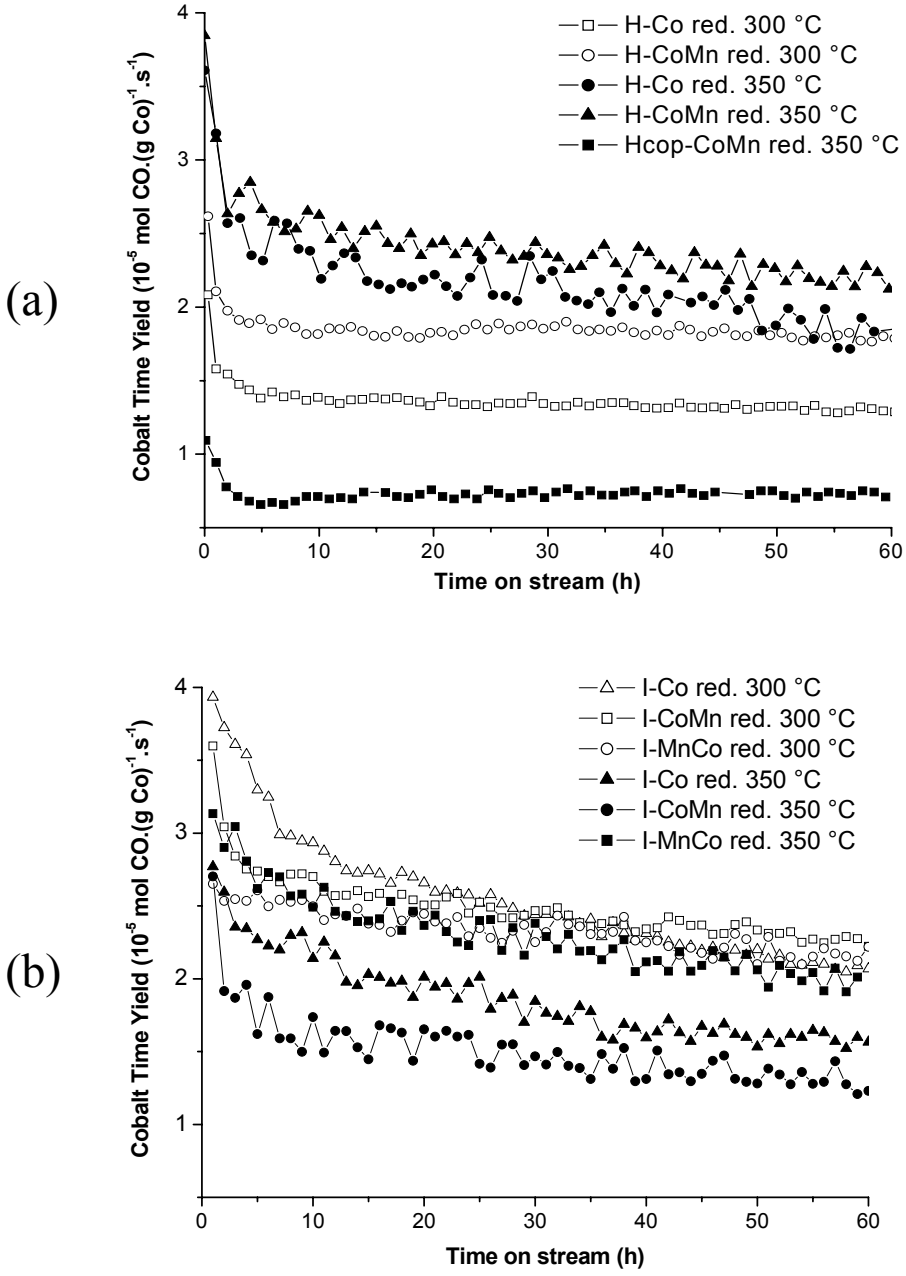


**Figure 11.** Evolution of activity during 60 h of F-T reaction in the IWI (a) and HDP (b) catalysts after reduction at 300 and 350 °C. The activities are expressed as Co-time yield.

to the small cobalt particles present in the catalysts, which are prone to deactivate during FT reaction as a result of the occurrence of SMSI effects with a $TiO_2$ support [21-22]. SMSI effects are expected to occur at high temperatures, leading to a partial blockage of the small particles and consequently to a decrease in activity. This phenomenon would also explain the initial drop in activity for the catalysts during the first stage of FT reaction since the small

**Table 6.** Overview of catalytic performances of the Co/TiO$_2$ and Co/Mn/TiO$_2$ catalysts after reduction at 300 and 350 °C. The table includes the extents of cobalt reduction achieved, as measured with XANES.

| Catalyst | Red. Temp. | % Co$^0$ reduction | Selectivity | | | Activity | |
|---|---|---|---|---|---|---|---|
| | | | % $CH_4$ | % $C_{5+}$ | α values[a] | Co-time yield[b] | T.O.F[c] |
| I-Co | 350 °C | 100 | 21 | 48 | 0.69 | 1.64 | 4.28 |
| I-CoMn | | 100 | 21 | 45 | 0.66 | 1.31 | 3.93 |
| I-MnCo | | 100 | 20 | 47 | 0.67 | 2.12 | 6.18 |
| H-Co | | 95 | 32 | 28 | 0.54 | 2.08 | 4.45 |
| H-CoMn | | 90 | 25 | 34 | 0.58 | 2.57 | 8.74 |
| Hcop-CoMn | | ~5 | 17 | 47 | 0.67 | 0.80 | 5.20 |
| I-Co | 300 °C | 100 | 17 | 54 | 0.72 | 2.31 | 6.04 |
| I-CoMn | | 48 | 18 | 51 | 0.69 | 2.34 | 7.02 |
| I-MnCo | | 97 | 18 | 51 | 0.69 | 2.32 | 6.68 |
| H-Co | | 40 | 23 | 43 | 0.65 | 1.32 | 2.81 |
| H-CoMn | | ~5 | 18 | 50 | 0.68 | 1.81 | 6.15 |

particles might deactivate as a result of re-oxidation or site blockage by $TiO_x$. Additionally, the activity of the I-CoMn catalyst is lower than the I-Co catalyst due the presence of manganese, which might also block some of the small cobalt particles, similarly as the SMSI effect already explained. A similar manganese effect on the activity of SBA-15-supported cobalt catalysts has been reported by Martinez *et al.* [42], in which they used similar range of cobalt dispersions (19-21 %) as in our I-CoMn catalyst.

The IWI catalysts are significantly more selective towards the formation of higher hydrocarbons after reduction at 300 °C (50-54 % $C_{5+}$ and 17-18 % $CH_4$), than at 350 °C (45-48 % $C_{5+}$ and 20-21 % $CH_4$). This decrease in selectivity can be ascribed to the formation of small unreduced cobalt particles and/or some titanate compounds, as previously suggested in the literature [43-44]. On the other hand, no significant differences in product selectivity due to the presence of manganese are found for I-CoMn and I-MnCo, since the I-Co catalyst reduced at 300 °C is the most selective towards the $C_{5+}$ fraction of products and displays the highest chain growth probability (0.72).

For the HDP catalysts an opposite reduction temperature-activity dependency is found, as shown in Table 6. The highest Co-time yields are displayed for the H-Co and H-CoMn

catalysts reduced at 350 °C, with values of 2.08 and 2.57 $10^{-5}$ mol CO (g Co)$^{-1}$s$^{-1}$, respectively. Reduction at 300 °C, however, results in a decrease of the Co-time yields to 1.32 and 1.81 $10^{-5}$ mol CO (g Co)$^{-1}$s$^{-1}$ for the same catalysts. The Hcop-CoMn catalyst is the least active (0.80 mol CO (g Co)$^{-1}$s$^{-1}$) due to its lower cobalt reducibility. Hence, the activity of this group of catalysts is dependent on the cobalt reduction extents, being proportional to the percentage of $Co^0$. Since the cobalt reducibility of these catalysts is very low at 300 °C, the cobalt particles are expected to remain larger, thereby leading to lower Co-time yields. On the other hand, the H-CoMn catalyst displays in all cases higher Co-time yields than H-Co, regardless its lower cobalt dispersion and lower reducibility. Remarkably, the TOF numbers after reduction at 350 °C are twice as high in H-CoMn (8.74 $10^{-3}$ s$^{-1}$) than in H-Co (4.75 $10^{-3}$ s$^{-1}$). This indicates that larger cobalt particles than ~5 nm and containing a manganese promoter have a higher intrinsic activity in the FT reaction than smaller particles as those contained in H-Co. The small particles are, moreover, rapidly deactivated during the first stage of FT reaction.

The selectivity of the HDP catalysts is also largely influenced by the reduction temperature and the presence of manganese. The highest $C_{5+}$ selectivities are obtained for H-CoMn and H-Co reduced at 300 °C, with values of 50 and 43 %, respectively. After reduction at 350 °C the catalysts display lower $C_{5+}$ selectivities of 34 and 28 %, respectively. Therefore, a cobalt reduction extent-selectivity dependency is found for this group of catalysts, since lower reduction extents result in a higher $C_{5+}$ selectivity and lower $CH_4$ production. Finally, it is important to note that the presence of manganese in the H-CoMn and Hcop-CoMn catalysts leads in all cases to an increase of the chain growth probability and to a decrease of the $CH_4$ production, compared to the manganese-free catalyst. These results clearly illustrate a manganese promotion effect obtained in the HDP catalyst, leading to an improvement of the FT performances.

Finally, it is worthwhile to comment on the high $CH_4$ selectivity found for the HDP catalysts after reduction at 350 °C compared to the IWI catalysts that may be due to different causes. As reported in literature, the existence of unreduced cobalt species (e.g. titanates or $CoO_x$) is known to catalyze the WGS reaction [42-44] thus increasing the effective $H_2/CO$ ratio at the surface of the catalyst. Hence, a first explanation for the higher $CH_4$ is the increase of the WGS activity leading to higher hydrogenation rates, and consequently, to a higher $CH_4$ selectivity. The presence of these unreduced phases has been demonstrated by EXAFS and XPS. Nevertheless, since the FT experiments were carried out at pressures of 1 bar and low CO conversions (3 - 6 %), the WGS activity may be negligible. Therefore, another possible explanation is that the presence of very small cobalt particles provides active sites for the

formation of $CH_4$ and not for the polymerization reaction. The existence of very small cboalt particles has been demonstrated by TEM, XPS and XAFS.

## Discussion

*In situ* XAFS results at the Co and Mn K-edges in combination with TEM and XPS analysis have provided valuable information on the physico-chemical properties of the cobalt active sites in the catalysts as well as their level dispersion after reduction. The preparation method and reduction temperature strongly influences the chemistry of the cobalt phase and its FT catalytic behavior. An overview of the structural results for the two groups of Co/$TiO_2$ and Co/Mn/$TiO_2$ catalysts is presented including a more thorough discussion on structure-performance relationships.

***1. Catalysts prepared by incipient wetness impregnation***

A first group of Co/Mn/$TiO_2$ catalysts, were synthesized stepwise using the IWI method (chapter 3). These materials after calcination were composed of $Co_3O_4$ clusters with sizes of around 20-35 nm, and a $MnO_2$ phase dispersed over $TiO_2$ without a marked interaction with the $Co_3O_4$. The cobalt was fully reduced to $Co^0$ at 350 °C in the all cases, ruling out a large manganese influence on the cobalt reducibility. Remarkably, reduction led to the formation of small particles in the range of 3-6 nm. These $Co^0$ particles are orders of magnitude smaller than the initial $Co_3O_4$ clusters, indicating the occurrence of a re-dispersion of the cobalt phase presumably due to the rupture of the $Co_3O_4$ clusters into smaller cobalt aggregates. In this respect, the $TiO_2$ support seems to play a crucial role in stabilizing small metal particles. Thus, a driving force leading to the formation of small $Co^0$ particles seems to be the occurrence of Co-$TiO_2$ interactions during the reduction process from $Co_3O_4$ to $Co^0$. On the other hand, the presence of manganese did not influence the cobalt dispersion to a great extent.

As a result of the high cobalt dispersion achieved in these catalysts a drawback is encountered, since the small $Co^0$ particles were less active and less stable for the FT reaction. According to literature $Co^0$ particles in the range of 6 to 200 nm should exhibit a similar intrinsic activity for the CO hydrogenation, whereas particles below 6 nm appear to be less active [23, 45]. Although the reason for this phenomenon has not been elucidated, different explanations have been proposed, such as re-oxidation of small $Co^0$ particles by steam released under FT conditions or surface carbide formation. Another possible cause is the occurrence of SMSI effects, occasionally reported for $TiO_2$-supported catalysts. The occurrence of SMSI may result in a blockage of small $Co^0$ particles by migration of $TiO_x$ over-layers onto the surface, leading to a decrease in activity [21-22]. Similarly, cobalt atoms

may diffuse into the $TiO_2$ lattice resulting in the formation of titanates, which are inactive for the FT reaction.

Our results show that the IWI catalysts contain Co particles smaller than 6 nm and interestingly, their activity is lower after reduction at 350 °C than at 300 °C. Hence, a negative influence of $TiO_2$ appear to cause this effect. Even though EXAFS showed a 100 % bulk Co reduction at 350 °C, the surface of the particles may be covered by $TiO_x$ species causing the blocking of some active sites and therefore, a decrease in the activity.

Finally, the use of manganese was not beneficial for the catalytic performances, since the three catalysts displayed very similar selectivity and activity. Taking into account that the catalysts contain very small cobalt particles, the results suggest that manganese does not effectively promote cobalt particles with sizes in the range of 2-5 nm. On the contrary, a decrease in activity was occasionally obtained most likely as a result of a blocking of the active sites by the manganese species.

***2. Catalysts prepared by homogeneous deposition precipitation***

A second group of $Co/Mn/TiO_2$ catalysts were synthesized by the HDP method and by a combination of the IWI and HDP methods (chapter 3). After calcination the catalysts were composed of $Co_3O_4$ clusters with sizes of around 10-15 nm and a manganese phase, which was localized in intimate contact with the cobalt. Due to this initial Co-Mn association in the catalysts, the reduction from $Co_3O_4$ to cobalt metal was somewhat hampered, this effect being more severe when $Co_{3-x}Mn_xO_4$ solid solutions were present in the catalyst precursors. In addition, the HDP catalysts were found to be less reducible than the other group prepared by IWI, since they did not fully reduce to cobalt metal at any of the conditions employed. The remaining unreduced cobalt is thought to exist in a dispersed form in intimate contact with the $TiO_2$ surface (e.g., as cobalt titanate or $CoO_x$). This result was also supported by XPS, which demonstrated the existence of some dispersed cobalt species covering the $TiO_2$ surface.

The cobalt particle size distribution was also largely affected by the presence of manganese in the HDP catalysts. While reduction of a $Co/TiO_2$ catalyst resulted in the formation of very small $Co^0$ particles (~ 2-4 nm), reduction of the $Co/Mn/TiO_2$ catalysts also led to the formation of larger agglomerates with sizes in the range of 8-15 nm. Hence, the manganese appears to act as a glue keeping the cobalt particles in a less segregated state, as a result of the decrease in the cobalt reducibility. Therefore, it is considered that manganese, when mixed with the cobalt particles, may play a role protecting the cobalt against an excessive spreading over $TiO_2$. In this respect, an initial Co-Mn interaction seems to be required in order to obtain this effect.

The size of cobalt particles present in the catalysts was found to strongly influence the FT catalytic performances. Remarkably, the Co/Mn/$TiO_2$ catalyst displayed a higher activity than the Co/$TiO_2$ catalyst, at all reduction temperatures employed. Since the umpromoted Co/$TiO_2$ catalyst contained smaller $Co^0$ particles than the Mn-promoted catalyst, the results suggest that the larger $Co^0$ particles promoted with manganese have a higher intrinsic activity for the FT reaction. In addition, the stability of the Co/Mn/$TiO_2$ catalysts was also largely improved due to the presence of manganese, since they displayed lower deactivation rates during the first stage of FT reaction.

With respect to the selectivity, the presence of manganese notably improved the $C_{5+}$ selectivity, while suppressing the $CH_4$ production. This shift in selectivity is most likely caused by a decrease in the hydrogenation rate during the FT synthesis, which is indicative of a more oxidized cobalt surface composition in which adsorption of $H_2$ is suppressed and the chain growth probability is increased. Manganese in this respect decreases the amount of metallic cobalt surface, resulting in a different favorable termination path of the growing alkyl-chain during the FT reaction. This promotion effect is obtained as a result of an intimate interaction of the manganese species with the active cobalt phase.

## Conclusions

The synthesis method and pretreatment conditions are key variables affecting the final active site distribution in Co/Mn/$TiO_2$ Fischer-Tropsch catalysts. The addition of manganese to $TiO_2$-supported cobalt catalysts provides remarkable improvements in terms of FT activity, selectivity and stability. The use of manganese gives rise to a decrease of the cobalt reducibility, this effect being largely enhanced provided that Co-Mn interactions take place in the catalyst precursors. In addition, an increase of the $Co^0$ particle sizes can be obtained after catalyst activation as a result of a protection from an excessive spreading of the cobalt phase. The manganese species are able to induce beneficial effect by decreasing the deactivation rate in the FT reaction and possibly, by increasing the turnover frequency of the cobalt active sites for the CO hydrogenation. Furthermore, a decrease in the amount of $Co^0$ in the catalysts leads to a shift in selectivity towards the formation of higher hydrocarbons, due to the increase of the chain growth probability. Nonetheless, large cobalt particles are required in order to gain this promotion effect, since small cobalt particles are prone to undergo coverage and blockage by $MnO_x$ and/or $TiO_x$ species and thus, to a lower number of active sites for the FT reaction. In other words, manganese promotion effects are largely influenced by the preparation method and pretreatment conditions and are only experimentally observable in well-defined cases.

## Acknowledgements

Access to the synchrotron facilities at the ESRF (BM26 DUBBLE-experiment 26-01-191) was arranged through the general support of NWO, and we wish to acknowledge the assistance and advice of Sergey Nikitenko during the XAFS measurements. Ad Mens and Cor van der Spek are kindly acknowledged respectively for the XPS and TEM measurements. The work also benefited from fruitful discussions with Heiko Oosterbeek, Herman Kuipers and Carl Mesters from Shell Global Solutions.

## References

[1] C.H. Bartholomew, R.C. Reuel, *Ind. Eng. Chem.*, 1985, **24**, 56.
[2] R. Riva, H. Miessner, R. Vitali, G. del Piero, *Appl. Catal. A: General,* 2000, **196**, 111.
[3] M. Vob, D. Borgmann, Wedler. *J. Catal.*, 2002, **212**, 10.
[4] K.E. Coulter, A.G. Sault, *J. Catal,,* 1995, **154**, 56.
[5] B. Ernst, S. Libs, P. Chaumette, A. Kiennemann, *Appl. Catal. A: General,* 1999, **186**, 145.
[6] Y. Brik, M. Kacimi, M. Ziyad, F. Bonzon-Verduraz, *J. Catal.*, 2001, **202**, 118.
[7] Z. Zsoldos, T. Hoffer, L. Guczi, *J. Phys. Chem*., 1991, **95**, 798.
[8] S. Vada, A. Hoff, E. Adnanes, D. Schanke, A. Holmen, *Top. Catal*., 1995, **2**, 155.
[9] G. Jacobs, T. K. Das, Y. Zhang, J. Li, G. Racoillet, B. H. Davis, *Appl. Catal. A: General*, 2002, **233**, 263.
[10] M. Kraum, M. Baerns, *Appl. Catal. A General*, 1999, **186**, 189.
[11] N. Tsubaki, S. L. Sun, K. Fujimoto, *J. Catal*., 2001, **199**, 236.
[12] C. L. Bianchi, *Catal. Lett.,* 2001, **76**, 155.
[13] A.G. Ruiz, A.S. Escribano, I.R. Ramos, *Appl. Catal. A: General*, 1994, **120**,71.
[14] S. Bessell, *Stud. Surf. Sci. Catal*., 1994, **81**, 479.
[15] E. Kikuchi, R. Sorita, H. Takahashi, T. Matsuda, *Appl. Catal. A: General*, 1999, **186**, 121.
[16] L. Fu, C.H. Bartholomew, *J. Catal*., 1985, **92**, 376.
[17] J.H. Lee, D.K. Lee, S.K Ihm, *J. Catal*., 1988, **113**, 544.
[18] E. Iglesia, S.L. Soled, R.A. Fiato, *J. Catal*., 1992, **137**, 212.
[19] H. Schulz, Z. Nie, F. Ousmanov, *Catal. Today*, 2002, **71**, 351.
[20] G. Jacobs, P. M. Patterson, Y. Zhang, T. Das, *Appl. Catal. A: General*, 2002, **233**, 215.
[21] M.A. Vannice, *J. Catal*., 1982, **74**, 199.
[22] G.L. Haller, D.E. Resasco, *Adv. Catal*., 1989, **36**, 173.
[23] G.L. Bezemer, J.H. Bitter, H.P.C.E. Kuipers, H. Oosterbeek, H. Holewijn, X. Xu, F. Kapteijn, A.J. van Dillen, K.P. de Jong, Submitted to J. Catal.
[24] J. Barrault, *Stud. Surf. Sci. Catal.*, 1982, **11**, 225.
[25] M. Van der Riet, R.G. Copperthwaite, G.J. Hutchings, *J. Chem. Soc. Farad. Trans.*, 1987, **83**, 2963.

[26] T. Riedel, M. Cleys, G. Schulz, G. Schaub, S. Nam, K. Jun, M. Choi, G. Kishan, K. Lee, *Appl. Catal. A: General*, 1999, **186**, 201.

[27] M.J. Keyser, R.C. Everson, R.L. Espinoza, *Appl. Catal. A: General*, 1998, **171**, 99.

[28] H. Kölbel, F. Engelhard, *Erdöl und Kohle*, 1949, **2**, 52.

[29] M.F. Goes, P.J.M. Rek, D. Schaddenhorst, J-P. Lange, J.J.C. Geerlings, H. Oosterbeek, 1999, US5981608 Patent.

[30] M. Vaarkamp, B.L. Mojet, M.J. Kappers, J.T. Miller, D.C. Koningsberger, *J. Phys. Chem.*, 1995, **99**, 16067.

[31] N. Binstead, J.W. Campbell, S. J. Gurman, P.C. Stephenson, EXAFS Analysis Programs; Laboratory, D., Ed. Warrington, 1991.

[32] D.A. Shirley, *Phys. Rev. B*, 1972, **5**, 4709.

[33] O.L.J. Gijzeman, XPS Layer Analysis Program, Debye Institute, Surface Science Division, Utrecht University, The Netherlands.

[34] H.P.C.E. Kuipers, *Sol. St. Ion*., 1985, **16**, 15.

[35] D. Ciuparu, P. Haider, M. Fernandez-Garcia, Y. Chen, S. Lim, G.L. Haller, L. Pfefferle, *J. Phys. Chem. B***,** 2005**, 109**, 16332.

[36] Q. Liang, K. Chen, W. Hou, Q. Yan, *Appl. Catal. A General*, 1998, **166**, 191.

[37] D.A. Fletcher, R.F. McMeeting, D. Parking, *J. Chem. Inf. Comput. Sci*., 1996, 36, 746.

[38] E. Rios, P. Chartier, J.L. Gautier, *Sol. St. Sci*., 1999, **1**, 267.

[39] A. Venezia, *Catal. Today*, 2003, **77**, 359.

[40] Y. Shao, W. Chen, I. Wold, J. Paul, *Langmuir*, 1994, **10**, 178.

[41] S. Hűfner, Photoelectron Spectroscopy, (Springer, 1995).

[42] A. Martinez, C. Lopez, F. Marquez, I. Diaz, *J. Catal*., 2003, **220**, 486.

[43] R.C. Reuel, C.H. Bartholomew, *J.Catal*., 1984, **85**, 78.

[44] B.G. Johnson, C.H. Bartholomew, D.W. Goodman, *J. Catal*., 1991, **128**, 231.

[45] C.H. Bartholomew, R.C. Reuel, *Ind. Eng. Chem. Prod. Res. Dev*., 1985, **24**, 56.

# 5

# Chemical State and Location of Manganese Oxide Promoter in Titania-Supported Cobalt Fischer-Tropsch Catalysts


## Abstract

The chemical composition of manganese in a series of $Co/Mn/TiO_2$ Fischer-Tropsch (FT) catalysts was investigated by XAFS at the Mn K-edge after *in situ* reduction treatments. The location and dispersion of manganese in the reduced catalysts was analysed by STEM-EELS making use of elemental chemical maps to identify all the existent phases. Manganese that was present in the calcined catalysts as $Mn^{4+}/Mn^{3+}$ mixtures readily reduced to $Mn^{2+}$ in a $H_2$ flow at 300 and 350°C. EXAFS combined with STEM-EELS revealed the formation of two well-distinguished manganese compounds upon reduction; (1) a highly dispersed $Ti_2MnO_4$-type phase located at the $TiO_2$ surface, and (2) a less dispersed MnO phase located in the proximity of the cobalt particles. Furthermore, the MnO was also found to exist partially mixed with the CoO phase in the form of rock salt $Mn_{1-x}Co_xO$-type solid solutions, which were mainly detected at the surface of the cobalt particles. The relative amounts of $Ti_2MnO_4$, MnO, and $Mn_{1-x}Co_xO$ in the catalysts turned out to be largely dependent on the initial level of Co-Mn interactions in the precursor catalysts as well as the reduction temperature. The Co/Ti and Mn/Co XPS ratios have been used to illustrate the migration of MnO towards the $TiO_2$ surface and spreading occurring upon reduction. Under Fischer-Tropsch conditions MnO and $Mn_{1-x}Co_xO$ phases can remain in close interaction with the $Co^0$ sites, thereby altering their electronic properties and inducing a promotion effect on the catalytic performances. CO hydrogenation tests carried out at pressures of 1, 4, 8, and 18 bar indicated that the $C_{5+}$ selectivity was significantly enhanced when using manganese oxide promoter and at high pressures.

## Introduction

The outcome of many catalytic reactions can be altered by the introduction of small amounts of promoter elements. Some promotion examples are the addition of alkali metals to Fe- and Ru-based ammonia synthesis catalysts [1] and Ag-based epoxidation catalysts [2-3]. The addition of promoters generally affects the catalyst active site composition by increasing the number of active sites (structural promotion) or by increasing the intrinsic activity of the active site (electronic promotion).

Fischer-Tropsch (FT) synthesis is a clear example in which the addition of promoters has played an important role. This has led to enhancements of the selectivity of Co-based catalysts towards the desired hydrocarbon fractions (e.g., $C_{5+}$ hydrocarbons), and to the reduction of the non-economic products (e.g. methane). A broad range of promoters has been studied for supported cobalt FT catalysts [4]. For example, some noble metals (Ru, Re and Pt) have been frequently reported to enhance the reducibility of the cobalt particles leading to higher metal dispersions [5-7]. On the other hand, numerous transition metal oxides (e.g., Cr, V and Mo) have been shown to affect the FT selectivity by shifting the product composition to different hydrocarbons fractions [8-10]. Beneficial effects from the use of promoters are, however, only obtained provided they are added in a suitable amount and manner, leading to synergistic effects between the promoter and the cobalt nanoparticles. In this respect, the state and location of the promoters appear to play a crucial role in their effectiveness to promote the catalytic performances. For instance, metal oxide promoters are thought to be located at the metal surface as sub-monolayer coverage, thereby inducing electronic effects on the active sites.

Although the use of manganese as a promoter for Co-based catalysts has been occasionally reported in literature [11-12], there is little information available on the chemical state of manganese species and on their interaction with active cobalt particles. It is remarkable to notice that under typical FT activation conditions (i.e., $H_2$ flow at 250-350 °C) manganese does not display a lower oxidation state than 2+, since reduction to metallic state ($Mn^0$) requires temperatures above 1200 ºC [13]. Some works performed on $TiO_2$-supported manganese catalysts have noticed an influence of the catalyst preparation method as well as the manganese loading on the oxidation state and dispersion of manganese [14-15]. The occurrence of manganese spreading over the $TiO_2$ support during the reduction process has been suggested by other authors, who attributed this phenomenon to a strong manganese-$TiO_2$ interaction [15].

In this work a series of Co/Mn/$TiO_2$ catalysts have been characterized after reduction treatments by the XAFS and STEM-EELS techniques, which were applied to investigate the chemical state of manganese and its location and level of dispersion. This study was carried

out on the same $Co/Mn/TiO_2$ catalytic systems dealt in the previous chapters, which present in the calcined state all the possible manganese locations at the catalyst surface. The purpose of this work was to establish the effect of the activation treatment on the manganese chemical state and location and moreover, to elucidate the occurrence of interactions with the cobalt and $TiO_2$ particles. Finally, a $Co/Mn/TiO_2$ catalyst was used as a case study to investigate the manganese spreading occurring during reduction, using an XPS quantitative analysis. This catalyst has been also tested in the FT reaction at various pressures and compared with a manganese-free $Co/TiO_2$ catalyst.

## Experimental

*X-ray absorption spectroscopy fine structure*

X-ray absorption spectroscopy fine structure (XAFS) data were collected on DUBBLE (BM26A) at the European Synchrotron Radiation Facility (ESRF, Grenoble, France), operating under beam conditions of 6 GeV, 200 mA, 2x1/3 filling mode using a Si (111) double-crystal monochromator. XAFS signals were measured in fluorescence mode at the Mn K edge (6554 eV). The XAFS measurements were carried out *in situ* under dynamic atmosphere with an in-house reactor cell operating at 1 bar [16]. Appropriate amounts of sample were finely crushed and pressed at 2 bar into 0.7 $cm^2$ pellets. The temperature was raised at a rate of 5 ºC/h from RT to 300 and 350 ºC and held for 2 h under flows of 100 ml/min 50% $H_2$/He. After 2 h reduction the catalysts were measured under the same conditions holding the final temperature. EXAFS spectra were measured at the end of each treatment, whilst XANES spectra were recorded continuously throughout the reduction.

Data reduction of experimental X-ray absorption spectra was performed with the program EXBROOK [17]. A pre-edge background subtraction and normalization was carried out by fitting a linear polynomial to the pre-edge region and a cubic spline at the post-edge region of the absorption spectrum. A smooth atomic background was then obtained. EXAFS refinements were performed with the EXCURV98 package [17]. Phase shifts and backscattering factors were calculated *ab initio* using Hedin-Lundqvist potentials. Refinements were carried out using $k^1$ and $k^3$ weighting in the range of 3.5 to 8.5 $Å^{-1}$. The amplitude reduction factors (AFAC parameters) were calibrated from the fit of the Mn metal foil, which was fixed at 0.80.

*Scanning transmission electron microscopy with electron energy loss spectroscopy*

Scanning transmission electron microscopy with electron energy loss spectroscopy (STEM-EELS) experiments were performed on reduced/passivated catalysts. The oxidized

$Co/Mn/TiO_2$ samples were firstly dried in a flow of air at 120 °C for 30 min. Subsequently, the flows were brought to 50 % $H_2$/He and the temperature was raised from 120 to 350 °C at a rate of 5 °C/min. After 2 h reduction, a passivation was carried out at 150 °C in a 5 % $CO_2$/He flow during 30 min. The activated catalysts were powdered, ultrasonically dispersed in ethanol, and finally dropped on a holey amorphous carbon film supported on a copper grid. The oxygen K edge and the titanium, manganese, and cobalt $L_{2,3}$ edges were monitored using a 100 keV STEM instrument (VG HB 501) equipped with a field emission source and a parallel Gatan 666 EELS spectrometer. The instrument was in operation in Orsay and produced EELS spectra with 0.5 eV energy resolutions and sub-nanometer spatial resolution of 0.3 nm, within a typical acquisition time less than a second per pixel. For details concerning the experimental set-up we refer to the work of Stephan *et al.* [18]. After scanning the sample, appropriate areas were selected for measuring detailed 2D TEM-EELS images. For each of the reduced/passivated samples we have investigated six chemical maps containing from eight to twelve cobalt nanoparticles.

*X-ray photoelectron spectroscopy*

X-ray photoelectron spectroscopy (XPS) data were collected with a Vacuum Generators system, using a CLAM-2 hemispherical analyzer for electron detection. Non-monochromatic Al ($K_\alpha$) X-ray radiation was used, employing an anode current of 20 mA at 10 keV. XPS measurements were performed before and after *in-situ* reduction treatments in a $H_2$ flow at 350 °C for 2 and 4 h inside a reaction chamber. This chamber was connected to the vacuum system of the spectrometer allowing the samples to be transferred into the measurement chamber without exposure to air after the $H_2$ treatments. The binding energies obtained for $Co_{2p}$, $Ti_{2p}$, and $Mn_{2p}$ photoelectron peaks were corrected for charge shifts using the $C_{1s}$ = 285 eV peak as reference. The intensities of the 2p peaks of the three elements (Co, Ti and Mn) were used for quantitative analysis to calculate the atomic ratios of the elements, assuming the composition of the samples to be uniform throughout the area probed by XPS. To calculate the 2p peak areas of the three elements, backgrounds were subtracted according to the procedure suggested by Shirley [19]. These areas are proportional to the number of photo electrons produced for a given flux of incoming X-rays ($\phi_x$), the number of incident X-ray photons per $cm^2$ s. The number of photoelectrons (N) produced per $\phi_x$ depends only on the material constants:

$$\frac{N}{\phi_x \mathrm{A}} = \sigma\rho\lambda$$

Where A is the probed area of the sample, σ is the cross section for photoionization, ρ the atomic density, and λ the inelastic mean free path, provided that only electrons perpendicular

to the surface are detected. For an infinitely thick sample $I_{obs}$ is defined as the observed intensity, which can be calculated for any chemical compound knowing the σ (tabulated for all chemical compounds), ρ and λ. Thus, the atomic ratio of a given element A and B can be calculated from:

$$\frac{\rho^{A}}{\rho^{B}} = \frac{I^{A}_{OBS}}{I^{B}_{OBS}} \frac{ASF^{B}}{ASF^{A}}$$

Where ASF are the sensitivity factors calculated with the cross section values published elsewhere [20] according to the formula:

$$ASF = \sigma\lambda \frac{1}{\sqrt{E_{Kin}}\,(eV)}$$

*Fischer-Tropsch catalytic measurements*

The catalysts were tested in the FT reaction using a stainless steel reactor (volume of about 1 ml) designed to enable the operation of up to 6 reactors, which can be stacked on top of each other (Fig. 1). In this reactor feed gases are supplied from the top of the reactor over the catalyst, while the products leave the reactor also at the top. Silco steel treatments of the inner side of the reactor were applied to make it virtually inactive. The reaction temperature was measured with a Chromel/Alumel thermocouple. The samples were activated in a $H_2$ flow at 300 ˚C for 1 h. The reaction was carried out at 220 °C, $H_2$/CO ratio of 2, and at pressures of 1, 4, 8 and 18 bars. The residence time was kept constant by adjusting the inlet syngas flow at 1, 4, 8 and 18 ml/min, respectively. In this way, the CO conversions were kept low (< 1%) in order to operate under real differential conditions and to prevent condensation of high weight products. The product composition was analyzed on-line using a Chrompack-9001 gas chromatograph equipped with a Poraplot Q column for separation of $C_1$ to $C_5$ and a CP-Sil-5 column for separation of $C_6$ to $C_{20}$, and flame ionization detectors (FID). Results were evaluated by means of Co-time yield ($10^{-6}$ mol CO (g Co)$^{-1}$ s$^{-1}$) and selectivity expressed in percentages of CO conversion to $CH_4$ and $C_{5+}$ fraction of products.

## Results and discussion

### *Manganese chemical state in the reduced Co/Mn/$TiO_2$ catalysts*

The electronic state of manganese was investigated by XANES after the *in situ* reduction treatments. Fig. 1 presents the first derivative spectra of the XANES obtained for all the catalysts after reduction at 300 and 350 °C, along with the MnO reference material. It can be observed that all the XANES spectra display a maximum of the first derivative at 6547.9 eV as the MnO material. This indicates that a pure $Mn^{2+}$ oxidation state is present in all reduced catalysts independently of the reduction temperature. However, the XANES spectrum of MnO shows much more structure whilst the maximum of its first derivative is divided into two peaks. This difference in the general shape of the spectra of the catalysts with that of bulk MnO clearly points out the amorphous and dispersed character of the manganese phase, which has a 2+ valence although a different local structure. Below we will show that the local structure of manganese belongs in all cases to a combination of tetrahedral coordination as in $Ti_2MnO_4$, and octahedral coordination as in MnO.

The local environment around manganese (i.e., number and distances of neighboring atoms) was determined by EXAFS. The Fourier transforms for all the reduced catalysts are presented in Fig. 2. The spectra exhibit a very short-range order, since only a main peak at 2.0-2.2 Å corresponding to a Mn–O coordination shell can be observed, whereas a second Mn–Mn shell that appears at ca. 3.0 Å is in most cases very weak or even negligible. As the XANES analysis has already showed, this is a clear indication of a high level of disorder,

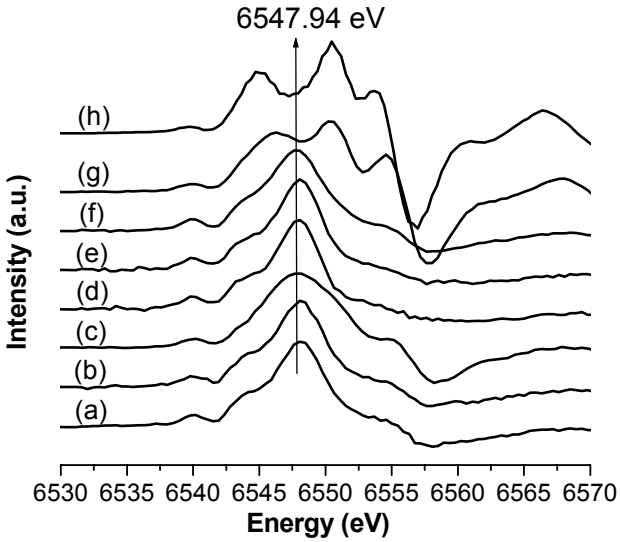


**Figure 1.** First derivative of the XANES at the Mn K-edge for the I-CoMn (a), I-MnCo (b), and H-CoMn (c) reduced at 300 °C and I-CoMn (d), I-MnCo (e), H-CoMn (f), and Hcop-CoMn (g) reduced at 350 °C and a MnO material (h).

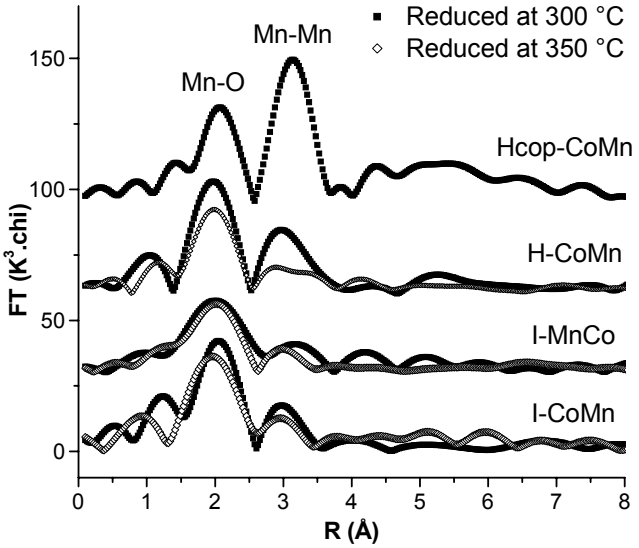


**Figure 2.** $k^3$-weighted Fourier transforms of the experimental EXAFS spectra at the Mn K-edge for the I-CoMn, I-MnCo, H-CoMn and Hcop-CoMn catalysts after 2 h reduction at 350 °C and 300 °C.

pointing to the existence of highly dispersed manganese phases. Furthermore, the level of manganese dispersion is related to the cobalt reduction extent, since the catalysts with the highest reduction extents (chapter 4) exhibit the shortest-range order around the Mn atoms. For this reason, the catalysts reduced at 300 °C generally lead to a more intense Mn–Mn peak than after reduction at 350 °C. The exception is the Hcop-CoMn catalyst, which features two intense peaks due the presence of a more bulk-type phase.

The coordination parameters obtained by the R-space analysis of the EXAFS data of all the catalysts are summarized in Table 4, along with the crystallographic data of MnO and $Ti_2MnO_4$ materials [21] included for comparison. The coordination numbers and inter-atomic distances obtained for the Mn–O and Mn–Mn shells vary significantly from one catalyst to another. Coordination numbers of the Mn–O shell range between 5.6 and 4.1, whereas the Mn–O distances vary from 2.15 Å to 2.04 Å. Comparison of these values with those corresponding to the MnO and $Ti_2MnO_4$ compounds indicates that Mn atoms possess an average oxygen coordination consisting of a combination of four-fold and six-fold coordination, indicating the formation of mixtures of both types of structures. Both MnO and $Ti_2MnO_4$ compounds contain $Mn^{2+}$ ions, the first being in octahedral ($O_h$) and the second in tetrahedral ($T_d$) coordination, respectively [21], which is in good agreement with the XANES results that revealed a $Mn^{2+}$ oxidation state in all samples. Both manganese crystallographic structures existent in the reduced catalysts are illustrated in Fig. 3. The relative fractions of MnO and $Ti_2MnO_4$ can be moreover evaluated by the Mn–O coordination numbers, which range from a minimum of 4.0 for a pure $Ti_2MnO_4$ compound to a maximum of 6.0 for a pure

**Table 1.** Results of the EXAFS analysis at the Mn K-edge for the catalysts reduced at 300 and 350 °C and for MnO and $Ti_2MnO_4$ reference materials (n.a = not applicable).

| Sample | Red temp (°C) | R (Å) Mn-O | N atoms | $2\sigma^2$ (Å) | R (Å) Mn-Mn | N atoms | $2\sigma^2$ (Å) |
|---|---|---|---|---|---|---|---|
| MnO | n.a | 2.22 | 6.0 O | n.a | 3.14 | 12.0 Mn | n.a |
| $Ti_2MnO_4$ | n.a | 2.02 | 4.0 O | n.a | 3.72 | 4.0 Mn | n.a |
| I-CoMn | 300 | 2.09 | 4.8 O | 0.022 | 3.03 | 1.3 Mn | 0.005 |
| | 350 | 2.04 | 4.1 O | 0.022 | 2.91 | 0.4 Mn | 0.001 |
| I-MnCo | 300 | 2.08 | 5.0 O | 0.030 | 3.05 | 1.5 Mn | 0.032 |
| | 350 | 2.06 | 4.4 O | 0.027 | 3.00 | 0.7 Mn | 0.009 |
| H-CoMn | 300 | 2.07 | 5.3 O | 0.007 | 2.98 | 4.3 Mn | 0.026 |
| | 350 | 2.07 | 5.1 O | 0.027 | 3.04 | 2.3 Mn | 0.025 |
| Hcop-CoMn | 350 | 2.15 | 5.6 O | 0.025 | 3.07 | 11.9 Mn | 0.033 |

MnO. Due to the relatively lower X-ray scattering power of Ti [22] and the highly disordered state of the manganese ions, the contribution of Ti to the Fourier transform was not considered in our fitting process. We also note that the Mn–Ti distances in $Ti_2MnO_4$ are 3.57 Å [21], which are much longer than the distances found for the catalysts by EXAFS. Hence, the second Mn–Mn shell observed is merely attributed to the presence of MnO species and decreases in intensity when more $Ti_2MnO_4$ is formed during reduction. The Mn–Mn coordination numbers are therefore, indicative of the fraction of manganese present in the form of MnO. Based on these observations, the amounts of MnO and $Ti_2MnO_4$ present in all the reduced catalysts could be estimated.

The lowest coordination number for the Mn–O shell was obtained for the I-CoMn catalyst reduced at 350 °C. In this catalyst manganese features almost pure four-fold coordination (4.1 O), with distances of 2.04 Å and a very weak Mn–Mn shell at 2.91 Å with only 0.4 Mn neighboring atoms. As already discussed in a previous study [23], these data reveal that manganese belongs almost entirely to a $Ti_2MnO_4$-type phase. This $Ti_2MnO_4$ is expected to exist in a highly dispersed state over the $TiO_2$ support as suggested by the very weak Mn–Mn peak, and by the relatively flat profile of its XANES spectrum. Similar results were obtained in the I-MnCo catalyst reduced at 350 °C although the obtained values suggest that the amount of titanate is somewhat lower. This data confirms that a variable amount of $Ti_2MnO_4$

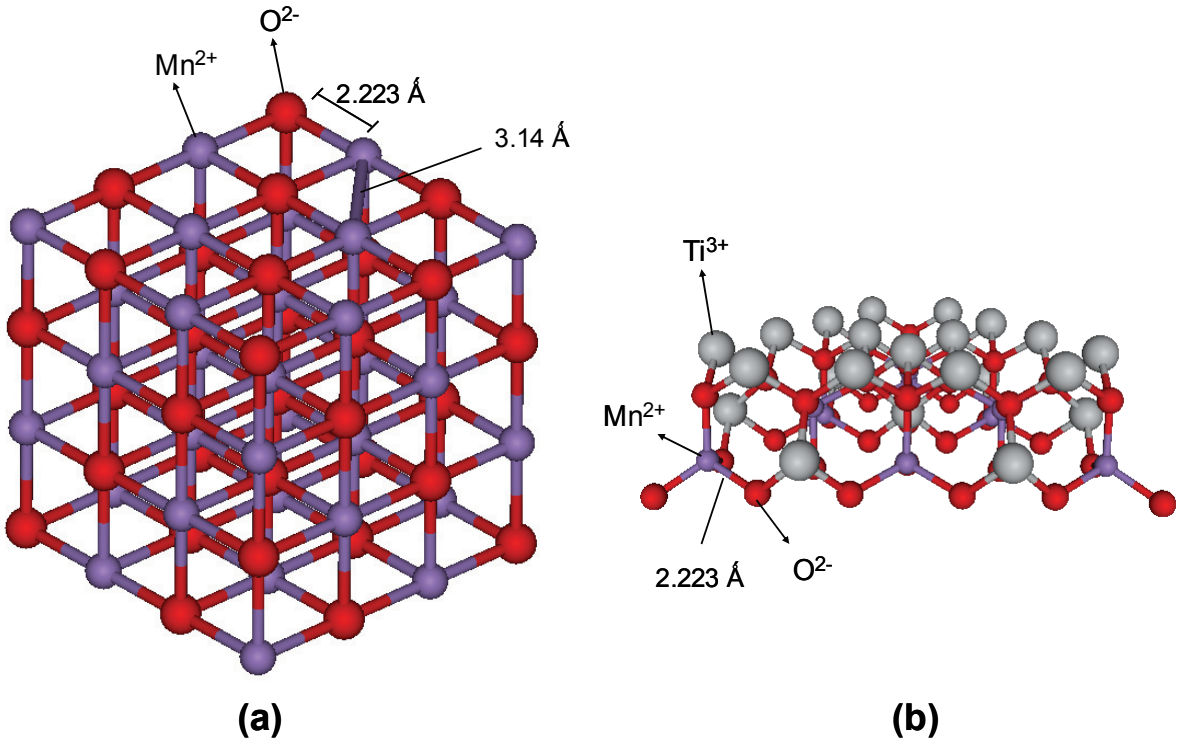


**Figure 3.** Crystallographic structure of MnO with $Mn^{2+}$ in $O_h$ sites (A), and $Ti_2MnO_4$ (B) with $Mn^{2+}$ in $T_d$ sites. The figures illustrate several unit cells for both structures including the Mn-O distances.

phase is present in the reduced catalysts, being formed in larger amounts after reduction at 350 °C, as indicated by the lower Mn–O and Mn–Mn coordination numbers and the slightly shorter Mn–O bonds. In I-CoMn reduced at 300 °C, the Mn–O distances of 2.09 Å and 0.9 Mn neighboring atoms point towards the presence of more MnO and less $Ti_2MnO_4$ than after reduction at 350 °C. In general the amounts of MnO present in the IWI catalysts are found to be small indicating that manganese should exist mostly in the form of a $Ti_2MnO_4$ layer at the surface of $TiO_2$.

Very different results were obtained for the Hcop-CoMn catalyst, in which manganese features nearly a six-fold coordination with longer inter-atomic distances (2.15 Å) than in all the other catalysts. Additionally, a second Mn–Mn shell with 11.6 atoms at 3.07 Å was obtained. Although these data are very similar to the structural parameters of bulk MnO material, the Mn–O and Mn–Mn bond distances (2.15 and 3.07 Å) are significantly shorter than in the MnO reference material (2.20 and 3.14 Å). These results combined with the XANES analysis that showed the presence of a pure $Mn^{2+}$ oxidation state, as well as in the EXAFS results at the Co K-edge (chapter 4) that revealed the occurrence of longer Co–O and Co–Co bonds than in pure CoO, strongly suggests the formation of a MnO-CoO solid solution. Indeed, it is well known in literature [22] that since MnO and CoO have similar

cubic rock-salt structures, they readily form rock-salt solid solutions of the type $Mn_{1-x}Co_xO$ over a full range of compositions ($0 < x < 1$). Since $Co^{2+}$ is smaller than $Mn^{2+}$ [24], the progressive incorporation of $Co^{2+}$ into the MnO structure by substitution of the $Mn^{2+}$ sites is accompanied by a linear decrease of the cell parameter from 4.446 Å to 4.263 Å, when x increases in $Mn_{1-x}Co_xO$ from 0 to 1. This would perfectly account for the shortening of the Mn–O and Mn–Mn distances observed in this catalyst relative to those in the bulk MnO material. The cell parameters for different x values in the rock salt $Mn_{1-x}Co_xO$ solid solutions as obtained by XRD calculation [22] are gathered in Table 3, along with the theoretical bond distances. A simulation of the x value corresponding to the bond distances found in Hcop-CoMn (2.15 and 3.07 Å) gives for this catalyst a stoichiometry close to $Mn_{0.25}Co_{0.75}O$.

**Table 3**. Chemical and structural data for various rock-salt monoxides with different compositions (M = Co or Mn).

| X ($Mn_{1-x}Co_xO$) | Cell parameter (Å) | M–O (Å) | M–M (Å) |
|---|---|---|---|
| 0.000 | 4.446 | 2.223 | 3.144 |
| 0.319 | 4.375 | 2.187 | 3.093 |
| 0.472 | 4.352 | 2.176 | 3.077 |
| 0.625 | 4.316 | 2.158 | 3.052 |
| 1.000 | 4.263 | 2.131 | 3.014 |

In the H-CoMn sample reduced at 350 °C the Mn–O average distance of 2.07 Å and the number of manganese neighboring atoms of 2.3 indicate that manganese is partially present as $Ti_2MnO_4$ and $MnO/Mn_{1-x}Co_xO$ mixtures. The same catalyst reduced at 300 °C contains more $MnO/Mn_{1-x}Co_xO$ phases, as can be concluded from the higher Mn–Mn coordination number of 4.3. However, the Mn–O distance remains the same (2.07 Å) regardless the reduction temperature, suggesting that the amount of $Mn_{1-x}Co_xO$ is increased or the amount of $Co^{2+}$ incorporated in the solid solution is higher. This effect of the reduction temperature is closely related to the cobalt reduction extent. Since the reduction extent is much lower at 300 °C, the mixing of CoO with MnO is enhanced.

The overall results indicate that the formation of MnO and $Mn_{1-x}Co_xO$ phases takes place in the catalysts prepared by HDP to a greater extent than in the IWI catalysts, which generally contain larger amounts of $Ti_2MnO_4$-type phases, as revealed mainly by the lower number of Mn neighboring atoms. Nevertheless, the very short Mn–Mn distances (ranging between 2.98 to 3.05 Å) suggest that a large relative amount of cobalt is mixed with the MnO in the IWI

catalysts, and therefore they likely contain $Mn_{1-x}Co_xO$ solid solutions with a very high value of x. Hence, these finding suggest that a dispersed manganese species are also covering the cobalt surface in the IWI catalysts, resulting in the formation of $Mn_{1-x}Co_xO$ solutions.

To conclude, it is found that all catalysts form mixtures of a $Ti_2MnO_4$ dispersed phase and $Mn_{1-x}Co_xO$ solid solutions with variable x values, ranging from pure MnO to $Mn_{1-x}Co_xO$ rich in cobalt. An exact quantification of these phases, however, has not been attempted, since the manganese exists heterogeneously distributed on the catalyst surface.

***Location of manganese as investigated by STEM-EELS***

Chemical maps based on EELS spectra were used to investigate the physical state and location of the manganese compounds in the catalysts after reduction. Fig. 4, 5, 6 and 8 show several greyscale chemical maps of the Ti, Co and Mn elements obtained for each of the reduced $Co/Mn/TiO_2$ catalysts. These chemical maps exhibit a luminosity proportional to the number of given atoms encountered by the electron beam in each sub-area, and thus, provide valuable information on the Co, Mn, and Ti elemental distributions in the scanned areas. Additionally, colored chemical maps were produced by overlapping the individual Ti, Co, and Mn chemical maps, which were previously colored in green, red and blue, respectively.

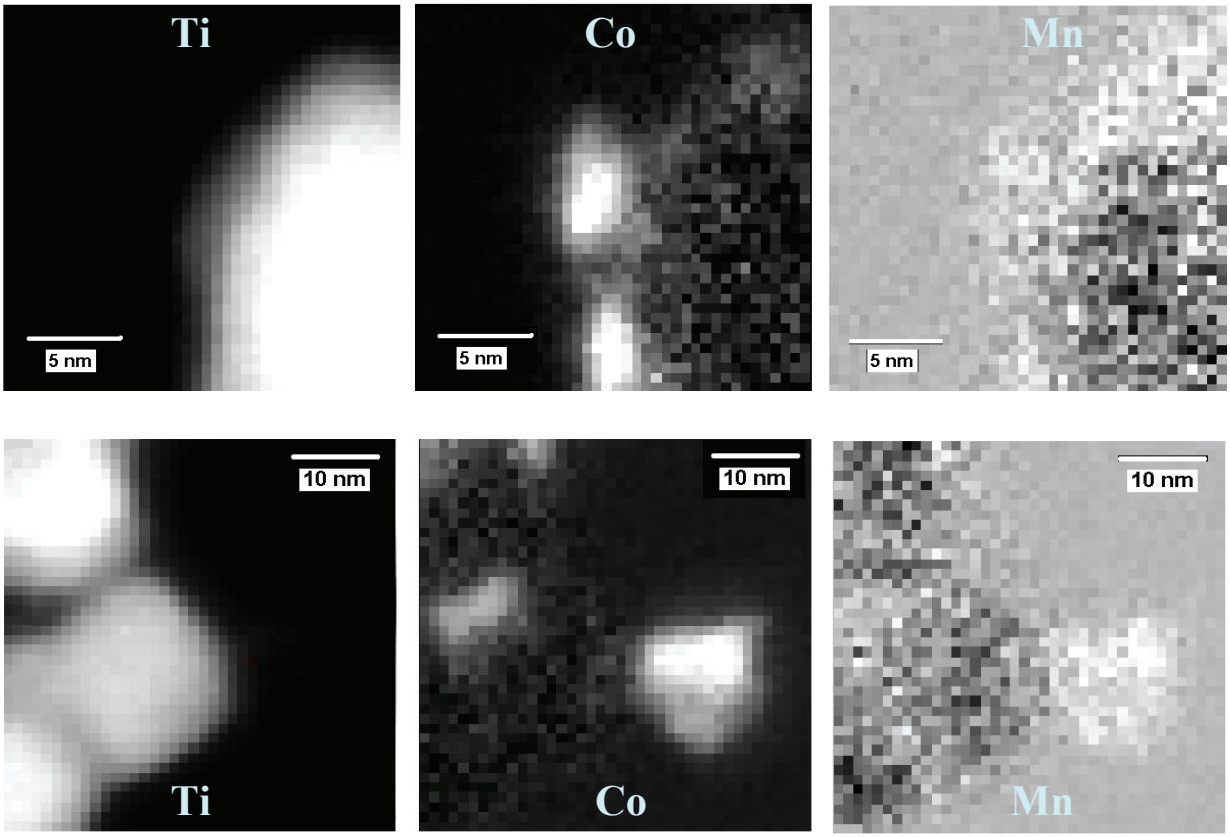


**Figure 4.** Grayscale EELS Ti L-edge, Co L edge, and Mn Ledge, chemical maps for the for the I-CoMn catalyst after reduction and passivation in two different areas (top and bottom). The images were recorded with a spatial increment of 1 and 2 nm, respectively.

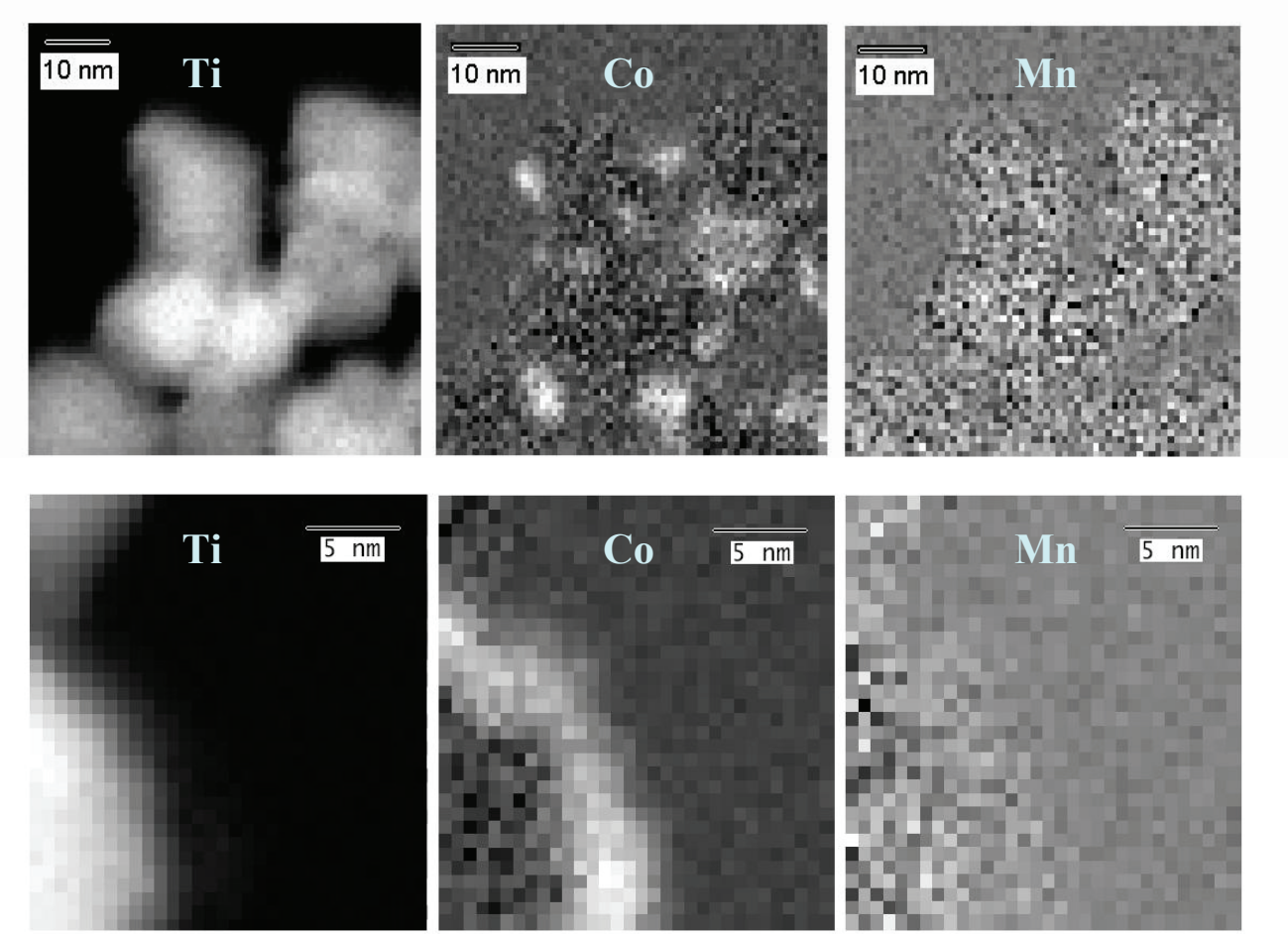


**Figure 5.** Grayscale EELS Ti L-edge, Co L edge, and Mn Ledge, chemical maps for the for the I-MnCo catalyst after reduction and passivation in two different areas (top and bottom). The images were recorded with a spatial increment of 1 and 2 nm, respectively.

The colored chemical maps for the reduced catalysts are presented in the Appendix A (p. 169-171), enabling a more straightforward evaluation of the manganese and cobalt interactions in the various catalysts.

Fig. 4 shows two greyscale chemical maps obtained for I-CoMn. In the first example (Fig. 4 top), two very small cobalt particles of around 5 nm are visualized at the surface of the $TiO_2$, whilst the Mn signal is detected in small concentrations covering the $TiO_2$ surface. We note that the highly dispersed manganese phase is difficult to visualize in the chemical maps due to the low signal/noise ratio, and for this reason an evaluation of the EELS spectra is required to evidence its existence in a given sub-area. The presence of manganese mainly at the external surface of the $TiO_2$ particle was confirmed by analysis of the EELS spectra, which revealed a weak Mn signal localized in those areas. In the other chemical map (Fig. 4 bottom), a large supported cobalt particle of around 10 nm can be visualized, while other smaller cobalt particles are superimposed with the $TiO_2$ material. Interestingly, the Mn signal

is also detected at the same sub-areas as cobalt, as well as at the $TiO_2$ surface. This result is rather surprising, since the formation of Co/Mn mixed oxides is not expected to occur in this catalyst to a great extent, as previously indicated by EXAFS. In fact, EXAFS revealed for the I-CoMn catalyst a $Ti_2MnO_4$-type phase as the major compound, and hence, only minor amounts of manganese would be expected mixed with the cobalt. A possible cause of this result is likely related to an effect of the passivation, since the re-oxidation of the cobalt surface may favor the mixing of MnO and CoO. This also suggests that the $Mn^{2+}$ species are mobile and can undergo a migration from the $TiO_2$ surface towards the cobalt surface upon passivation. Nevertheless, a careful evaluation of the overall chemical maps for I-CoMn (Appendix, p. 169) indicates that the manganese phase is more often localized at the $TiO_2$ surface, rather than decorating the $Co^0$ particles.

Two EELS chemical maps illustrating the situation for the I-MnCo sample are presented in Fig. 5. These results show a high resemblance with the previous catalyst, the visualization of manganese being rather difficult due to the low signal to noise ratio. The manganese appears to be highly dispersed, as observed in Fig. 5 (top). This chemical map reveals a very diffuse Mn signal in all the areas corresponding to $TiO_2$. In the same region, several supported cobalt particles with sizes of ~3-7 nm can be distinguished. In Fig. 5 (bottom), a cobalt aggregate can be seen in the form of a layer with a thickness of around 3-5 nm covering the $TiO_2$ surface. Although the Mn chemical map does not provide a clear visualization of the manganese phase, the EELS spectra show that a very weak Mn signal is present in the same sub-areas as the cobalt layer, suggesting the incorporation of small amounts of manganese into the CoO phase. Because of the low manganese loadings in most of the catalysts, we considered a reliable quantitative determination of the concentration to be infeasible.

The combined information obtained by STEM-EELS and EXAFS indicate that in the IWI catalysts reduction leads to a spreading of manganese over the $TiO_2$ surface, which results in the formation of a highly dispersed $Ti_2MnO_4$-type phase. Additionally, some small amounts of MnO can also interact with the Co particles to form a mixed CoO/MnO phase (i.e., $Mn_{1-x}Co_xO$ solid solutions). The small size of the cobalt particles visualized in the chemical maps is also in line with the TEM results presented in chapter 4, confirming the presence of particles of around 5.0 nm.

A very different situation was found for the HDP catalysts with respect to their cobalt particle size distribution and their cobalt-manganese interaction. Fig. 6 presents the elemental chemical maps obtained for the reduced H-CoMn sample. Three large supported cobalt clusters can be observed on the $TiO_2$ surface with variable sizes of around 12-16 nm. In general terms, the size of the cobalt particles was found to be much larger for the HDP catalysts than for the other group (see also Appendix). On the other hand, Fig. 6 reveals the

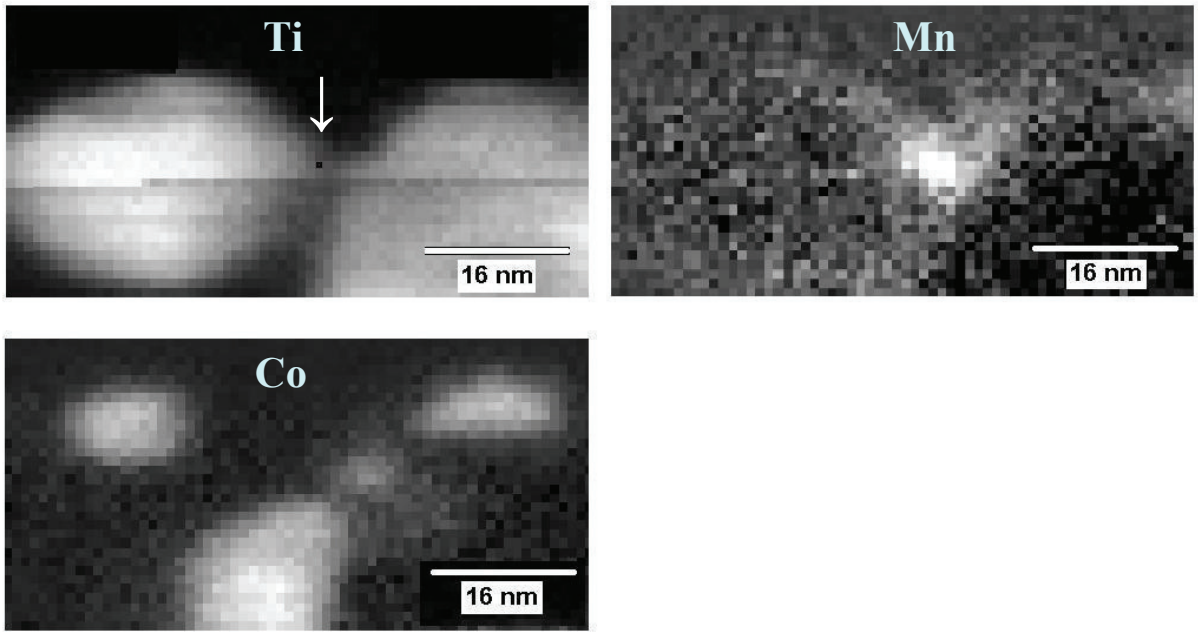


**Figure 6.** Grayscale EES Ti L-edge, Co L edge, and Mn Ledge, chemical maps for the for the I-MnCo catalyst after reduction and passivation in two different areas (top and bottom images). An arrow shows the starting point and direction of the line scan presented in Fig. 7.

presence of a manganese agglomerate clearly distinguished in the vicinity of the cobalt particles. The image also shows a more diffuse Mn signal covering at the $TiO_2$ surface, which indicates also the existence of a manganese dispersed phase. Taking into account the EXAFS results the two identified manganese phases can be ascribed to; (1) a $Ti_2MnO_4$-type phase highly dispersed at the $TiO_2$ surface, and (2) an agglomerate of MnO present in the proximity of the cobalt phase. In addition, a Mn signal is also detected in the same sub-areas as cobalt, indicating that it is also mixed at the surface of the Co particles in the form of $Mn_{1-x}Co_xO$ solutions. To evaluate the relative intensity of each element, a line scan was carried out along the chemical map of Fig. 6. This line scan is plotted in Fig. 7 and runs from top to bottom, as indicated with an arrow. As observed, the Mn signal is fairly associated with the $TiO_2$, given that their intensity profiles follow a similar trend, whereas the Co signal is more associated with the absence of $TiO_2$ material. However, a clear interface between cobalt and manganese is observed, confirming a certain Co-Mn association in the H-CoMn catalyst after reduction. A weak Mn signal is also detected along the cobalt particle pointing out the presence of manganese species mixed with the cobalt particle.

The EELS results obtained for the reduced Hcop-CoMn sample are shown in Fig. 8. The chemical map shows a very large cobalt cluster (> 20 nm) localized at the edge of the $TiO_2$ particle. Remarkably, the Mn signal is clearly present in the same sub-areas as cobalt. This result demonstrates the existence of CoO and MnO mixtures in the reduced Hcop-CoMn catalyst, in agreement with the EXAFS results.

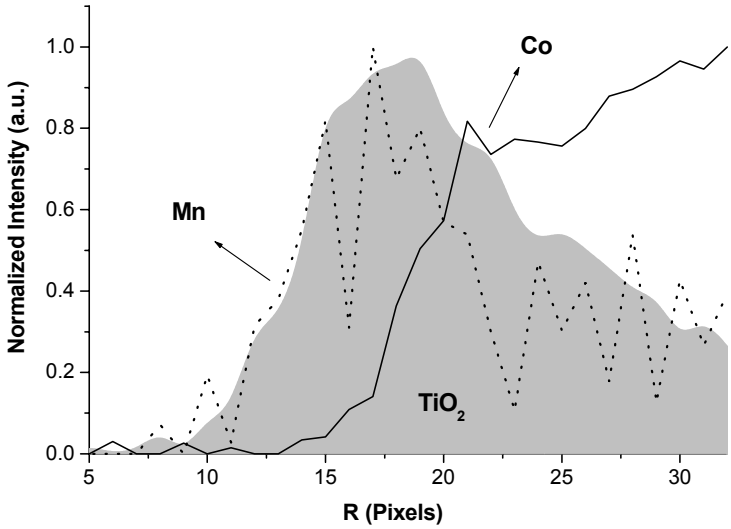


**Figure 7.** Line scans carried uot on the EELS images of presented in Fig. 7. The scan is a vertical line, which runs from top to bottom. The intensities of Ti, Mn, and Co have been normalized to 1 and the area below the $TiO_2$ curve is filled with gray to indicated the surface topography.

Finally, to summarize the STEM-EELS results have shown that the size of the cobalt particles is much larger in the HDP catalysts than in the IWI catalysts. On the other hand, the combined STEM-EELS and EXAFS results have indicated that in the H-CoMn catalyst manganese exists as variable mixtures of $Ti_2MnO_4$ and $MnO/Mn_{x-1}Co_xO$, the later being in the proximity of the cobalt particles and also covering the cobalt surface. In the case of the Hcop-CoMn catalyst the results have clearly shown that $Mn_{x-1}Co_xO$ solutions compose the bulk cobalt particle. These findings are in excellent agreement with the results reported in

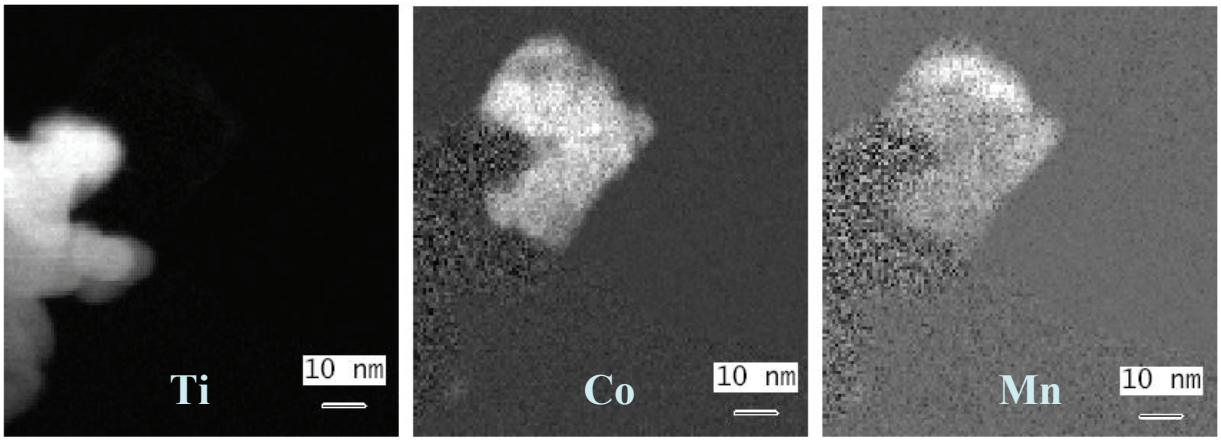


**Figure 8.** Grayscale EELS Ti L-edge, Co L edge, and Mn Ledge, chemical maps for the for the Hcop-CoMn catalyst after reduction and passivation.

chapters 3 and 4, in which it was shown that the reducibility of the Hcop-CoMn material was largely suppressed as a result of the incorporation of manganese into the $Co_3O_4$ structure after calcination. This also accounts for the low cobalt reducibility of the Hcop-CoMn catalyst compared to all other catalysts (chapter 4).

An overview of the major manganese phases formed in the Co/Mn/$TiO_2$ catalysts after reduction is illustrated in Fig. 9. As observed, the IWI catalysts contain the highest amount of a $Ti_2MnO_4$-type phase covering the $TiO_2$ surface in a highly dispersed state. Little amounts of manganese species have also been found to exist in these catalysts at the cobalt surface forming rock salt solid solutions (i.e., $Mn_{1-x}Co_xO$). On the other hand, the H-CoMn catalyst is represented in Fig. 9 containing a mixture of $Ti_2MnO_4$ and MnO phases, the later being concentrated close to the cobalt in the form of small clusters as well as partially mixed with the CoO at the surface of the cobalt particles in the form of $Mn_{1-x}Co_xO$ solutions. The amount of $Mn_{1-x}Co_xO$ phase in the H-CoMn catalysts is, moreover, significantly greater than in the IWI catalysts. Finally, the Hcop-CoMn catalyst contains the highest amount of $Mn_{1-x}Co_xO$, which is more homogeneously distributed in the $TiO_2$-supported particles.

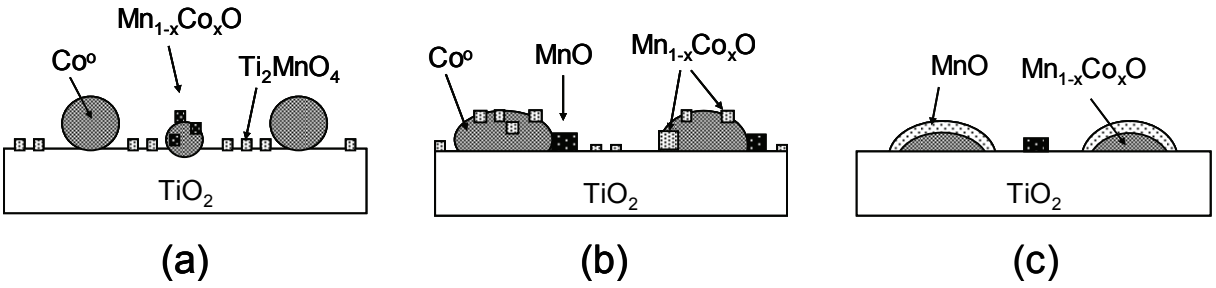


**Figure 9.** Schematic representation of the I-CoMn and I-MnCo (a), H-CoMn (b), and Hcop-CoMn (c) catalysts with the Mn composition and locations as expected from the EXAFS results.

***Migration of manganese species towards the $TiO_2$ surface***

To investigate the changes in manganese dispersion occurring throughout the reduction of the H-CoMn catalyst, the XPS spectra collected before and after *in situ* reduction treatments were used quantitatively and compared with the unpromoted Co/$TiO_2$ counterpart. As shown in chapter 3, the H-CoMn catalyst before reduction contains a $MnO_2$ phase associated with the $Co_3O_4$ particles. Additionally, some amounts of $Mn^{3+}$ were also found to exist partially mixed as $Co_{3-x}Mn_xO_4$ solid solutions at the interface of both compounds. Since manganese cannot be reduced to a $Mn^0$ state under the conditions employed, it will always remain as an oxide. Therefore, it is expected that reduction from $Co_3O_4$ to cobalt metal would cause the migration of the MnO species towards the $TiO_2$ surface, due to a higher affinity with an oxide. This

manganese migration was investigated by quantitative XPS comparing the Co/Ti and Mn/Co atomic ratios obtained for a $Co/TiO_2$ and $Co/Mn/TiO_2$ catalysts during the reduction process.

The Co 2p XPS spectra for the H-Co and H-CoMn catalysts after 4 h reduction are shown in Fig. 10. The spectra feature two sharp peaks attributed to the Co $2p_{3/2}$ and Co $2p_{1/2}$ photoelectron transitions with a maximum at 778.1 and 793.2 eV, respectively. These energy values and spectral shapes correspond to a $Co^0$ oxidation state, as previously reported in other work [25], indicating that reduction to $Co^0$ was achieved in both catalysts to a high extent. However, the presence of a shoulder at higher energies (~ 6 eV) in both spectra suggests also the existence of some unreduced cobalt phase. This shoulder is, moreover, more pronounced for the H-CoMn catalyst pointing to a lower reduction extent achieved at the cobalt surface in to the presence of MnO. This result is perfectly in line with the reduction studies reported in chapter 4, which revealed a decrease of the bulk cobalt reducibility in the catalysts containing manganese.

To investigate the changes in the surface composition of the H-Co and H-CoMn catalysts during the reduction process the elemental atomic ratios were compared before and after reduction. In Table 4 the Co/Ti, Mn/Co and Mn/Ti atomic ratios for both catalysts after calcination and after 2 and 4 h of reduction are given. Before reduction a lower Co/Ti ratio is obtained for the Mn-promoted catalyst (0.24 compared to 0.32) suggesting a physical association of $Co_3O_4$ and $MnO_2$ or a coverage of $Co_3O_4$ by $MnO_2$. This effect would account for the lower Co/Ti ratio in H-CoMn since the coverage of cobalt by $MnO_2$ would certainly lead to a weaker cobalt XPS signal. This result is in line with STEM-EELS (chapter 3), in which the occurrence of physical and chemical associations was demonstrated.

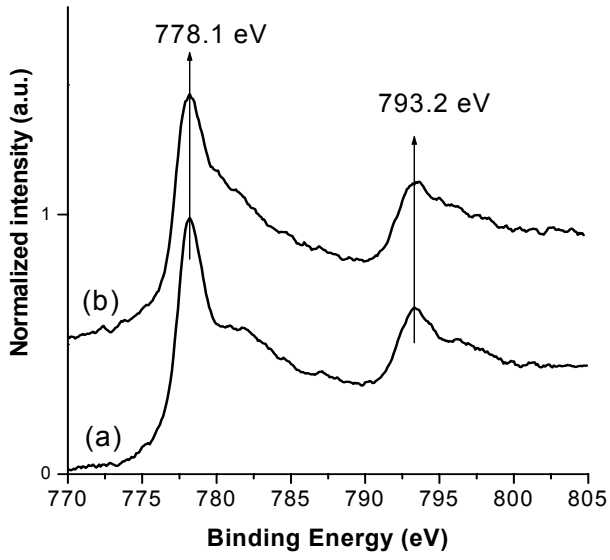


**Figure 10.** Co 2p core-level spectra of the H-Co (a) and H-CoMn (b) catalysts after 4 h reduction in $H_2$ flow at 350 °C.

**Table 4.** XPS elemental atomic ratios in the H-Co and H-CoMn catalysts before and after 2 h and 4 hours reduction at 350 ºC.

| | H-Co | H-CoMn | | |
|---|---|---|---|---|
| **Atomic ratio** | **Co/Ti** | **Co/Ti** | **Mn/Co** | **Mn/Ti** |
| After calcination[a] | 0.32 | 0.24 | 0.54 | 0.13 |
| After reduction[b] 2 h | 0.25 | 0.27 | 0.86 | 0.22 |
| After reduction[b] 4 h | 0.24 | 0.28 | 0.88 | 0.25 |

[a]In airflow at 400 °C, [b]In $H_2$ flow at 350 °C.

The Co/Ti ratios change differently in both catalysts upon the reduction treatment. In the H-Co catalyst the Co/Ti ratio decreases from 0.32 to 0.24 after 4 h reduction. This decrease is expected according to the increase in the cobalt atomic densities and a decrease of the inelastic mean free path of the electrons upon the phase transition from $Co_3O_4$ to $Co^0$, as reported in other work [25]. In the case of the H-CoMn catalyst the reduction has an opposite effect on the atomic ratios, as indicated by the slight increase of Co/Ti from 0.24 to 0.28. This result points to a decrease of the Ti intensity and an increase of the Co intensity upon reduction when manganese is contained in the catalyst. Moreover, the Mn/Co and Mn/Ti ratios are largely increased as a function of the reduction time, as a result of an increase of the Mn signal. Hence, these changes in the atomic ratios are likely related to the enrichment of the manganese species at the $TiO_2$ surface after reduction that leads to an increase of the Mn/Co, Mn/Ti and Co/Ti ratios. This fact can be explained by the migration of manganese species towards the support as soon as the $Co_3O_4$ is reduced to $Co^0$. Since the manganese remains in a $Mn^{2+}$ state, it has a higher affinity for an oxidic phase than for the cobalt metal. This migration from the $Co^0$ particles results in an increase of the Co signal, since there is more available cobalt surface. As revealed by EXAFS and STEM-EELS, reduction leads to the formation of MnO clusters in the proximity of the cobalt particles, as well as a spreading over $TiO_2$ resultin in the formation of a $Ti_2MnO_4$-type phase. Therefore, the presence of large amounts of MnO in the proximity of the cobalt particles is most likely induced by the initial Co-Mn association in the catalyst precursor (i.e., before reduction).

The $TiO_2$ P25 material used contains around 75 % of anatase phase and at the surface the concentration of coordinatively unsaturated $Ti^{4+}$ ions varies between 4.5 and 7 $Ti^{4+}/nm^2$, whereas the concentration of the insolated $Ti^{4+}$-OH groups is not more than 0.5 $OH/nm^2$ [26-27]. Considering the anchoring sites of $Mn^{2+}$ ions as the hydroxyl groups in the vicinity of the coordinatively unsaturated $Ti^{4+}$ ions, and assuming one $Mn^{2+}$ ion per two $Ti^{4+}$ ions via an

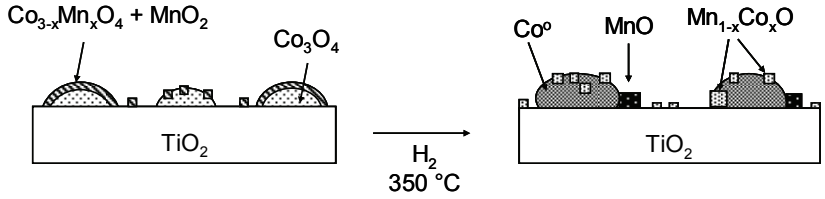


**Figure 11.** Schematic representation of the H-CoMn catalyst before and after the reduction treatment. The reduction leads to a partial migration of MnO towards the $TiO_2$ causing a segregation of the $Mn^{2+}$ species over the surface of $TiO_2$.

oxygen bridge, [28] a monolayer coverage would be reached at around 1.9 wt% manganese loading. Hence, in the H-CoMn catalyst containing more than 2 wt% manganese loading, the monolayer coverage could be easily reached. This argument accounts for the dramatic increase in the Mn/Co and Mn/Ti atomic ratios, since a covering of the $TiO_2$ surface by manganese causes a large decrease of the Ti signal. Furthermore, this effect is indicative of the occurrence of a strong Mn-$TiO_2$ interaction as suggested in the literature [28]. As revealed in this work, the strong Mn-$TiO_2$ interaction results from a partial reduction of the $TiO_2$ surface leading to the formation of $Ti_2MnO_4$ compounds. Nevertheless, a fraction of manganese remains in the form of small MnO clusters in the vicinity of the cobalt and largely mixed at the cobalt surface as $Mn_{1-x}Co_xO$ solutions.

The migration of the manganese phase occurring in the H-CoMn catalyst during $Co_3O_4$ reduction to Co metal is illustrated in Fig. 11. As observed, manganese forms different compounds over the catalyst surface.

***Fischer-Tropsch catalysis at various pressures***

The catalytic performances of the H-Co and H-CoMn catalysts were compared after 22 h of reaction at 1 bar, and consecutively after 8 h at 4, 8 and 18 bar. The activity was calculated as the % CO converted into hydrocarbons without taking into account other side reactions (i.e., $CO_2$ formation). The catalytic results for both catalysts at the different pressures are presented in Table 5. As observed, the H-CoMn catalyst exhibit higher Co-time yields than the H-Co catalyst at all pressures. The activity slightly increases by raising the pressure from 1 to 18 bar for both catalysts, yielding values of Co-time yield respectively of 2.2 and 2.5 $10^{-6}$ mol CO g $Co^{-1}s^{-1}$ for H-Co, and of 3.2 to 4.0 $10^{-6}$ mol CO g $Co^{-1}s^{-1}$ for H-CoMn. These higher activities of the H-CoMn catalysts are not caused by a higher cobalt dispersion, since it was previously found (chapter 4) that H-CoMn contains larger $Co^0$ particles with average size of 5.3 nm. For the H-Co catalyst, average particles of 3.2 nm were found. Hence, the increase in Co-time yield is inherent to the larger particles, which lead to a higher intrinsic CO

hydrogenation activity. On the other hand, the H-CoMn catalyst displays higher $C_{5+}$ selectivities and lower $CH_4$ productions. This shift in selectivity is accompanied by an increase in the chain growth probability ($\alpha$) at all pressures (e.g., from 0.69 to 0.71 at 1 bar and from 0.79 to 0.83 at 18 bar). The paraffin to olefin ratios increase with increasing reaction pressures and slightly decrease in the presence of MnO.

The results point towards a different favorable termination path of the growing alkyl chain during FT reaction upon incorporation of manganese in the catalyst material. We attribute the suppression of $CH_4$ formation to a decrease of the hydrogenation rate, which favors the formation of higher hydrocarbons ($C_{5+}$). This phenomenon appears to be related to the lower ability of the MnO-promoted catalyst to chemisorb hydrogen that is affected by the higher amount of $Co^{\delta+}$ in the actived material, since it has been demonstrated that the MnO indeed exists mixed at the surface of the cobalt particles decreasing the amount of metallic surface. Finally, higher olefin selectivities (i.e., lower propane/propene ratio) were obtained for the MnO-promoted catalyst at all the pressures, pointing to a decrease of the secondary hydrogenation rate during FT reaction. The increase of the pressure also led to an increase in olefin production. Similar relationships between the pressure and paraffin/olefin ratios or $C_{5+}$ selectivity have been previously described in literature [29].

**Table 5.** Fischer-Tropsch catalytic results for the H-Co and H-CoMn catalysts at pressures of 1, 4, 8 and 18 bar.

| Catalyst | Pressure (bar) | Co-time yield[a] | $CH_4$ selectivity (wt %) | $C_{5+}$ selectivity (wt %) | Propane to propene ratio | $\alpha$ values[b] |
|---|---|---|---|---|---|---|
| H-Co | 1 | 2.2 | 29 | 43 | 0.09 | 0.69 |
| | 4 | 2.1 | 28 | 56 | 0.14 | 0.81 |
| | 8 | 2.6 | 32 | 51 | 0.25 | 0.80 |
| | 18 | 2.5 | 32 | 55 | 0.26 | 0.79 |
| H-CoMn | 1 | 3.2 | 24 | 46 | 0.08 | 0.71 |
| | 4 | 2.8 | 22 | 64 | 0.08 | 0.84 |
| | 8 | 3.0 | 26 | 59 | 0.16 | 0.80 |
| | 18 | 4.0 | 27 | 59 | 0.21 | 0.83 |

[a]Co-time yield: $10^{-6}$.mol CO.(g Co)$^{-1}$.s$^{-1}$.
[b]As calculated from the slope between $C_3$ and $C_7$ in the ASF distribution plot, according to the equation $\log W_n/n = \log(\ln^2 \alpha) + n \log \alpha$, where $W_n$ is the weight fraction of the products with $n$ carbon number.

## Conclusions

Manganese can form multiple compounds after catalyst activation either with the $TiO_2$ surface or with the cobalt particles. Reduction of $Co/Mn/TiO_2$ catalysts at 300 and 350 °C result in the formation of $Mn^{2+}$ species, which can exist in the form of MnO agglomerates or as highly disordered $Ti_2MnO_4$-type phase. The latter compounds are not expected to play a role under Fischer-Tropsch reaction and therefore can be regarded as spectator species. The formation of $Ti_2MnO_4$, moreover, implies the occurrence of a partial reduction of the $TiO_2$ surface to $Ti^{3+}$, which is in line with the SMSI phenomena reported in the literature. Manganese is also can also react with the cobalt after reduction and form rock salt $Mn_{1-x}Co_xO$ solid solutions at the surface of the cobalt particles. The reduction temperature plays an important role on the distribution of the manganese phases on the catalysts. Hence, reduction at higher temperatures increases the manganese spreading over the $TiO_2$ leading to more formation of $Ti_2MnO_4$. On the other hand, the MnO and $Mn_{1-x}Co_xO$ compounds remain at the surface of the cobalt particles being able to induce a beneficial effect on the FT catalytic performances, such as improvements in the activity and $C_{5+}$ selectivity. With the above findings we establish for the first time in this type of catalytic systems the chemical structure and spatial location of manganese, which can be of interest for the development of improved Co-based FT catalysts in the near future.

## Acknowledgements

The authors gratefully acknowledge the University de Nord (Paris) for the possibility to perform STEM-EELS measurements. Odile Stephan and Alexandre Gloter are kindly acknowledged for help and support during the STEM-EELS experiments. We thank H. Oosterbeek and H.P. Calis from Shell Global Solutions for the high-pressure catalytic tests. Fig. 1 was kindly provided by H. Oosterbeek.

## References

[1] J.J. Mortensen, B. Hammer, J. Norskov, *Phys. Rev. Lett.,* 1998, **80**, 4333.

[2] J.G. Serafin, A.C. Liu, S.R. Seyedmonir, *J. Mol. Catal., 1998,* **131**, 157.

[3] R.A. van Santen, H.P.C. Kuipers, Adv. Catal., 1987, **35**, 265.

[4] F. Morales, B.M. Weckhuysen, *Catalysis, Royal Society of Chemistry,* 2006, **19**, in press.

[5] M. Hoang, A.E. Hughes, T.W. Turney, *Appl. Surf. Sci*., 1993, **72,** 55.

[6] D. Bazin, L. Borko, Z. Koppany, I. Kovacs, G. Stefler, L.I. Sajo, Z. Schay, L. Guczi, *Catal. Lett*., 2002, **84**, 169.

[7] Z. Zsoldos, T. Hoffer, L. Guczi, *J. Phys. Chem*., 1991, **95**, 798.
[8] A.G. Ruiz, A.S. Escribano, I.R. Ramos, *Appl. Catal. A: General*, 1994, **120**,71.
[9] S. Bessell, *Stud. Surf. Sci. Catal*., 1994, **81**, 479.
[10] E. Kikuchi, R. Sorita, H. Takahashi, T. Matsuda, *Appl. Catal. A: General*, 1999, **186**, 121.
[11] J. Barrault, *Stud. Surf. Sci. Catal.,* 1982, **11**, 225.
[12] Van der Riet, M.; Copperthwaite, R.G.; Hutchings, G.J.J. *J. Chem. Soc. Farad. Trans 1*, 1987, **83**, 2963.
[13] B.R. Strohmeier, D.M. Hercules, *J. Phys. Chem*., 1984, **88**, 4922.
[14] M. Kantcheva, M.U. Kucukkal, S. Suzer, *J. Catal.,* 2000, **190**, 144.
[15] M. Kantcheva, *J. Catal.,* 2001, **204**, 479.
[16] M. Vaarkamp, B.L. Mojet, M.J. Kappers, J.T. Miller, D.C. Koningsberger, *J. Phys. Chem*., 1995, **99**, 16067.
[17] Binstead, N., Campbell, J. W., Gurman, S. J., Stephenson, P. C., EXAFS Analysis Programs; Laboratory, D., Ed. Warrington, 1991.
[18] O. Stephan, A, Gloter, D. Imhof, M. Kociak, K. Suenaga, M. Tence, C. Colliex, *Surf. Rev. Lett*., 2000, **7**, 475.
[19] D.A. Shirley, *Phy. Rev. B*, 1972, **5**, 4709.
[20] J.H. Scofield, *J. Electron Spectr. Rel. Phenom,* 1976, **8**, 129.
[21] D.A. Fletcher, R.F. McMeeting, D. Parking, *J. Chem. Inf. Comput. Sci.,* 1996, **36**, 746.
[22] J.M. Jimemez Mateos, J. Morales, J.L. Tirado, *Thermoch. Act.,* 1988, **133**, 257.
[23] F. Morales, D. Grandjean, F.M.F. de Groot, O. Stephan, B.M. Weckhuysen, *Phys. Chem. Chem. Phys*., 2005, **7**, 568.
[24] Wells, A.F., Structural Inorganic Chemistry, 5th Ed., Clarendon Press, Oxford, 1984.
[25] R. Riva, H. Miessner, R. Vitali, G. Del Piero, *Appl. Catal. A: General*, 1999, **196**, 111.
[26] K. Hadjiivanov, D. Klissurski, A. Davydov, *J. Chem. Soc. Faraday Trans 1*, 1998, **84**, 34.
[27] K. Hadjiivanov, J. Lamotte, J. Lavalley, *Langmuir*, 1997, **13**, 3374.
[28] M. Kantcheva, M.U. Kucukkal, S. Suzer, *J. Catal.*, 2000, **190**, 144.
[29] E.W. Kuipers, I.H. Vinkenburg, H. Oosterbeek, *J. Catal.,* 1994, **152**, 137.

# 6

# Influence of Manganese Oxide on the Adsorption Properties of Titania-Supported Cobalt Fischer-Tropsch Catalysts


## Abstract

The effect of MnO promoter on the CO and $H_2$ adsorption properties of $TiO_2$-supported cobalt catalysts was studied by diffuse reflectance infrared spectroscopy. A $Co/TiO_2$ catalyst with a cobalt loading of 8.0 wt% was impregnated with different amounts of MnO (1.21, 2.15, 2.89 and 2.95 wt%). XRD and TPR indicated that after calcination there is an intimate association of manganese with cobalt that results in the formation of smaller $Co_3O_4$ particles with lower reducibility. TEM and $H_2$-chemisorption showed a drastic decrease in cobalt particle sizes upon reduction, while the $H_2$ chemisorption was largely suppressed due to an influence of the $TiO_2$ support. Manganese was found to decrease the extent of cobalt interaction with $TiO_2$ leading to higher $H_2$ chemisorption uptakes. MnO species were also detected at the surface of the Co particles after reduction influencing the ability of the active Co sites to bind CO. By increasing the MnO content in the catalysts the CO vibrations were largely modified, whereas the linear to bridge intensity ratio of bonded CO decreased. FT catalytic results at pressures of 1 bar showed a linear increase of the $C_{5+}$ selectivity from 36 % for the MnO-free sample, to 61 % for the sample containing 2.95 wt% MnO. The CO hydrogenation activity reached a maximum at intermediate MnO loading (1.5 wt %) and decreased at higher MnO loadings, probably due to an excessive coverage of cobalt by MnO. A decrease of the paraffin to olefin ratio was also observed in the MnO-promoted catalysts indicating a decrease of the extent of hydrogenation reactions involved in FT synthesis.

## Introduction

Infrared spectroscopy is a sensitive technique for investigating the surface properties of solids and for acquiring information on the nature of the catalyst surface, especially when used in combination with probe molecules [1-6]. Unfortunately, conventional transmittance infrared spectroscopy is not an option for measurements on $Co/TiO_2$ catalyst systems because of the sudden drop in light transmission when the catalysts are reduced [7]. With Diffuse Reflectance Infrared Fourier Transform Spectroscopy (DRIFTS) however, it is possible to study slightly transmitting materials with a sensitivity that is potentially orders of magnitude higher than in transmission mode. This has been demonstrated for $Fe/Al_2O_3$ and $Co/Al_2O_3$ [8] and $Co/TiO_2$ catalysts [9].

In this research, carbon monoxide was used to probe the surface of $Co/TiO_2$ catalysts promoted with little amounts of MnO. Carbon monoxide can accept electron density (Lewis acid) from metal surface sites (Lewis base) forming carbonyl complexes. In vibrational spectroscopy, most carbonyl complexes exhibit strong and sharp vibrational bands [10] between 2100 $cm^{-1}$ and 1800 $cm^{-1}$. In the case of electron donating sites, vibrational modes of carbon monoxide are red-shifted with respect to free gaseous carbon monoxide, which gives vibration bands at 2173 $cm^{-1}$ and 2108 $cm^{-1}$. This phenomenon can be explained in terms of simple molecular orbital (MO) theory. The $5\sigma$ orbital of the CO molecule forms a $\sigma$ bond with an empty orbital of the metal. For electron rich surfaces a back-donation from the metal into the antibonding $\pi$ orbitals of the CO molecule takes place, causing a weakening of the C≡O bond. The result is a red shift of the CO stretching frequency compared to that of the gas phase carbon monoxide and the appearance of two principal IR bands: one in the region between 2100 and 1900 $cm^{-1}$, which is assigned to CO linearly coordinated to $Co^0$, a bridge bonded one between 1850 and 1800 $cm^{-1}$, and a multiple bridge bonded ($\leq$ 1800 $cm^{-1}$). The extent of the shift can thus provide valuable information about the Lewis basicity of the metal sites [10-11]. Furthermore, the intensity ratio of the linear and bridged bonded bands can be used as a measure for the electronic state of the Co nanoparticles [12].

The objective of this chapter is to provide a systematic characterization of $Co/TiO_2$ catalysts loaded with different amounts of MnO using DRIFTS in combination with CO and $CO/H_2$ as probe molecules. By monitoring the position of the absorption bands of surface-bonded CO molecules information on the nature of the surface cobalt particles was obtained. It will be shown that DRIFTS in combination with XRD, TPR, TEM and $H_2$-chemisorption lead to a comprehensive understanding of the manganese effect on the cobalt active site composition. Additionally, Fischer-Tropsch catalytic tests have indicated that the MnO loading in the catalysts can largely influence both the activity and selectivity by altering the electronic density of the cobalt surface.

## Experimental

*Catalyst synthesis*

Cobalt (~ 8 wt%) was deposited on the $TiO_2$ support (Degussa P25) according to the HDP method [13] using cobalt nitrate (Merck) and urea (Across). After filtering and drying at 120 ºC overnight, the catalyst precursors were loaded with various amounts of Mn (1.21, 2.15, 2.89, and 2.95 wt %) by the IWI method. A final calcination in a flow of air at 350 ºC for 4 h (ramp = 5 ºC/min) led to catalysts denoted as $HCo_xMn_y$, x and y being the relative amount of Co and Mn, respectively. An overview of the five catalysts prepared together with their metal loadings as determined by XRF analysis is shown in Table 1.

**Table 1.** Overview of the catalysts prepared together with the metal loadings.

| Sample code | Co[a] wt% | Mn[a] wt% | Mn:Co ratio |
|---|---|---|---|
| HCo | 7.77 | 0.0 | 0.00 |
| HCo20Mn2 | 7.01 | 1.21 | 0.17 |
| HCo20Mn3 | 6.98 | 2.15 | 0.31 |
| HCo20Mn4 | 7.12 | 2.89 | 0.41 |
| HCo20Mn5 | 6.54 | 2.95 | 0.45 |

[a]As determined by XRF assuming the Co and Mn to be present in the form of $Co^0$ and MnO.

*Catalyst characterization*

Cobalt and manganese loadings in the oxidized catalysts were determined by XRF with a Spectro X-lab 2000 instrument.

The catalysts were analysed after calcination by X-ray diffraction (XRD) making use of an Enraf-Nonius CPS 120 XRD apparatus equipped with a curved position-sensitive INEL detector and a Co $K\alpha_1$ radiation source ($\lambda$ = 1.78897 Å). The line broadening of the $Co_3O_4$ diffraction peaks localized at 70º and 77º $2\theta$ values were used to estimate the crystallite sizes.

Temperature programmed reduction (TPR) experiments were performed on a Micromeretics Autochem-II instrument with a TCD detector. The samples were initially dried in Ar at 120 ºC for 20 min and after the TCD signal stabilized the temperature was raised from 40 to 700 ºC at a rate of 10 ºC/min.

Reduced and passivated HCo, HCo20Mn3 and HCo20Mn5 catalysts were analysed by transmission electron microscopy (TEM) in a Tecnai 20 FEG TEM microscope operating at 200 kV and equipped with an EDX analyser. The samples were first dried in a flow of air at 120 ºC for 30 min and then reduced in a 50 % $H_2$/He flow at 350 for 2 h (ramp = 5 ºC/min). A

passivation was carried out at 150 ºC in a flow of 20 % $CO_2$/He for 30 min. The samples were then crushed, ultrasonically dispersed in ethanol and dropped on a holey carbon film on a copper grid.

Hydrogen chemisorption measurements were carried out making use of a Micromeritics ASAP 2010C equipment. The samples were initially dried at 120 ºC in a He flow for 30 min and subsequently reduced in a 50% $H_2$/He flow at 350 ºC for 2 h (ramp = 5 ºC/min). The $H_2$-adsorption isotherms were measured at 150 ºC, being the temperature recommended by Reuel and Bartholomew [14]. The % Co dispersions were calculated assuming a complete cobalt reduction and stoichiometry of 1 hydrogen atom adsorbed per cobalt surface atom.

DRIFTS experiments were carried out on a Perkin Elmer FTIR 2000 series infrared spectrometer. DRIFTS spectra were collected using a Harrick "Praying Mantis" DRIFT accessory equipped with a gas flow cell with $CaF_2$ windows. CO adsorption at RT and CO/$H_2$ adsorption at 220 ºC were performed in all reduced samples before collecting the spectra. The powdered samples were initially loaded in the reactor and reduced in 40 ml/min $H_2$ flow at 350 ºC for 2 h (heating rate of 5 ºC/min). After reduction, the samples were cooled down at a rate of 5 ºC/min in 40 ml/min He flow to 30 ºC. At this temperature a background spectrum was recorded (100 scans, resolution 4 $cm^{-1}$) and subsequently CO flows of 20 ml/min were fed to the cell during 30 min. After flushing He to remove the gaseous CO from the cell, DRIFTS spectra were collected with a resolution of 4 $cm^{-1}$ and accumulating 100 scans. For the CO/$H_2$ adsorption experiments the samples were reduced using the same procedure described above, after which the temperature was brought to 220 ºC under flowing He. Background spectra (resolution 4 $cm^{-1}$, 50 scans) were collected before the gas feed was switched to a mixture of 45 ml CO/$H_2$ (1:2 ratio). DRIFTS spectra were continuously recorded during 2 h reaction. After 2 h the cell was flushed with He in order to remove the gas phase reactants before collecting spectra.

*Catalyst characterization*

Catalysts were tested at 1 bar and 220 ºC using CO/$H_2$ (1:2 ratio) after reduction treatments at 350 ºC 2 h in hydrogen. Typically 50 mg of catalyst samples (particles 0.25-0.50 mm) were diluted in SiC (particles 0.22 mm) to achieve isothermal plug-flow conditions. Gas hourly space velocities of 3010 $h^{-1}$ were used in all experiments leading to CO conversions around 1 %. The hydrocarbon product composition was analyzed on-line during the first 60 h of reaction using a Varian CP-3800 gas chromatograph equipped with a fused silica column of 50 m length and a flame ionization detector (FID). Catalytic data were monitored during 60 h, after which a pseudo stationary state was reached.

## Results and discussion

### *Catalyst characterization after calcination*

The XRD patterns of the unpromoted and manganese-promoted Co/$TiO_2$ catalysts in the calcined state are given in Fig. 1. The results show the distinct diffraction lines originating from the $TiO_2$ support (i.e., anatase and rutile phases) as well as small contributions from the $Co_3O_4$ phase, the most intense lines being located at 36º, 52º, 70º, and 77º 2$\theta$. These peaks are clearly wider than those corresponding to the $TiO_2$ due to a line broadening resulting from the small size of the $Co_3O_4$ crystallites. Furthermore, diffraction lines corresponding to $Co_3O_4$ are more intense for the HCo catalyst and become weaker by increasing the manganese loading, pointing to a less $Co_3O_4$ crystalline character in the presence of manganese. As already discussed in chapter 2, manganese interacts with the $Co_3O_4$ after calcination leading to the formation of some amounts of $Co_{3-x}Mn_xO_4$ solid solutions. This effect may result in a decrease of crystallinity of the $Co_3O_4$ particles. Line-broadening analysis of the diffraction peaks at 70º and 77º 2$\theta$ were used to estimate $Co_3O_4$ crystallite sizes in the different samples, as summarized in Table 2. By increasing the manganese loading in the catalysts the domain size of the $Co_3O_4$ particles was found to decrease slightly from 24 nm in the Co/$TiO_2$ catalyst, to 14.0 nm in the sample with 2.95 wt% MnO loading. Therefore, we conclude that the addition of small amounts of manganese to the Co/$TiO_2$ catalysts alters the average $Co_3O_4$

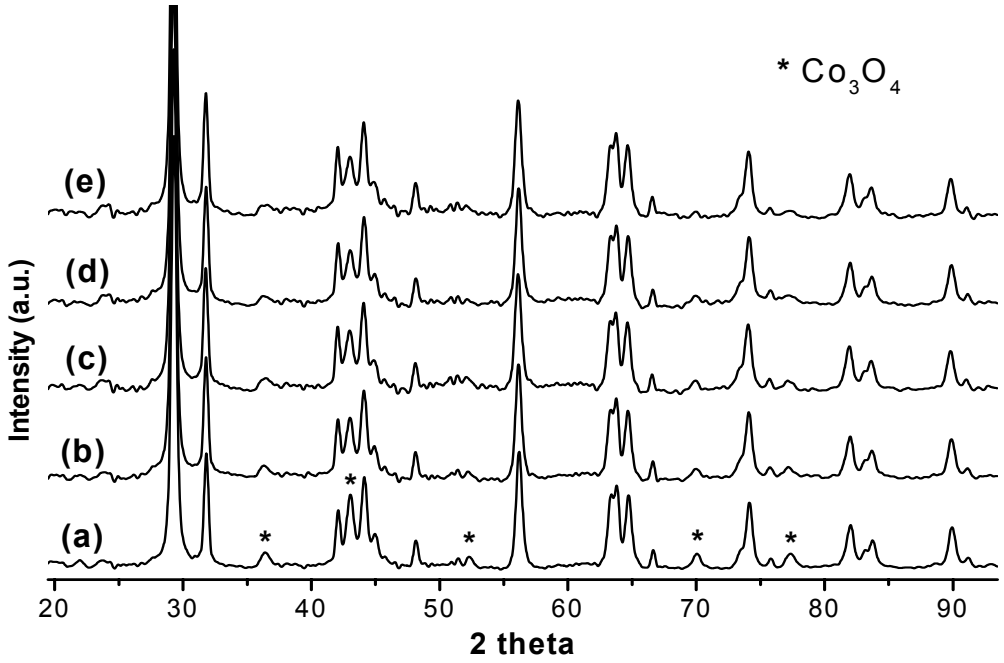


**Figure 1.** XRD patterns of the HCo (a), HCo20Mn2 (b), HCo20Mn3 (c), HCo20Mn4 (d) and HCo20Mn5 (e) catalysts after calcination.

**Table 2.** $Co_3O_4$ particle size calculation using the line-broadening analysis of diffraction lines at 70º and 77º $2\theta$.

| Sample code | Peak maximum | $Co_3O_4$ size (nm) | Peak maximum | $Co_3O_4$ size (nm) | Average $Co_3O_4$ size (nm) |
|---|---|---|---|---|---|
| HCo | 70.05 | 28.1 | 77.36 | 21.2 | 24.7 |
| HCo20Mn2 | 69.99 | 25.1 | 77.28 | 23.0 | 24.0 |
| HCo20Mn3 | 69.91 | 19.0 | 77.18 | 19.3 | 19.2 |
| HCo20Mn4 | 69.91 | 12.2 | 77.09 | 10.4 | 11.3 |
| HCo20Mn5 | 69.90 | 15.6 | 77.20 | 12.4 | 14.0 |

particle size due to an intimate interaction. The likely mixing of manganese with the $Co_3O_4$ phase is also reflected in the $2\theta$ positions of the diffraction lines, which are slightly shifted to smaller angles for all $Co/Mn/TiO_2$ catalysts. This phenomenon has been earlier ascribed to a decrease in the cell parameter upon incorporation of $Mn^{3+}$ ions into the $Co_3O_4$ lattice [15].

The TPR profiles of the calcined samples given in Fig. 2 show three distinct peaks around 275, 350 and 450 ºC, which are ascribed to the reduction steps from $Co_3O_4$ to CoO and subsequently to $Co^0$. Analysis of the peak areas (i.e., $H_2$ consumption) indicates that the first peak located around 275 ºC stem from the first cobalt reduction step, whereas the other two peaks at around 350 and 450 ºC, stem from reduction of CoO to $Co^0$. However, due to the presence of manganese in the catalysts and the likely formation of mixed oxides, the reduction profiles may contain variable contributions of different compounds. For this reason a

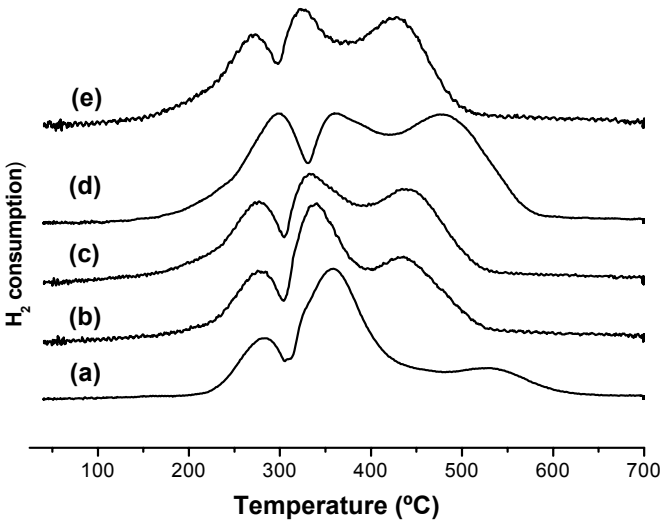


**Figure 2.** TPR profiles of the calcined HCo (a), HCo20Mn2 (b), HCo20Mn3 (c), HCo20Mn4 (c), and HCo20Mn5 (d) catalysts.

quantification of the areas was not taken into account and the data was merely used to evaluate the manganese influence on the relative areas and position of the distinct peaks. The first conclusion drawn from the comparison of the TPR profiles is that manganese strongly influences the overall reduction of $Co_3O_4$, generally by hampering the reducibility. This is clearly suggested when an evaluation of the relative area of the peak around 450 ºC is considered, which appears at higher temperatures in the MnO-promoted materials. This effect of manganese on the cobalt reducibility is attributed to its association with the $Co_3O_4$ particles as already suggested from the XRD results. These results are moreover, in line with previous reported work, from which it was concluded that the addition of manganese to a Co/$TiO_2$ catalyst hampers the cobalt reducibility [16-18].

***Catalyst characterization after reduction***

TEM was used to study the cobalt morphology and particle size distribution in the reduced and passivated Co/$TiO_2$ sample, as well as in the Co/Mn/$TiO_2$ samples with 2.15 and 2.95 wt% manganese. Two examples of TEM images obtained for each sample are given in Fig. 3. The supported cobalt (oxide) phase is observed at the $TiO_2$ surface as small spherical particles with a broad particle size distribution and morphology, although the majority of the cobalt particles have sizes ranging from 2 to 7 nm. In addition, some larger agglomerates of around 8-12 nm can be also observed in the TEM images indicated by an arrow. These agglomerates are formed of smaller particles bonded together. The cobalt particles were generally more easily distinguished in the Mn-free sample, possibly due to a covering by manganese oxide, which makes the visualization of the particles less obvious. Comparison of the cobalt particle sizes obtained by TEM and XRD indicates that reduction leads to a dramatic decrease in the sizes, probably caused by a re-dispersion and stabilization of the small particles on the $TiO_2$ surface. An exact estimation of the average cobalt size was, however, not attempted due to the broad particle size distributions. Hence, the data was used as an indication of the cobalt morphology and approximate size (Table 3).

$H_2$-chemisorption measurements were carried out to determine the number of available surface $Co^0$ sites in the different catalysts after reduction. The $H_2$ uptake data and calculated cobalt dispersions for the five samples under study are presented in Table 3. It is remarkable to notice that the obtained values for cobalt dispersion are much smaller than those expected according to the TEM results. As observed, dispersions of 1.23 % and 4.63 % were obtained for the HCo and HCo20Mn3 samples, respectively. Although we assumed a complete cobalt reduction, the TPR results suggest that this may be incomplete. Nonetheless, in situ EXAFS experiments (not shown) have indicated that these catalysts after reduction at 350 ºC have cobalt reduction degrees higher than 95 %. Hence, the $H_2$ uptakes were expected to be much

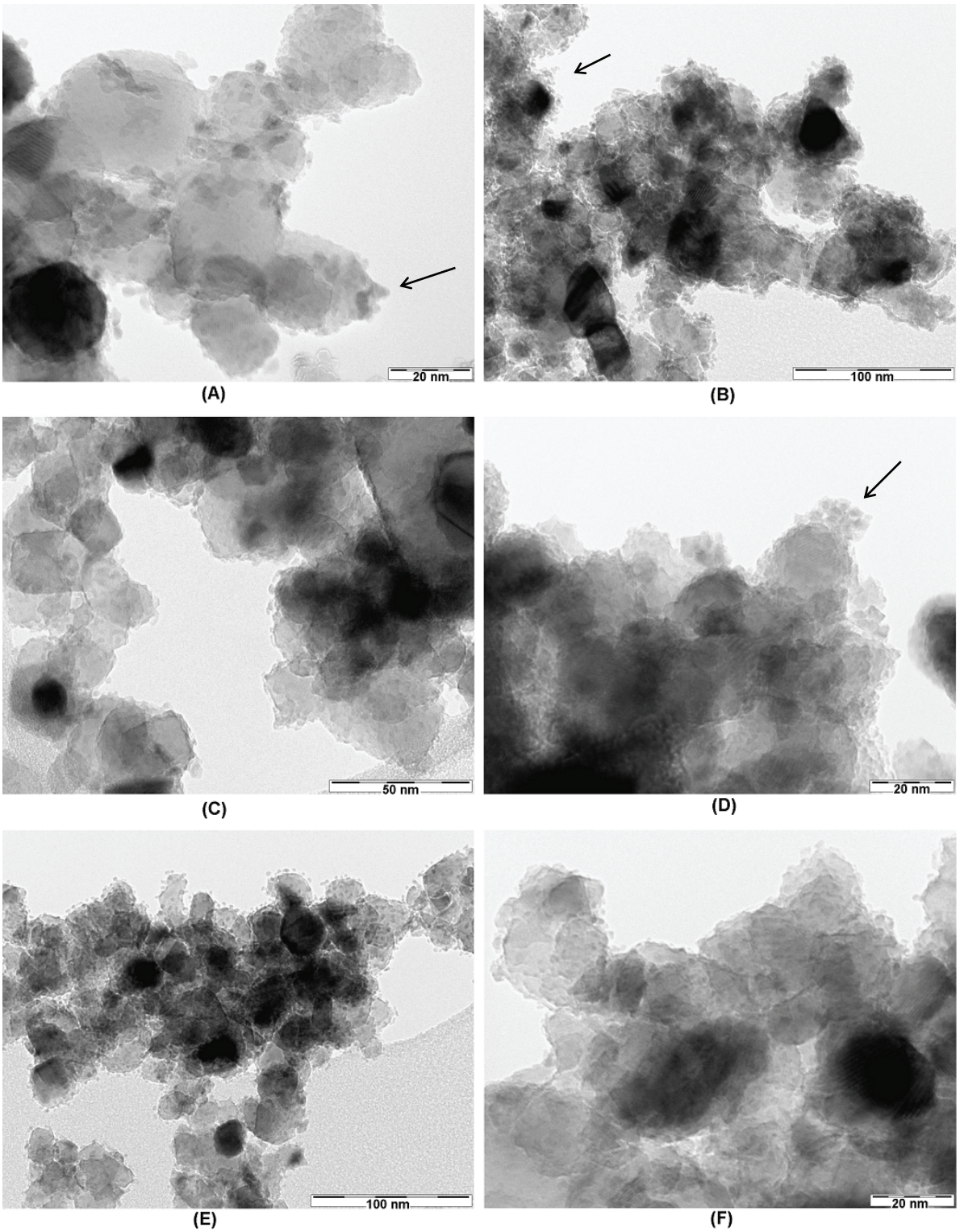


**Figure 3.** TEM images of the reduced HCo (A, B), HCo20Mn3 (C, D) and HCo20Mn5 (E, F) catalysts. The images show for all the samples the presence of very small cobalt particles (~2-7 nm) covering the $TiO_2$ surface. In addition, some images show the presence of larger cobalt agglomerates (~10-15 nm), as indicated by an arrow.

**Table 3**. Hydrogen chemisorption uptakes and cobalt dispersion together with TEM particle sizes

| Sample | $H_2$ uptake (mmol/g) | Cobalt dispersion (%) | TEM cobalt particle size (nm) |
|---|---|---|---|
| HCo | 0.010 | 1.23 | 2-7 |
| HCo20Mn2 | 0.024 | 3.02 | - |
| HCo20Mn3 | 0.037 | 4.63 | 2-10 |
| HCo20Mn4 | 0.021 | 2.67 | |
| HCo20Mn5 | 0.017 | 2.20 | 2-6 |

higher than the values reported in Table 3. The $H_2$ uptakes obtained for the different catalysts correspond to particle sizes [14] ranging from 78 nm to 21 nm, for HCo and H20CoMn3, respectively. These values for Co particle sizes are much larger than those shown by TEM, and therefore it clearly indicates that the hydrogen chemisorption is highly suppressed for these catalytic systems. As a consequence, their actual dispersion is claimed to be much higher than these reported values. Comparison of these results with other reported data on cobalt supported on carbon nanofibers catalysts [19], suggest that the $TiO_2$ support may be highly responsible for the decrease in hydrogen chemisorption. It is well known, that the reduction conditions applied to these materials lead to a partial reduction of the $TiO_2$ surface, possibly causing the appearance of SMSI effects [20]. The formation of $TiO_x$ overlayers upon reduction would indeed, cause a blocking of surface $Co^0$ sites and consequently a decrease in the $H_2$-chemisorption [21]. We therefore, ascribe the low values of cobalt dispersions reported for these catalysts to the occurrence of SMSI effects. Another interesting observation is that the $H_2$ uptake significantly increases for the Co/$TiO_2$ catalysts upon addition of 1.21 and 2.15 wt% MnO, giving higher cobalt dispersions of 1.23%, 3.0% and 4.73%, respectively. This possibly indicates that small amounts of MnO may prevent to some extent the interaction of cobalt with the $TiO_2$ support resulting in higher $Co^0$ surface areas. As discussed in chapter 4, manganese is known to highly spread over the $TiO_2$ surface forming a $Ti_2MnO_4$-type phase. Hence, the presence of this compound in the vicinity of the cobalt particles may prevent the occurrence of cobalt-support interaction effects (i.e., the coverage of the cobalt metal surface by TiOx species upon reduction), thereby increasing the hydrogen chemisorption uptake. However, at higher MnO loadings of 2.89 and 2.95 wt% the hydrogen uptake decreases again. The reason for this observed effect is most probably the blocking of the cobalt active sites by MnO species, which are known to cover also the cobalt metal surface. Therefore, the presence small amounts of manganese oxide in the Co/$TiO_2$ catalysts has a beneficial effect on the amount of available cobalt metal exposed at the surface.

***Study of the $TiO_2$-supported Co nanoparticles by DRIFT spectroscopy***

*CO adsorption experiments at RT*

To gain insight into the surface properties of these 5 different catalysts DRIFTS measurements were carried out after reduction and exposure to CO. Fig. 4 shows the CO adsorption DRIFTS spectra for the catalysts with different manganese loadings. Three regions can be distinguished in the presented spectra. A first region between 2250 $cm^{-1}$ and 2090 $cm^{-1}$ contains two bands at 2173 $cm^{-1}$ and 2108 $cm^{-1}$ corresponding to the rotational state transitions of the CO gas phase, which were observed even after flushing for extended periods of time. This indicates that the cell cannot be purged efficiently enough to remove all the CO gas phase, although these bands do not interfere with the bands of interest. The second region, between 2060 $cm^{-1}$ and 1990 $cm^{-1}$, is assigned to CO linearly-bonded to the surface cobalt metal sites [7-9, 22]. Peak fitting indicated that three different peak contributions are present; a main a peak centered around 2050 $cm^{-1}$ and another contribution of a band centered around 2030 $cm^{-1}$, which was more pronounced for some of the manganese promoted catalysts. The third region, roughly below 1900 $cm^{-1}$, is assigned to CO bridge-bonded to cobalt metal sites [9]. Because of the possibility of two-fold, three-fold and even four-fold bridge bonding, the shape and position of the absorption bands varied in the different catalysts. Nevertheless, the catalysts with a clear CO bridge-bonded peak showed an absorption centered around 1850

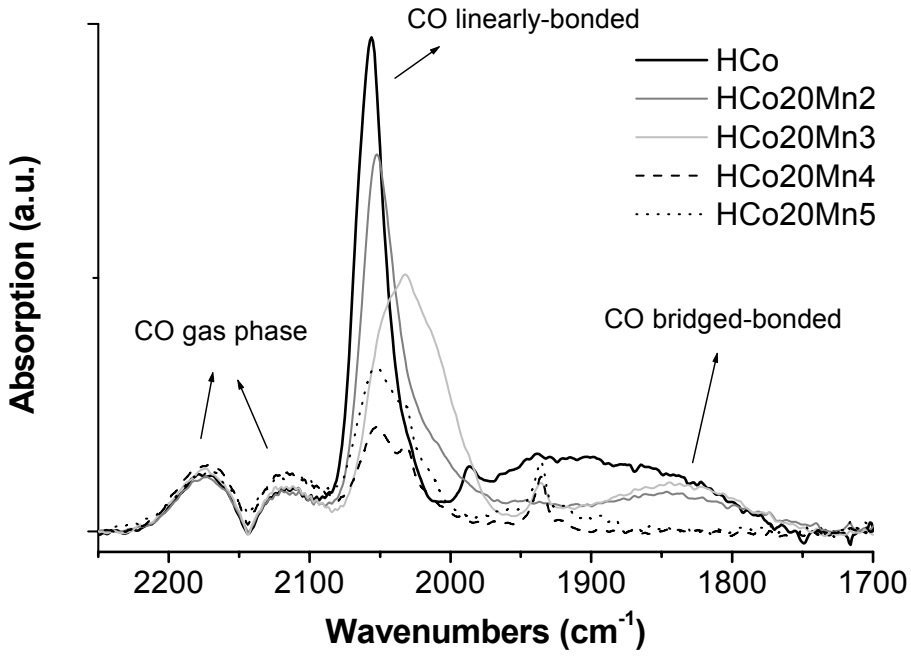


**Figure 4.** DRIFTS spectra measured after CO adsorption at RT for the various $Co/TiO_2$ and $Co/Mn/TiO_2$ catalysts reduced at 350 °C.

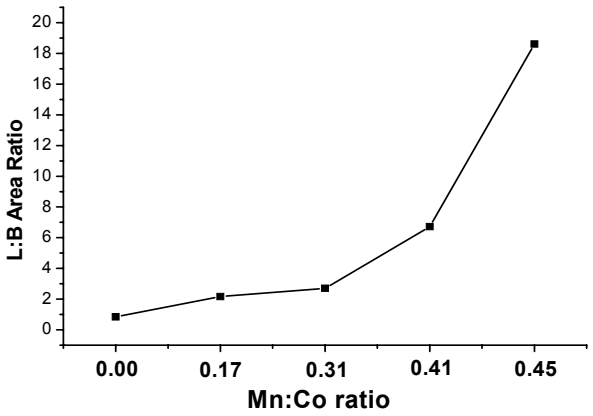


**Figure 5.** Linear to bridge bonded CO obtained by peak analysis in the different catalysts as denoted by their Mn to Co ratio: 0.00 (HCo), 0.17 (HCo20Mn2), 0.31 (HCo20Mn3), 0.41 (HCo20Mn4), and 0.45 (HCo20Mn5).

$cm^{-1}$. Finally, a sharp absorption band at 1935 $cm^{-1}$ is present in the spectra with the highest manganese loadings (HCo20Mn3, HCo20Mn4 and HCo20Mn5). This peak most likely corresponds to CO interacting with the manganese oxide species present on the $TiO_2$ support. Although, the nature of this absorption could not be elucidated, comparable vibration frequencies of CO adsorbed on manganese species were found in the literature [23].

For the IR spectra presented in Fig. 4 distinct linear and bridge CO absorptions respectively around 2050 $cm^{-1}$ and 1850 $cm^{-1}$ are observed. The overall absorption intensity decreases with increasing MnO loading, while the general absorption mode is clearly altered. In contrast to the HCo sample which presents a single sharp CO absorption at 2050 $cm^{-1}$, the increasing MnO loading results in a different CO absorption band at lower wavenumbers. The presence of manganese, therefore, largely influences the CO adsorption properties of the Co sites, indicating that a direct interaction with the Co particles exists. As was already demonstrated in chapter 4, a fraction of the manganese remains located at the surface of the Co particles after catalyst reduction and hence, it can directly influence the CO adsorption properties.

On the other hand, the presence of bridge bonded CO was much more pronounced for the Mn-free catalysts and tended to disappear for high manganese loadings. To better evaluate this phenomenon, the relative areas of linear to bridge CO absorption bands were calculated by fitting the different peaks, which were subsequently background subtracted. The results of the peak analysis are illustrated in Fig. 5. It can be observed that the ratio of linear to bridge adsorbed CO clearly increases with increasing MnO loading in the catalysts. However, we note that the accuracy for the calculation of peak areas was rather low for the two samples with the highest MnO loadings, due to an almost negligible CO-bridge adsorption. Nevertheless, the data may be used to illustrate the fact that upon manganese addition the occurrence of CO-bridge adsorption is clearly suppressed. A possible cause for this

phenomenon is the change in electronic properties of the cobalt metal induced by the interaction with MnO species located at the surface of the Co particles. Manganese has been earlier shown (chapter 5) to be mainly present as $Mn^{2+}$, which is a Lewis acid and thus, can accept electron density from the cobalt metal. By doing this, the Lewis basicity of the metal is reduced and its Fermi level is somewhat lowered. This results in a more electron deficient cobalt metal surface when manganese is present at the Co surface. The Lewis acidity of cations can be measured according to the Kamlet–Talf parameter, which expresses the ability of a cation to accept an electron pair, and a high value corresponds with a strong Lewis acid character. $Mn^{2+}$ with a Kamlet–Taft value of 4.28 [6] is a strong Lewis acid and thus, directly influences the local environment of adsorbed CO, since the cobalt has less electron density available for the back-donation of electrons into the π* orbitals of the CO molecule. As a result the C≡O bond gains strength and therefore, less bridge CO species are observed in the IR spectra for the MnO-promoted catalysts compared to Mn-free catalysts. These findings are in line with earlier CO adsorption infrared studies on supported zeolite platinum metal particles [1].

*CO + $H_2$ adsorption experiments at 220 ºC*

Similar conditions used for the Fischer-Tropsch catalytic tests were employed to measure DRIFT spectra for the different catalysts, which enabled the monitoring of species present at the catalyst surfaces during the first stage of reaction. The reported spectra reported in the

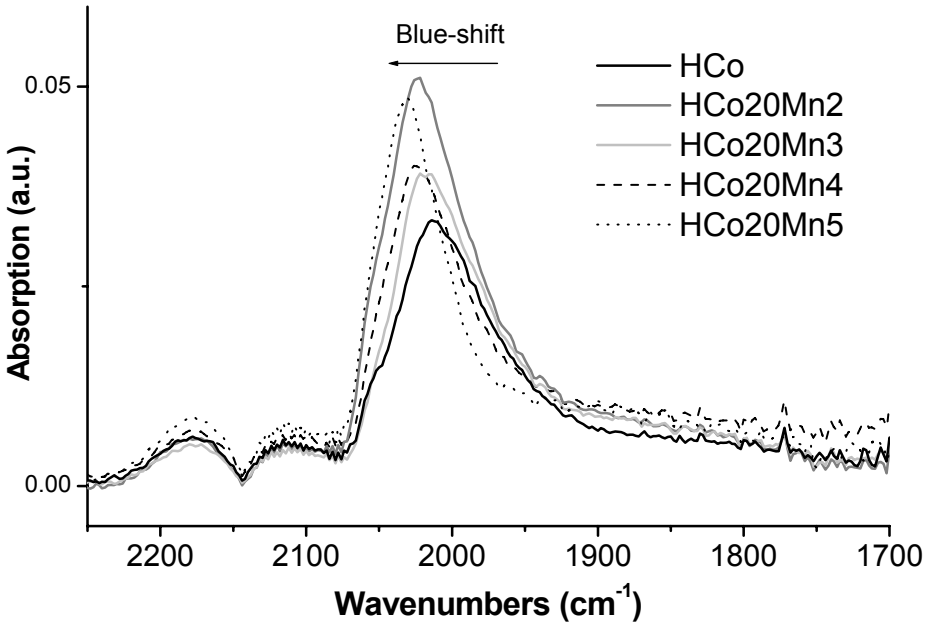


**Figure 6.** DRIFTS spectra of the CO region for the different $Co/TiO_2$ and $Co/Mn/TiO_2$ catalysts after 2 h exposure to $H_2$/CO gas mixtures.

following correspond to surface species adsorbed at the surface after 2 h exposure to $H_2$/CO mixtures at 220 ºC. Three main spectral regions were evaluated: the CO absorption region (2250−1700 $cm^{-1}$) as previously discussed in the latter experiment, and the hydrocarbon and carbonate absorption regions, present respectively at wavenumbers in the range of 3000−2800 $cm^{-1}$ and 1650−1300 $cm^{-1}$. The different regions will be now discussed separately.

The CO region (2250−1700 $cm^{-1}$) given in Fig. 6 shows three main features. The two peaks at 2176 $cm^{-1}$ and 2108 $cm^{-1}$ are assigned to gaseous CO. These peaks were observed even after flushing for extended periods of time. The broad peak centered around 2020 $cm^{-1}$ is assigned to CO linearly adsorbed to cobalt metal sites. We note that the peak intensities were not considered in a quantitative manner, since the differences in absorption were very small compared to the experimental error of the measurements. Hence, the data was only used for qualitative purposes. As observed in Fig. 5, the peak originating from linearly adsorbed CO shifts to higher wavenumbers with increasing manganese content in the catalysts. On going from the HCo sample to the sample with higher MnO loading (HCo20Mn5), the peak significantly shifts from 2012 $cm^{-1}$ to 2031 $cm^{-1}$. This blue-shift is in accordance with the earlier explanation that the presence of $Mn^{2+}$ at the surface of the $Co^0$ particles lowers its Lewis basicity and consequently the C≡O bond gains strength, leading to the higher vibration frequencies.

In contrast with the CO adsorption experiments, no bridge-bonded CO was observed in the DRIFT spectra collected after $H_2$/CO exposure at 220 °C. This is in sharp contrast with the linearly adsorbed CO species, which were still present at the catalyst surface. Hence, it can be proposed that in the presence of hydrogen the bridged CO may be very rapidly hydrogenated to hydrocarbons.

The hydrocarbon region (3000−2800 $cm^{-1}$) is presented in Fig. 7. Three main bands can be distinguished in the spectra centered around 2966, 2927 and 2875 $cm^{-1}$. The first two bands are assigned respectively to the symmetric $–CH_3$ and $–CH_2$ stretch vibrations [20]. The band at 2867 $cm^{-1}$ originates from a combination of the asymmetric $–CH_2$ and $–CH_3$ vibrations at 2860 $cm^{-1}$ and 2875 $cm^{-1}$, respectively. The detection of these vibration bands indicates that hydrocarbon fragments are indeed attached to the cobalt surface after performing the Fischer-Tropsch reaction and flushing with helium. These hydrocarbon fragments belong to the different chains and monomer species consisting in a broad range of potential products. Nevertheless, due to the large number of possible species adsorbed at the catalyst surface it is not possible to quantify or evaluate any hydrocarbon distribution. The adsorbed species may vary from a simple monomer of one carbon atom ($-CH_2$ and $–CH_3$) to longer chain hydrocarbons. Nevertheless, some differences are observed when normalizing the spectra to the peak at 2966 $cm^{-1}$, since the broad band consisting of asymmetric $–CH_2$ and $–CH_3$

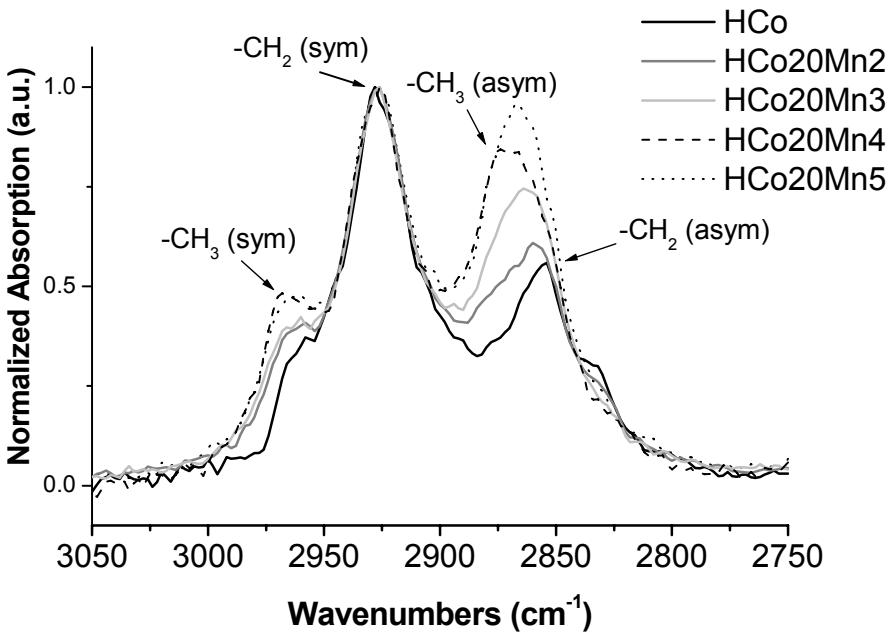


**Figure 7.** DRIFTS spectra of the hydrocarbon region for the different $Co/TiO_2$ and $Co/Mn/TiO_2$ catalysts after 2 h exposure to $H_2/CO$ gas mixtures.

vibrations linearly increase upon increasing MnO loading in the catalysts, although more research is needed to elucidate the cause for this trend. The results reported should be merely taken as an illustration of the usefulness of the DRIFTS technique to monitor hydrocarbon species present at the catalyst surface during the Fischer-Tropsch reaction. It is thereby demonstrated that the CO hydrogenation and chain growth reactions take place under the IR measurement conditions, although quantitative information cannot be directly gained without other complementary data provided by other characterization techniques.

The carbonate region (1700−1300 $cm^{-1}$) is given in Fig. 8. Two main peaks can be observed around 1590 and 1375 $cm^{-1}$ corresponding to $CO_3^{2-}$ groups bonded to the titania support [25]. Two bands at 1450 $cm^{-1}$ and 1375 $cm^{-1}$ originate from the symmetric and asymmetric O–C–O vibrations of the surface bonded $CO_3^{2-}$ species. The carbonates species are also bridge bonded to the support, leading to the appearance of a peak around 1570 $cm^{-1}$ and a shoulder peak at around 1330 $cm^{-1}$. By increasing the manganese content in the catalysts the total absorption of the carbonate peaks increases. In this case, differences in peak intensities are relatively large and hence, a semi-quantitative analysis was considered. The carbonate absorption bands, linearly increased in intensity going from HCo to HCo20Mn5, which suggests that the amount of carbonate adsorbed species was favored by the presence of manganese. This may indicate that manganese either has some kind of role in accommodating the carbon dioxide on the $TiO_2$ support or that it catalyzes the conversion of carbon monoxide

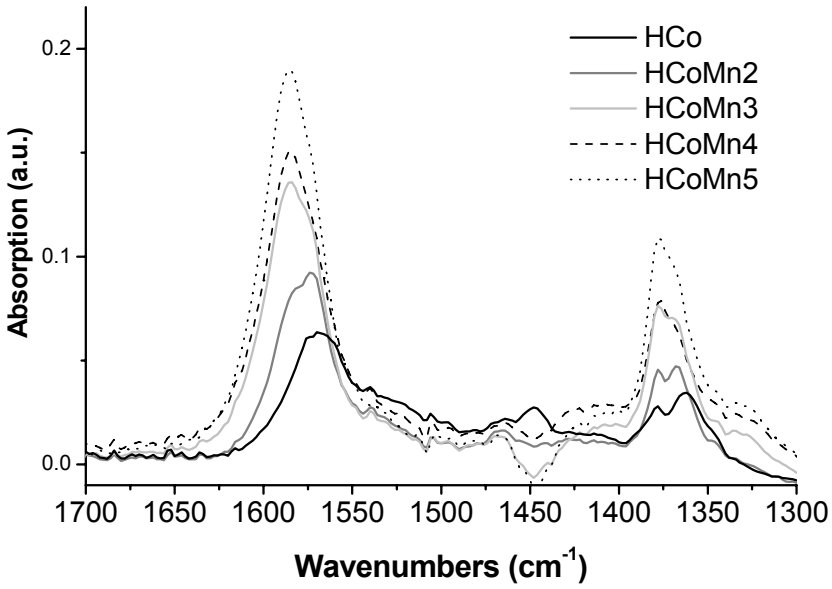


**Figure 8.** DRIFTS spectra of the carbonate region for the different Co/TiO$_2$ and Co/Mn/TiO$_2$ catalysts after 2 h exposure to H$_2$/CO gas mixtures.

to carbon dioxide. The latter effect has been earlier reported in literature where manganese oxide was proposed to catalyze the water-gas shift reaction [26-27]. The occurrence of this reaction has important implications for the Fischer-Tropsch synthesis, since it may largely influence the final product selectivity by affecting the hydrogen partial pressure under reaction conditions. The results therefore indicate that manganese is also localized at the TiO$_2$ surface influencing its surface properties. From earlier results reported in chapter 5 the manganese is known to highly spread over the TiO$_2$ surface during reduction, leading to the formation of Ti$_2$MnO$_4$ phases.

***Catalysis***

The catalytic results obtained after 40 h of reaction are given in Table 4. The presence of manganese in the catalysts clearly influences their selectivity and to a lower extent their activity. The $C_{5+}$ selectivity is gradually increasing with increasing MnO loading, from 36.6 wt% to 61.3 wt% for HCo and HCo20Mn5, respectively. This increase in $C_{5+}$ selectivity occurs mainly at the expense of the $CH_4$ formation, which is decreased from 28.4 wt% to 14.1 wt% for the HCo and HCo20Mn5 catalysts, respectively. The gradual shift in selectivity displayed by the catalysts loaded with various amounts of MnO is illustrated in Fig. 9.

The product distribution obtained for the different catalysts are in accordance with the ASF kinetics [28]. Using the ASF distribution we determined the chain growth probability (α)

**Table 4.** FT catalytic performances after 40 h reaction at 1 bar and 220 °C (Activity: $10^{-5}$ mol CO g $Co^{-1}$ $s^{-1}$).

| Sample | Activity | $CH_4$ (wt %) | $C_{5+}$ (wt %) | Chain growth probability (α) |
|---|---|---|---|---|
| HCo | 0.53 | 28.4 | 36.6 | 0.62 |
| HCoMn2 | 0.72 | 21.2 | 43.8 | 0.64 |
| HCoMn3 | 0.93 | 20.2 | 45.1 | 0.65 |
| HCoMn4 | 0.86 | 17.3 | 53.9 | 0.71 |
| HCoMn5 | 0.87 | 14.1 | 61.3 | 0.77 |

from the slope of the linear part of the plot. The α values largely increase upon MnO addition, going from a minimum of 0.62 for the umpromoted catalyst, to a maximum of 0.77 for HCo20Mn5. The activity, on the other hand, increases to a maximum of 0.93 $10^{-5}$ mol CO g $Co^{-1}$ $s^{-1}$, for MnO loadings of 2.15 wt% and subsequently decreases for higher MnO loadings. These results nicely show that by loading the catalysts with small amounts of MnO the cobalt particles become more selective to high weight products. In addition, the activity of the cobalt particles is also increased, although an excessive coverage by MnO results in a lowering of the activity probably because some of the active sites are blocked. The TEM results have indicated that the size of the cobalt particles is similar in all the catalysts and hence, the increase in activity for the MnO-promoted catalysts is not caused by an increase of the number of active sites, but most probably by an increase of the intrinsic activity of the Co

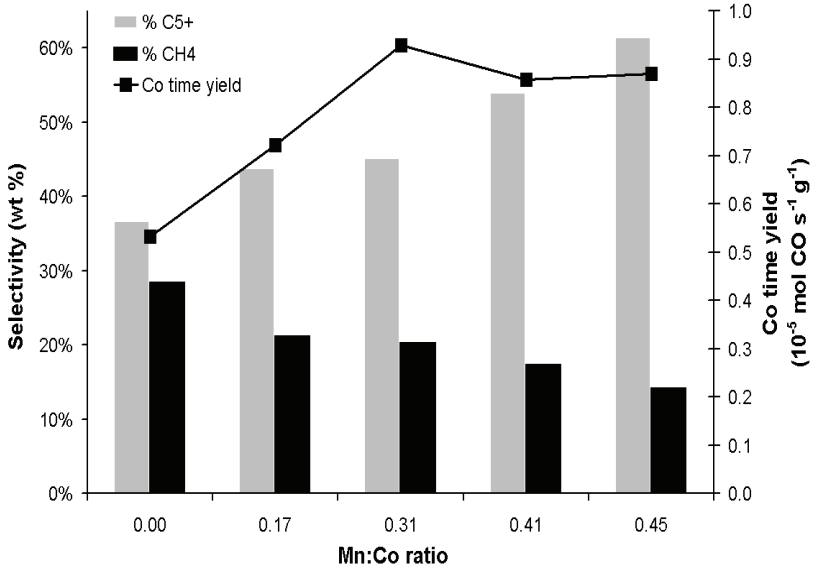


**Figure 9.** Influence of the MnO loading on the FT activity and the $C_{5+}$ and $CH_4$ selectivity of the $Co/TiO_2$ and $Co/Mn/TiO_2$ catalysts under study.

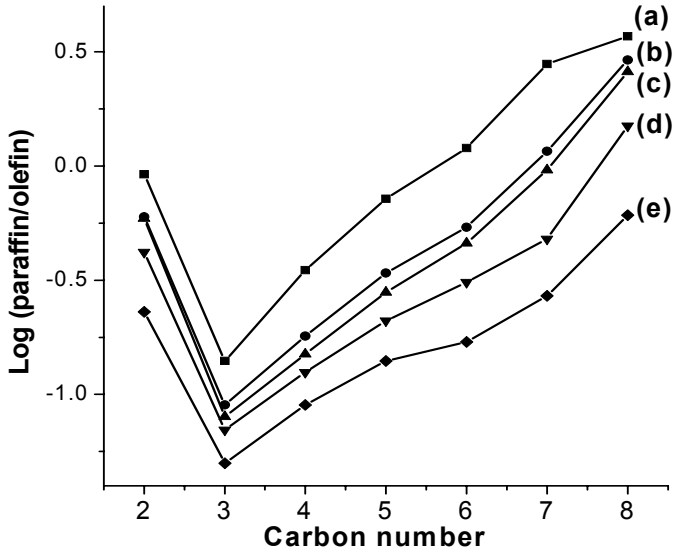


**Figure 10.** Influence of MnO on the paraffin to olefin ratio for the HCo (a), HCo20Mn2 (b), HCo20Mn3 (c), HCo20Mn4 (d) and HCo20Mn5 (e) catalysts under study.

active sites. This conclusion is also backed up by earlier studies that showed that larger cobalt particles promoted by MnO display higher turnover frequencies for the CO hydrogenation reaction (chapter 3).

An interesting observation is that the activity measured for the different catalysts can be directly correlated to the hydrogen chemisorption uptakes. At intermediate MnO loading of 2.15 wt% the highest hydrogen uptake was obtained, which is in accordance with the highest catalytic activity. This strongly suggests that manganese may play an important role in optimizing the amount of accessible cobalt metal sites by decreasing the extent of interaction between the cobalt phase and the $TiO_2$ support.

The presence of MnO in the catalysts leads to another remarkable effect on the product selectivity. By increasing the MnO loading the fraction of olefin products is gradually raised. This effect is illustrated in Fig. 10 showing the P/O ratios as a function of the MnO loading in the different catalysts. As observed, the P/O ratio for all the hydrocarbon fractions is clearly decreasing with increasing MnO loading. This result suggests that the hydrogenation abilitiy of the cobalt particles is lowered upon coverage by small amounts of MnO. This effect is directly involved in the higher production of olefins for the MnO-promoted catalysts since the chain growth termination step by $H_2$ addition is slightly suppressed. As a consequence, the hydrocarbon chains adsorbed at the cobalt surface have a higher chance to grow, thereby resulting in longer hydrocarbon chains as products.

By comparing the paraffin to olefin ratios obtained for the various samples with the linear to bridge CO intensity ratio measured by DRIFTS, it is worthwhile to note that the occurrence of a more intense bridge CO absorption band possibly suggests that the catalyst is more likely

to exhibit hydrogenation reactions, since a bridge adsorbed CO molecule has a weaker C–O bond, and therefore can be more easily hydrogenated. The HCo catalyst presented the strongest bridge CO adsorption and also the highest $CH_4$ selectivity. Hence, a higher relative concentration of bridge bonded CO species may possibly lead to a low $C_{5+}$ selectivity because these species are rapidly hydrogenated at the catalyst surface, leading to the formation of mainly $CH_4$. Overall results clearly point out that MnO at the surface of the $Co^0$ particles suppresses the formation of $CH_4$ by lowering the occurrence of hydrogenation reactions in the FT synthesis.

## Conclusions

The presence of manganese in $Co/TiO_2$ catalysts results in a decrease of the cobalt reducibility as a result of the intimate association between cobalt and manganese oxides. Hydrogen chemisorption in the reduced catalysts was strongly suppressed as a result of the coverage of cobalt by $TiO_x$ and MnO species. In this respect, the presence of small amounts of manganese was found to increase the available $Co^0$ surface, presumably by preventing the strong cobalt-$TiO_2$ interactions. The use of DRIFTS in combination with CO and $CO/H_2$ has demonstrated that manganese species remain at the surface of the cobalt particles after catalyst reduction, thereby altering the electronic properties of the $Co^0$ sites. $Mn^{2+}$ withdraws electron density from the $Co^0$ sites leading to a weaker CO bonding to the metal. This effect results in a lower hydrogenation rate during Fischer-Tropsch reaction and consequently to the formation of more olefins and $C_{5+}$ products. In addition, clear trends were found in the catalytic performances and DRIFTS CO absorption bands with increasing MnO loading in the $Co/TiO_2$ catalysts.

## Aknowledgements

Emiel de Smit is kindly acknowledged for his experimental work and contribution to this chapter. We thank Tom Visser and Fouad Soulimani for their help and support in the DRIFTS experiments.

## References

[1] T. Visser, T.A. Nijhuis, A.M.J. van der Eerden, K. Jenken, Yaying Ji, W. Bras, S. Nikitenko, Y. Ikeda, M. Lepage, B. M. Weckhuysen, *J. Phys. Chem. B,* 2005, **109,** 3822.

[2] J.W. Niemantsverdriet, Spectroscopy in Catalysis, (VCH, 1993).

[3] J.A. Anderson, M. Fernandez Garcia, Supported Metals in Catalysis, Catal. Sci. Series, Vol. 5, (Imperial College Press, 2005).

[4] A. Davydov, Molecular Spectroscopy of Oxide Catalyst Surfaces, (Wiley, 2003).

[5] B.M. Weckhuysen (Ed.), In-situ Spectroscopy of Catalysts, (American Scientific Publishers, 2004).

[6] Y. Marcus, Ion Properties, (Marcel Dekker, 1997).

[7] A.A. Davydov, M.P. Komarova, V.F. Anufrienko, N.G. Maksimov, *Kinet. Katal.,* 1973, **14**, 15.

[8] V.B. Kazanzsky, A.V. Zaitev, V.Yu. Borovkov, A.L. Lapidus, *App. Catal*., 1988, **40**, 17.

[9] B. Mothebe, D.J. Duvenhage, V.D. Sokolovskii et al., *Stud. Surf. Sci. Catal*., 1997, **107**, 1

[10] R.A. van Santen, P.W.N.M. van Leeuwen, J.A. Moulijn, B.A. Averill, Catalysis: An Integrated Approach, Second, revised and enlarged edition, (Elsevier, 1999) p.508.

[11] J. Ryczkowski, *Catal. Today*, 2001, **68**, 263.

[12] B.L. Mojet, J.T. Miller, D.C. Koningsberger, *J. Phys. Chem. B*, 1999, **103**, 2724.

[13] A.J. van Dillen, J.W. Geus, L.A.M. Hermans, J. Van der Meijden, *Stud. Surf. Sci. Catal,* 1997, **2**, 677.

[14] R.C. Reuel, C.H. Bartholomew, *J. Catal*., 1984, **85**, 63.

[15] J.L. Martin de Vidales, E. Vila, R. Rojas, O. Garcia-Martinez, *Chem. Matter.*, 1995, **7**, 1716.

[16] F. Morales, F.M.F de Groot, P. Glatzel, E. Kleimenov, H. Bluhm, M. Havecker, A. Knop-Gericke, B.M. Weckhuysen, *J. Phys Chem. B,* 2004, **108**, 16201.

[17] F. Morales, F.M.F. de Groot, O.L.J. Gijzeman, A. Mens, O. Stephan, B.M. Weckhuysen, *J. Catal.* 2005*,* **230,** 301.

[18] F. Morales, D. Grandjean, A. Mens, F.M.F. de Groot, B.M. Weckhuysen, 2005, *J. Phys. Chem. B.,* submitted.

[19] G.L. Bezemer, P.B. Radstake, U. Falke, H. Oosterbeek, A.J. van Dillen, K.P. de Jong, *J. Catal.,* 2006, **237**, 152.

[20] M. A. Vannice, *J. Catal.,* 1982, **11**, 225.

[21] G.L. Haller, D.E. Resasco, *Adv. Catal.,* 1989, **36**, 173.

[22] A.A. Davydov and N.Coville, *Russian Chemical Bulletin*, 1995, **44**, 1866.

[23] K. Nakamoto, Infrared and Raman Spectra of Inorganic and Coordination Compounds, Part B, Applications in Coordination, Organometallic, and Bioinorganic Chemistry, 5th Edition (Wiley, 1997).

[24] G.R. Fredriksen, E.A. Blekkan, D. Schanke, A. Holmen, *J. Phys. Chem.* 1993, **97**, 308.

[25] L.F. Liao, C.F. Lien, D.L. Shieh, M.T. Chen, J.L. Lin, *J. Phys. Chem. B,* 2002, **106**, 43.

[26] T. Riedel, M. Cleys, G. Schulz, G. Schaub, S. Nam, K. Jun, M. Choi, G. Kishan, K. Lee, *Appl. Catal, A,* 1999, **186**, 201.

[27] M.J. Keyser, R.C. Everson, R.L. Espinoza, *Appl. Catal A,* 1998, **171**, 99.

[28] E. Iglesia, *Appl. Catal. A*, 1997, **161**, 50.

# 7

# *In-situ* Soft X-ray Absorption Spectroscopy of Titania-Supported Cobalt Catalysts Promoted with Manganese Oxide


## Abstract

The reduction behavior of a series of $Co/TiO_2$ and $Co/Mn/TiO_2$ Fischer-Tropsch catalysts has been investigated by in-situ soft X-ray absorption spectroscopy (XAS). In-situ XAS measurements of the Co and Mn $L_{2,3}$ edges in the catalysts and in a $Co_3O_4$ material have been carried out during reduction treatments in $H_2$ at a pressure of 2 mbar and at temperatures up to 425˚C. Additionally, the catalysts have been measured after in-situ $H_2$ reduction at 0.5 bar and under FT conditions of 1 bar and $H_2/CO$ ratio of 2. The changes of Co and Mn 3d valences and the symmetries throughout the reduction process have been determined by comparison of the spectra with theoretical calculations based on the charge transfer multiplet code. Linear combinations of the reference spectra have led to an estimation of the average Co valence in the various spectra for the catalysts. $TiO_2$ is found to have a strong influence on the reducibility of the Co oxides, since unsupported $Co_3O_4$ is rapidly reduced to $Co^0$ at 425ºC and 2 mbar, whereas $Co_3O_4$ supported on $TiO_2$ is only reduced to a mixture of CoO and $Co^0$, even after 12 h at the same conditions. The presence of Mn further retards the reduction of the $TiO_2$-supported $Co_3O_4$ particles by decreasing the amount of $Co^0$. The oxidized $Co/Mn/TiO_2$ catalysts contain $Mn^{III}$ and $Mn^{IV}$ species, which are readily reduced to $Mn^{II}$ at temperatures lower than 300˚C and pressures of 2 mbar. Remarkably the $Mn^{III}$ and $Mn^{IV}$ species are reduce to $Mn^{II}$ even upon exposure of the catalysts to the X-ray beam at RT. Under conditions of 0.5 bar $H_2$ and 315 ºC the $Co_3O_4$ particles are largely reduced to $Co^0$. Finally, a slight re-oxidation of the cobalt surface was observed in the $Co/Mn/TiO_2$ catalyst after FT reaction, whereas no changes were detected for the $Co/TiO_2$ catalyst.

## Introduction

The use of in-situ techniques for the characterization of surfaces in heterogeneous catalysts is becoming an important tool to investigate these materials under reaction conditions. Photons in the range 100–1000 eV are suitable probes for the electronic structure of reacting surfaces. Their interaction with solid matter leads to photoabsorption processes, which can be detected by the electrons released typically from a surface depth of several nanometers, making the low-energy XAS technique surface sensitive. In recent years, it has become possible to perform XAS measurements at pressure ranges of 1–10 mbar [1], which allows the carrying out *in-situ* treatments of the catalysts (e.g., calcinations and reductions), providing useful information about the surface composition under conditions that are closer to the actual operating conditions. The $L_{2,3}$ XAS spectral shapes of the 3d transition metal oxides can be simulated accurately using the charge transfer multiplet code [2-4]. These calculations take into account the local symmetry and hybridization of the elements under study. In general, they reproduce the $L_{2,3}$ XAS very well, thereby yielding information on the local symmetry (octahedral vs. tetrahedral, high-spin vs. low-spin) including the crystal field values and symmetry dependent covalence [5].

In our study, *in-situ* XAS measurements during reduction treatments were carried out with a series of $Co/TiO_2$ and $Co/Mn/TiO_2$ catalysts and with a bulk $Co_3O_4$. With this work we aim to investigate the valences and symmetry of Mn and Co at different temperatures during the reduction and moreover, to evaluate the influence of $TiO_2$ support on the reducibility of the Co oxides due to the so-called metal–support interaction. Bazin and co-workers have performed similar experiments before on $Co/SiO_2$ catalysts [6]. In their study, they carried out the XAS measurements in a UHV chamber, which was coupled to another chamber for the sample treatments. However, this fact can significantly affect the cobalt sites. For instance, the changes in pressure/gas environment before and during the measurements can influence the average valence state of the cobalt sites. *In-situ* XAS studies on other catalyst system reveal that significant changes in the average valence can occur within oxide materials [7]. In this chapter we also present a new interesting approach in an attempt to study the cobalt oxidation state under "real" FT conditions; i.e., at 220 ºC, 1 bar and under $CO/H_2$ environment. In addition, the influence of Mn on the Co oxidation state during the FT reaction is evaluated.

## Experimental

### *Catalysts and materials*

A group of $TiO_2$-supported catalysts was synthesized using the homogeneous deposition precipitation (HDP) technique to load the Co, and incipient wetness impregnation (IWI) to load the Mn, as described in detail in Chapter 3. Commercial Degussa P25 titania (surface area of 45 $m^2/g$ and pore volume of 0.27 $cm^3/g$) was used as support material, and $Co(NO_3)_2.6H_2O$ (Acros Organics, p.a.) and $Mn(NO_3)_2.4H_2O$ (Merck, p.a.) were used as metal precursors. Two $Co/TiO_2$ catalysts denoted as H-Co1 (8.0 wt % Co) and H-Co2 (7.7 wt % Co) and two $Co/Mn/TiO_2$ catalysts denoted as H-CoMn1 (7.8 wt % Co and 2.6 wt % Mn) and H-CoMn2 (7.0 wt % Co and 2.2 wt % Mn) were used for the experiments. The Co and Mn loadings in the calcined samples were determined by X-ray fluorescence analysis (XRF) using a Spectro X-lab 2000 spectrometer. The high purity $Co_3O_4$ material was obtained from Merck and the MnO, $Mn_2O_3$ and $MnO_2$ reference compounds from Aldrich.

### *In-situ soft X-ray absorption spectroscopy*

The soft X-ray absorption spectra of the manganese $L_{2,3}$ edge (635–660 eV), cobalt $L_{2,3}$ edge (770–800 eV) and the titanium $L_{2,3}$ edge (450–470 eV) were measured at beamlines U56/2-PGM-2 and U49/2-PGM-1 at BESSY (Berlin). The spectral resolution of the monochromators was ~0.2 eV. The instrumentation for in situ XAS and XPS measurements is described elsewhere [8]. A stainless steel *in-situ* cell was used in which the powdered samples were fixed in a sample holder. The X-ray absorption spectral shape was measured with the ionized gas conversion total electron yield, which has a probing depth of approximately 4 nm. The electron yield signal was measured by applying a voltage of 27 V on the first aperture, which is electrically isolated from the cell. A schematic drawing and a photograph of the detector system are displayed in Fig. 1 and 2. With this detector Knop-Gericke and coworkers successfully bridged the 'pressure gap' for suitable XAS investigations in the soft energy range 250 eV $\leq h\upsilon \leq$ 1000 eV [9-11].

A first set of experiments on the beamline U56/2 were carried out during reduction treatments under a dynamic atmosphere (i.e., flowing in $H_2$). The H-Co1, H-CoMn1, and $Co_3O_4$ samples were inserted into the chamber, which was subsequently pumped down to vacuum. After approximately 5 min the chamber was brought under pure hydrogen (100 ml/min) using a mass flow controller. A gas mixing system regulated the flow and the total pressure at the sample position, which was 2 mbar during the experiments. After optimization of the signal, by tuning the slit size and the spot of the incoming beam, the temperature was increased from RT to 425 °C with a ramp of 5 °C/min. The ramp was temporary stopped at 300 °C, 350 °C and 425 °C to measure both Co and Mn L edges. The bulk $Co_3O_4$ was

measured at 385 °C in addition to the same temperatures used to measure the catalysts. In addition, the catalysts were held under a $H_2$ atmosphere at 425 °C for 12 h to evaluate further changes in the spectra as a function of reduction time.

In a second set of experiments on the U49/2 beamline, the H-Co2 and H-CoMn2 catalysts were initially reduced during 1 h under a flow of $H_2$ at 0.5 bar and 315 °C (temperature ramp of 5 °C/min) in a chamber for treatments. This chamber was coupled to another measurement chamber allowing the transfer under the same gas environment. The reduced samples were transferred to the measurement chamber after pumping down to 1 mbar pressure. After collecting the spectra, the samples were again transferred to the chamber for treatments, in which the reaction conditions were adjusted to 1 bar, 220 ºC, and $H_2$/CO flow (ratio of 2). The reaction was performed during 2 h, after which the samples were transferred to the measurement chamber under the same gas environment, after decreasing the pressure to 1 mbar. XAS spectra were then collected at the same FT conditions, but at pressures of 1 mbar. In all the experiments the out-flowing gas from the reactor was connected to a masspack in order to analyze the product composition.

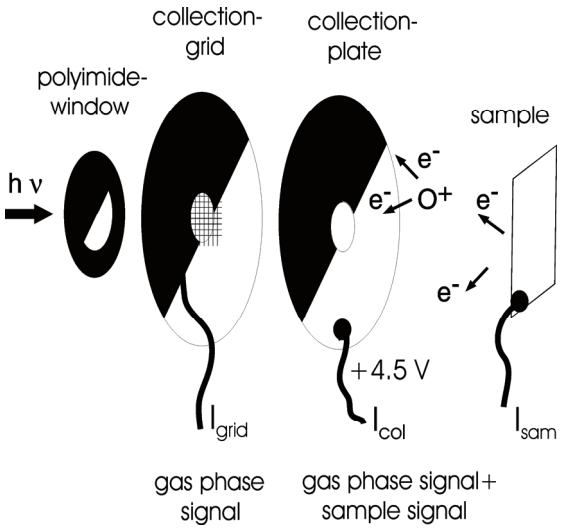


**Figure 1.** Detection scheme for *in-situ* XAS. The synchrotron radiation enters the reaction cell through the left window. The detection consists of two collector plates. Auger and secondary electrons originating from the sample are multiplied by interaction with the gas phase and detected by the plate on the right. On the second grid, which is shielded from the sample, the gas phase signal is measured. The picture was kindly provided by Axel Knop-Gericke.

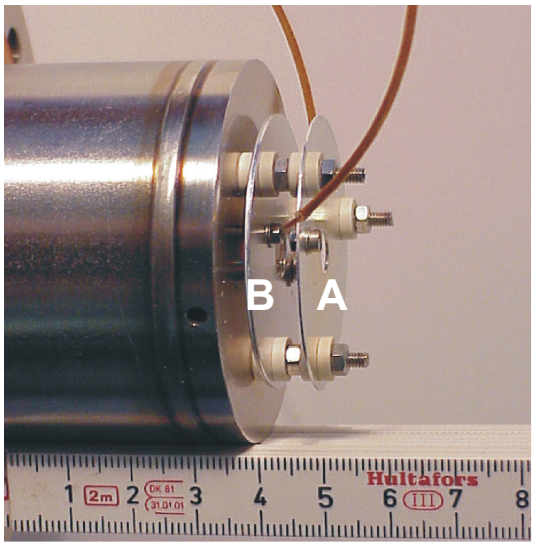


**Figure 2.** Photograph of the detection system for *in-situ* soft XAS. The radiation enters the reaction cell from the right. The position of the collection plates are indicated by (A) where all the Auger and secondary electrons are detected, and (B) where only the gas phase signal is measured. The photo was kindly provided by Axel Knop-Gericke.

## Results and discussion

### *XAS at the Co L-edges (pressures of 2 mbar)*

The Co $L_{2,3}$ edge spectra of the bulk $Co_3O_4$ material measured during the reduction treatment from RT up to 425 ºC are presented in Fig. 3. It can be observed that the shape of the spectra dramatically changes by increasing the temperature, while the maximum energy peak is shifting to a lower energy. These spectral changes are due to a shift from higher to lower cobalt valence and variations in the symmetry of the cobalt atomic states upon reduction. Comparison of the experimental spectra with the theoretical simulations (Fig. 2) lead to a better understanding of these spectral shapes. The spectrum measured at RT corresponds to a mixture of $Co^{II}$ and $Co^{III}$ oxidation states (ratio of 1/2) characteristic of $Co_3O_4$. Indeed, $Co_3O_4$ has a spinel type structure with the oxygen atoms arranged in a fcc structure, and $Co^{II}$ ($T_d$) and $Co^{III}$ ($O_h$) cations are located in tetrahedral and octahedral coordination, respectively [12]. As soon as the temperature increases, the shape of the spectra becomes more purely $Co^{II}$ since $Co_3O_4$ is reduced to CoO. In the CoO, the $Co^{II}$ cations are arranged octahedrally coordinated by oxygen atoms. When the temperature reaches 385 ºC, the measured spectrum corresponds to pure CoO, as revealed by a comparison with the reference sample (Fig. 4). This confirms the complete shift of cobalt to $Co^{II}$ ($O_h$) at 385 ºC. The consecutive reduction of CoO to $Co^0$ easily occurs at 425ºC, at which point the pure $Co^0$ spectrum is obtained. This spectrum consists of a single peak at the $L_3$ edge, characteristic of Co metal [13].

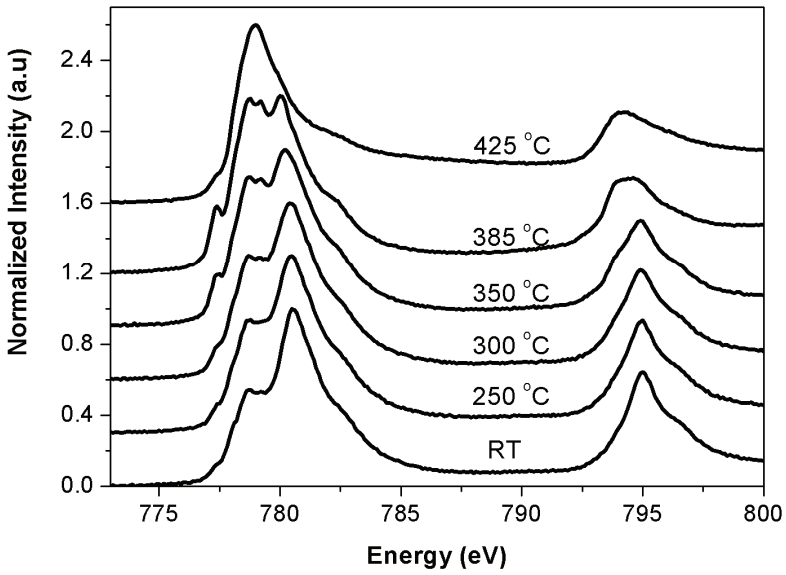


**Figure 3.** Co $L_{2,3}$ edges for bulk $Co_3O_4$ during reduction from RT to 425°C. All spectra have been normalized from zero to one.

Fig. 4 shows the Co 2p X-ray absorption spectra of CoO and $LiCoO_2$, together with the charge transfer multiplet (CTM) calculations of the cobalt sites. CoO contains octahedral $Co^{II}$ sites and $LiCoO_2$ contains octahedral $Co^{III}$ sites. The charge transfer parameters of the $Co^{II}$ ($O_h$) sites have been optimized to CoO, following the literature data [14]. These parameters are collected in Table 1. The CTM spectrum of $Co^{II}$ ($O_h$) includes the calculated energy-intensity multiplet spectrum. These stick spectra have been broadened with the 2p lifetime broadening and an experimental broadening that is assumed to be a Gaussian. The Lorentzian broadening is 0.4 eV for the $L_3$ edge and 0.8 eV for the $L_2$ edge. The Gaussian broadening is 0.4 eV. Similarly, the $Co^{II}$ ($O_h$) site has been optimized to $LiCoO_2$. In case of $LiCoO_2$ the agreement is not exactly correct, and the experimental spectrum has a clear shoulder at 781 eV and a less structured shoulder/peak at 785 eV.

A comparison of the CTM calculations of octahedral $Co^{III}$ and tetrahedral $Co^{II}$ with $Co_3O_4$ is presented in Fig. 5. These simulations confirm that $Co_3O_4$ indeed consists of octahedral low-spin ($^1A_1$) $Co^{III}$ and tetrahedral high-spin ($^4A_2$) $Co^{II}$ sites. Comparison to the $LiCoO_2$ specrum in Fig. 2 showed that also $LiCoO_2$ contains low-spin ($^1A_1$) $Co^{III}$ sites.

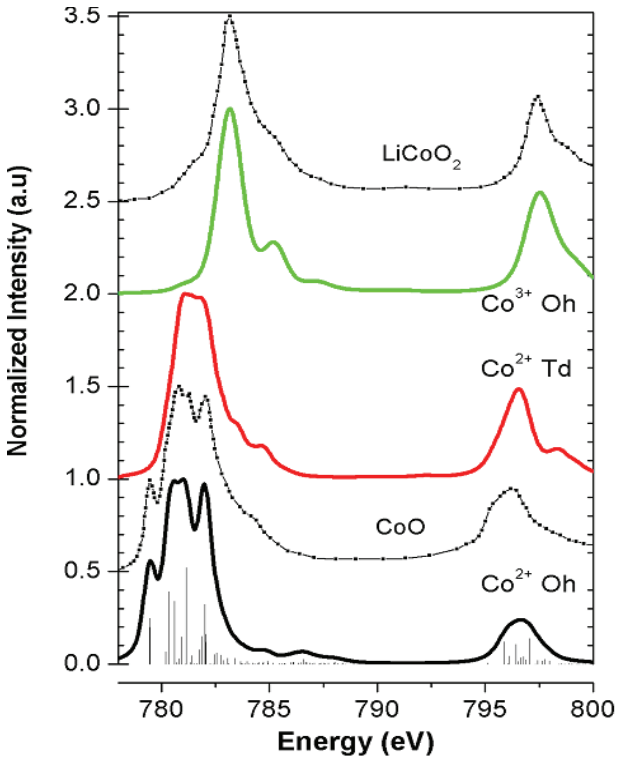


**Figure 4.** Co $L_{2,3}$ edges of the reference compounds $LiCoO_2$ and CoO, together with charge transfer multiplet (CTM) calculations of the cobalt sites. From bottom to top, the spectra are respectively, the CTM calculation of $Co^{II}$ ($O_h$), the CoO spectrum, the CTM calculation of $Co^{II}$ ($T_d$), the CTM calculation of $Co^{III}$ ($O_h$) and the $LiCoO_2$ spectrum. The CoO and $LiCoO_2$ spectra, reproduced from Ref. [11-12], are reproduced by the calculations shown below them.

**Table 1.** Charge transfer parameters used for the calculations of theoretical spectra.

| Parameter | CoO | $LiCoO_2$ | $Co^{II}$ in $Co_3O_4$ |
|---|---|---|---|
| site symmetry | $Co^{II}$ ($O_h$) | $Co^{III}$ ($O_h$) | $Co^{II}$ ($T_d$) |
| electronic symmetry | High-spin: $^4T_1$, split by spin-orbit to E' | low-spin: $^1A_1$ | high-spin: $^4A_2$, |
| ionic crystal field [10Dq] * | 0.6 | 1.9 | -0.3 |
| charge transfer energy [Δ]** | 3.0 | 4.5 | 7.0 |
| hopping $e_g$-electrons* [$t_e$] | 2.0 | 2.0 | 1.0 |
| hopping $t_{2g}$-electrons* [$t_t$] | 1.0 | 1.0 | 2.0 |

The addition of twice the spectrum of $Co^{III}$ plus once the spectrum of $Co^{II}$ is used to simulate the experimental spectrum of $Co_3O_4$. Some discrepancies are visible in the simulation, but these are mostly due to the imperfect simulation of the low-spin ($^1A_1$) $Co^{III}$ sites, as it was also the case for the $LiCoO_2$ spectrum in Fig. 2. Exactly like the $LiCoO_2$ spectrum, also $Co_3O_4$ has extra intensity at 781 eV and a less pronounced structure at 785 eV. Taking this into account, the simulations confirm that $Co_3O_4$ consists of octahedral low-spin ($^1A_1$) $Co^{III}$ and tetrahedral high-spin ($^4A_2$) $Co^{II}$ sites.

Fig. 6 shows the comparison of the CoO reference spectrum with the experimental spectrum of $Co_3O_4$ at 385 ˚C. Because the $L_3$ edge shows much more structure than the $L_2$ edge, we only show the $L_3$ edge region. The good agreement confirms that at 385˚C, $Co_3O_4$ is

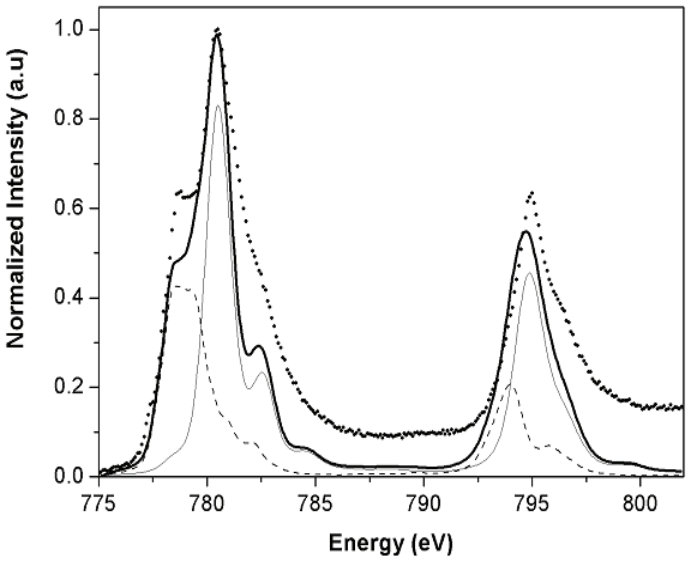


**Figure 5.** The CTM calculations of octahedral $Co^{III}$ (thin solid) and tetrahedral $Co^{II}$ (dashed). These spectra have been added with a 2:1 ratio (thick solid) to simulate the experimental $Co_3O_4$ spectrum (points).

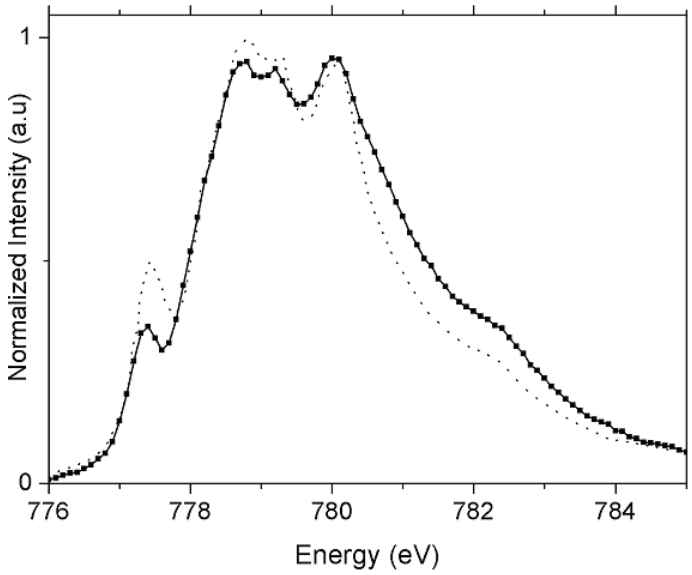


**Figure 6.** Comparison of the RT CoO reference spectrum (dotted) with the experimental spectrum of $Co_3O_4$ at 385˚C (solid, with solid squares).

indeed fully reduced to CoO. There are, however, some small differences visible. The shoulder at 777 eV is smaller in the reduced $Co_3O_4$ and the peaks at ~ 779-780 eV are slightly lower in the reduced $Co_3O_4$. A reason for these small differences can be found in the difference in measurement temperature between CoO reference (RT) and the $Co_3O_4$ sample (385 ˚C). It is known that the X-ray absorption spectra of CoO have temperature dependence due to the population of excited states [14-15]. In addition, it is likely that in the reduced $Co_3O_4$ the crystallinity of the CoO is not perfect and there will be some variation in site symmetry, oxygen vacancies, etc. These variations will make the resulting spectrum slightly different and may explain the small differences observed.

In conclusion, it is found from the reference compounds and from the CTM calculations that $Co_3O_4$ is a mixture of octahedral ($^1A_1$) $Co^{III}$ and tetrahedral ($^4A_2$) $Co^{II}$ sites. During reduction, the $Co^{III}$ is reduced to octahedral ($^4T_1$) $Co^{II}$; in addition, the tetrahedral ($^4A_2$) $Co^{II}$ sites are modified into octahedral ($^4T_1$) $Co^{II}$ sites in CoO. All spectra at intermediate temperatures can be considered as a linear combination of the spectra of $Co_3O_4$ and CoO.

The Co $L_{2,3}$ edges of the catalysts were measured at 25, 300, 350, and 425 °C, in addition to another measurement performed after 12 h at 425°C. It was found that the reduction behavior was rather similar in both catalysts, but significantly different to the bulk cobalt oxide discussed above. As an example, we show the spectra of the $Co/Mn/TiO_2$ catalyst in Fig. 7. At RT the spectra of both catalysts correspond to (mainly) $Co_3O_4$. The reduction of $Co_3O_4$ to CoO is achieved at lower temperatures than in the bulk $Co_3O_4$. This might be due to the lower cobalt content in the catalyst, which results in less time needed to achieve the complete reduction to CoO. In none of the catalysts did the CoO compounds significantly

reduce to $Co^0$ at 425˚C. Instead, the spectra consist mainly of CoO with only a small amount of $Co^0$. These results indicate that CoO supported on $TiO_2$ is difficult to reduce to $Co^0$ at the conditions used in this experiment (i.e., 2 mbar of $H_2$ at 425˚C).

To quantify the changes of the Co valence throughout the reduction, linear combinations of the spectra of the pure Co compounds were used to calculate the Co average valence at each temperature. For these calculations, the experimental spectra of bulk cobalt measured at RT, 385, and 425 ˚C were used as the spectra of the pure $Co_3O_4$, CoO and $Co^0$ compounds, respectively. Hence, the change of cobalt valence with temperature could be monitored and compared in both the catalysts and the bulk $Co_3O_4$ during the reduction. Fig. 8 shows a comparison of the bulk $Co_3O_4$ with the H-CoMn1 catalyst. It can be observed that unsupported $Co_3O_4$ is reduced to $Co^0$ at 425°C, in contrast with the $TiO_2$-supported cobalt catalyst that is only partly reduced under the same conditions. Furthermore, some differences in the amount of cobalt metal were found between both catalysts after the full reduction. The surface Co compositions were calculated for both catalysts after 12 h of reduction at 425 ˚C. The compositions obtained were 39 % $Co^0$ and 61 % CoO for the H-Co catalyst and 25 % $Co^0$ and 75 % CoO for the H-CoMn catalyst. Therefore, the presence of Mn in the catalyst was found to decrease the amount of $Co^0$ obtained after $H_2$ reduction at a pressure of 2 mbar.

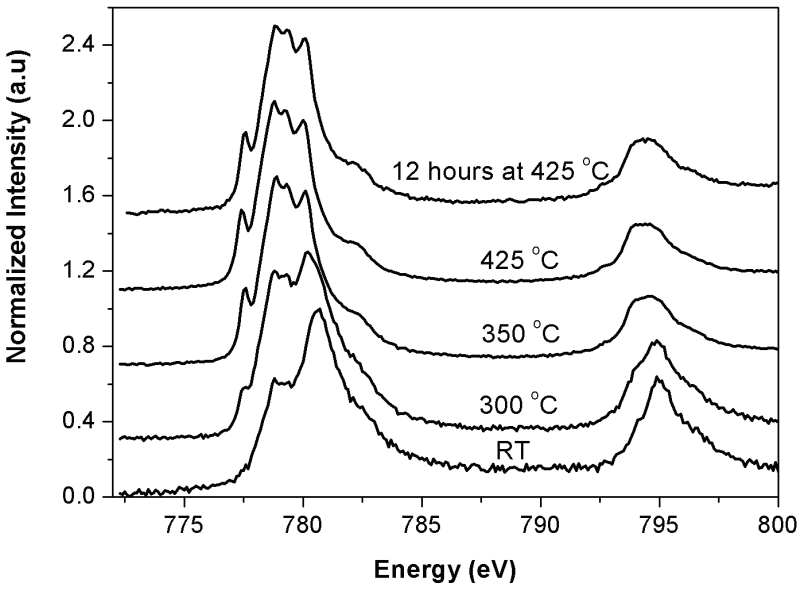


Figure 7: The Co $L_{2,3}$ edges measured for the H-CoMn catalyst during reduction. At RT the spectrum corresponds mainly to $Co_3O_4$, which is reduced to CoO at 350 °C. After 12 h of reduction at 425 °C the spectrum corresponds to CoO + $Co^0$.

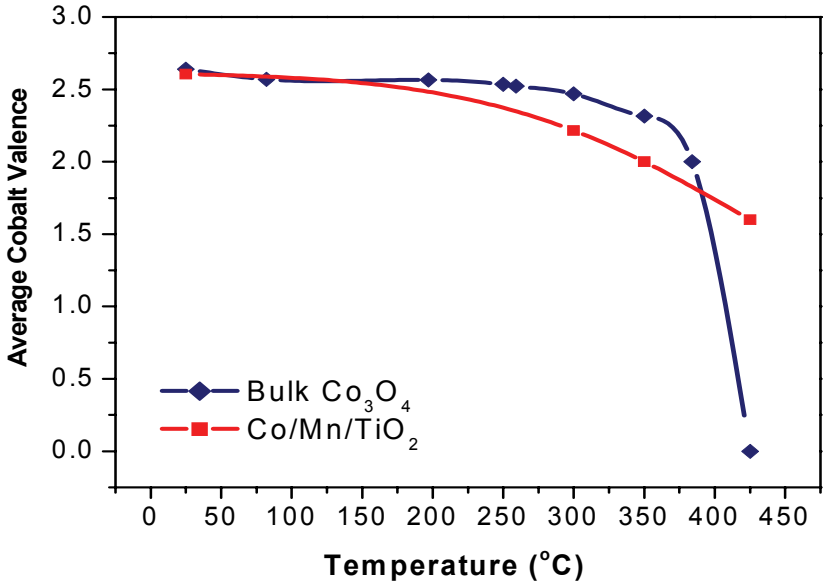


**Figure 8.** Comparison of the average Co valence for the bulk $Co_3O_4$ and the H-CoMn catalyst during the reduction treatment.

### *XAS at the Manganese L-edges (pressures of 2 mbar)*

The three manganese reference compounds were measured at RT in order to obtain the spectra of pure $Mn^{IV}$, $Mn^{III}$, and $Mn^{II}$. Fig. 9 presents the 2p X-ray absorption spectra of MnO, $Mn_2O_3$ and $MnO_2$ references. The Mn spectra can again be simulated using CTM calculations, as discussed previously [15]. We will now use these reference compounds in the analysis of the Mn spectra of the catalyst.

The Mn $L_{2,3}$ edges of the H-CoMn catalyst were measured at the same conditions as Co, at RT and during the reduction at 300, 350, and 425 ˚C. Changes in the shape of the spectra were found between RT and 300 ˚C, whereas the spectra did not change more by raising the

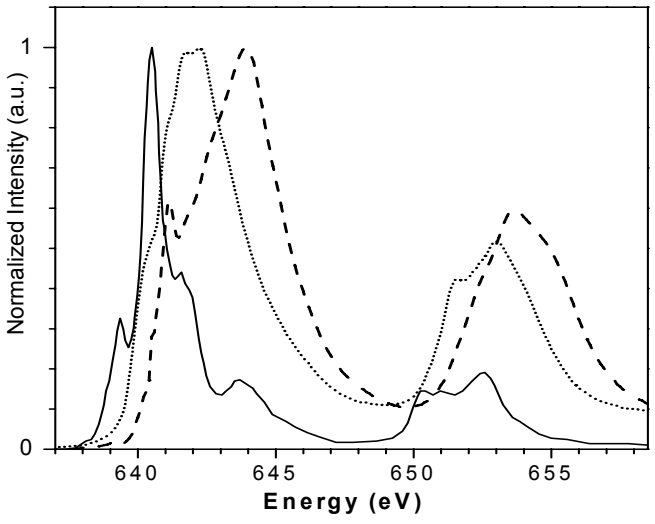


**Figure 9.** Mn $L_{2,3}$ edges of the manganese reference compounds MnO (solid), $Mn_2O_3$ (dots) and $MnO_2$ (dashed).

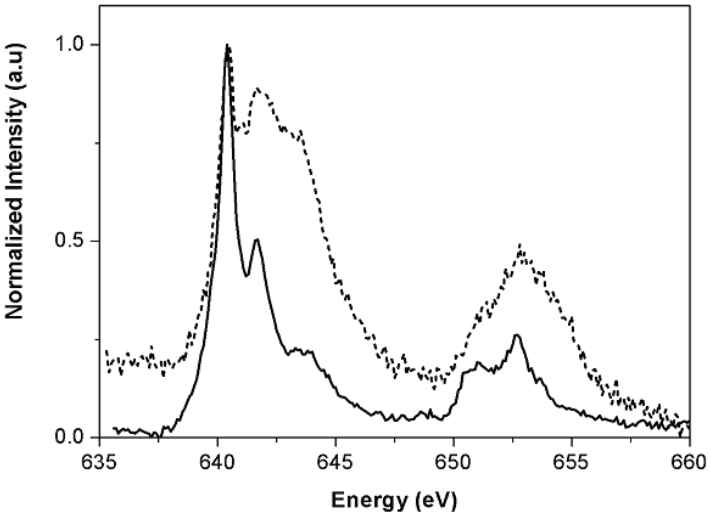


**Figure 10.** Mn $L_{2,3}$ edges of $Co/Mn/TiO_2$ catalyst before (dashed) and after (solid) the reduction treatment.

temperature above 300˚C. For this reason, we only show the spectra before and after the treatment (Fig. 10). By comparing the measured spectra of the catalyst with the reference compounds, it can be concluded that the Mn contained in the calcined catalyst consists of a mixture of $Mn^{II}$ and $Mn^{III}$, with some admixture of $Mn^{IV}$. Nevertheless, the spectral quality does not allow for an accurate quantification of the amount of each compound. The spectral shape indicates that $Mn^{III}$ is the predominant Mn species, which are most likely in the form of solid solutions $Co_{3-x}Mn_xO_4$ as discussed in chapter 3 and also reported in literature [13-14]. Upon reduction, the Mn present in the catalysts is fully reduced to $Mn^{II}$ already at 300 ºC, and no other variations are found in the spectra recorded at higher temperatures. The absence of the peak at 639 eV in the experimental spectra of the catalysts is due to a smaller value of the crystal field, which is influenced by defects in the crystal structure. These results indicate a high stability of $Mn^{II}$ at these reduction conditions in agreement with the EXAFS results presented in chapter 4, in which the manganese was found to be always in a $Mn^{2+}$ oxidation state, either forming MnO or $Ti_2MnO_4$ compounds.

The amount of $Mn^{IV}$ found for the oxidized H-CoMn catalyst is small and moreover, a $Mn^{II}$ component is detected, which is not in agreement with the hard x-ray EXAFS results. The spectra at the Mn K-edge (chapter 3) show that the H-CoMn1 calcined catalyst contains mainly a $MnO_2$ phase ($Mn^{IV}$), whereas some additional amounts of $Mn^{III}$ species are present mixed with the $Co_3O_4$ particles in the form of solid solutions $Co_{3-x}Mn_xO_4$. To understand this discrepancy between the EXAFS and soft XAS results, the Mn valence of a calcined $Co/Mn/TiO_2$ catalyst was monitored as a function of exposure time by the X-ray beam. This experiment was carried out with a catalyst containing 5 wt % Mn and 20 wt % Co, at RT, and at a pressure of 1 mbar. The spectra collected at the Mn $L_3$ edge during approximately the first 10 min are shown in Fig. 11. It is clear noticed that the spectral shape changes rapidly, the

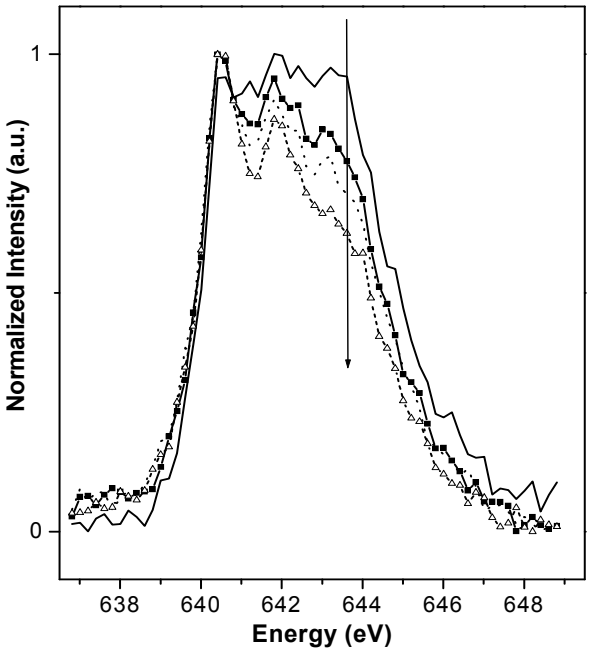


**Figure. 11.** Mn $L_3$ edge for an oxidized $Co/Mn/TiO_2$ catalyst as a function of exposure time by the X-ray beam. First spectrum (solid line), after 2 min (solid line with squares), after 4 min (dotted line), after 6 min (dashed line with triangules).

spectra becoming more reduced as a function of exposure time. It is observed that the first spectrum corresponds mainly to a mixture of $Mn^{IV}$ and $Mn^{III}$ species, whereas by increasing the exposure time the $Mn^{II}$ component (with a single sharp peak at 640 eV) becomes more dominant. These results indicate the reduction of the Mn species due to the X-ray beam. The Mn species in the catalysts are therefore, very sensitive to the X-ray beam and readily reduce to $Mn^{II}$ state within a short exposure time. This interesting finding also suggests that for the H-CoMn catalysts shown in Fig. 10, the spectrum obtained at the Mn K-edge before the reduction is most likely already affected by the X-ray beam. For this reason, the spectrum contains an unexpected $Mn^{II}$ component, taking into account the EXAFS results at the Mn K-edge (chapter 3). The variation of metal valence due to an influence of the beam seems to be a more general phenomenon, which has been also encountered by other authors. Similarly, in a recent work Mesu *et al.* reported on the reduction of copper upon exposition with hard X-rays [16].

***XAS measurements under Fischer-Tropsch conditions (pressure of 1 bar)***

To investigate the variations in the Co valence of the catalysts surface under Fischer-Tropsch conditions, the Co $L_{2,3}$ edges of the H-Co2 and H-CoMn2 catalysts were measured after reduction at a pressure of 0.5 bar. Subsequently, the catalysts were also treated under FT synthesis conditions and measured in-situ under reaction conditions. Soft XAS spectra were collected after transferring the samples to the measurement chamber and maintaining the

same gas environment and temperature, although at lower pressures of 1 mbar. The obtained spectra for both the $Co/TiO_2$ and Mn-promoted $Co/TiO_2$ catalysts were compared in order to investigate the influence of Mn promoter on the Co valence at the surface of the Co particles. Fig. 12 presents the spectra for the H-Co2 and H-CoMn2 catalysts after reduction and during FT reaction. It is observed that reduction of the Co oxide to Co metal, under the conditions employed (i.e., 0.5 bar $H_2$ and 315 ºC), is almost fully achieved in both catalysts. This is confirmed when comparing the spectral shape for the catalysts with that for the $Co_3O_4$ reference material reduced at 425 ºC (Fig. 3), which is composed of a single peak without any features, characteristic of metallic cobalt. Furthermore, the Mn-promoted catalyst is slightly less reduced than H-Co2 as revealed by the less sharp spectral shape. This result in line with the reduction studies at pressures of 2 mbar shown above, from which it was concluded that the manganese retards the cobalt reducibility at the surface of the catalysts. On the other hand, it is interesting to notice that the spectra obtained after FT reaction reveal some changes occurring in the average Co valence, although only for the H-CoMn2 catalyst. It is observed that a slight re-oxidation of the H-CoMn2 catalyst is reflected in the spectra by the appearance of some features at 776.2 and 779.0 eV, corresponding to a $Co^{II}$ state. For the H-Co2 catalyst, however, no significant changes are observed in the comparison of the spectra measured after reduction and after FT reaction. Hence, the occurrence of a re-oxidation at the surface of the Co particles appears to be induced by the presence of manganese oxide species in the catalyst. The manganese existing in a $Mn^{2+}$ oxidation state has been earlier shown by STEM-EELS and EXAFS to exist in a highly dispersed state as $Ti_2MnO_4$ covering the $TiO_2$ surface and also mixed at the surface of the Co nanoparticles in the form of solid solutions $Mn_{1-x}Co_xO$. For details concerning these results we refer to chapter 5 and to other published works [17-19].

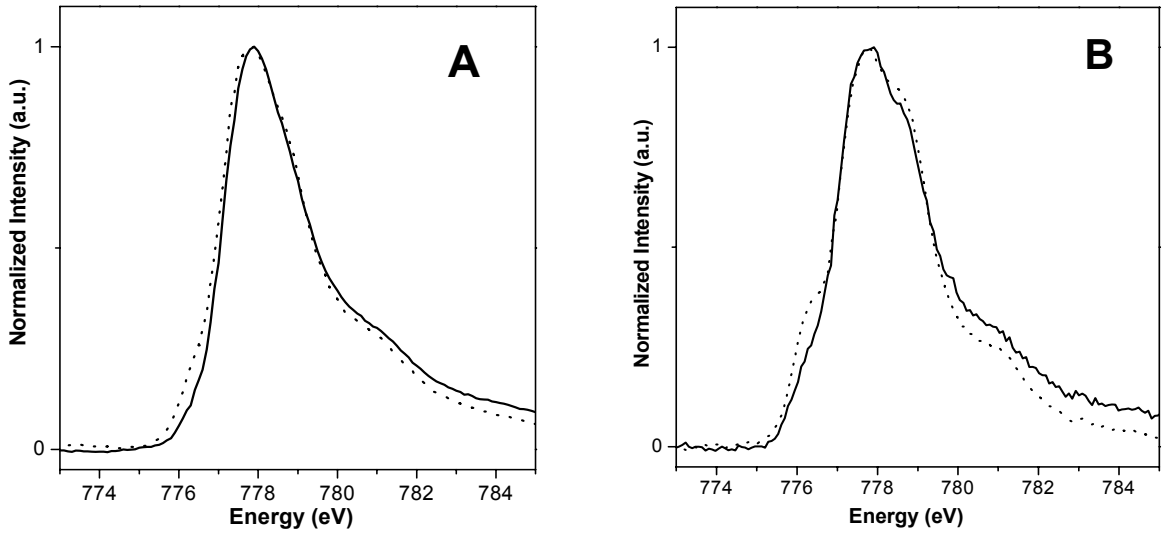


**Figure 12.** Co $L_3$ edge spectra of the H-Co2 (A) and H-CoMn2 (B) catalysts after reduction in $H_2$ at 0.5 bar and 315 ºC during 2 h (solid line), and after 3 h FT reaction at 1 bar and 220 ºC (dotted line).

## Discussion

The use of soft X-ray absorption spectroscopy as a tool for studying the composition of catalyst surfaces can be of great interest for determining the oxidation state of 3d transition metals during the activation of the catalysts. Moreover, the fact that most catalytic reactions take place at the surface of the metal particles makes this technique very attractive for studying catalytic systems, since the information obtained corresponds to a depth of a few nanometers into the metal surface, and not to the bulk. Nevertheless, the low-pressure conditions (1-5 mbar) required to perform these measurements are still far from the actual operation conditions (1 bar or higher). Therefore, the information obtained with the XAS technique cannot be directly correlated with that from other characterization techniques. Additionally, other problems may be encountered when an accurate determination of the valence of some metals is aimed, e.g., the Mn valence of Co/Mn/$TiO_2$ FT catalysts have been found to be affected by the X-ray beam, resulting in a premature reduction. This also indicates that $Mn^{II}$ is the most stable species and are always present in the catalysts after reduction.

The analysis of the XAS spectra allowed us to calculate the valences of both transition metals, which play a role during FTS reaction (i.e., Co and Mn), after reduction and under FT reaction conditions. It turned out that the $TiO_2$ support has a strong influence on the reduction behavior of the cobalt oxides, since CoO could not be largely reduced to $Co^0$ in none of the supported catalysts at pressures of 2 mbar, whereas a bulk $Co_3O_4$ material could be fully reduced to metallic Co at the same conditions. Hence, it is reasonable to consider the occurrence in the catalysts of strong cobalt–support interactions (SMSI), which makes it difficult for the CoO reduction to occur in the presence of $TiO_2$ support. As reported in literature [20-21], SMSI are likely to occur with the $TiO_2$ support when using high reduction temperatures, at which migration of $TiO_x$ over-layers onto the Co surface may result in a suppression of the Co reducibility. Since, the reduction treatments were performed at temperatures of 425 ºC, most likely SMSI are taking place in the catalysts. The low $H_2$ pressures of 2 mbar employed is, furthermore, not sufficient to achieve a high Co reduction extent. As a result both catalysts reduced at pressures of 2 mbar, contain mixtures of CoO and $Co^0$ and thus, the samples can be ordered, from most to least metallic, as follows: $Co_3O_4$ > H-Co1 > H-CoMn1. We can therefore conclude that both $TiO_2$ and Mn have a negative effect on the reducibility of the Co surface. The presence of Mn in the catalyst further decreases the Co reducibility at 2 mbar conditions. We note that the presented results do not allow judging exactly what kind of mixture between $Co^0$ and $Co^{II}$ exists. Possible options are physical mixture of Co and CoO, the existence of another phase, for example a sub-oxide and/or a changed microstructure. Here we note that the CoO nanoparticles are quite small (~2-10 nm) and in case of a mixed metal-oxide particle there will be a significant percentage of cobalt

atoms that will neither feel a potential as pure Co (nanosize) metal or that of pure CoO. The only conclusion we would like to draw is the measured ratio of Co to CoO, which best explains the observed spectral shape.

Finally, a similar trend with respect to the Co reducibility is found from the reduction experiments at 315 °C and 1 bar. At these reduction conditions the catalysts are largely reduced to $Co^0$ in percentages rounding 90 %. The presence of Mn in the $Co/Mn/TiO_2$ catalyst again further retards the reduction of the Co particles. Upon the Fischer-Tropsch synthesis the $Co/Mn/TiO_2$ catalyst undergoes a slight re-oxidation at the surface of the Co particles. This phenomenon results from the intimate contact of the CoO and MnO phases. It has been shown extensively that the bulk cobalt and manganese phases exist mixed in the form of solid solutions (i.e., $Mn_{1-x}Co_xO$) at the surface of the Co nanoparticles [17-19].

## Conclusions

$TiO_2$ strongly influences the reduction behavior of $Co_3O_4$ particles by decreasing the extent of reduced cobalt present at the catalyst surface after reduction. This decrease in Co reducibility is less pronounced at conditions of higher pressure and lower temperature. The results point towards the existence of a strong $Co\text{-}TiO_2$ (metal–support) interaction, which largely hampers the Co reducibility at the surface of the reduced catalysts. Manganese oxide contained in the $Co/Mn/TiO_2$ catalysts before reduction existed as a mixture of $Mn^{II}$, $Mn^{III}$, and $Mn^{IV}$ species, which readily reduced to $Mn^{II}$ at conditions of low $H_2$ pressure and temperatures lower than 300°C. Furthermore, the manganese species were found to be very sensitive to the X-ray beam, undergoing reduction to $Mn^{II}$ at RT in a matter of minutes. The presence of manganese oxide in the catalysts had an additional effect on the Co reducibility decreasing the final amount of $Co^0$ compared to the $Co/TiO_2$ catalyst. This manganese effect on the Co oxidation state was also observed under Fischer-Tropsch conditions, at which a slight re-oxidation of the surface of the Co nanoparticles to $Co^{2+}$ occurred, probably as a result of a intimate MnO interaction with the surface of the cobalt particles.

## Acknowledgements

The authors thank the BESSY staff (E. Kleimenov, H. Bluhm and M. Havecker) for their continual support during the XAS measurements at the synchrotron in Berlin. Mr. I. Boussadkat (Utrecht University) is kindly acknowledged for assisting with the theoretical calculations.

## References


[1] A. Knop-Gericke, M. Havecker, T. Schedel-Niedrig, R. Schlogl, *Top. Catal.,* 2000, **10**, 187.

[2] F.M.F. de Groot, J.C. Fuggle, B.T. Thole, G.A. Sawatzky, *Phys. Rev. B.,* 1990, **42**, 5459.

[3] F.M.F. de Groot, *J. Elect. Spectr. Rel. Phen.,* 1994, **67**, 529.

[4] F.M.F. de Groot, *Chem. Rev.,* 2001, **101**, 1779.

[5] E.C. Wasinger, F.M.F. de Groot, K.O. Hedman, K.O. Hodgson, E.I. Solomon, *J. Am. Chem. Soc.,* 2003, **125**, 12894.

[6] D. Bazin, I. Kovacs, L. Guczi, P. Parent, C. Laffon, F.M.C. de Groot, O. Ducreux, *J. Catal.,* 2000, **189**, 456.

[7] W.M. Heijboer, A.A. Battiston, A. Knop-Gericke, M. Havecker, R. Mayer, H. Bluhm, R. Schlogl, B.M. Weckhuysen, D.C. Koningsberger, F.M.C. de Groot, *J. Phys. Chem. B,* 2003, **107**, 13069.

[8] D.F. Ogletree, H. Bluhm, G. Lebedev, C.S. Fadley, Z. Hussain, M. Salmeron, *Rev. Sci. Instr*., 2002, **73***,* 3872.

[9] A. Knop-Gericke, M. Havecker, T. Schedel-Niedrig, R. Schlogl, *Top. Catal*., 2000, **10**, 187.

[10] A. Knop-Gericke, M. Havecker, T. Schedel-Niedrig, R. Schlogl, *Catal. Lett.,* 2000, **66**, 215.

[11] A. Knop-Gericke, F.M.F. de Groot, J.A. van Bokhoven, T. Ressler, In-situ Spectroscopy of Catalysts, B.M. Weckhuysen (Ed.), American Scientific Publishers, Stevenson Ranch, CA, USA, 2004, p.107.

[12] K.J. Kim, Y.R. Park, *Solid State Commun.,* 2003, **127**, 25.

[13] C.T. Chen, Y. Idzerda, H.J. Lin, N.V. Smith, G. Meigs, E. Chaban, G.H. Ho, E. Pellegrin, F. Sette, F. *Phys. Rev. Lett.,* 1995, **75**, 152.

[14] F.M.F. de Groot, M. Abbate, J. Van Elp, G.A. Sawatzky, Y.J. Ma, C.T. Chen, F. Stte, *J. Phys. Condens. Matter.,* 1993, **5**, 2277.

[15] F.M.F. de Groot, *PhD Thesis*, 1991.

[16] J. G. Mesu, A.M.J. van der Eerden, F.M.F. de Groot, B.M. Weckhuysen, *J. Phys. Chem. B* 2005, **109**, 4042.

[17] F. Morales, D. Grandjean, F.M.F. de Groot, O. Stephan, B.M. Weckhuysen, *Phys. Chem. Chem. Phys*., 2005, **7**, 568.

[18] F. Morales, F.M.F. de Groot, O.L.J. Gijzeman, A. Mens, O. Stephan, B.M. Weckhuysen, *J. Catal.,* 2005, **230,** 301.

[19] F. Morales, D. Grandjean, A. Mens, F.M.F. de Groot, B.M. Weckhuysen, Submitted for publication in *J. Phys. Chem. B*.

[20] M.A. Vannice, *J. Catal*., 1982, **74**, 199.

[21] G.L. Haller, D.E. Resasco, *Adv. Catal*., 1989, **36**, 173.

# 8

# Summary and Concluding Remarks

An increasing demand for clean motor fuels and the recent rise of the crude oil prices are certainly causing an important shift, from crude oil to natural gas as feedstock for chemical industries. This shift involves the use of Fischer-Tropsch (FT) technology, in which high molecular weight hydrocarbons are synthesized from $CO/H_2$ mixtures through a surface-catalyzed polymerisation reaction using mostly Co-based FT catalysts. FT synthesis making use of Co-based catalysts has become a hotly pursued scientific topic in the catalysis community since it offers an interesting and economically viable route for the conversion of *e.g.* natural gas to sulphur-free diesel fuels. As a result, major oil companies have recently announced to implement this technology and major investments are under way to build large FT plants based on cobalt-based catalysts in *e.g.* Qatar.

Co-based FT catalysts generally consist of well-dispersed cobalt nanoparticles supported on e.g. $TiO_2$, $SiO_2$ or $Al_2O_3$, which are, nowadays, the support materials of choice for industrial applications. In addition, the catalysts are often loaded with small amounts of promoters, which alter their catalytic properties and thus, enhance their overall catalytic performances and catalyst lifetime. Due to the importance of promotion for developing novel catalyst materials, we have analyzed in the open literature almost every chemical element of the periodic table for its potential beneficial effects on the activity, selectivity and stability of supported cobalt catalysts. The efforts of this literature survey on promoters for cobalt-based FT catalysts were presented in **chapter 2**. In this review we made a classification of promoters on the basis of their mode of action, as following: (1) *structural promoters* affect directly the formation and stability of the active cobalt phase by altering the cobalt-support interfacial chemistry (e.g. Re, Pt, Rh and Ru) (2) *electronic promoters* affect directly the elementary steps involved in the turnover of the cobalt active site by altering the electronic properties of the cobalt nanoparticles (e.g., Ru, V, Mg and Ti) and (3) *synergistic promoters* affect indirectly the behaviour of the active cobalt phase, by changing the local reaction environment of the active site as a result of chemical reactions performed by the promoter element itself (e.g., Ni, Zr and La). Highlights reported in the literature on promotion were summarized, and special attention was given to our case study, the manganese promoter.

Research work described in this thesis aims to investigate MnO-promoted $TiO_2$-supported Co FT catalyst systems for the transformation of syngas into high weight hydrocarbon waxes. The main objectives have been to unravel the role played by manganese as a FT promoter and its influence on the physicochemical and catalytic properties of the Co active phase. An important goal has been to determine the chemical state and location of manganese after the main preparation steps involved in the preparation (i.e., calcination and activation). To this end we have made use of multiple powerful spectroscopic techniques, which have revealed new insights into the composition and structure of these catalyst materials. Furthermore, the

catalytic behavior in the FT reaction has been carefully evaluated in order to rationalize the results and to assess structure-performance relationships.

The first stage of research has focussed on the catalyst synthesis aiming to prepare suitable materials to study manganese promotion on $Co/TiO_2$ catalysis. The preparation of various $Co/Mn/TiO_2$ catalysts by either incipient wetness impregnation (IWI) or homogeneous deposition precipitation (HDP) has been described in **chapter 3.** The catalysts were characterized after calcination by XRD, XPS, STEM-EELS and XAFS. By varying the preparation method we succeeded in obtaining different $Co/Mn/TiO_2$ materials with manganese placed in all possible locations. All catalysts after calcination consisted of $TiO_2$-supported $Co_3O_4$ clusters with a variable range of sizes around 12 to 35 nm. The extent of manganese interaction with the Co phase was largely dependent on the preparation method: catalysts prepared stepwise by IWI contained a $MnO_2$ phase dispersed on the $TiO_2$ surface, whereas those prepared by HDP contained a $MnO_2$ phase mostly covering the $Co_3O_4$ particles and with some $Co_{3-x}Mn_xO_4$ solutions present at the interface. This type of spinel mixed Co-Mn oxides could be synthesized more homogeneously by co-precipitating both Co and Mn precursor salts in a single HDP step. All the Mn structures identified by EXAFS were nicely visualized in elemental chemical maps produced by STEM-EELS.

In **chapter 4** we have investigated the chemical state and morphology of the cobalt active phase in the different catalysts after performing reduction treatments. In situ XAFS measurements at the Co K-edge revealed that the catalysts are composed of variable mixtures of $Co^0$ and CoO, which ratio is largely dependent on the preparation method, reduction temperature, and presence and location of Mn. $Co^0$ particle sizes as estimated by EXAFS, TEM, and XPS were in excellent agreement and showed that the activation results in a dramatic decrease in the size of the Co particles, due to a re-dispersion of $Co^0$ over the $TiO_2$ during the reduction process. Manganese was found to decrease the bulk Co reducibility, this effect being more pronounced when manganese and cobalt were previously associated as mixed oxides. A direct consequence was that the excessive cobalt spreading was prevented in the Mn-promoted catalyst due to a decrease in the Co reducibility, and thus the catalysts turned out to have a larger Co particle size distribution. Correlation of the structural data and the FT catalytic results at conditions of 1 bar and 220 ºC showed that: (1) reduction at high temperatures may result in the occurrence of SMSI with $TiO_2$ leading to a decrease of both the activity and selectivity, (2) manganese when interacting with the cobalt phase induces an increase of the $C_{5+}$ selectivity as a result of the decrease of the amount of $Co^0$ in the catalysts, and (3) $Co^0$ particles larger than ~5 nm have a higher intrinsic activity (i.e., turnover frequencies) and are required in order to obtain a promotion effect from manganese.

A study of the chemical state and location of manganese was presented in **chapter 5** using a combination of STEM-EELS and XAFS at the Mn K-edge. In this chapter we reported that manganese largely segregates during the reduction process forming multiple compounds by interaction with the $TiO_2$ and/or the Co phases. The XAFS results after in situ reduction showed that manganese tends to spread out at the catalyst surface forming a $Ti_2MnO_4$-type phase, thus being lost for catalyst. Manganese was also found to exist as MnO particles in the vicinity of the $Co^0$ sites as well as mixed at the surface of Co particles in the form of $Co_{1-x}Mn_xO$. The latter species were demonstrated to play directly a role as electronic promoters, leading to improvements in FT selectivity. A case study using quantitative XPS was included to illustrate the migration of MnO from the top of the Co particles towards the $TiO_2$ surface upon reduction to $Co^0$.

In **chapter 6** we aimed to investigate the cobalt active sites on $Co/Mn/TiO_2$ catalysts containing different MnO loadings. Using DRIFTS in combination with CO and $CO/H_2$ probe molecules, and additionally XRD, TPR, TEM and $H_2$-chemisorption techniques, we have evaluated the effect of MnO on the adsorption properties of the Co nanoparticles. It was shown that $H_2$ uptake was strongly suppressed in the reduced catalysts, most likely due to the coverage of the Co sites by $TiO_x$ species. In this respect, the addition of small amounts of manganese increased the available $Co^0$ surface by decreasing the Co-$TiO_2$ interaction and thus preventing the occurrence of a strong metal support interaction effect with $TiO_2$. With the DRIFTS results we confirmed that MnO species cover the surface of the $Co^0$ particles in the working catalysts, altering the electronic properties of the Co sites, which were observed in the IR vibration bands. This effect resulted in a moderation of the hydrogenation reactions taking place during the FT synthesis, and consequently in the production of more olefins and $C_{5+}$ products. The usefulness of the DRIFTS technique with probe molecules to monitor the FT reaction has clearly been illustrated.

Finally, in **chapter 7** we reported on the use of *in situ* soft X-ray absorption spectroscopy as a novel technique to investigate the surface composition of $Co/Mn/TiO_2$ catalysts during the activation process and under "working" FT conditions. A main conclusion was that $TiO_2$ strongly influences the reduction behavior of the $Co_3O_4$ particles by decreasing the amount of Co metal at the surface of the catalysts. This effect was ascribed to the occurrence of strong metal support effects leading to the coverage of the Co nanoparticles by $TiO_x$ species and consequently to the protection against reduction. Furthermore, the presence of MnO in the catalysts was shown to influence the cobalt surface oxidation state in the reduced catalysts, leading to a less metallic behavior of the Co active particles.

Based on the results obtained in this thesis some main conclusions can be drawn on $Co/TiO_2$ Fischer-Tropsch catalysts promoted with manganese oxide:

a. MnO-promoted $TiO_2$-supported Co catalysts are extremely complex systems due to the large number of possible compounds involved, which are formed due to the interaction between the Co active phase and promoter or support material (e.g. $Co_{3-x}Mn_xO_4$, $Ti_2MnO_4$, $Co_{1-x}Mn_xO$, $CoTiO_3$). The presence of complex mixtures of active (e.g. $Co^0$ and MnO) and spectator (e.g. $Ti_2MnO_4$) species heterogeneously distributed at the catalyst surface makes the characterization a challenging task, which can be best overtaken by combining spectroscopic and microscopic techniques, which provide complementary information.
b. Manganese, when decorating as an oxide layer on top of the surface of the active $Co^0$, is clearly able to induce an electronic effect. This electronic promotion is evident from the effect on the catalyst selectivity, as well as by the CO IR adsorption properties (frequency shifts in metal-adsorbed CO and CO linear vs. bridged intensity ratio). Consequently, Mn-Co FT catalysts possess decreasing hydrogenation properties compared to Co FT catalysts, causing a shift in the product distribution towards more olefinic, and increasing the $C_{5+}$ production. In addition, an increase of the intrinsic activity (i.e., TOF) of the Co particles for Mn-promoted catalysts was found.
c. Besides the electronic promotion effect, Mn may also induce structural and synergistic promotion effects. When Mn is initially associated with the $Co_3O_4$ phase, it directly affects the Co phase formed during reduction by decreasing the Co reducibility and consequently the extent of segregation of the Co phase over the $TiO_2$ surface. In addition, Mn may prevent the loss of Co active phase by protecting it from forming $Ti_2CoO_4$ phases. Moreover, Mn possesses WGS behavior and therefore can be regarded as a WGS promoter. One could therefore state that Mn-promotion makes supported Co nanoparticles more “Fe-like”.
d. Manganese promotion effects are clearly obtained in catalysts containing large $Co^0$ particles (>~5 nm). Smaller $Co^0$ particles are in turn, prone to deactivate during FT reaction due to the coverage by $TiO_x$ or MnO species.

# 9

# Nederlandse Samenvatting

Een toenemende vraag naar schone brandstoffen en de recente prijsstijging van ruwe aardolie veroorzaken een belangrijke verschuiving van ruwe aardolie naar aardgas als grondstof voor de chemische industrieën. Deze verschuiving impliceert het gebruik van de Fischer-Tropsch (FT) technologie, waarin hoogmoleculaire koolwaterstoffen worden gesynthetizeerd uit $CO/H_2$ mengsels door een oppervlakte-gekatalyseerde polymerisatiereactie die plaatsvindt op o.a. kobalt nanodeeltjes. Het onderzoek naar kobalt-gebaseerde FT-katalysatoren is een populair wetenschappelijk onderwerp aangezien het een economisch haalbare route biedt voor de omzetting van bijvoorbeeld aardgas in zwavelvrije diesel. Het is dan ook niet verwonderlijk dat belangrijke oliemaatschappijen onlangs hebben aangekondigd om deze technologie te gaan toepassen in o.a. Qatar.

De op kobalt-gebaseerde FT katalysatoren bestaan uit goed-gedispergeerde kobalt nanodeeltjes op een $TiO_2$-, $SiO_2$- of $Al_2O_3$-drager. Daarnaast worden deze katalysatoren vaak beladen met kleine hoeveelheden promotoren, die hun katalytische prestaties en levensduur verbeteren. In de open literatuur wordt bijna elk chemisch element van het periodiek systeem als promotor onderzocht op zijn potentiële gunstige effecten voor de activiteit, de selectiviteit en de stabiliteit van de kobalt nanodeeltjes. Een gedetailleerd literatuuronderzoek over promotorelementen voor kobalt-gebaseerde FT-katalysatoren is beschreven in **hoofdstuk 2**. In dit overzicht maken wij een classificatie van promotoren op basis van hun werkwijze, bijvoorbeeld: (1) structurele promotoren beïnvloeden direct de vorming en de stabiliteit van de actieve kobaltfase door de kobaltgrensvlakchemie te veranderen (b.v. Re, Pt, Rh en Ru), (2) elektronische promotoren beïnvloeden direct de elementaire stappen betrokken bij de katalytische omzetting door de elektronische eigenschappen van de kobalt nanodeeltjes te veranderen (b.v. Ru, V, Mg en Ti) en (3) synergistische promotoren beïnvloeden indirect het gedrag van de actieve kobaltfase door het lokale reactiemilieu rond de actieve plaats te veranderen (b.v. Ni, Zr en La).

Het onderzoekswerk dat in dit proefschrift wordt beschreven heeft tot doel om MnO-gepromoteerde $TiO_2$-gedragen kobalt FT-katalysatoren te onderzoeken voor de transformatie van synthesegas in hoogmoleculaire koolwaterstoffen. We willen hierbij nagaan wat de rol is van mangaan als promotor op de fysicochemische en katalytische eigenschappen van de kobaltfase. Een belangrijk aspect hierbij is het bepalen van de chemische eigenschappen en exacte positie van mangaan na verschillende bereidingsstappen. Daarvoor hebben wij van een aantal krachtige spectroscopische en microscopische technieken gebruik gemaakt. Vervolgens is het katalytische gedrag zorgvuldig geëvalueerd om de resultaten te vertalen in kwalitatieve structuur-activiteitsrelaties.

Het eerste deel van het onderzoekswerk focuseerde zich op de synthese en karakterisering verschillende MnO-gepromoteerde kobalt FT-katalysatoren. De bereiding van deze

$Co/Mn/TiO_2$ katalysatoren gebeurde door impregnatie (IWI) of homogene depositie-precipitatie (HDP). De verkregen resultaten staan beschreven in **hoofdstuk 3**. De katalysatoren werden na calcinatie gekarakteriseerd door XRD, XPS, STEM-EELS en XAFS. Door de bereidingsmethode systematisch te variëren konden verschillende $Co/Mn/TiO_2$ materialen worden bereid waarbij mangaan voorkwam op verschillende plaatsen in het katalysatormateriaal. Alle katalysatoren bestonden na calcinatie uit $TiO_2$-gedragen $Co_3O_4$-clusters waarbij hun clustergrootte varieerde tussen 12 en 35 nm. De mate van interactie tussen mangaan en kobalt wordt bepaald door de bereidingsmethode: IWI-bereide katalysatoren bevatten een $MnO_2$-fase die zich uitsmeert op het oppervlak van $TiO_2$, terwijl katalysatoren die bereid zijn door de HDP-methode een $MnO_2$-fase bevatten op het oppervlak van $Co_3O_4$- alsook een $Co_{3-x}Mn_xO_4$-fase. Deze laatste verbinding kan ook direct gemaakt worden door de zouten van kobalt en mangaan in één enkele stap te coprecipiteren. Alle verbindingen van mangaan die door EXAFS werden geïdentificeerd konden ook gevisualiseerd worden met STEM-EELS.

In **hoofdstuk 4** hebben we de chemische samenstelling van de kobalt nanodeeltjes in de verschillende katalysatoren na reductie nader bestudeerd. In-situ XAFS metingen hebben aangetoond dat de katalysatoren samengesteld zijn uit een mengsel van $Co^0$ en CoO, waarbij de verhouding tussen $Co^0$ en CoO afhankelijk is van de bereidingsmethode, de reductietemperatuur en de aanwezigheid/plaats van mangaan. De CoO deeltjesgroottes, bepaald door EXAFS, TEM en XPS, tonen aan dat reductie leidt tot een sterke daling van de grootte van de gedragen kobalt nanodeeltjes. Dit is hoogstwaarschijnlijk te wijten aan het uitspreiden van $Co^0$ over de $TiO_2$-drager tijdens het reductieproces. Daarnaast blijkt mangaan de reduceerbaarheid van de kobalt nanodeeltjes te verminderen. Dit effect is meer uitgesproken wanneer mangaan en kobalt als gemengd oxide aanwezig zijn. Katalytische metingen bij 1 bar en 220 ºC toonden aan dat: (1) hoge reductietemperaturen kunnen resulteren in het onstaan van SMSI met de $TiO_2$ drager wat tot een daling van zowel de activiteit als selectiviteit leidt, (2) mangaan in de nabijheid van de kobaltfase een verhoging van de $C_{5+}$-selectiviteit kan veroorzaken door een daling van het percentage van $Co^0$, en (3) $Co^0$-deeltjes groter dan ongeveer 5 nm een hogere intrinsieke katalytische activiteit hebben dan deeltjes die kleiner zijn dan 5 nm. Deze grootte is ook minimaal vereist om de promotoreffecten van Mn waar te nemen.

**Hoofdstuk 5** beschrijft het gebruik van een combinatie van STEM-EELS en XAFS om de chemische samenstelling en locatie van Mn te bepalen in gereduceerde kobalt-katalysatoren. Het blijkt dat veel verschillende fasen kunnen worden gevormd op het drageroppervlak. In-situ XAFS metingen tonen aan dat mangaan neigt om zich tijdens reductie op het katalysatoroppervlak uit te spreiden en een $Ti_2MnO_4$-fase te vormen. Deze fase is niet meer

beschikbaar voor promotie en kan dus voor de katalytische reactie als verloren beschouwd worden. Het mangaan werd ook gevonden als MnO-deeltjes in de buurt van de $Co^0$-clusters evenals op het oppervlak van de kobalt nanodeeltjes in de vorm van een $Co_{1-x}Mn_xO$-fase. Het zijn deze laatste fases die verondersteld worden een actieve rol te spelen in de promotering van de gedragen kobalt nanodeeltjes.

In **hoofdstuk** 6 hebben we de actieve plaats van $Co/Mn/TiO_2$ katalysatoren, die verschillende MnO-beladingen bevatten, meer in detail onderzocht. Gebruikmakend van DRIFTS met CO en $CO/H_2$ als testmoleculen, naast XRD, TPR, TEM en $H_2$-chemisorptie, hebben wij het effect van het MnO-gehalte op de adsorptie-eigenschappen van kobalt nanodeeltjes bestudeerd. Het blijkt dat de $H_2$-opname sterk verminderd was in de gereduceerde kobaltkatalysatoren, waarschijnlijk door de gedeeltelijke bedekking van de kobalt nanodeeltjes door $TiO_x$. Daarnaast leidt toevoeging van kleine hoeveelheden mangaan tot een verhoging van het beschikbare kobaltoppervlak door een vermindering van de Co-$TiO_2$ interactie. DRIFTS toonde verder aan dat MnO de elektronische eigenschappen van de kobalt nanodeeltjes kan beinvloeden en dat dit effect direct resulteerde in een vermindering van de hydrogeneringsreacties die tijdens de FT-synthese plaatsvinden. Een gevolg hiervan is een verhoogde productie van olefinen en $C_{5+}$-producten. Het nut van DRIFTS om de FT-reactie te volgen werd hierbij duidelijk geïllustreerd.

Tot slot beschrijven we in **hoofdstuk 7** het gebruik van spectroscopie met zachte in-situ röntgenstralen als nieuwe techniek om de oppervlaktesamenstelling van $Co/Mn/TiO_2$ katalysatoren te onderzoeken tijdens de reductie- en FT-reactie. Een conclusie is dat de $TiO_2$-drager sterk het reductiegedrag van gedragen $Co_3O_4$-deeltjes beïnvloedt. Dit effect wordt toegeschreven aan de sterke interactie tussen de kobalt nanodeeltjes en het drageroppervlak. Daarnaast werd aangetoond dat de aanwezigheid van MnO in de katalysatoren de oxidatietoestand van het kobaltoppervlak in gereduceerde katalysatoren beïnvloedt, wat tot een verminderd metaalgedrag van de actieve kobalt nanodeeltjes leidt.

Gebaseerd op de verkregen resultaten kunnen enkele belangrijke conclusies getrokken worden aangaande mangaan-gepromoteerde $Co/TiO_2$ FT-katalysatoren:

a. MnO-gepromoteerde $Co/TiO_2$-katalysatoren zijn uiterst complexe katalysatorsystemen. Dit komt omdat er veel verschillende fasen, zoals $Co_{3-x}Mn_xO_4$, $Ti_2MnO_4$, $Co_{1-x}Mn_xO$ en $Ti_2CoO_4$, gevormd kunnen worden. De oorzaak hiervan moet gezocht worden in de sterke interactie tussen de actieve kobaltfase en de mangaanpromotor enerzijds en de interactie van beide componenten met het dragermateriaal anderzijds. De aanwezigheid van complexe mengsels van actieve fasen (b.v. $Co^0$ en MnO) en toeschouwers (b.v. $Ti_2MnO_4$) die heterogeen op het katalysatoroppervlak gespreid liggen maakt hun spectroscopische

karakterisering lastig. Daarom is een combinatie van spectroscopische en microscopische technieken een uitermate geschikte onderzoeksstrategie.

b. Mangaan, dat als oxidelaag op het oppervlak van actieve kobalt nanodeeltjes voorkomt, heeft een elektronisch promotoreffect. Deze elektronische promotie vertaalt zich duidelijk in de katalysatorselectiviteit, evenals in een verandering van de CO adsorptie-eigenschappen zoals waargenomen met DRIFTS. Derhalve hebben MnO-gepromoteerde katalysatoren dalende hydrogeneringseigenschappen in vergelijking met niet-gepromoteerde katalysatoren. Dit vertaalt zich in een verhoogde productie van alkenen en langere koolwaterstofketens.
c. Mangaan bezit ook structurele en synergistische promotoreffecten. Wanneer mangaan zich aanvankelijk aan de $Co_3O_4$-fase hecht, beïnvloedt het direct de kobaltfase die tijdens reductie wordt gevormd. Bovendien kan mangaan het verlies van de actieve kobaltfase verhinderen door het vormen van een beschermende $Ti_2CoO_4$-fase. Voorts bezit mangaan WGS-gedrag en zou men kunnen zeggen dat promotie door mangaan kan leiden tot de vorming van "ijzerachtige" kobalt nanodeeltjes.
d. Mangaan promotoreffecten zijn duidelijk zichtbaar bij katalysatoren die relatief grote (> 5 nm) kobaltdeeltjes bevatten. Kleinere kobaltdeeltjes worden gedeactiveerd tijdens FT-reactie door bedekking met $TiO_x$-of MnO-fasen.

# List of publications and presentations

## Publications

F. Morales Cano, O.L.J. Gijzeman, F.M.F. de Groot and B.M. Weckhuysen, *Manganese promotion in cobalt-based Fischer-Tropsch catalysis,* Stud. Surf. Sci. Catal. **147**, 2004, 271-276.

F. Morales, F.M.F. de Groot, P. Glatzel, E. Kleimenov, H. Bluhm, M. Havecker, A. Knop-Gericke and B.M. Weckhuysen, *In Situ Soft X-ray Absorption of Co/Mn/$TiO_2$ Catalysts for Fischer-Tropsch Synthesis*, J. Phys. Chem. B **108**, 2004, 16201-16207.

F. Morales, F.M.F. de Groot, O.L.J. Gijzeman, A. Mens, O. Stephan and B.M. Weckhuysen, *Mn promotion effects in Co/$TiO_2$ Fischer-Tropsch catalysts as investigated by XPS and STEM-EELS*, J. Catal. **230**, 2005, 301-308.

F. Morales, D. Grandjean, F.M.F. de Groot, O. Stephan and B.M. Weckhuysen, *Combined EXAFS and STEM-EELS study of the electronic state and location of Mn as promoter in Co-based Fischer-Tropsch catalysts*, Phys. Chem. Chem. Phys. **7**, 2005, 568-572.

F. Morales and B.M. Weckhuysen, *Promotion effects in Co-based Fischer-Tropsch Catalysis*, Catalysis, Royal Society of Chemistry, **19**, 2006, in press.

F. Morales, D. Grandjean, F.M.F. de Groot and B.M. Weckhuysen, *Co/Mn/$TiO_2$ Fischer-Tropsch catalysts investigated by in-situ XAFS at the Co and Mn K-edges,* submitted.

F. Morales, E. de Smit and B.M. Weckhuysen, *Effect of Mn loading on the Fischer-Tropsch performances of Co/Mn/$TiO_2$ catalysts studied by Diffuse Reflectance Infrared Spectroscopy,* in preparation.

## Oral presentations

F. Morales, F.M.F. de Groot and B.M. Weckhuysen, '*Mn promotion effects in Co-based catalysts for the Fischer-Tropsch synthesis*', **5th Netherlands Catalysis and Chemistry Conference**, Noordwijkerhout, The Netherlands, March 2004.

F. Morales, F.M.F. de Groot and B.M. Weckhuysen, '*Physicochemical interaction between transition metal oxides and metal clusters*' **7th Natural Gas Conversion Symposium**, Dalian, China, June 2004.

F. Morales and B.M. Weckhuysen, '*Physicochemical interactions between transition metal oxides and metal clusters: promoter effects in supported metal catalysis*' **228th ACS Fall National Meeting**, Philadelphia,USA, August 2004.

F. Morales, F.M.F. de Groot, D. Grandjean and B.M. Weckhuysen, '*Manganese promotion for Co/Mn/$TiO_2$ Fischer-Tropsch catalysts'* **NIOK Fischer-Tropsch workshop**, Utrecht, The Netherlands, October 2004.

F. Morales, F.M.F. de Groot, D. Grandjean and B.M. Weckhuysen, '*In-situ Spectroscopy for Co/Mn/$TiO_2$ Fischer Tropsch Catalysts*' **6th Netherlands Catalysis and Chemistry Conference**, Noordwijkerhout, The Netherlands, March 2005.

F. Morales, F.M.F. de Groot, D. Grandjean and B.M. Weckhuysen, '*Combined XPS, XAFS and STEM-EELS to study the electronic state and location of manganese in Co/Mn/$TiO_2$ catalysts for Fischer-Tropsch synthesis'* **19th North American Catalysis Society Meeting**, Philadelphia, USA, May 2005.

## Poster presentations

E. de Smit, F. Morales and B.M. Weckhuysen, '*Investigation of the active site composition of Manganese-promoted Co/$TiO_2$ Fischer-Tropsch catalysts'* **6th Netherlands Catalysis and Chemistry Conference**, Noordwijkerhout, The Netherlands, March 2005.

F. Morales, F.M.F. de Groot, B.M. Weckhuysen, *In-situ soft X-ray absorption and STEM-EELS of Co/Mn/$TiO_2$ Fischer-Tropsch synthesis*, **7th European Congress on Catalysis**, Sofia, Bulgaria, August 2005.

# Appendix A

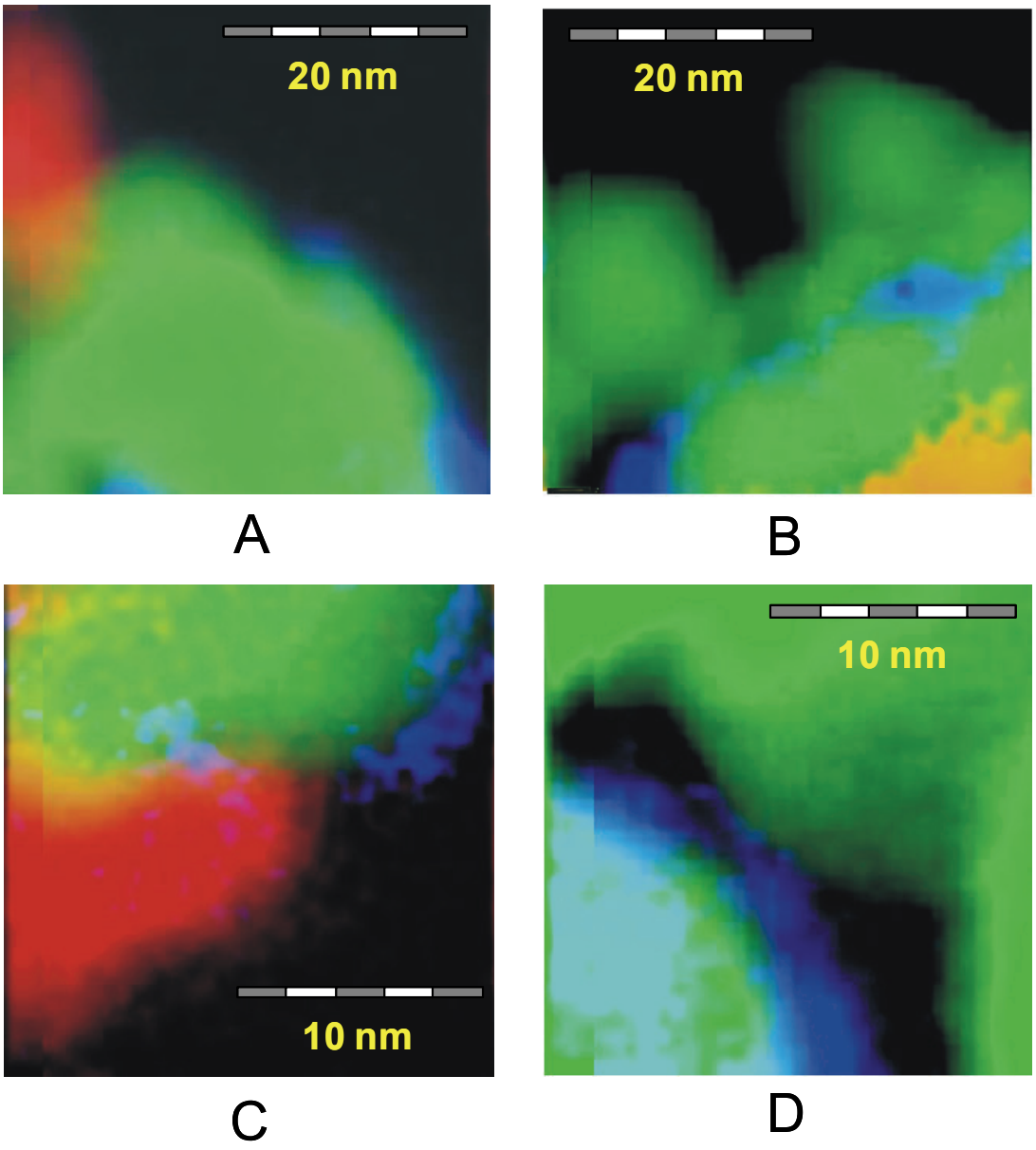


**Fig. A1.** Colored EELS chemical maps for the I-CoMn catalyst after calcination. The images have been created by merging the individual EELS chemical maps for Ti, Co and Mn given in green, red and blue colors, respectively. Images A and B show the presence of a large $Co_3O_4$ cluster (> ~20 nm) and a $MnO_2$ compound mainly covering the $TiO_2$ surface without interacting with the $Co_3O_4$. In images B and D the $MnO_2$ phase is clearly seen at the $TiO_2$ surface in a highly dispersed state. The overall situation for this sample is that $MnO_2$ and $Co_3O_4$ compounds are distributed separately at the surface of the $TiO_2$ support.

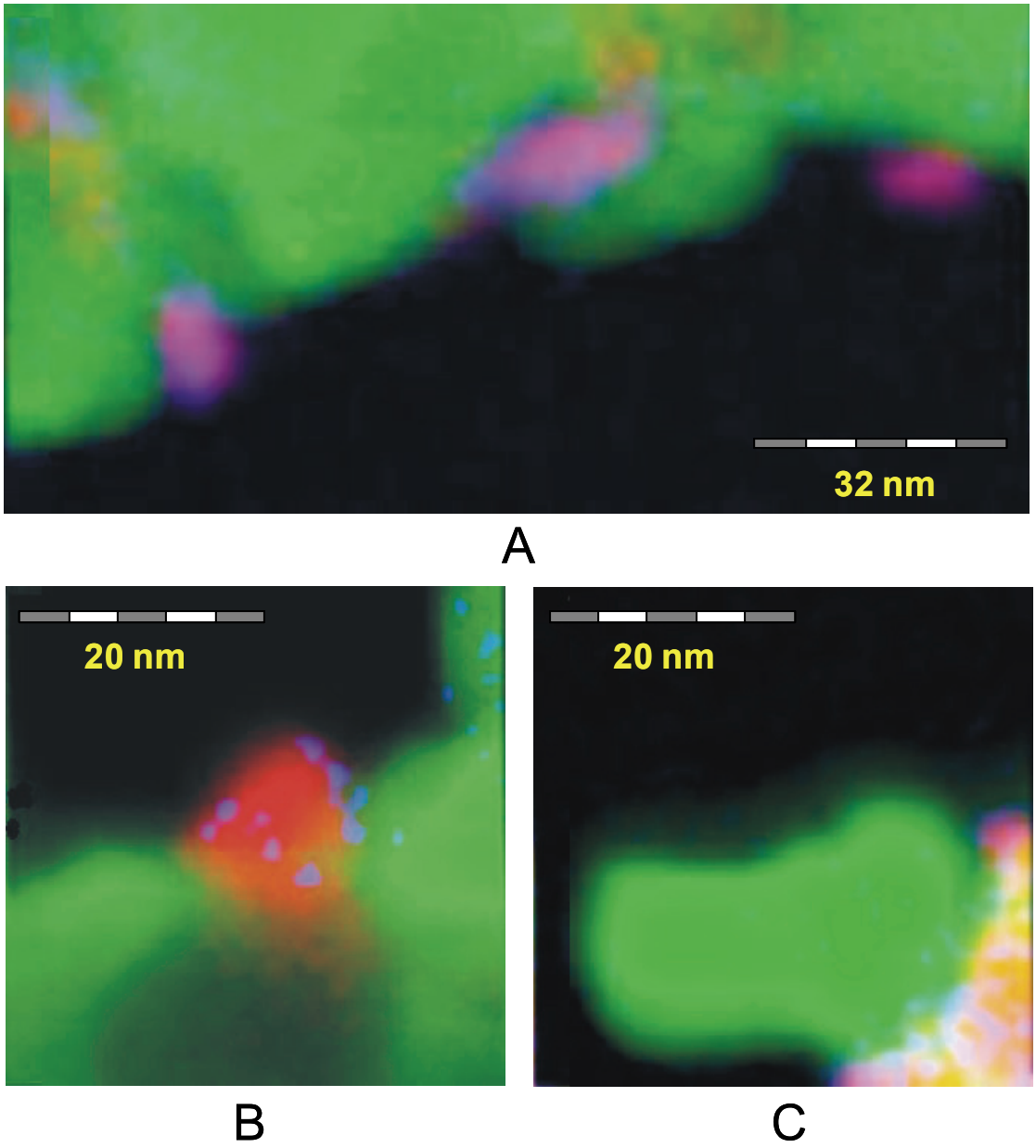


**Fig. A2.** Colored EELS chemical maps for the H-CoMn catalyst after calcination. Image A nicely illustrates the presence of particles in the range of 8-15 nm, which are composed of a mixture of $MnO_2$ and $Co_3O_4$, leading to a purple color (red + blue). This result was attributed to a coverage of the $Co_3O_4$ particles by $MnO_2$, resulting in the formation of $Co_{3-x}Mn_xO_4$ solid solutions. In images B and C a clear association of cobalt and manganese can also be seen. The overall situation for this sample is that the $MnO_2$ and $Co_3O_4$ compounds are closely associated with each other at the support surface.

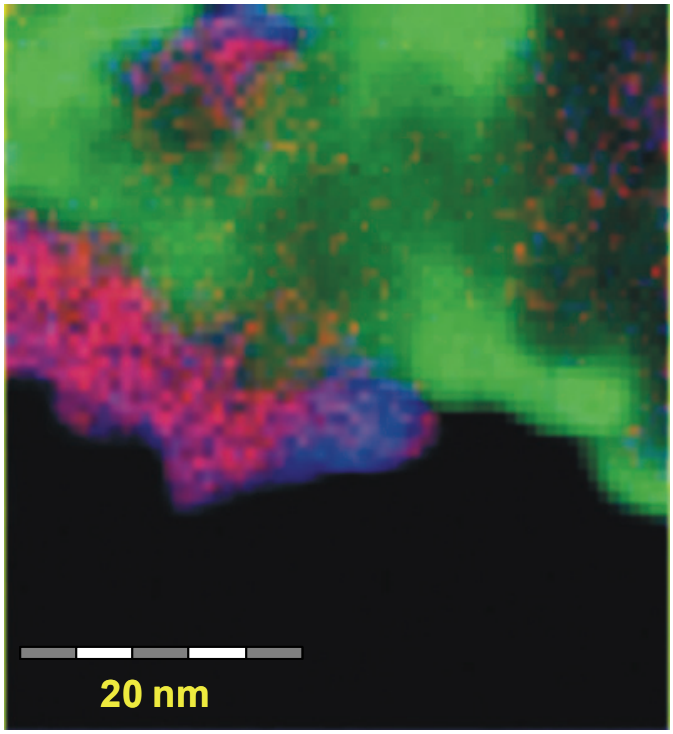


**Fig. A3.** Colored EELS chemical map for the Hcop-CoMn catalyst after calcination. The image nicely illustrates the intimate association of cobalt and manganese oxides to form mixed compounds, resulting in a purple colored cluster. The observed compound contains a rich-Mn area visible in blue. EXAFS results have indicated that the Co-Mn clusters are composed of spinel-type solid solutions $Co_{3-x}Mn_xO_4$. The average composition as estimated by XRD is $Co_{2.1}Mn_{0.9}O_4$.

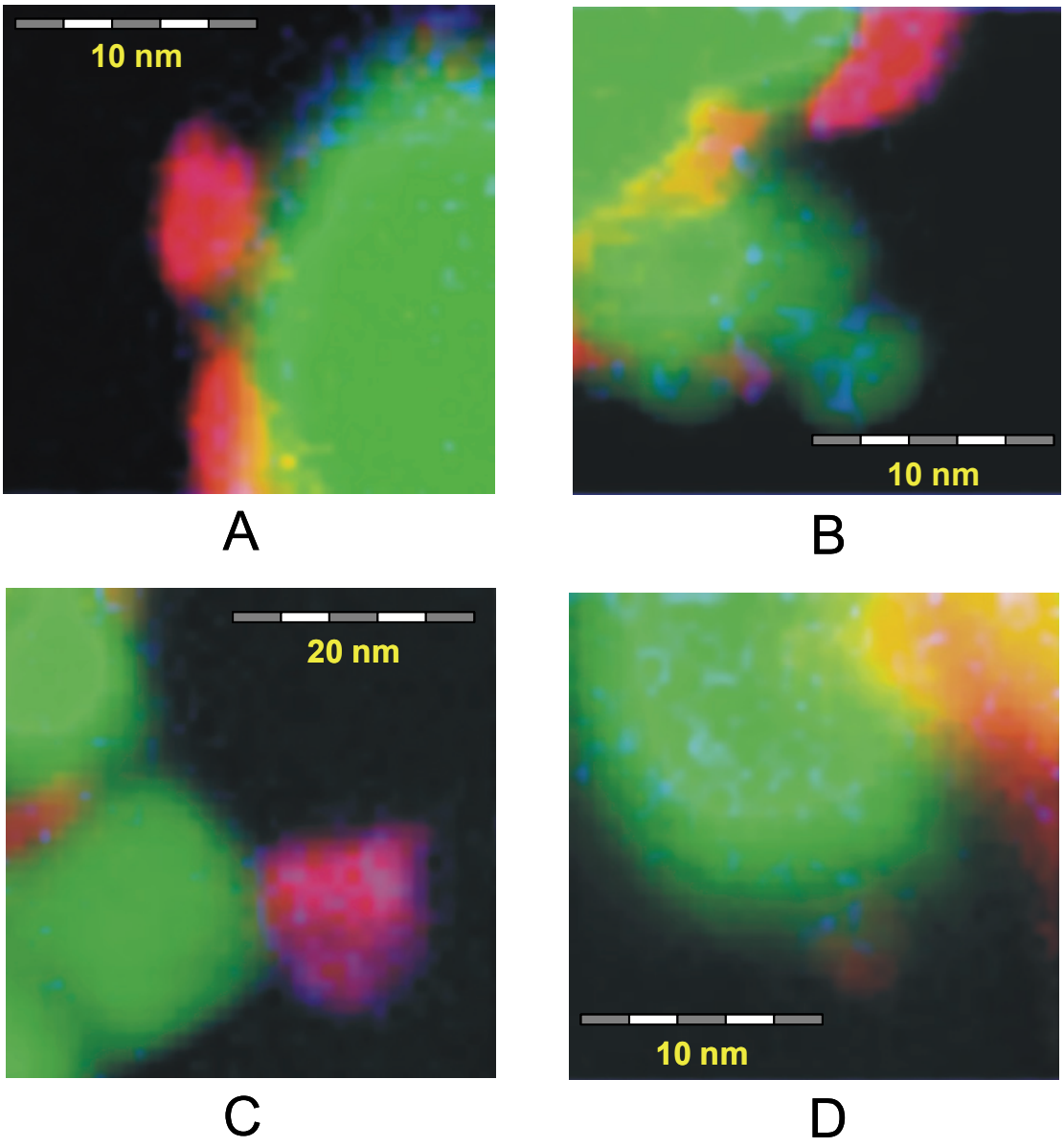


**Fig. A4.** Colored EELS chemical maps for the I-CoMn catalyst after reduction and passivation. The images have been created by merging the individual EELS chemical maps for Ti, Co and Mn given in green, red and blue colors, respectively. They reveal a highly dispersed manganese phase at the $TiO_2$ surface (images A, B and D). This dispersed phase was revealed to be a $Ti_2MnO_4$-type phase. Additionally, small amounts of MnO can be also seen at the surface of the cobalt particles in images B and C. The size of the cobalt particles estimated by STEM-EELS is in the range of 5-12 nm, which is much smaller than before reduction.

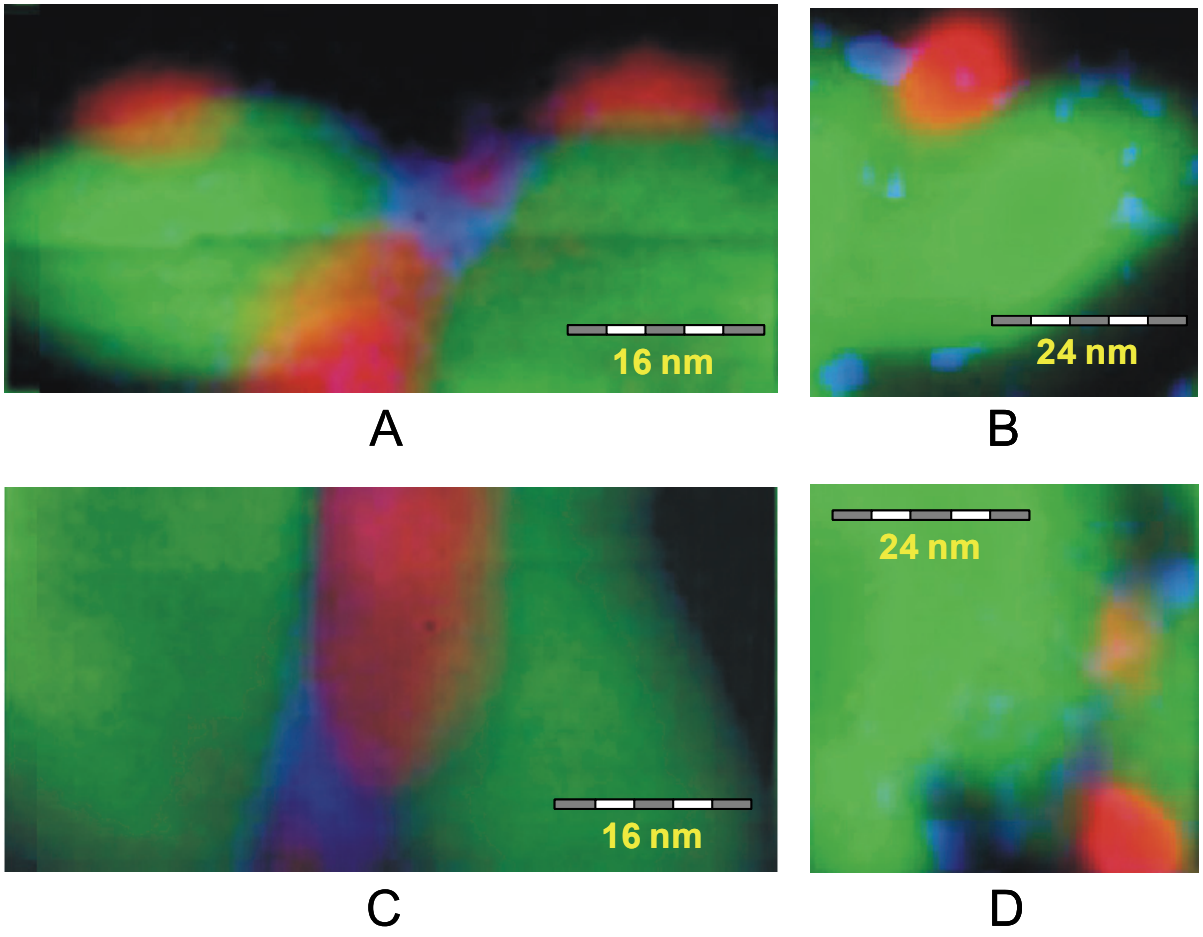


**Fig. A5.** Colored EELS chemical maps for the H-CoMn catalyst after reduction and passivation. Images A and C show that manganese is present in the form of agglomerates (composed of MnO and $Mn_{1-x}Co_xO$) mainly concentrated in the vicinity of the cobalt particles. The manganese is also detected at the surface of the cobalt particles as $Mn_{1-x}Co_xO$, as well as in a highly dispersed state at the $TiO_2$ surface (i.e., as a $Ti_2MnO_4$-type phase). The size of the cobalt particles estimated by STEM-EELS is in the range of 12-20 nm, which is much larger than that found for the I-CoMn catalyst.

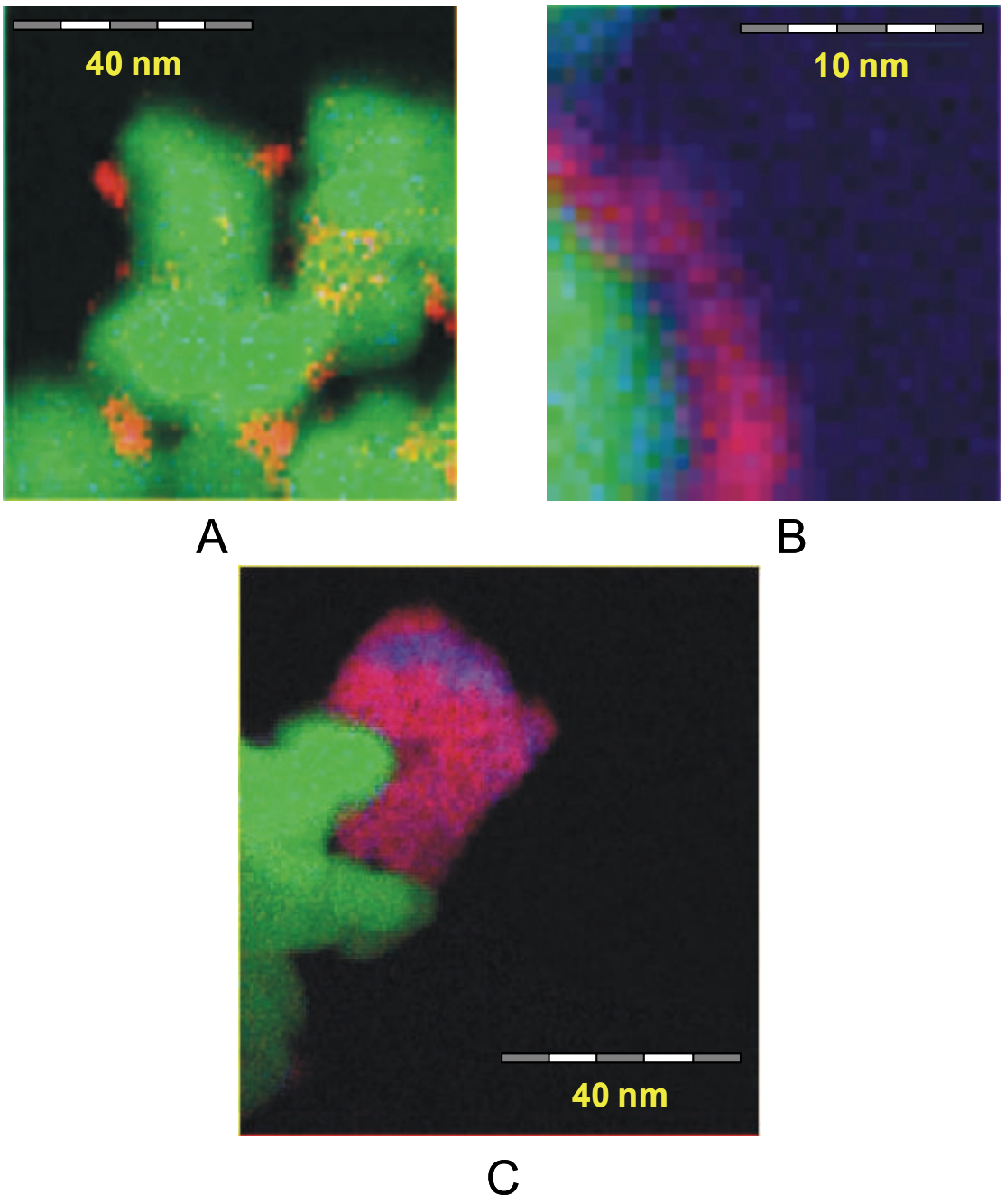


**Fig. A6.** Colored EELS chemical maps for the I-MnCo (A and B) and Hcop-CoMn (C) catalysts after reduction and passivation. Image A shows the presence of small cobalt particles with sizes around 3-7 nm, and the manganese phase is hardly visible due to its high level of dispersion. In image B the cobalt forms a layer at the $TiO_2$ surface and manganese can be observed in a highly segregated state. For the Hcop-CoMn catalyst image C nicely illustrate the mixture of CoO and MnO to form a rock-salt type ($Mn_{1-x}Co_xO$) solid solution.

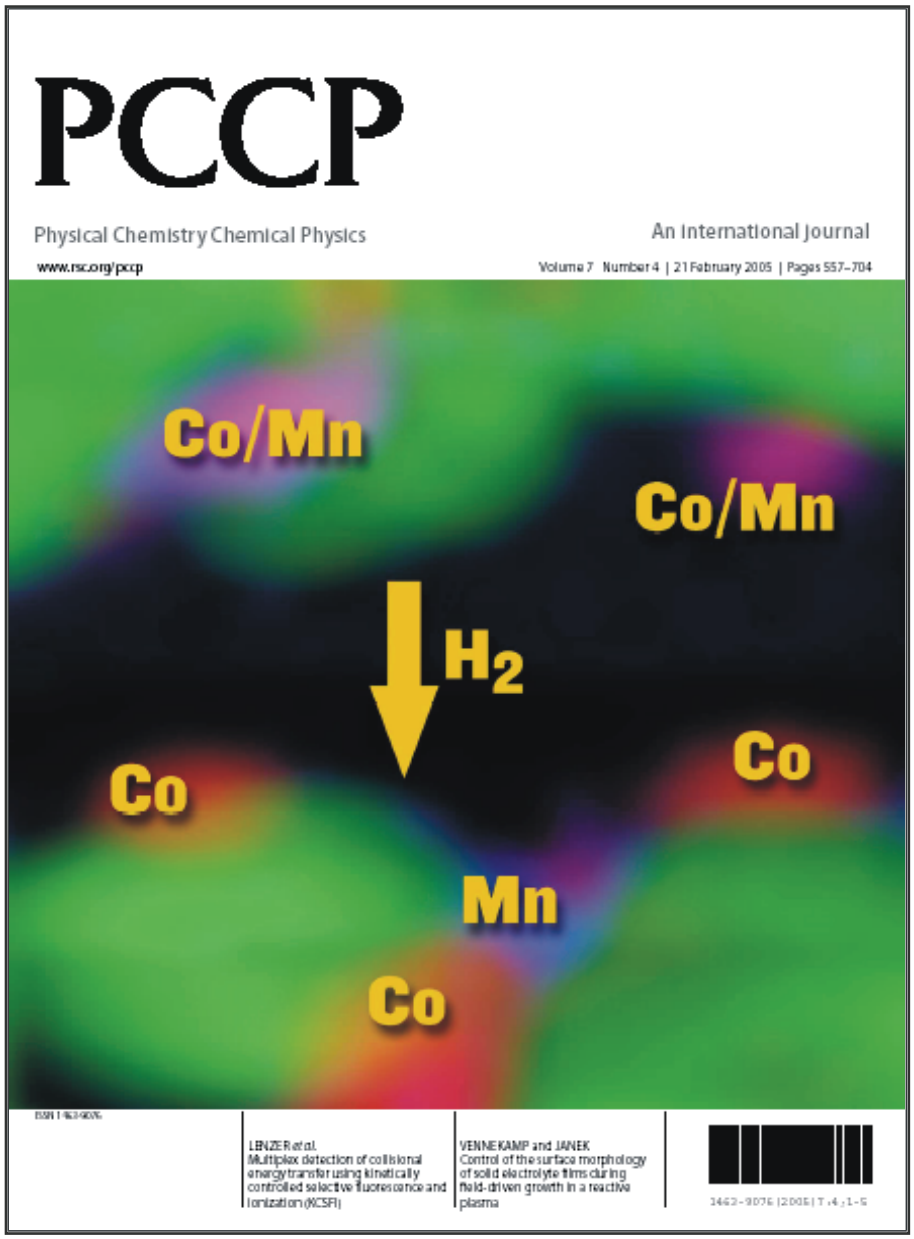


**Fig. A7.** Cover of the *Physical Chemistry Chemical Physics* journal, issue 4, 2005.

# Acknowledgements

So this is the end, with these last pages of the book I accomplish my PhD work after four years and a couple of months mostly learning, thinking, experimenting, catalyzing, travelling, and a lot of writing. Now I'm eager to see what's coming next. But before that, I wish to express my sincerely gratitude to all the people who have contributed to this work as well as to those who have helped in making this period of time pleasant and enjoyable. Doing my PhD in the Netherlands has been a fruitful experience both at a professional and personal level and has afforded me interacting with interesting people around the world. No doubt that discovering a life in the Netherlands was worth a PhD thesis.

Bert, my promoter, if you hadn't offered me this PhD position probably I would have never experienced life in the Netherlands. I am deeply grateful for the opportunity you have given me to work in your group and do interesting research within this beautiful environment in Utrecht. I am glad that I accepted this research project having a direct collaboration with Shell Global Solutions. Learning and investigating spectroscopy in the field of Fischer-Tropsch catalysis has been definitively stimulating and challenging. Thank you for all those scientific and friendly discussions, in which you always transmitted me enthusiasm and courage, and which inspired me to become a better scientist. You have also contributed to improve the form of my thesis and I sincerely thank you for that.

Frank, it has been a pleasure to have you as my co-promoter. With you I've done pretty interesting experiments with X-rays and electrons and I've been able to make some fruitful collaborations. Your help and support in some of the data interpretation has been crucial to improve the quality of this work. You also performed the theoretical calculations presented in chapter 7. Thank you for all you have done.

Emiel, I am glad you chose to be my student during the final year. You have done a great job and your contribution is nicely reflected in chapter 5. All those long sessions in front of the IR spectrometer finally paid off. Soon it will be your turn to investigate some promoters for Fischer-Tropsch catalysts in your own PhD and I wish you a lot of success. My gratitude also goes to Tom and Fouad for their contribution to the IR results.

Didier, thank you for being much involved in the XAFS results and for your important contribution to this thesis. I enjoyed the time we spent with the XAFS experiments in Grenoble during that hectic and exciting night shift. I appreciate your help with the XAFS analysis and all those friendly discussions we had. I wish you the best in France.

Onno, it's a pity that I did not too often seek advice from you. Thank you for all the conversations we had on the XPS results and for your help to handle the XPS analysis software. I hope you spent a nice holidays in the beautiful city of Madrid.

Heiko Oosterbeek, you have been our Shell supervisor and have contributed to my understanding with some of the results. I am very grateful to you for your guidance and knowledgeable discussions. My sincerely gratitude also goes to Herman Kuipers and Carl Mesters for the enthusiastic and fruitful discussions, and to Shell Global Solutions for the funding, which has enabled to carry out the research presented in this thesis.

Gerbrand and Ferry, it has been a pleasure to have you as office-mates for all these years. We always shared a friendly atmosphere, although sometimes a bit "cold" when trying to adjust the optimum temperature in the office :-). I will always remember those funny FIFA competitions we had on Fridays and when you tried to beat Real Madrid. I appreciate your willingness for help in all those "little things", such as *Dutch to English* translations, etc. I wish you the best in your careers. Ferry, we've been office-mates from the beginning of our PhDs until the end and I'll be very glad to see you as a "paranimf". Finally my last office-mate, Nadia, it was nice having you around these six months and to share some cheerful chatting with you. I wish you good luck preparing catalysts and lots of fun in Utrecht.

Leendert, since our projects have been very much related and both sponsored by Shell, we've had the chance to work together and exchange many ideas. We also experienced together the exciting journey to the NGCS conference and discovered a bit of China. By the way, that trip was with no doubt one of the highlights of my PhD period. Thank you for all the nice and funny moments we spent in Dalian, Hamburg, Grenoble and Utrecht. My gratitude also goes to Krijn de Jong for his enthusiastic discussions on the TEM results and his interesting contribution to the Shell meetings.

During my trip to the NAM conference in US I had some fun hanging out in downtown Philadelphia with some colleagues. Thanks Stephan, Cristina, Xander, Leon and Harry for those enjoyable days.

My gratitude also goes to all the people who helped performing my *in situ* XAFS measurements in the different synchrotrons. First, the XAFS team in Grenoble: Didier, Leendert and Yihua. Second, the soft XAS team in Berlin: Frank, Daniel, Peter, Willem and Ingmar. And finally the XAFS team in Hamburg: Ad, Kees, Leendert and Harry. I have to say that I really enjoyed some of the hectic moments setting up the experiments and collecting data, as well as other more relaxed moments driving, chatting and dinning in cozy restaurants.

There are many other people who also contributed to this thesis and I wish to thank all of them: Ad Mens (XPS), Cor (TEM), Vincent (TPR and $H_2$-chemisorption), Marjan (SEM), Ad (XRF), Fred (technical support) and Jan den Boesterd (cover design). Odile Stephan and Alex

Glotter thanks to you and your group in Orsay for the opportunity to perform the STEM-EELS experiments. The chemical maps have enabled the design of a beautiful cover picture.

Thanks a lot Monique, Dymph, and Thea for being always so friendly and helpful.

I wish to thank the whole Catalysis Department for all the extra-work activities: coffee breaks, *borrels*, sports, football games, department days, etc, and particularly all the other foreign colleagues with whom I have spent more time. Thank you all for those enjoyable moments gathering in the canteen for the lunch breaks and also for the social events. Agnieszka I appreciated that you read my thesis and checked for mistakes. I wish you all good times in Utrecht.

My social life outside work could not have been so cheerful without meeting some nice people throughout these four years: Juan (Spain), Wojtek (Poland), Virginia (Argentina), Alberto (Spain), Lorenzo (Italy), April (Indonesia), Timo (Venezuela), Sana (Slovenia), Elsa (France), Leo (Indonesia), Maarten (Holland), Jeroen (Holland), Giorgous (Greece), Gianluca (Italy), Eyk (Germany), Hugo (Portugal), my flatmate DJ David (Holland) and others. Many of you no longer live in the Netherlands but I hope that you will pay a visit once in a while. I pretty much enjoyed all those nights at *Mick O'Connels*, *Jam Primus*, and those weekends hanging out in Utrecht partying and chatting, and I hope that we'll keep our friendship for good.

Un saludo muy fuerte para todos mis amigos de Madrid con los que a pesar de la distancia, hemos mantenido el contacto y una fuerte amistad. Fue realmente grande veros a muchos de vosotros por Utrecht y teneros de invitados en mi casa (Alfredo, Israel, Diego, Alberto, Carlos y Ester, y Jorge). A ver si alguno os animais y os escapais unos dias de Madrid para verme en la defensa, que luego habra una buena fiesta de celebración!.

Querida mama y querido papa, como pasa el tiempo! ya son mas de cuatro años desde que me vine a Holanda y tengo que decir que nunca he dejado de echaros de menos a vosotros y a los hermanos, aunque por lo menos nos seguimos viendo muy a menudo. Gracias por vuestro apoyo durante todo este tiempo, sin vosotros yo no seria nadie. Me encantó veros unos dias en Utrecht, y tambien a Sole y Jorge!. Un abrazo muy fuerte para papa, mama, mis hermanos Sole, Carlos, Javier y Lucia, mi cuñado Jorge y mis sobrinitos. Vaya donde vaya y este donde este, siempre me tendreis cerca. Os quiero mucho!

Finally, I wish to thank a very special person with whom I have shared great and unforgettable days during these last months. Rita, you've given me a lot of strength to finish the thesis and you have made this last stage of my PhD definitely the most pleasant. See you soon, szeretlek!

***Fernando***

# Curriculum Vitae

Fernando Morales Cano was born on September 23, 1977 in Madrid, Spain. In 1995 he received his secondary school diploma (Science studies) from Instituto de San Pedro in Tres Cantos (Madrid). After secondary school he studied Chemistry at the University Autonoma de Madrid, from which he graduated (Master's Degree) in June 2001 with the specialty of Organic Chemistry. During his last year study at the university he was awarded with a scholarship in Repsol YPF (Spanish Petrochemistry Company), where he carried out a period of six months research at the department of propylene oxide. His work covered the synthesis of catalysts and testing in olefin oxidation reactions. In December 2001 he moved to Utrecht University, Department of Inorganic Chemistry and Catalysis (Utrecht, The Netherlands) to start his PhD training under the supervision of Prof. B.M. Weckhuysen. His research project was financed by Shell Global Solutions and most of his relevant results are presented in this thesis.